

1. Introduction

The stable low-earth orbital speed of a satellite is approximately 8 km/s. When a space vehicle enters the earth's atmosphere with this speed, the kinetic energy of the gas (viewed from the reference frame of the vehicle) is converted to thermal energy in the stagnation region of the vehicle. The specific enthalpy of the gas in the stagnation region is then approximately

$$h \simeq U^2/2 = 32\text{MJ/kg}.$$

The specific heat of a diatomic perfect gas of molecular weight 29 is

$$c_p = \frac{7}{2} \frac{R}{\mathcal{M}} \simeq 1000\text{J/(kgK)}.$$

Hence, the temperature of the gas, if it were to remain a perfect gas, would rise to

$$T = h/c_p \simeq 32000\text{K}.$$

At this high temperature, the mean value of the molecular speed would be approximately 3000 m/s, and the number of molecular collisions for which the relative motion has a kinetic energy exceeding the dissociation energy of the molecule becomes significant. Consequently, a significant part of the thermal energy is used for dissociation and the stagnation temperature is substantially reduced.

The perfect gas model is therefore unsatisfactory for this region. The dissociation energy for nitrogen is approximately 34 MJ/kg and that for oxygen 17 MJ/kg. These are comparable magnitudes to $U^2/2$. Even if the gas remains in thermodynamic equilibrium, we therefore need a new model to describe the relation between pressure, density and temperature to replace the equation of state of the perfect gas (which approximates the behavior of many gases so well over a wide range of conditions).

However, if we consider a material element of the free-stream gas and follow it across the shock, we observe that it experiences a sudden jump in state. In order for it to regain thermodynamic equilibrium after passing the shock, it must be dissociated via many molecular collisions. This process takes time, the so-called relaxation time. We can no longer make the assumption (usual in continuum perfect gas dynamics) that the gas is in thermodynamic equilibrium immediately after the thin shock, but we have to develop a model for the relaxation zone as well. The fact that this introduces a characteristic time changes the type of the material model in a fundamental way, as we shall see in examples. The first task, however, is to introduce an equilibrium model, i.e., one that relates the state variables for the case when the gas is in thermodynamic equilibrium.

Both for the equilibrium and the non-equilibrium models, we shall restrict the discussion in most of this course to a simplified representation of gas which, in its undissociated state, is a symmetrical diatomic gas, in order to understand the new features of flows in this regime with the simplest model that accounts for the essential features. A refinement for more accurate (and more elaborate) representation is left to a later part of the course.

Chemical Equilibrium

Consider a system enclosed in an adiabatic wall. Let hydrogen and oxygen be present in the system at room temperature. This is a state of constrained equilibrium, since, in the true, unconstrained equilibrium state, the hydrogen and oxygen would be combined to water according to the reaction



Since this reaction occurs only infinitely slowly at room temperature, we speak of a constrained equilibrium.

The constraint may be removed by introducing a platinum catalyst which causes the reaction to proceed spontaneously. Since this is a nonequilibrium adiabatic process, the entropy increases

$$\Delta S > 0. \quad \text{with rigid walls} \quad (A2)$$

Thus the entropy of the unconstrained equilibrium state is higher than that of the constrained equilibrium state. Since the system is adiabatic, the internal energy E and volume V remain constant. We may therefore express the results as follows:

For given values of E and V the entropy of a system in unconstrained equilibrium has a maximum value.

In unconstrained equilibrium we may write

$$S = S(E, V). \quad (A3)$$

To describe the system in a constrained equilibrium state we must introduce at least one further parameter ξ say, which in our example could be the ratio of the mass of H_2 to that of H_2O , such that

$$S = S(E, V, \xi). \quad (A4)$$

A necessary condition for unconstrained equilibrium would then be

$$\frac{\partial S(E, V, \xi)}{\partial \xi} = 0, \quad \frac{\partial^2 S(E, V, \xi)}{\partial \xi^2} < 0. \quad (A5)$$

This condition permits us to determine (for a given function $S(E, V, \xi)$) what value ξ takes at a given E and V in unconstrained equilibrium.

Since the system is homogeneous even in constrained equilibrium and therefore has a uniquely definable temperature T , and pressure p , the Gibbs relation

$$TdS = dE + pdV$$

may be extended to our situation:

$$TdS = dE + pdV + \Gamma d\xi \tag{A6}$$

where the new variable Γ has the following meaning

$$\Gamma = T \frac{\partial S(E, V, \xi)}{\partial \xi} = - \frac{\partial E(S, V, \xi)}{\partial \xi} \tag{A7}$$

In a situation in which many different reactions between $n + 1$ species may occur,

$$S = S(E, V, \xi_1, \dots, \xi_n)$$

and

$$TdS = dE + pdV + \sum_{i=1}^n \Gamma_i d\xi_i$$

$$\Gamma_i = T \partial S(E, V, \xi_{k \neq i}, \xi_i) / \partial \xi_i.$$

The condition that S has a maximum for fixed E and V is equivalent to the condition that the free enthalpy G has a minimum at constant p and T .

To show this, consider a small system A whose wall is flexible and diathermic, contained in a huge system B which in turn is enclosed by a rigid, adiabatic wall. The temperature and pressure of the two systems will thus always be the same. Let A be initially in a constrained equilibrium state and proceed by a suitable process to unconstrained equilibrium. Let B be in unconstrained equilibrium before and after the process. Flexible diathermic inner walls and adiabaticity of the outer walls give

$$\Delta V_A = -\Delta V_B$$

$$\Delta E_A = -\Delta E_B$$

Also

$$\Delta S = \Delta S_A + \Delta S_B \geq 0 \tag{A8}$$

Since p, T are constant, we may integrate

$$TdS = dE + pdV$$

for system B

$$\Delta S_B = \frac{1}{T}(\Delta E_B + p\Delta V_B) = -\frac{1}{T}(\Delta E_A + p\Delta V_A)$$

Substituting in ΔS above,

$$\Delta S = \Delta S_A - \frac{1}{T}\Delta E_A - \frac{p}{T}\Delta V_A = \frac{1}{T}(T\Delta S_A - \Delta E_A - p\Delta V_A) \geq 0,$$

or

$$\Delta(TS_A - E_A - pV_A) \geq 0,$$

so that

$$\Delta G_A = \Delta(E - TS + pV)_A \leq 0. \quad (A9)$$

Thus the Gibbs enthalpy of system A always decreases, or at best remains constant. The Gibbs enthalpy therefore goes to a minimum at unconstrained equilibrium for given T, p .

$$\frac{\partial G(T, p, \xi)}{\partial \xi} = 0, \quad \frac{\partial^2 G(T, p, \xi)}{\partial \xi^2} > 0$$

– equil. (A10)

Now return to the chemical reaction $2H_2 + O_2 \rightleftharpoons 2H_2O$. If x_1, x_2, x_3 are the masses of H_2, O_2, H_2O resp., dx_1 is not independent of dx_2 . If m_1, m_2, m_3 are the molecular masses we may see that

$$\begin{aligned} dx_1 &= 2m_1 d\lambda \\ dx_2 &= m_2 d\lambda \\ dx_3 &= -2m_3 d\lambda \end{aligned}$$

describes a suitable relation between the changes of masses for a given degree $d\lambda$ of change in the reaction. More general reactions are described by

$$dx_i = \nu_i m_i d\lambda.$$

The ν_i are called stoichiometric coefficients. From (A 10) the reaction will proceed until G reaches a minimum corresponding to equilibrium. Hence at equilibrium,

$$\frac{dG}{d\lambda} = 0. \quad (A11)$$

It is necessary to express G for a mixture of (ideal) gases. To do this, recall that

$$p = \sum \rho_i R_i T = \sum \frac{x_i}{V} R_i T = \sum p_i$$

and

$$S = \sum x_i s_i(\nu_i, T) = \sum S_i$$

$$H = \sum x_i h_i(T)$$

since the variables H and S are extensive and because of Dalton's law of partial pressures. H and S may be written as

$$H = \sum x_i \left[\int (c_p)_i dT + (h_o)_i \right]$$

$$S = \sum x_i \left[\int (c_p)_i \frac{dT}{T} - R_i \ln \frac{p_i}{p_*} + (s_o)_i \right],$$

where p_* is the reference pressure at which h and s take the values h_o and s_o . Hence

$$(c_p)_i(T) \text{ assumed known} \quad G = H - TS = \sum x_i \left[w_i(T) + R_i T \ln \frac{p_i}{p_*} \right] \quad (A12)$$

where w_i is used as an abbreviation for the lengthy expression resulting from forming $H - TS$. It is a function of T .

Returning to (A11) we now see that to satisfy it,

$$\frac{dG}{d\lambda} = \sum \left\{ \frac{dx_i}{d\lambda} \left[w_i + R_i T \ln \frac{p_i}{p_*} \right] + x_i R_i T \frac{d}{d\lambda} \ln \frac{p_i}{p_*} \right\} = 0 \quad (A13)$$

Consider first the last term in the curly brackets: it is

$$\sum \frac{x_i R_i T}{p_i} \frac{dp_i}{d\lambda} = \sum \frac{x_i R_i T V}{x_i R_i T} \frac{dp_i}{d\lambda} = V \frac{dp}{d\lambda}.$$

At constant pressure, this is zero. Hence the requirement (A13) boils down to

$$\sum [\nu_i m_i w_i(T) + \nu_i m_i R_i T \ln \frac{p_i}{p_*}] = 0$$

or

$$\sum \ln \left(\frac{p_i}{p_*} \right)^{\nu_i} = -\frac{1}{RT} \sum \nu_i m_i w_i(T).$$

Rewriting this as a product:

$$\Pi \left[\left(\frac{p_i}{p_*} \right)^{\nu_i} \right] = K(T) = \exp \left[\frac{-\sum \nu_i m_i w_i(T)}{RT} \right]$$

(A14)

This is the Law of Mass Action, which constrains the partial pressures for chemical equilibrium. The numerator of the exponential may be expressed in terms of the energy released in the reaction. For example, in the dissociation of a simple diatomic gas, it is simply the dissociation energy. The left hand side may also be expressed as a product over the concentrations, and this form will actually be used in the equilibrium model for this part of the course.

REVIEW OF STATISTICAL MECHANICS

There are seven conserved scalar variables of motion: The three components of linear momentum, the three components of angular momentum, and the energy. If we deal with macroscopic systems, the sum of the contributions to the linear momentum from the individual particles gives the linear momentum of the system as a whole, *i. e.*, is a property of the global motion of the system relative to an inertial frame of reference. We consider only systems that are stationary or that move with constant velocity relative to an inertial frame. The same applies to the angular momentum, and we consider only systems that are not rotating as a whole.

Thus the only conserved quantity that characterizes the macroscopic systems of interest to us is the energy. In an insulated system of constant volume, E and V are constant, and the microscopic arrangement of the particles is changing all the time at constant energy. There is an extremely large number of possible ways in which the system can be arranged to have the same energy E . We speak of a very large number of microstates of the system. The probability of each microstate of a system depends on how often that microstate occurs in a very long time, compared with the rest of the microstates. There is no particular reason to suppose that any one microstate is more probable than any other, each has the same energy that characterizes it. The fundamental assumption of statistical mechanics is that:

All microstates of a system that have the same energy are equally probable.

Put another way, the probability that a system is in a particular microstate depends only on the energy of the microstate:

$$P = P(E).$$

Now consider an ensemble of a very large number of closed systems, all prepared in the same way, and all in equilibrium with a huge heat reservoir which has a particular temperature T . Otherwise each system is insulated. The energy of a particular system of the ensemble is then able to fluctuate around the equilibrium value as it interacts with the reservoir. What is the probability that one of the systems in this ensemble is in a particular microstate with energy E ?

Consider two of the systems of the ensemble and call them A and B . Let the probability that system A is in a microstate with energy E_A be $P_A(E_A)$. Similarly $P_B(E_B)$. Now consider A and B together as a composite system. The probability that $A + B$ is in a microstate with

energy E_{A+B} we call $P_{A+B}(E_{A+B})$. The individual systems behave independently, so that

$$P_{A+B}(E_{A+B}) = P_{A+B}(E_A + E_B) = P_A(E_A)P_B(E_B).$$

If three functions are related as in

$$f_1(x)f_2(y) = f(x+y),$$

the functions f_1 and f_2 have certain properties: Differentiating with respect to x ,

$$f_1'(x)f_2(y) = f'(x+y).$$

The prime denotes differentiation with respect to the argument of the function. Similarly,

$$f_2'f_1 = f'.$$

Dividing both of these by f_1f_2 ,

$$\frac{f_1'}{f_1} = \frac{f'}{f_1f_2} = \frac{f_2'}{f_2}.$$

The left side ~~depends only on x~~ , the right side ~~depends only on y~~ , so ~~that~~ both sides must be independent of both x and y . *is independent of y* *is independent of x* *to be equal,*

It follows that

$$\frac{1}{P_A} \frac{dP_A}{dE_A} = \frac{1}{P_B} \frac{dP_B}{dE_B} = -\beta,$$

where β is independent of the two energies and may depend only on properties of the reservoir and is the same for all the systems of the ensemble. Hence,

$$P(E) = C \exp(-\beta E).$$

The constant C is determined by the normalization condition *(system has to be in one of its possible microstates)*

$$\sum_k P(E_k) = C \sum_k \exp(-\beta E_k) = 1,$$

where the sum is understood to go over all *possible* microstates.

Now introduce the partition function

$$Q = \frac{1}{C} = \sum_k \exp(-\beta E_k).$$

If Q is known, all macroscopic thermodynamic properties of the system can be obtained.

For example, the average energy of the system

$$\bar{E} = \sum_k E_k P(E_k) = \frac{1}{Q} \sum_k E_k \exp(-\beta E_k).$$

We may relate this to the derivative of Q w.r.t. β :

$$\bar{E} = -\frac{\partial \ln Q}{\partial \beta}.$$

The value of β

Consider a monatomic gas in which particle i has kinetic energy ε_i . We can determine the sum in Q approximately by pretending that the energy is smoothly distributed. This approximation is good if the quantum states are close together. In general, the energy of a particle depends on its position and velocity. We therefore have to integrate the probability that a particle is in a particular volume element of space and has a particular velocity over all physical space and velocity space for all particles, in order to calculate Q .

$$Q = \int_V \int_V \dots \int_V \int_{-\infty}^{\infty} \int_{-\infty}^{\infty} \dots \int_{-\infty}^{\infty} e^{-\beta\varepsilon_1} e^{-\beta\varepsilon_2} \dots e^{-\beta\varepsilon_N} d\mathbf{r}_1 d\mathbf{r}_2 \dots d\mathbf{r}_N dv_1 dv_2 dv_3 \dots dv_N.$$

Here the \mathbf{r} are the position vectors and the \mathbf{v} are the velocity vectors of the N particles. With the assumption that the interaction potential energy is negligible, the integrals over the position all contribute a factor V , and the integrals over the velocities are independent of each other, so that

$$Q = V^N \int_{-\infty}^{\infty} \int_{-\infty}^{\infty} \int_{-\infty}^{\infty} e^{-\beta m_1 v_1^2 / 2} dv_{1x} dv_{1y} dv_{1z} \dots \int_{-\infty}^{\infty} \int_{-\infty}^{\infty} \int_{-\infty}^{\infty} e^{-\beta m_N v_N^2 / 2} dv_{Nx} dv_{Ny} dv_{Nz}.$$

If the particles are identical, the integrals over the velocities are all the same, so

$$Q = V^N \left(\int_{-\infty}^{\infty} e^{-\beta m v^2 / 2} dv \right)^{3N},$$

or

$$Q = V^N \left(\frac{2\pi}{\beta m} \right)^{3N/2}.$$

This is the partition function of a perfect, monatomic gas of N identical particles. Note that, since this may be written as

$$Q = \left[V \left(\frac{2\pi}{\beta m} \right)^{3/2} \right]^N,$$

the concept of a particle partition function

$$Q_p = V \left(\frac{2\pi}{\beta m} \right)^{3/2}$$

is useful in this case. We can now get the internal energy of the system from this by differentiation of the logarithm w.r.t. β :

$$\bar{E} = -\frac{\partial \ln Q}{\partial \beta} = \frac{3N}{2\beta}.$$

For a perfect, monatomic gas the internal energy is

$$\bar{E} = \frac{3}{2}NkT,$$

where k is Boltzmann's constant, so that

$$\beta = \frac{1}{kT}.$$

Although this derivation has assumed a perfect, monatomic gas, it is a general result. Recall that β has to be the same for all systems at the same temperature, and that it may depend only on the temperature. The above result shows how it depends on the temperature.

Other thermodynamic functions

Think of Q as a function of β and V :

$$Q = Q(\beta, V).$$

Then,

$$d(\ln Q) = \frac{\partial \ln Q}{\partial \beta} d\beta + \frac{\partial \ln Q}{\partial V} dV$$

From E above,

$$d(\ln Q) = -E d\beta + \frac{\partial \ln Q}{\partial V} dV$$

or

$$d(\ln Q + E\beta) = \beta dE + \frac{\partial \ln Q}{\partial V} dV.$$

Solving this for dE ,

$$dE = kT d(\ln Q + E\beta) - kT \frac{\partial \ln Q}{\partial V} dV.$$

Recall that

$$dE = TdS - pdV,$$

and compare, to get

$$dS = k d(\ln Q + E\beta),$$

or

$$S - S_0 = k (\ln Q + E\beta),$$

and

$$p = kT \frac{\partial \ln Q}{\partial V}.$$

For example, in the case of a perfect monatomic gas, where

$$Q = V^N \left(\frac{2\pi}{\beta m} \right)^{3N/2},$$

this leads to

$$pV = NkT,$$

$$E = \frac{3}{2}NkT,$$

$$S - S_0 = Nk \ln \frac{V}{V_0} + \frac{3}{2}Nk \ln \frac{T}{T_0}.$$

When a system is composed of more complicated particles, the ε have to be expressed in terms of the parameters that define the energy for these particles. Accordingly, the partition function will be different, but the thermodynamic functions can still be obtained from Q in the same way.

If the spacing of the quantum energy states of the particle is a significant fraction of kT , it is not a good approximation to replace the sum with an integral. This is particularly true at low temperatures. An example of where we can do the discrete states sum analytically is in the harmonic-oscillator model of molecular vibration, which we will use later in the course.

STATISTICAL MECHANICAL FORM OF LAW OF MASS ACTION

Consider a large number of systems in equilibrium on one side with a thermal reservoir and on the other with a particle reservoir. The systems are otherwise rigid and insulated. The systems are open in the sense that they are able to exchange particles with the particle reservoir, so that the number of particles in a system can fluctuate. An example of an open system is a liquid in equilibrium with its own vapor. For such an ensemble of equally prepared systems, the fundamental assumption of statistical mechanics is extended to

All microstates of a system that have the same energy and the same number of particles are equally probable.

Put another way, the probability that a system is in a particular microstate depends only on the energy and the number of particles of the microstate:

$$P = P(E, N).$$

As before, we consider a composite system $A + B$ made up of two of the systems. Let the probability that system A is in a microstate with energy E_A and number N_A be $P_A(E_A, N_A)$. Similarly $P_B(E_B, N_B)$. The probability that $A + B$ is in a microstate with energy E_{A+B} and number $N_A + N_B$ we call $P_{A+B}(E_{A+B}, N_{A+B})$. The individual systems behave independently, so that

$$P_{A+B}(E_{A+B}, N_{A+B}) = P_{A+B}(E_A + E_B, N_A + N_B) = P_A(E_A, N_A)P_B(E_B, N_B).$$

By a similar argument as that applied to the closed system before, we obtain

$$P_A(E, N) = \mathcal{Q}^{-1} \exp(-\beta E + \beta \mu N),$$

where β is a constant characterizing the thermal reservoir, and μ is a constant characterizing the particle reservoir. \mathcal{Q} is the so-called grand canonical partition function defined by the normalization condition:

$$\mathcal{Q} = \sum_{N=0}^{\infty} \sum_k e^{\beta \mu N - \beta E_k}.$$

The quantity μ is called the chemical potential and is equal to the specific Gibbs potential. With this, by the same arguments as before, we see that

$$\bar{N} = kT \frac{\partial}{\partial \mu} (\ln \mathcal{Q})$$

and

$$\bar{E} = -\frac{\partial}{\partial\beta}(\ln\mathcal{Q}) + \mu kT \frac{\partial}{\partial\mu}(\ln\mathcal{Q}).$$

Now consider a closed system in which a number N_{ab} of particles of a diatomic molecular gas AB is in chemical equilibrium with number N_a of A and a number N_b of B . Consider each of the species as a separate open system exchanging particles with the other two acting as particle reservoirs. Let the total number of microstates of the system of A -particles that have energy ε_j , be $W_a = W_a(N_{aj})$. Then the total number of microstates of the system is

$$\Omega = \sum W_a(N_{aj}) W_b(N_{bj}) W_{ab}(N_{abj}),$$

where the sum is to be taken over all possible sets of the numbers. These sets are restricted by the constraints that the number of atoms of A and the number of atoms of B are constant:

$$\sum_j N_{aj} + \sum N_{abj} = N_A$$

$$\sum_j N_{bj} + \sum N_{abj} = N_B$$

Furthermore the restriction

$$\sum_j N_{aj}\varepsilon_{aj} + \sum_j N_{bj}\varepsilon_{bj} + \sum N_{abj}(\varepsilon_{abj} - D) = E$$

applies, because the total energy of the system is made up of these parts. Here, account has been taken of the fact that the energy origin of the atoms and molecules differs by the dissociation energy D . It turns out that only the maximum value of the product of the W 's contributes significantly to Ω . Hence we put $\Omega = W_{\max} = W$, say. It is convenient to deal with $\ln W$.

$$\ln W = \ln W_a + \ln W_b + \ln W_{ab}.$$

It may be shown that, at sufficiently large temperatures and low densities,

$$\ln W_a = \sum_j N_{aj} \left(\ln \frac{C_{aj}}{N_{aj}} + 1 \right),$$

where C_{aj} is the number of ways in which the atom A can be arranged to have the same energy ε_j .

To maximize $\ln W$, consider the small change in it as a consequence of small changes in the contributing terms, and set them equal to zero:

$$\delta(\ln W) = \sum_j \frac{\partial(\ln W)}{\partial N_{aj}} \delta N_{aj} + \sum_j \frac{\partial(\ln W)}{\partial N_{bj}} \delta N_{bj} + \sum_j \frac{\partial(\ln W)}{\partial N_{abj}} \delta N_{abj} = 0.$$

Substituting,

$$\sum_j \ln \frac{C_{aj}}{N_{aj}} \delta N_{aj} + \sum_j \ln \frac{C_{bj}}{N_{bj}} \delta N_{bj} + \sum_j \ln \frac{C_{abj}}{N_{abj}} \delta N_{abj} = 0.$$

These changes are constrained by the conditions

$$\sum_j \delta N_{aj} + \sum_j \delta N_{abj} = 0,$$

$$\sum_j \delta N_{bj} + \sum_j \delta N_{abj} = 0,$$

and

$$\sum_j \varepsilon_{aj} \delta N_{aj} + \sum_j \varepsilon_{bj} \delta N_{bj} + \sum_j (\varepsilon_{abj} - D) \delta N_{abj} = 0.$$

Using the method of Lagrange multipliers the most general solution of this problem gives the equilibrium values of the N (for maximum W) as

$$N_{aj} = C_{aj} \exp(\beta \mu_a - \beta \varepsilon_{aj}),$$

$$N_{bj} = C_{bj} \exp(\beta \mu_b - \beta \varepsilon_{bj}),$$

$$N_{abj} = C_{abj} \exp(\beta[\mu_a + \mu_b + D] - \beta \varepsilon_{abj}).$$

Now the total number of particles of A is

$$N_a = \sum_j N_{aj},$$

and similarly for the other two gases, so that

$$N_a = e^{\beta \mu_a} \sum C_{aj} e^{-\beta \varepsilon_{aj}},$$

$$N_b = e^{\beta \mu_b} \sum C_{bj} e^{-\beta \varepsilon_{bj}},$$

$$N_{ab} = e^{\beta(\mu_a + \mu_b + D)} \sum C_{abj} e^{-\beta \varepsilon_{abj}}.$$

Eliminating the μ 's and D from the equations for the N_j by using these three equations, and recognizing that *the particle partition function*

$$Q = \sum_j C_j e^{-\varepsilon_j/kT},$$

we get

$$N_{aj} = N_a \frac{C_{aj} e^{\varepsilon_{aj}/kT}}{Q_a},$$

$$N_{bj} = N_b \frac{C_{bj} e^{\varepsilon_{bj}/kT}}{Q_b},$$

$$N_{abj} = N_a N_b \frac{C_{abj} e^{\varepsilon_{abj}/kT}}{Q_{ab}}.$$

*C_j being no. of ways
to arrange particles
to have ε_j*

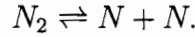
Also, by eliminating the μ 's from the expression for the total numbers, through forming the quotient

$$\frac{N_{ab}}{N_a N_b} = \frac{Q_{ab}}{Q_a Q_b} e^{D/kT},$$

we obtain the statistical-mechanical form of the Law of Mass Action.

2. The Equilibrium Model

Following Lighthill [1] we consider the simplest case of a symmetrical diatomic gas, e.g. nitrogen, in dissociation equilibrium:



In equilibrium, the number density of atoms (n_N) and the number density of molecules (n_{N_2}) are related through

$$\frac{n_N^2}{n_{N_2}} = \frac{Q_N^2}{Q_{N_2}} e^{-D/kT}, \quad (2.1)$$

where D is the dissociation energy per molecule, k is Boltzmann's constant and the Q are the partition functions of the components N and N_2 . Equation (2.1) is the law of mass action. If the energy of the gas is independent of the relative position of the particles (sufficiently low density) the Q may be resolved into factors according to the types of states over which they are summed as follows:

$$Q_N = Q_N^T \cdot Q_N^E \quad (2.2)$$

$$Q_{N_2} = Q_{N_2}^T \cdot Q_{N_2}^R \cdot Q_{N_2}^V \cdot Q_{N_2}^E, \quad (2.3)$$

where the indices T, R, V and E signify pertinence to the degrees of freedom translation, rotation, vibration and electronic excitation.

a) Translation: In quantum-statistical mechanics, the particle partition function is defined as

$$Q = \sum_{\substack{\text{all} \\ \text{states}}} e^{-\frac{\epsilon}{kT}},$$

where ϵ is the energy level of the state of the particle. In the following, we use the quantum-statistical mechanics results for the different degrees of freedom. In the case of translation, the approximation that the energy spacing of the states is very small compared to the energy of the state, which has been made earlier in the derivation of the partition function of the perfect monatomic gas this was justified, but with vibration and ionization involved this is not always true, so it is more convenient to use the quantum-statistical results.

$$Q_N^T = \frac{(2\pi mkT)^{\frac{3}{2}} V}{h^3}. \quad (2.4)$$

where m is the mass of the atom, V is the volume of the system, h is Planck's constant, and

$$Q_{N_2}^T = \frac{(4\pi mkT)^{\frac{3}{2}} V}{h^3}. \quad (2.5)$$

b) Rotation:

$$Q_{N_2}^R = \frac{1}{2} \cdot \frac{8\pi^2 I k T}{h^2} \equiv \frac{1}{2} \frac{T}{\theta_r}, \quad (2.6)$$

where I is the moment of inertia of the molecule, θ_r is the characteristic temperature of rotation. Typical values are

$$\begin{aligned} O_2 & : & \theta_r & = 2.07K \\ N_2 & : & \theta_r & = 2.86K \\ H_2 & : & \theta_r & = 85.4K. \end{aligned}$$

c) Vibration:

The atoms in a molecule exert a force on each other that depends on the distance between them. The potential of this force is sketched in the figure.

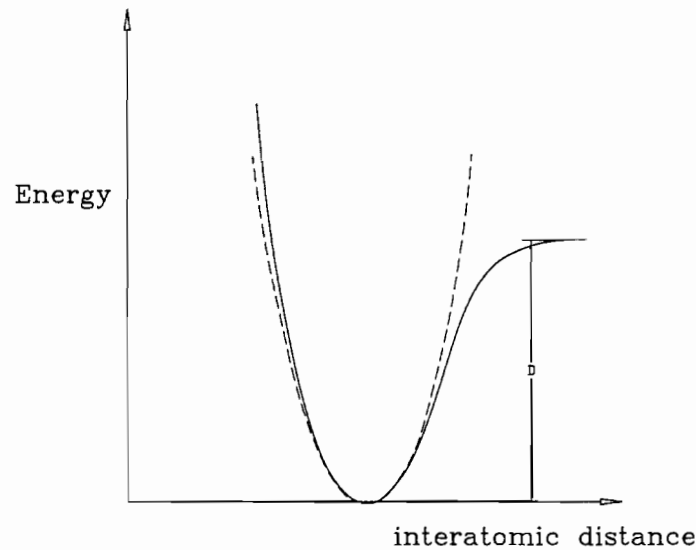


Figure 1. Potential energy of a molecule as function of interatomic distance. The dashed curve is a parabola and corresponds to the harmonic-oscillator model.

A first approximation to this potential is the harmonic oscillator indicated here by the dashed-line parabola. For the harmonic oscillator,

$$Q^v = \frac{1}{1 - e^{-\frac{h\nu}{kT}}} \equiv \frac{1}{1 - e^{-\theta_v/T}}. \quad (2.7)$$

$$\begin{aligned} O_2 & , & \theta_v & = 2230K \\ N_2 & , & \theta_v & = 3340K \\ H_2 & , & \theta_v & = 6100K. \end{aligned}$$

d) Electronic Excitation:

The energy levels of electronic excitation of some of the components of air yield

$$\begin{aligned} Q_O^E &= 5 + 3e^{\frac{-228K}{T}} + e^{\frac{-327K}{T}} + O(e^{\frac{-23000K}{T}}) \\ Q_{O_2}^E &= 3 + 2e^{\frac{-11300K}{T}} + O(e^{\frac{-23000K}{T}}) \\ Q_N^E &= 4 + O(e^{\frac{-28000K}{T}}) \\ Q_{N_2}^E &= 1 + O(e^{\frac{-28000K}{T}}) \end{aligned}$$

At temperatures below $10000K$ the neglected terms contribute less than 3%.

Before substituting these expressions in the law of mass action (2.1) we introduce the degree of dissociation α which is the mass fraction of dissociated gas

$$\alpha \equiv \frac{n_N}{n_N + 2n_{N_2}}, \quad (2.9)$$

and observe that the density ρ is related to n_{N_2} through

$$\rho = \frac{m}{V}(n_N + 2n_{N_2}). \quad (2.10)$$

It follows that

$$\frac{\alpha^2}{1 - \alpha} = \frac{n_N^2}{2n_{N_2}(n_N + 2n_{N_2})} = \frac{m}{2\rho V} \frac{n_N^2}{n_{N_2}}. \quad (2.11)$$

substituting the Q -values for N and N_2 into (2.1) and using (2.11) leads to

$$\frac{\alpha^2}{1 - \alpha} = \frac{e^{-\theta_d/T}}{\rho} \left\{ \frac{m (\pi m k T)^{3/2}}{2 h^3} \cdot \frac{2\theta_r}{T} (1 - e^{-\frac{\theta_d}{T}}) \frac{(Q_N^E)^2}{Q_{N_2}^E} \right\}, \quad (2.12)$$

where the characteristic temperature for dissociation is

$$\theta_d = \frac{D}{k}. \quad (2.13)$$

$$N_2 : \theta_d = 113200K$$

$$O_2 : \theta_d = 59500K.$$

The expression in curly brackets in (2.12) has the dimension of density. We give it the symbol ρ_d . ρ_d is a function of temperature, which is, however almost independent of temperature over a fairly wide range and may be regarded as being approximately constant within this range. Within this approximation, (2.12) may be written as

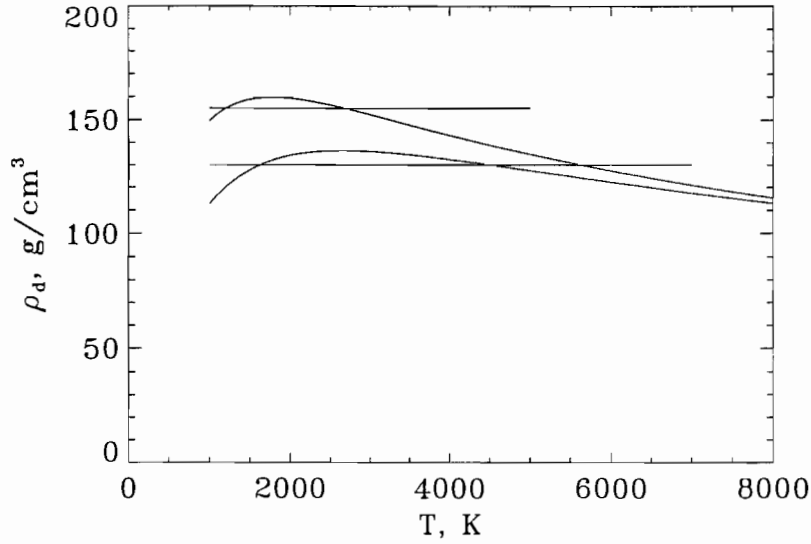


Figure 2. The characteristic density plotted for oxygen (upper curve) and nitrogen. The horizontal lines represent the approximation made by the IDG.

$$\frac{\alpha^2}{1 - \alpha} = \frac{\rho_d}{\rho} e^{-\theta_d/T}. \quad \leftarrow \text{equilibrium!} \quad (2.14)$$

The error in α made by the assumption $\rho_d = \text{constant}$ amounts typically to 0.3% at $\alpha = 0.5$ and 0.5% at $\alpha = 1$.

The thermal equation of state for the mixture of N and N_2 is

$$p = \frac{kT(n_N + n_{N_2})}{V} = \frac{kT}{2V}(\alpha + 1)(n_N + 2n_{N_2})$$

or

$$p = \frac{k}{2m} \rho T (1 + \alpha). \quad (2.15)$$

Equations (2.14) and (2.15) replace the thermal equation of state of the perfect gas, *i.e.*, $p = \frac{k}{2m} \rho T$. An additional equation is needed here, since the additional variable α is to be determined. The model gas described by (2.15) and (2.14) is the Ideal Dissociating Gas introduced by Lighthill (IDG).

Exercise (2.1) Show that, if electronic excitation does not contribute significantly to the variation of ρ_d with temperature, ρ_d depends only on constants and T/θ_v . Hence show that the maximum of ρ_d occurs at a particular value of T/θ_v . Determine this value.

Exercise 2.2 Determine the values of θ_d and ρ_d for hydrogen, and the range of temperature over which H_2 may be considered to a good approximation as an IDG. Use $D = 4.476eV$, $\theta_r = 85.4K$, $\theta_v = 6100K$. Electronic excitation: H_2 : ground state degeneracy = 1 First excited state level = $11.4eV$. H : ground state degeneracy = 2, first excited state level = $10.15eV$. [$1eV = (11600K) \cdot k$].

References

Lighthill, M.J. 1957 *Dynamics of a Dissociating Gas*. J. Fluid Mech. Vol 2 pt 1, p.1

Vincenti, W.G. & Kruger, C.H., Jr. 1965 *Introduction to Physical Gas Dynamics*. Krieger, Chapter V.

Liepmann, H.W. & Roshko, A. *Elements of Gas Dynamics*. Wiley, 1957. Chapter 1, sections 14-18.

Herzberg, G. *Molecular Spectra and Molecular Structure: I. Spectra of Diatomic Molecules*. Van Nostrand, 1950.



3. Caloric Properties of The IDG

For the determination of the caloric properties of the IDG, we use the result from statistical mechanics that the internal energy E of a system of n identical particles is

$$E = kT^2 n \frac{\partial}{\partial T} (\ln Q) \quad (3.1)$$

where the partition function Q is $Q(T, \rho)$, and the density is sufficiently small for the energy to be independent of the relative position of the particles.

Extending this formula to the case of a system with n_N atoms and n_{N_2} molecules, we assume that the presence of the molecules does not influence the internal energy of the atoms and vice versa. It is also necessary to take account of the fact that the ground state of the atom lies above that of the molecule by an energy $D/2$ per atom (since energy D is required to produce 2 atoms in their ground state from one molecule in its ground state).

Hence, for n_N atoms and n_{N_2} molecules,

$$E = kT^2 \left\{ n_N \frac{\partial}{\partial T} (\ln Q_N) + n_{N_2} \frac{\partial}{\partial T} \ln Q_{N_2} \right\} + \frac{1}{2} D n_N. \quad (3.2)$$

The quantity ρ_d that we assume to be constant (independent of T) is given by (see equation 2.1)

$$\rho_d \equiv \frac{Q_N^2}{Q_{N_2}} (= \text{constant}). \quad (3.3)$$

Its constancy implies that

$$n_N \frac{\partial}{\partial T} (\ln Q_N) + n_{N_2} \frac{\partial}{\partial T} (\ln Q_{N_2}) = (n_N + 2n_{N_2}) \frac{\partial}{\partial T} (\ln Q_N). \quad (3.4)$$

In the temperature range of our interest, the electronic excitation of the atom (N) does not play a significant role. Hence

$$Q_N = 4 \cdot \frac{(2\pi m k T)^{3/2}}{h^3} V, \quad (3.5)$$

(see equations 2.5 , 2.4 and p.8) therefore,

$$\frac{\partial}{\partial T} (\ln Q_N) = \frac{3}{2T}. \quad (3.6)$$

Substituting in (3.2), and using (3.4) leads to

$$E = \frac{3}{2} kT (n_N + 2n_{N_2}) + \frac{1}{2} D n_N. \quad (3.7)$$

Just like equation (2.14), equation (3.7) is, of course, also only an approximation to reality, which is applicable only within a limited temperature range. In order to bring out the error incurred by the approximation we write equation (3.7) in the more general form

$$\frac{E - \frac{1}{2}D \cdot n_N}{kT} = A(T)n_N + 2 \cdot B(T)n_{N_2}. \quad (3.8)$$

The approximation (3.7) implies $A = B = 3/2$. In the temperature range from 2000 K to 9000 K A and B deviate from 1.5 by less than 1% and less than 5% respectively in the case of nitrogen. With (3.7) we may write the specific internal energy,

$$e = E/[m(n_N + 2n_{N_2})] \quad (3.9)$$

$$e = \frac{k}{2m}(3T + \alpha\Theta_d).$$

(3.10)

For flowing media, the specific enthalpy

$$h = e + p/\rho \quad (3.11)$$

is often a more convenient quantity than e . Using (2.15) and (3.10) we obtain

$$h = \frac{k}{2m}[(4 + \alpha)T + \alpha\Theta_d],$$

(3.12)

the caloric equation of state of the IDG.

Equations (2.14), (2.15) and (3.12) describe a material model which supplies a sufficient set of conditions for the purposes of equilibrium flow. To give an **example** we consider the steady flow of a gas in state 1 (index 1) through a normal shock and seek the equilibrium state after the shock for an IDG and a perfect gas. The equations to be solved are

IDG:

$$\begin{aligned} h &= \frac{k}{2m}[(4 + \alpha)T + \alpha\Theta_d] \\ p &= \frac{\rho k}{2m}(1 + \alpha)T \\ \frac{\alpha^2}{1 - \alpha} &= \frac{\rho d}{\rho} e^{-\Theta_d/T} \end{aligned}$$

Perfect gas

$$h = \frac{k}{2m} \cdot \frac{7}{2}T$$

$$p = \frac{\rho k}{2m}T$$

Both perfect gas and IDG:

mass	ρu	$=$	$\rho_1 u_1$
momentum	$p + \rho u^2$	$=$	$p_1 + \rho_1 u_1^2$
energy	$h + \frac{u^2}{2}$	$=$	$h_1 + \frac{u_1^2}{2}$

For a given state 1 and given m, ρ_d, Θ_d , these 6 equations form a system from which the 6 unknown quantities may be determined

$$\{m, \rho_d, \Theta_d\} \implies \{\rho, u, p, h, T, \alpha\}.$$

For the perfect gas, 5 unknowns are determined from 5 equations

$$\{m, c_p\} \implies \{\rho, u, p, h, T\}.$$

It is interesting to consider equation (3.12) in the limiting cases $\alpha = 0$ and $\alpha = 1$.

For $\alpha = 0$, $h = 4 \cdot kT/(2m)$. This corresponds to a diatomic perfect gas with 6 degrees of freedom. Since there are 3 translational and 2 rotational degrees of freedom, this is equivalent to one vibrational degree of freedom being excited; i.e., the IDG in the undissociated state is like a diatomic gas, whose vibrational mode is “half-excited.” The error made by this approximation is small in the range where the IDG applies, because $\alpha\Theta_d$ represents a very much larger energy store than $kT/2m$, when α is say 0.25 and $T \sim \Theta_d/15$. For $\alpha = 1$, i.e., the fully dissociated monatomic gas, $\alpha\Theta_d$ is a constant and the mass of the particles is m . Thus the specific heat at constant pressure is $\frac{5}{2} \cdot \frac{k}{m}$ as it should be for a monatomic perfect gas.

The ratio of specific heats accordingly is 4/3 at $\alpha = 0$, and 5/3 at $\alpha = 1$, (for processes in which α does not vary, frozen flow).

The material equations (2.14), (2.15) and (3.12) represent relations between the quantities ρ, p, T, α, h , which are plotted in dimensionless form in the diagrams.

The second is a so-called Mollier-diagram in which the specific enthalpy is plotted against the specific entropy.

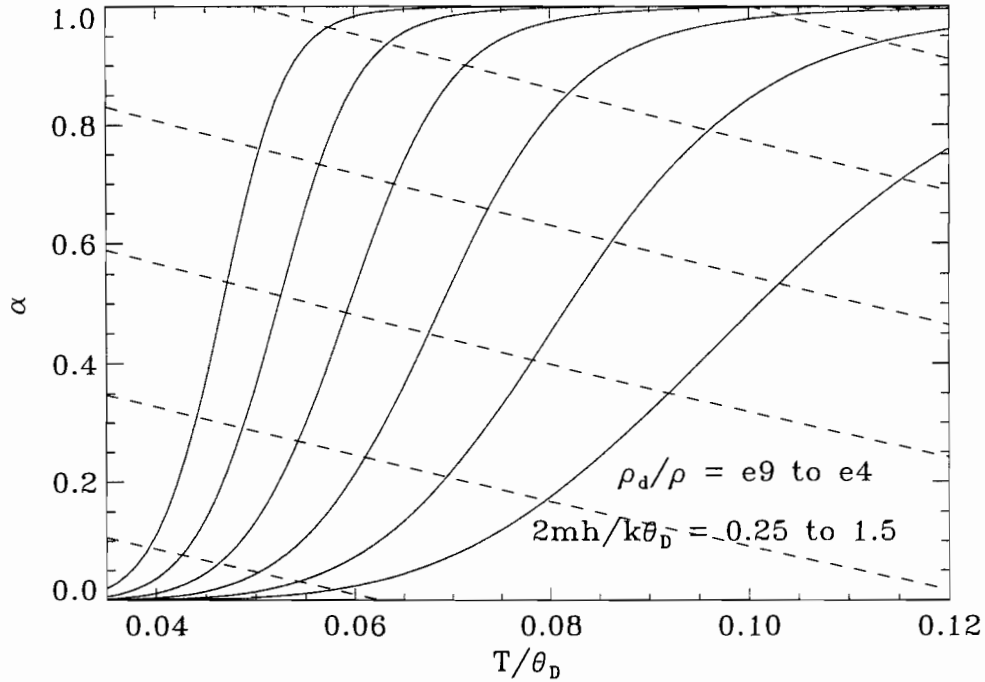


Figure 1. Behavior of the IDG.

The latter is obtained by integrating

$$Tds = dh - \frac{1}{\rho} dp, \quad (3.13)$$

a corollary of the first and second laws of thermodynamics.

Exercise 3.1 (from V + K)

Show that for the IDG in equilibrium,

$$\frac{2sm}{k} = 3 \ln \frac{T}{\Theta_d} + \alpha(1 - 2 \ln \alpha) - (1 - \alpha) \ln(1 - \alpha) - (1 + \alpha) \ln \frac{\rho}{\rho_d} + \text{const.} \quad (3.14)$$

Exercise 3.2

Use an accurate Mollier chart for nitrogen to plot the error made by equation (3.12) against T at a particular value of s/R_{N_2} . Chart supplied. Use equation (2.15) to determine α from the chart.

References

Vicenti & Kruger: chapter V

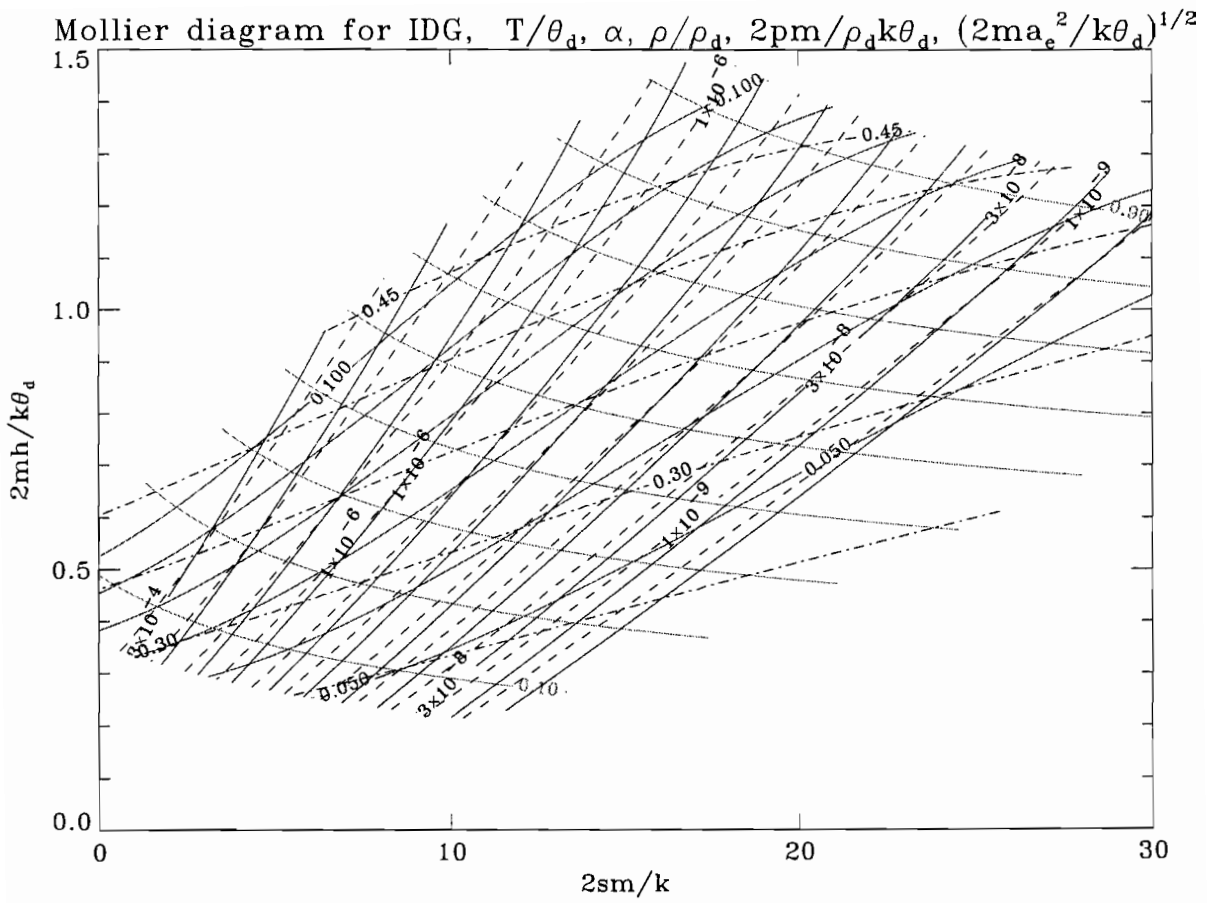


Figure 2. Mollier diagram for the IDG.



4. The Non-Equilibrium Model

As has been indicated in the introduction, dissociation of the gas requires many high-energy collisions. Hence, in many cases, the time taken for the gas to reach a new equilibrium state (e.g., after crossing a shock) is comparable to the characteristic time of the flow (body dimension divided by flow speed).

In such situations the equilibrium model (2.14) is not valid, and we need a model equation specifying the rate at which the gas dissociates. We consider the reversible chemical reaction



in which M may be N_2 or N . This representation of the reaction is intended to illustrate that the N_2 molecule is dissociated by collision with M and that the collision partner M remains unchanged by the collision.

In the recombination (reverse reaction 4.1) it is necessary that the two atoms collide at the same instant at which the third body M also collides with them; for, if the third body were not present, the energy released during the recombination (the dissociation energy) could not be carried away from the two atoms, and they would remain dissociated. Thus recombination requires three-body collisions. Dissociation requires only two-body collisions.

In order to dissociate a molecule from its ground state the energy of the collision between N_2 and M has to exceed D . The number of molecular collisions that lead to a dissociation per volume and time is equal to the collision frequency (Z) multiplied by the fraction of collisions whose energy exceeds D , ($Z(D)/Z$), multiplied by the probability that such a collision is a dissociating collision (P). For the forward rate:

$$\left(\frac{dn_N}{dt}\right)_f = -2 \left(\frac{dn_{N_2}}{dt}\right)_f = 2PZ \frac{Z(D)}{Z} V. \quad (4.2)$$

The hard-sphere model of the theory of molecular collisions gives

$$Z = \frac{2n_{N_2}n_M}{\sigma V^2} \bar{d}^2 \left(\frac{2\pi kT}{m^*}\right)^{\frac{1}{2}}. \quad (4.3)$$

$\sigma = 1$ for $M = N$ and $\sigma = 2$ for $M = N_2$. \bar{d}^2 is the so-called collision cross section, and

$$m^* = \frac{m_{N_2}m_M}{m_{N_2} + m_M} \quad (4.4)$$

is the reduced mass.

The fraction of molecules that have energy exceeding D can be approximated in the case when the colliding particles have only translational energy and for sufficiently small T/θ_d by

$$\frac{Z(D)}{Z} = e^{\frac{-D}{kT}} = e^{\frac{-\theta_d}{T}}. \quad (4.5)$$

If the internal degrees of freedom of the colliding partners are excited, (rotation, vibration)

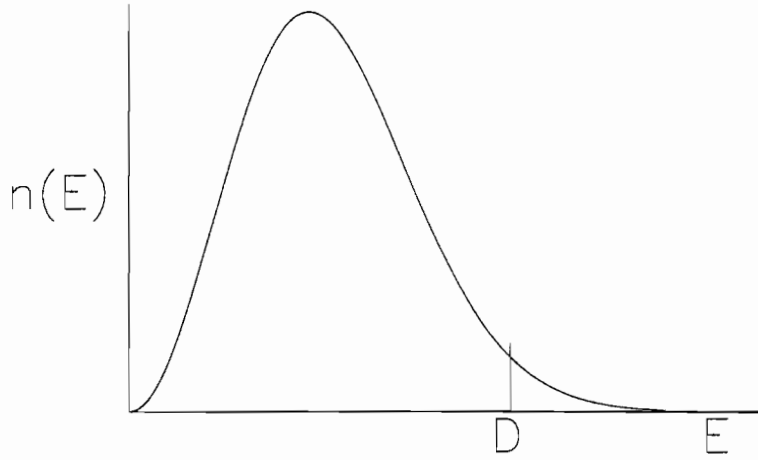


Figure 1. The area under the curve and to the right of D is $Z(D)/Z$.

the value of $Z(D)/Z$ is increased, since dissociation from an already excited state requires less energy. For sufficiently small T/θ_d the result is then

$$\frac{Z(D)}{Z} = \frac{1}{(s-1)!(kT)^s} \int_D^\infty e^{\frac{-E}{kT}} E^{(s-1)} dE, \quad (4.6)$$

where $2s$ is the number of excited (square-term) degrees of freedom of the colliding particles. If $T/\theta_d \ll s-1$, the integral may be approximated and

$$\frac{Z(D)}{Z} \doteq \frac{(\theta_d/T)^{s-1}}{(s-1)!} e^{-\theta_d/T}. \quad (4.7)$$

Substituting (4.7) and (4.3) in (4.2) yields

$$\frac{1}{V} \left(\frac{dn_N}{dt} \right)_f = 2 \left\{ P \cdot \frac{2d^2}{\sigma(s-1)!} \left(\frac{2\pi k}{m^*} \right)^{\frac{1}{2}} T^{\frac{1}{2}} \left(\frac{\theta_d}{T} \right)^{s-1} e^{-\theta_d/T} \right\} \frac{n_{N_2}}{V} \cdot \frac{n_M}{V}. \quad (4.8)$$

We now put $\{\} \equiv k_f/N_{AV}$. The forward reaction rate “constant” k_f is dependent essentially on temperature; the other variables in $\{\}$ are difficult to determine theoretically. k_f is therefore usually written as

$$k_f = C_f T^{\eta_f} e^{-\theta_d/T}, \quad (4.9)$$

and the material “constants” C_f and η_f are determined experimentally. Avogadro’s number $N_{AV} = 6.02 \times 10^{23}$ appears here because chemists use the notation of molar density for species concentration rather than the particle density (n/V) chosen here.

In measurements of k_f deviations from the Arrhenius straight line are absorbed by the factor T^{η_f} in (4.9). According to equation (4.8), η_f should be $\frac{3}{2} - s$. In many cases, this is, however, not confirmed by experiment. Furthermore, it must be noted that the parameters C_f and η_f have to be determined anew for each collision partner M . In our case there are therefore four material constants to define the overall forward reaction rate.

In order to return to our notation of chapters 2, 3, we put

$$\frac{n_N}{V} = \frac{\alpha \rho}{m}, \quad \frac{n_{N_2}}{V} = \frac{(1 - \alpha) \rho}{2m}$$

and obtain

$$\frac{d}{dt} \left(\frac{d\alpha}{dt} \right)_f = \frac{1}{\rho V} \left(\frac{dn_N}{dt} \right)_f = C_f T^{\eta_f} e^{-\theta_d/T} \cdot (1 - \alpha) \frac{n_M}{V N_{AV}}. \quad (4.10)$$

It is now necessary to determine the reverse reaction rate, since the total dissociation rate is

$$\frac{d\alpha}{dt} = \left(\frac{d\alpha}{dt} \right)_f + \left(\frac{d\alpha}{dt} \right)_r. \quad (4.11)$$

If the gas is in equilibrium, and density and temperature are constant, then the total number of dissociating collisions and the total number of recombining collisions within the system per unit time are equal. Hence $(d\alpha/dt)^*$ is zero. Denoting equilibrium conditions with an asterisk,

$$\left(\frac{d\alpha}{dt} \right)_r^* = - \left(\frac{d\alpha}{dt} \right)_f^* = -(1 - \alpha^*) C_f T^{\eta_f} e^{-\theta_d/T} \frac{n_M}{V N_{AV}}. \quad (4.12)$$

But in equilibrium, (eqn. 2.14)

$$\frac{\alpha^{*2}}{1 - \alpha^*} = \frac{\rho_d}{\rho} e^{-\theta_d/T}. \quad (4.13)$$

Substituting in (4.12) yields

$$\left(\frac{d\alpha}{dt} \right)_r^* = -\alpha^{*2} \frac{\rho}{\rho_d} C_f T^{\eta_f} \frac{n_M}{V \cdot N_{AV}}, \quad (4.14)$$

giving an expression for the reverse reaction rate when the gas is in equilibrium.

We now make the assumption that this result does not only apply in equilibrium, but also when the gas is significantly far away from equilibrium. Combining (4.14) with (4.10) according to (4.11) we obtain

$$\frac{d\alpha}{dt} = C_f T^{\eta_f} \left\{ (1 - \alpha) e^{-\theta_d/T} - \frac{\rho}{\rho_d} \alpha^2 \right\} \frac{n_M}{V N_{AV}}. \quad (4.15)$$

Summing the contributions from the two reactions for $M = N$ and $M = N_2$,

$$\frac{d\alpha}{dt} = \left[C_{fN} T^{\eta_{fN}} \alpha + C_{fN_2} T^{\eta_{fN_2}} \frac{1 - \alpha}{2} \right] \cdot \frac{\rho}{\mathcal{M}} \left\{ (1 - \alpha) e^{-\theta_d/T} - \alpha^2 \frac{\rho}{\rho_d} \right\}, \quad (4.16)$$

Where \mathcal{M} is the molecular weight $m N_{AV}$ of the atomic gas. Measurements [5] give for $6000K < T < 14000K$

$$M = N_2 : C_f = 2.3 \times 10^{29 \pm 0.2} \text{cm}^3 \text{mol}^{-1} \text{s}^{-1} K^{3.5}, \quad \eta_f = -3.5 \quad (4.17a)$$

$$M = N : C_f = 8.5 \times 10^{25 \pm 0.2} \text{cm}^3 \text{mol}^{-1} \text{s}^{-1} K^{2.5}, \quad \eta_f = -2.5 \quad (4.17b)$$

Since the uncertainties in such measurements are fairly large, the approximation made by Freeman (1958) is appropriate:

$$\frac{d\alpha}{dt} = C \rho T^\eta \left\{ (1 - \alpha) e^{-\theta_d/T} - \frac{\rho}{\rho_d} \alpha^2 \right\}.$$

(4.18)

With the values (4.17), we obtain, for $\alpha = 0.25, T = 10000K$

$$C = 2.1 \times 10^{24} \text{cm}^3 \text{g}^{-1} \text{s}^{-1} (K)^{2.5}, \quad \eta = -2.5. \quad (4.19)$$

Equation (4.18) is the model for the reaction rate that we shall adopt in the remainder of Part I of this course.

Discussion of eqn (4.18)

1. The dimensions of $C \rho T^\eta$ are (time)⁻¹.
2. The curly bracket is a measure of the departure of the system from equilibrium. At equilibrium, $\{\} = 0$. If $\{\} > 0$ there are more molecules than corresponds to equilibrium, and when $\{\} < 0$ there are too many atoms for equilibrium.



$$\frac{da}{dt} = C_f T^{n_f} e^{-\theta_d / T} (1-\alpha) \frac{n_m}{V N_{Av}}$$

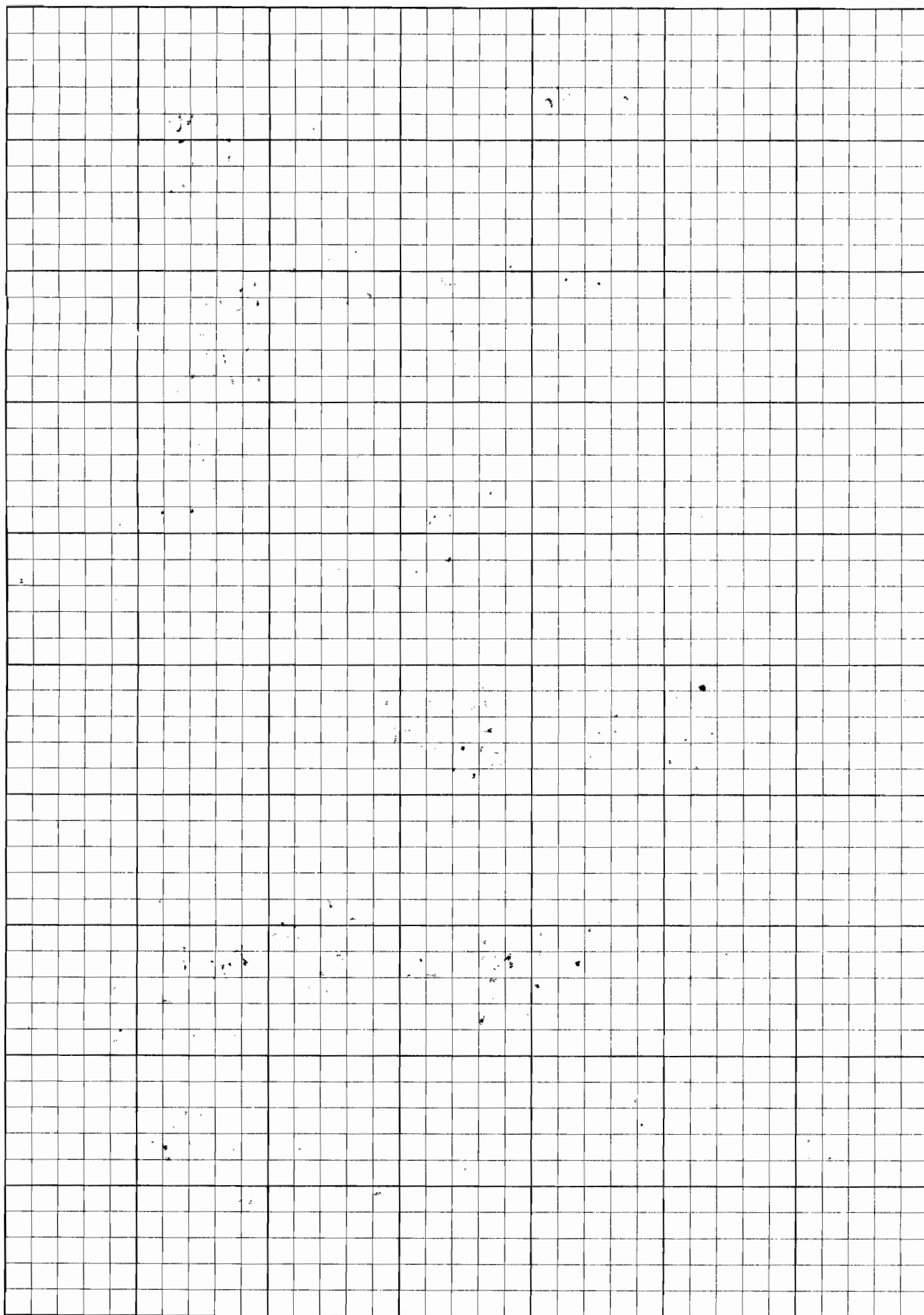
$$-\alpha^2 \frac{p}{p_d} C_f T^{n_f} \frac{n_m}{V N_{Av}}$$

$$= C_f T^{n_f} \frac{n_m}{V N_{Av}} \left[(1-\alpha) e^{-\frac{\theta_d}{T}} - \alpha^2 \frac{p}{p_d} \right]$$

$$\frac{n_m}{V N_{Av}} = \frac{n_m m}{V m N_{Av}} = \frac{n_m m / p}{p V (\rho)}$$

$$= \left[C_{fN} T^{n_{fN}} \cdot \frac{n_{mN}}{pV} + C_{fN_2}^{n_{fN_2}} \frac{n_{mN_2}}{pV} \right] \frac{p}{m} \left[\right]$$

$$= \left(C_{fN} T^{n_{fN}} \alpha + \left(\frac{1-\alpha}{2} \right) C_{fN_2} T^{n_{fN_2}} \right)$$



3. The dissociation rate (first term in $\{ \}$ multiplied by factor outside $\{ \}$) is proportional to the density. The recombination rate (second term in $\{ \}$ multiplied by factor outside $\{ \}$) is proportional to the square of the density. This is a fact which has very important consequences for gas dynamics.
4. The derivative d/dt applies here to a thermodynamic system which may be understood as a material element in a flowing medium in the following sections. Accordingly, it is to be understood as the substantial derivative D/Dt in that case.
5. The material properties introduce a characteristic time (see 1. above) Thus the non-equilibrium model puts the IDG (noneq.) into the class of materials with (fading) memory.

Exercise 4.1

In a plot of α vs $\log (T/\theta_d)$ draw a few contours of [the square bracket in equation (4.16) divided by (14 times $T^{2.5}$)] i.e., of C , with $\eta = -2.5$. Take $\theta_d = 113200K$. Hence discuss the step from (4.16) to (4.18) in the light of the error bar of the experiments in (4.17).

References

- Kewley D.J. & Hornung, H.G.(1974) *Chem. Phys. Letters* **25** p.531.
Freeman, N.C. (1958) *J. Fluid Mech.* **4** p.407.
Vincenti & Kruger, Chapter VII.



Ae234 Assignment No. 1, due 18 April, 2002

QUESTION 1

Show that, if electronic excitation does not contribute significantly to the variation of ρ_d with temperature, ρ_d can be expressed as a function of constants and T/θ_v . Hence show that the maximum of ρ_d occurs at a particular value of T/θ_v . Determine this value.

QUESTION 2

Determine the values of θ_d and ρ_d for hydrogen, and the range of temperature over which hydrogen may be considered to a good approximation as an IDG. Use $D = 4.476$ eV, $\theta_r = 85.4$ K, $\theta_v = 6100$ K. Electronic excitation: molecule: ground state degeneracy = 1, first excited state level = 11.4 eV; atom: ground state degeneracy = 2, first excited state level = 10.15 eV. [1 eV = (11600K)*k].

QUESTION 3

Obtain an expression for the dimensionless specific entropy, sm/k , of an IDG as a function of α , T/θ_d , and ρ/ρ_d , by integrating the Gibbs relation

$$T dS = dh - \frac{1}{\rho} dp.$$



5. Normal Shock in IDG

We consider flow of an IDG through a normal shock in the frame of reference in which the shock is stationary, i.e., in steady flow. To the left of the shock the gas is in the spatially and temporally uniform state 1. To the right of the shock the state of the gas depends on the distance x from the shock since dissociation requires finite time. The figure shows schematically the behavior of some of the relevant quantities. Far from the shock, the gas eventually reaches an equilibrium state. It is assumed here that the conditions immediately

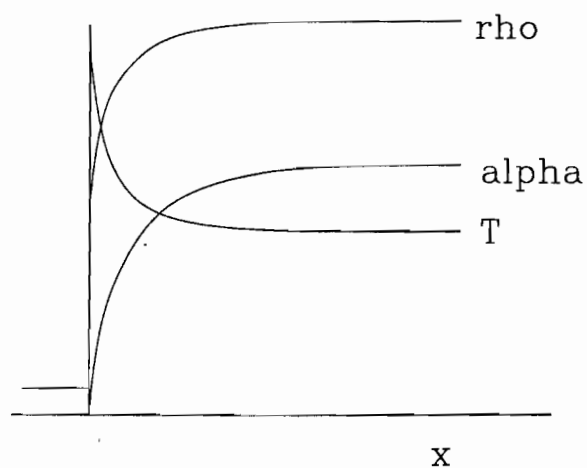


Figure 1. Sketch of dissociative relaxation after a normal shock.

after a thin shock correspond to those which a perfect gas at the composition α_1 would reach across a normal shock from state 1, i.e., the translational/rotational shock is very thin and may be regarded as having thickness zero. This is valid when the mean free path of the gas is small compared with values of x that interest us. This is usually the case in regimes where dissociation plays a significant role.

For the problem at hand, the following equations apply

$$\begin{aligned}\rho u &= \rho_1 u_1 \\ p + \rho u^2 &= p_1 + \rho_1 u_1^2 \\ h + u^2/2 &= h_1 + u_1^2/2 \\ p &= (k/2m)\rho T(1 + \alpha) \\ h &= (k/2m)[(4 + \alpha)T + \alpha\Theta_d]\end{aligned}$$

and either

$$\frac{\alpha^{*2}}{1 - \alpha^*} = \frac{\rho_d}{\rho} e^{-\theta_d/T}, \quad (5.2)$$

or

$$\frac{d\alpha}{dt} = C\rho T^\eta \left[(1 - \alpha) e^{-\theta_d/T} - \alpha^2 \frac{\rho}{\rho_d} \right], \quad (5.3)$$

depending on whether we are dealing with an equilibrium flow or a nonequilibrium flow, in other words, on whether we are interested in the process leading to equilibrium or not. The latter may be the case for example, if the relaxation length $u/(C\rho T^\eta)$ is very much smaller than any lengths of interest to us.

Initially, we use the first five of the above equations to derive a relation between ρ and α which is valid for both equilibrium and nonequilibrium flow. For this purpose we introduce the dimensionless quantities

$$K = \frac{mu_1^2}{k\Theta_d}, \quad H_0 = \frac{2mh_0}{k\Theta_d}, \quad P = \frac{p_1}{\rho_1 u_1^2}, \quad (5.4)$$

where $h_o = h_1 + u_1^2/2$. These three numbers together with α_1 and ρ_1/ρ_d describe the state 1. Using (5.4) in the last of (5.1),

$$H_0 = (4 + \alpha) \frac{T}{\Theta_d} + \alpha + \frac{u^2}{u_1^2} K. \quad (5.5)$$

Eliminating p from the second and fourth of (5.1),

$$\frac{1}{2K} \cdot \frac{T}{\Theta_d} = \left[P + 1 - \frac{\rho_1}{\rho} \right] \frac{\rho_1}{\rho} \cdot \frac{1}{1 + \alpha}. \quad (5.6)$$

Substituting (5.6) in (5.5) with the first of (5.1) gives

$$- \left(\frac{\rho_1}{\rho} \right)^2 \frac{7 + \alpha}{1 + \alpha} K + 2K \frac{\rho_1}{\rho} \frac{4 + \alpha}{1 + \alpha} (P + 1) + (\alpha - H_0) = 0. \quad (5.7)$$

Only one of the roots of this quadratic in ρ_1/ρ has physical significance. It is

$$\frac{u}{u_1} = \frac{\rho_1}{\rho} = \frac{4 + \alpha}{7 + \alpha} (1 + P) \left\{ 1 - \sqrt{1 - \frac{(H_0 - \alpha)(7 + \alpha)(1 + \alpha)}{K(4 + \alpha)^2(1 + P)^2}} \right\},$$

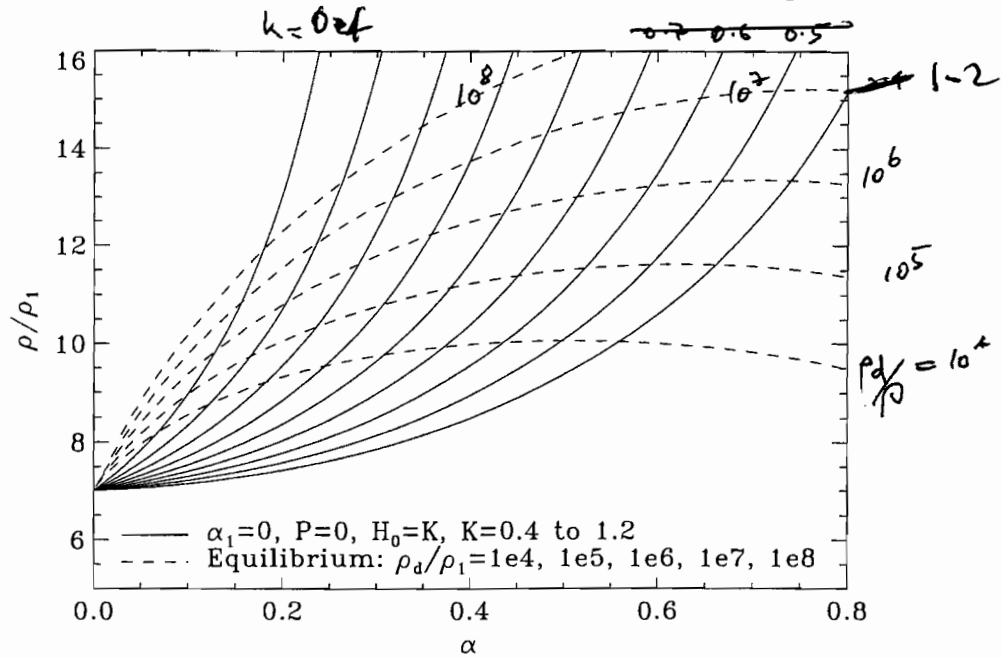
(5.8)

see [7].

The case $h_1 \ll u_1^2/2$ is of particular interest. It leads immediately to $H_0 = K$; and $P \ll 1$. For this limiting case (5.8) reduces for $\alpha = 0$ and $\alpha_1 = 0$ (i.e., immediately after the shock) to

$$\frac{\rho_2}{\rho_1} = 7.$$

It differs from the density jump of a perfect diatomic gas, which for strong shocks is 6, because the vibrational degrees of freedom of the IDG are effectively half excited. The density ratio $\rho(\alpha)/\rho_1$ obtained from equation (5.8) is plotted here for the case $P = 0, H_0 = K$. In order to use this information, it is necessary to invoke either equation (5.2) or equation (5.3), depending on whether the equilibrium or non-equilibrium solution is sought.



Density as function of α . Full line: (5.8), dashed line: equilibrium.

a) equilibrium flow

We write equation (5.8) formally as

$$\frac{\rho_1}{\rho} = f(\alpha, P, H_0, K) \quad (5.9)$$

and use (5.8) to write (5.6) formally as

$$\frac{T}{\Theta_d} = g(\alpha, P, H_0, K) \quad (5.10)$$

For equilibrium flow, the 6th equation required to determine the 6 unknowns is the algebraic

equation (5.2). Substituting (5.9) and (5.10) in (5.2), we obtain

$$\frac{\alpha^{*2}}{1 - \alpha^*} = \frac{\rho_d}{\rho_1} \cdot f^* e^{-\frac{1}{g^*}}, \quad (5.11)$$

where the asterisks indicate equilibrium. For a given value of ρ_d/ρ_1 , equation (5.11) can be solved iteratively yielding α^* and, (5.9) ρ_1/ρ^* . If we plot this against α^* for the case $H_0 = K$, $P = 0$, $\alpha_1 = 0$, we obtain a set of curves with ρ_d/ρ_1 as parameter. It is particularly striking that the density ratio can reach very much higher values in the case of the IDG than in a perfect diatomic gas, if significant amounts of dissociation occur after the shock. For nitrogen at $u_1 = 6$ km/s, $\rho_1 = 1.3 \times 10^{-5}$ g/cm³, we obtain $K = 0.54$, $\rho_1/\rho_d = 10^{-2}$. The resulting values of $\alpha^* = 0.24$, $\rho^*/\rho_1 = 11.4$, $T^* = 8000$ K.

b) Nonequilibrium flow

In this case we invoke the differential equation (5.3) instead of the algebraic equation (5.2) in order to complete the set. Substituting (5.9) and (5.10) in (5.3) we obtain

$$\frac{d\alpha}{dt} = C \rho_1 \Theta_d^\eta \frac{g^\eta}{f} \left[(1 - \alpha) e^{-\frac{1}{g}} - \alpha^2 \frac{\rho_1}{\rho_d} \cdot \frac{1}{f} \right] \quad (5.12)$$

as a function of α and free-stream parameters. For the one-dimensional steady flow under consideration here, we may write $d/dt = ud/dx = u_1 f d/dx$. Hence,

$$\frac{d\alpha}{dx} = \frac{C \rho_1 \Theta_d^\eta}{u_1} \frac{g^\eta}{f^2} \left[(1 - \alpha) e^{-\frac{1}{g}} - \alpha^2 \frac{\rho_1}{\rho_d} \cdot \frac{1}{f} \right], \quad (5.13)$$

or

$$\frac{d\alpha}{dx} = \frac{C \rho_1 \Theta_d^\eta}{u_1} F(\alpha, K, H_0, P, \frac{\rho_1}{\rho_d}, \eta) \quad (5.18)$$

where F is a known function defined by (5.13, 5.9, 5.10). For a given IDG and given state 1 upstream of the shock, the r.h.s. is therefore known as a function of α . Numerical quadrature of the equation

$$\int_0^\alpha \frac{d\alpha'}{F(\alpha', H_0, K, P, \frac{\rho_1}{\rho_d}, \eta)} = \int_0^x \frac{C \rho_1 \Theta_d^\eta}{u_1} dx' = \frac{C \rho_1 \Theta_d^\eta}{u_1} x \quad (5.19)$$

leads to a curve $\alpha(x)$.

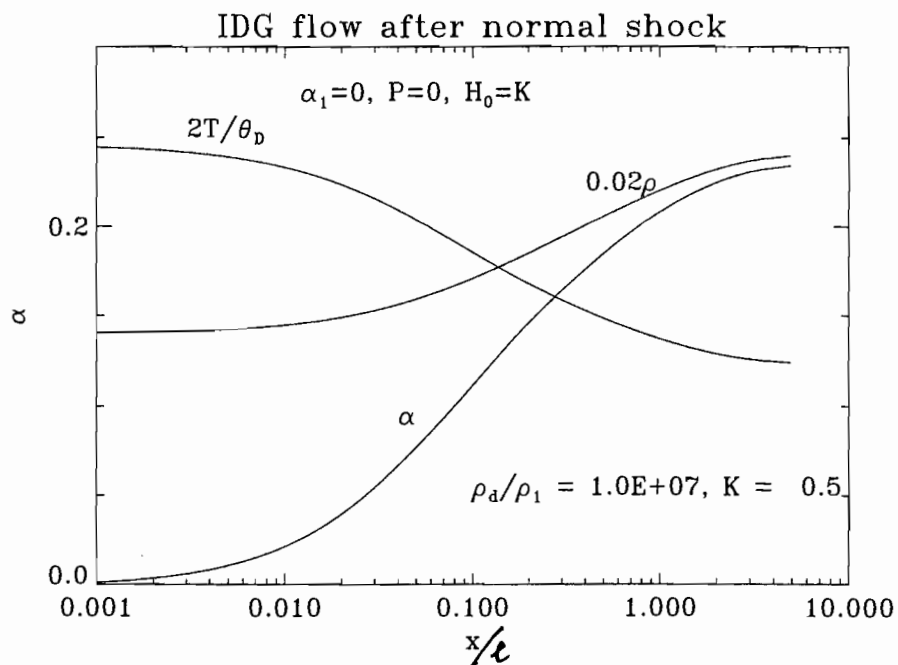
In the example chosen above for equilibrium flow, the characteristic length

$$\ell \equiv \frac{u_1}{C \rho_1 \Theta_d^\eta}$$

is 1.2 mm. The plot shows the result of such an integration for $\alpha(x)$, $T(x)$, $\rho(x)$.

Note the temperature peak immediately after the shock and the strong density rise. Both are consequences of the finite dissociation rate.

Since $\ell \sim \rho_1^{-1}$ and since ρ_1/ρ_d mainly influences only the equilibrium condition, the characteristic length for finite rate dissociative effects is inversely proportional to the density.



Example of an integration of equation (5.19).

It is interesting to superpose the two diagrams showing ρ as functions of α in order to show the path to equilibrium. For this purpose we select the curve $\rho_d/\rho_1 = 10^6$ and plot it. Choosing $K = 0.6$, for example, we see that the states (ρ, α) traversed by the gas as it passes from the frozen state at $x = 0$ to the equilibrium state at $x = \infty$ is prescribed by the equation (5.8). This is therefore a very useful result, especially since it is in closed form. It does not appear in any textbook.

It remains to discuss the behavior of pressure and enthalpy behind the shock. For the case $H_0 = K, P = 0$, the conservation of energy and momentum (equations 5.3 and 5.2) may be rewritten as

$$\frac{2h}{u_1^2} = 1 - \frac{u^2}{u_1^2} = 1 - \left(\frac{\rho_1}{\rho}\right)^2,$$

$$\frac{p}{\rho_1 u_1^2} = 1 - \frac{\rho u^2}{\rho_1 u_1^2} = 1 - \frac{\rho_1}{\rho}.$$

Since ρ_1/ρ is small in the relaxation region, the pressure changes only slightly and the enthalpy hardly at all. In the case calculated, the pressure change from shock to equilibrium

is 6% and the enthalpy change 1.3%. We conclude that dissociative relaxation influences the pressure and enthalpy only slightly, while temperature and density are dramatically affected.

References

[7] Hornung H. G. J. Fluid Mech. 53 pp. 149-176 (1972)

[8] Freeman N.C. J. Fluid Mech. 4 p.407 (1958)

Vincenti & Kruger Chapters VI and VII.

Momentum

$$\frac{\partial \underline{u}}{\partial t} + \underline{u} \cdot \nabla \underline{u} = -\frac{1}{\rho} \nabla p$$

$$\frac{\partial \underline{u}'}{\partial t} + \cancel{2\underline{u}_0 \cdot \nabla \underline{u}'} = -\frac{1}{\rho_0} \nabla p'$$

$$\boxed{\frac{\partial \underline{u}'}{\partial t} + \frac{1}{\rho_0} \nabla p' = 0}$$

Continuity

$$\frac{\partial \rho}{\partial t} + \underline{u} \cdot \nabla \rho + \rho \nabla \cdot \underline{u} = 0$$

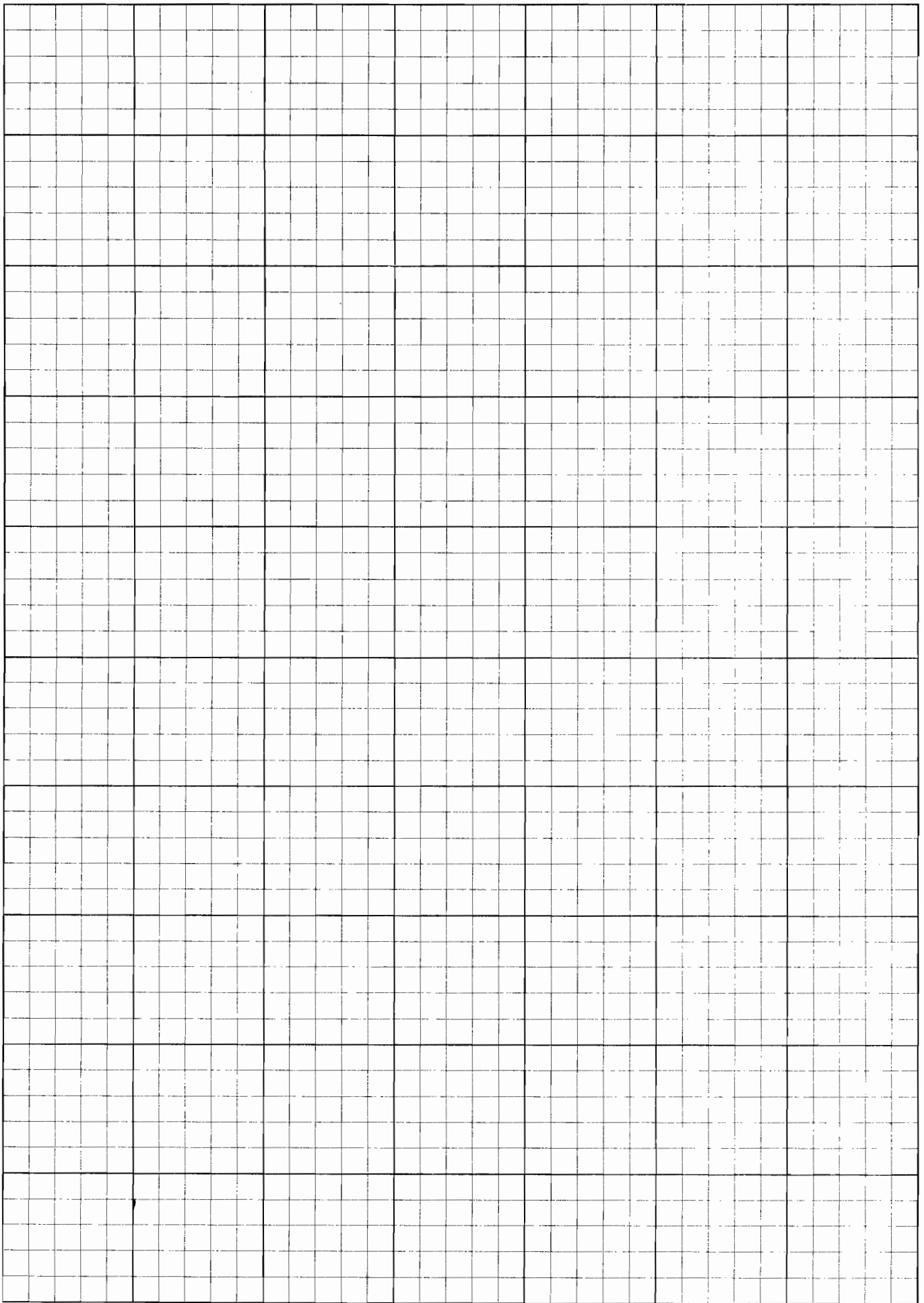
$$\frac{\partial \rho'}{\partial t} + \cancel{\underline{u}_0 \cdot \nabla \rho'} + \cancel{\rho' \cdot \nabla \rho_0} + \rho_0 \nabla \cdot \underline{u}' + \cancel{\rho' \cdot \nabla \cdot \underline{u}_0} = 0$$

$$\boxed{\frac{\partial \rho'}{\partial t} + \rho_0 \nabla \cdot \underline{u}' = 0}$$

One-d

$$\frac{\partial u'}{\partial t} + \frac{1}{\rho_0} \frac{\partial p'}{\partial x} = 0$$

$$\frac{\partial \rho'}{\partial t} + \rho_0 \frac{\partial u'}{\partial x} = 0$$



6. Speed of Sound

In order to relate the speed of sound to the material properties, consider a gas at rest (p_0, ρ_0) and superimpose on this state a small pressure perturbation $p'(\mathbf{x}, t)$ which leads to corresponding small density and velocity perturbations $\rho'(\mathbf{x}, t)$, $\mathbf{u}'(\mathbf{x}, t)$. The inviscid momentum equation in linearised form for the disturbance quantities is then

$$\frac{\partial \mathbf{u}'}{\partial t} + \frac{1}{\rho_0} \text{grad } p' = 0. \quad (6.1)$$

The corresponding form of the continuity equation is

$$\frac{\partial \rho'}{\partial t} + \rho_0 \text{div } \mathbf{u}' = 0. \quad (6.2)$$

For sufficiently small frequencies the compressions and expansions in a sound wave occur adiabatically. To show this, consider a sinusoidal distribution of disturbance pressure along the x -axis at an instant of time. With this pressure wave will be associated a temperature distribution that is also sinusoidal. The order of magnitude of the temperature gradient will be T'_m/λ , where T'_m is the amplitude of the temperature disturbance, and λ is the wavelength. If the wave were stationary in the gas, the order of magnitude of the heat that would have to be transported from the higher to the lower temperature region of one wavelength per unit area, in order to flatten the temperature distribution, would be

$$T'_m C_p \rho \lambda.$$

The time it would take to transport this heat would be

$$\begin{aligned} \Delta t_T &= \frac{\text{amount of heat to transport}}{k \text{ temperature gradient}} \\ &= \frac{T'_m C_p \rho \lambda}{k T'_m / \lambda} \\ &= \frac{\lambda^2 \rho C_p}{k}, \end{aligned}$$

where k is the thermal conductivity of the gas. The time taken for the wave to propagate through one wavelength is

$$\Delta t_p = \frac{\lambda}{a},$$

where a is the speed of sound. The ratio of the two times is

$$\frac{\Delta t_T}{\Delta t_p} = \frac{\lambda \rho C_p a}{k}.$$

For adiabatic behavior it is necessary for the transport time to be much larger than the propagation time, or

$$\frac{1}{\lambda} \ll \frac{\rho C_p a}{k}$$

or, with $f = a/\lambda$,

$$f \ll \frac{a^2 \rho C_p}{k} = \frac{a^2 Pr}{\nu},$$

where Pr is the Prandtl number and ν the kinematic viscosity of the gas. In room temperature air this frequency is approximately 5 GHz, so the assumption that the thermodynamic processes associated with sound waves may safely be assumed to be adiabatic in most cases.

For adiabatic equilibrium changes of state,

$$p' = \left(\frac{\partial p_0}{\partial \rho_0} \right)_s \rho'. \quad (6.3)$$

Substituting this in (6.2) gives

$$\frac{\partial p'}{\partial t} + \rho_0 \left(\frac{\partial p_0}{\partial \rho_0} \right)_s \text{div } \mathbf{u} = 0. \quad (6.4)$$

We define a disturbance potential

$$\mathbf{u}' \equiv \text{grad } \phi.$$

Substituting in (6.1) leads to

$$p' = -\rho_0 \frac{\partial \phi}{\partial t}. \quad (6.5)$$

Using this in (6.4) gives the wave equation

$$\frac{\partial^2 \phi}{\partial t^2} - \left(\frac{\partial p_0}{\partial \rho_0} \right)_s \nabla^2 \phi = 0, \quad (6.6)$$

in which the wave speed, i.e., the speed of small disturbances or the speed of sound is given by

$$a = \sqrt{\left(\frac{\partial p_0}{\partial \rho_0} \right)_s}.$$

(6.7)

In chemical thermodynamics it is usual to extend the concept of entropy change to processes for which the initial and final states of the system are constrained equilibrium states. This leads to the equation (see Vincenti & Kruger pp. 70-75, also eqn. A6)

$$T ds = dh - \frac{1}{\rho} dp + (\mu_{N_2} - 2\mu_N) d\alpha, \quad (6.8)$$

which differs from (3.13) in the last term. In equilibrium, i.e., for a reversible process,

$$\mu_{N_2}^* - 2\mu_N^* = 0, \quad (6.9)$$

so that (3.13) is recovered. The chemical potentials μ_{N_2} are the amounts by which the energy of the system is increased by the addition of molecules and atoms respectively, at constant temperature and pressure.

The specific enthalpy may be written more generally than eqn (3.12) as

$$h = h(p, \rho, \alpha), \quad (6.10)$$

so that

$$dh = \frac{\partial h}{\partial p} dp + \frac{\partial h}{\partial \rho} d\rho + \frac{\partial h}{\partial \alpha} d\alpha. \quad (6.11)$$

Substituting this in (6.8) yields

$$T ds = \left(\frac{\partial h}{\partial p} - \frac{1}{\rho} \right) dp + \frac{\partial h}{\partial \rho} d\rho + \left(\frac{\partial h}{\partial \alpha} + \mu_{N_2} - 2\mu_N \right) d\alpha. \quad (6.12)$$

First, consider frozen flow, i.e., processes where $d\alpha = 0$. For such processes $ds = 0$ demands, see (6.12),

$$\left(\frac{\partial p}{\partial \rho} \right)_{s, \alpha} = - \frac{\partial h / \partial \rho}{\partial h / \partial p - 1/\rho} \equiv a_f^2.$$

(6.13)

Example: In the special case of the perfect gas,

$$h = c_p T = \frac{C_p}{R} \frac{p}{\rho}.$$

Therefore,

$$\frac{\partial h}{\partial p} = \frac{C_p}{R} \cdot \frac{1}{\rho}, \quad \frac{\partial h}{\partial \rho} = - \frac{C_p}{R} \cdot \frac{p}{\rho^2}.$$

Hence,

$$a_f^2 = \frac{C_p p / (\rho^2 R)}{C_p / (\rho R) - 1/\rho} = \frac{C_p}{C_p - R} \frac{p}{\rho} = \gamma p / \rho.$$

For the IDG, (6.10) becomes

$$h = \frac{4 + \alpha}{1 + \alpha} \frac{p}{\rho} + \alpha \frac{k}{2m} \theta_d$$

and

$$dh = \frac{4 + \alpha}{1 + \alpha} \frac{dp}{\rho} - \frac{4 + \alpha}{1 + \alpha} p \frac{d\rho}{\rho^2} + (\quad) d\alpha.$$

Hence

$$a_f^2 = \frac{4 + \alpha}{3} \frac{p}{\rho}.$$

(6.14)

The effective value of the ratio of specific heats of a frozen IDG is seen to be $(4 + \alpha)/3$.

For equilibrium flows, $\alpha = \alpha^*(p, \rho)$. It follows, that

$$d\alpha = d\alpha^* = \frac{\partial \alpha^*}{\partial p} dp + \frac{\partial \alpha^*}{\partial \rho} d\rho. \quad (6.15)$$

Substituting in (6.12) and using (6.9) gives

$$Tds = \left(\frac{\partial h}{\partial p} + \frac{\partial h}{\partial \alpha} \frac{\partial \alpha^*}{\partial p} - \frac{1}{\rho} \right) dp + \left(\frac{\partial h}{\partial \rho} + \frac{\partial h}{\partial \alpha} \frac{\partial \alpha^*}{\partial \rho} \right) d\rho. \quad (6.16)$$

By putting $ds = 0$ we obtain

$$\left(\frac{\partial p}{\partial \rho} \right)_{s, \alpha = \alpha^*} = - \frac{\partial h / \partial \rho + \partial h / \partial \alpha \partial \alpha^* / \partial \rho}{\partial h / \partial p + \partial h / \partial \alpha \partial \alpha^* / \partial p - 1 / \rho} \equiv a_e^2.$$

(6.17)

Exercise 6.2

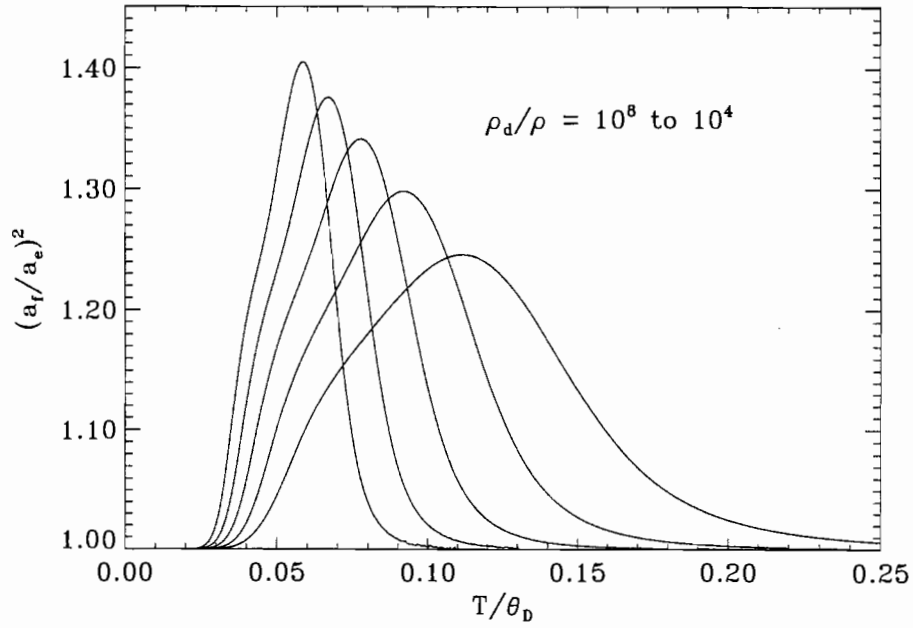
Show that, for an IDG in equilibrium

$$a_e^2 = \frac{p}{\rho(1 + \alpha^*)} \frac{\alpha^*(1 - \alpha^{*2})(1 + 2\frac{T}{\Theta_d}) + (8 + 3\alpha^* - \alpha^{*3})(\frac{T}{\Theta_d})^2}{\alpha^*(1 - \alpha^*) + 3(2 - \alpha^*)(\frac{T}{\Theta_d})^2}.$$

(6.18)

and that the following inequality holds

$$a_f \geq a_e.$$



The diagram shows the ratio $(a_f/a_e)^2$ for an IDG. For high temperatures, the gas is fully dissociated if in equilibrium, i.e., $\alpha^* = 1$ and equation (6.18) gives

$$a_e^2 = a_f^2 = \frac{5}{3} \frac{p}{\rho}$$

as is expected for a monatomic gas.

References

Vicenti & Kruger, pp. 70-75 and 254-259.

7. Nozzle Flow

Consider adiabatic steady flow through a Laval nozzle that is so slender that quasi-onedimensional flow applies to a good approximation. In such a situation the following conservation laws hold:

$$\frac{1}{u} \frac{du}{dx} + \frac{1}{\rho} \frac{d\rho}{dx} + \frac{1}{A} \frac{dA}{dx} = 0, \quad (7.1)$$

$$u \frac{du}{dx} + \frac{1}{\rho} \frac{dp}{dx} = 0, \quad (7.2)$$

$$\frac{dh}{dx} + u \frac{du}{dx} = 0, \quad (7.3)$$

where $A(x)$ is the cross-sectional area of the nozzle.

Writing

$$\frac{dp}{dx} = \frac{dp}{d\rho} \frac{d\rho}{dx}$$

and evaluating $d\rho/dx$ from (7.1),

$$\frac{dp}{dx} = \frac{dp}{d\rho} \cdot \rho \left[-\frac{1}{A} \frac{dA}{dx} - \frac{1}{u} \frac{du}{dx} \right]. \quad (7.4)$$

Combining (7.2) and (7.4) we obtain

$$u \frac{du}{dx} - \frac{dp}{d\rho} \left[\frac{1}{A} \frac{dA}{dx} + \frac{1}{u} \frac{du}{dx} \right] = 0$$

or

$$\frac{1}{u} \frac{du}{dx} = \frac{\frac{1}{A} \frac{dA}{dx}}{(u^2/d\rho) - 1}.$$

(7.5)

The denominator of the r.h.s. of (7.5) goes to zero at $u^2 = dp/d\rho$. If the left hand side is to remain finite at this point, the numerator must also be zero at this point, unless $dp/d\rho$ depends on du/dx . Stating this in the opposite way, for nonzero du/dx , $u^2 = dp/d\rho$ at the nozzle throat, unless $dp/d\rho$ depends on du/dx . The latter is the case, for example, if nonequilibrium flow occurs in the throat region. For equilibrium or frozen flow, the singularity occurs at the throat and it has saddle point character.

At this point we introduce the material properties into the discussion, in order to be able to make use of equation (7.3). To this end we write, for $h = h(p, \rho, \alpha)$

$$\frac{dh}{dx} = \frac{\partial h}{\partial p} \frac{dp}{dx} + \frac{\partial h}{\partial \rho} \frac{d\rho}{dx} + \frac{\partial h}{\partial \alpha} \frac{d\alpha}{dx}$$

and replace dp/dx in this equation from (7.2), $d\rho/dx$ from (7.1) and dh/dx from (7.3) to obtain

$$\frac{1}{u} \frac{du}{dx} = \frac{\frac{1}{A} \frac{dA}{dx} - \left(\frac{\partial h}{\partial \alpha} / \frac{\partial h}{\partial \rho} \right) \cdot \frac{1}{\rho} \frac{d\alpha}{dx}}{u^2 / \left\{ \frac{-\frac{\partial h}{\partial \rho}}{\frac{\partial h}{\partial p} - \frac{1}{\rho}} \right\} - 1}$$

(7.6)

a) *Frozen flow*, $d\alpha/dx = 0$

The expression in curly brackets in (7.6) is now recognized as the square of the frozen speed of sound a_f^2 , s. eq.(6.13). This is, of course, as it should be, since we are considering adiabatic flow, which, at constant composition, is isentropic, so that $dp/d\rho = (\partial p/\partial \rho)_{s,\alpha} = a_f^2$, s.eq.(6.7). Since the second term in the numerator is identically zero for $d\alpha/dx = 0$, we recover the condition that the saddle point occurs at the nozzle throat. At the throat we must therefore have $u^2 = a_f^2$ or $du/dx = 0$.

b) *Equilibrium flow*, $\alpha = \alpha^*(p, \rho)$.

In this case we can replace $d\alpha/dx$ in (7.6) by

$$\frac{d\alpha}{dx} = \frac{\partial \alpha^*}{\partial p} \frac{dp}{dx} + \frac{\partial \alpha^*}{\partial \rho} \frac{d\rho}{dx}.$$

Replacing dp/dx and $d\rho/dx$ from equations (7.2) and (7.3) in this expression and solving for

$\frac{1}{u} \frac{du}{dx}$:

$$\frac{1}{u} \frac{du}{dx} = \frac{\frac{1}{A} \frac{dA}{dx}}{u^2/a_e^2 - 1},$$

(7.7)

$$\frac{dh}{dx} = h_p \frac{dp}{dx} + h_p \frac{dp}{dx} + h_a \frac{dx}{dx}$$

$$-u \frac{du}{dx} = -h_p \rho u \frac{du}{dx} + h_p \left[\frac{\rho}{A} \frac{dA}{dx} + \frac{\rho}{u} \frac{du}{dx} \right] + h_a \frac{dx}{dx}$$

$$u \frac{du}{dx} \left[1 - \rho h_p - \frac{\rho h_p}{u^2} \right] = \frac{\rho h_p}{A} \frac{dA}{dx} - h_a \frac{dx}{dx}$$

$$\frac{1}{u} \frac{du}{dx} = \frac{\frac{h_p}{A} \frac{dA}{dx} - \frac{h_a}{\rho} \frac{dx}{dx}}{u^2 \left[\frac{1}{\rho} - h_p \right] - h_p}$$

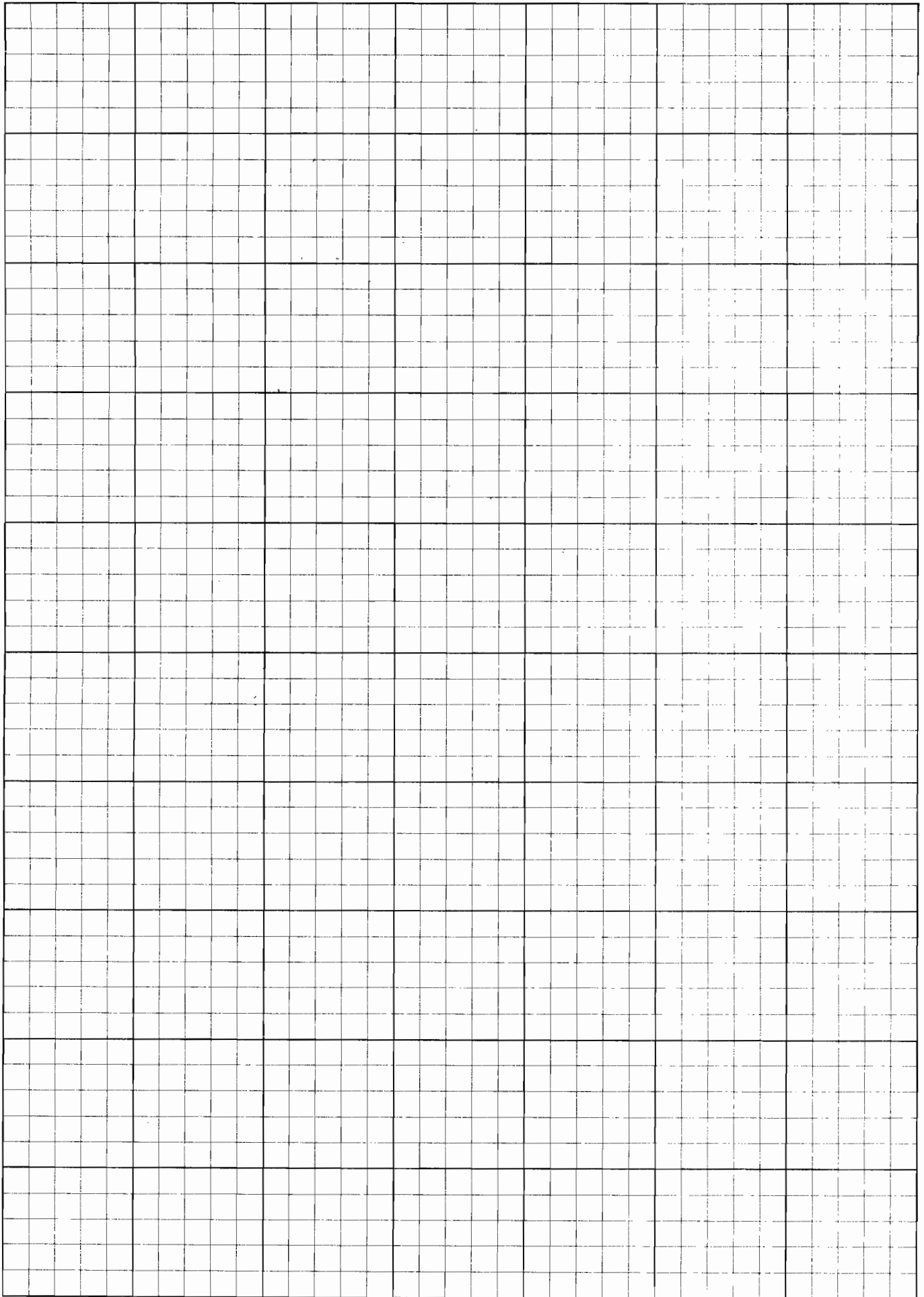
$$= \frac{\frac{1}{A} \frac{dA}{dx} - h_a/h_p \cdot \frac{1}{\rho} \frac{dx}{dx}}{\frac{u^2}{\left(\frac{-h_p}{h_p - \frac{1}{\rho}} \right)} - 1}$$

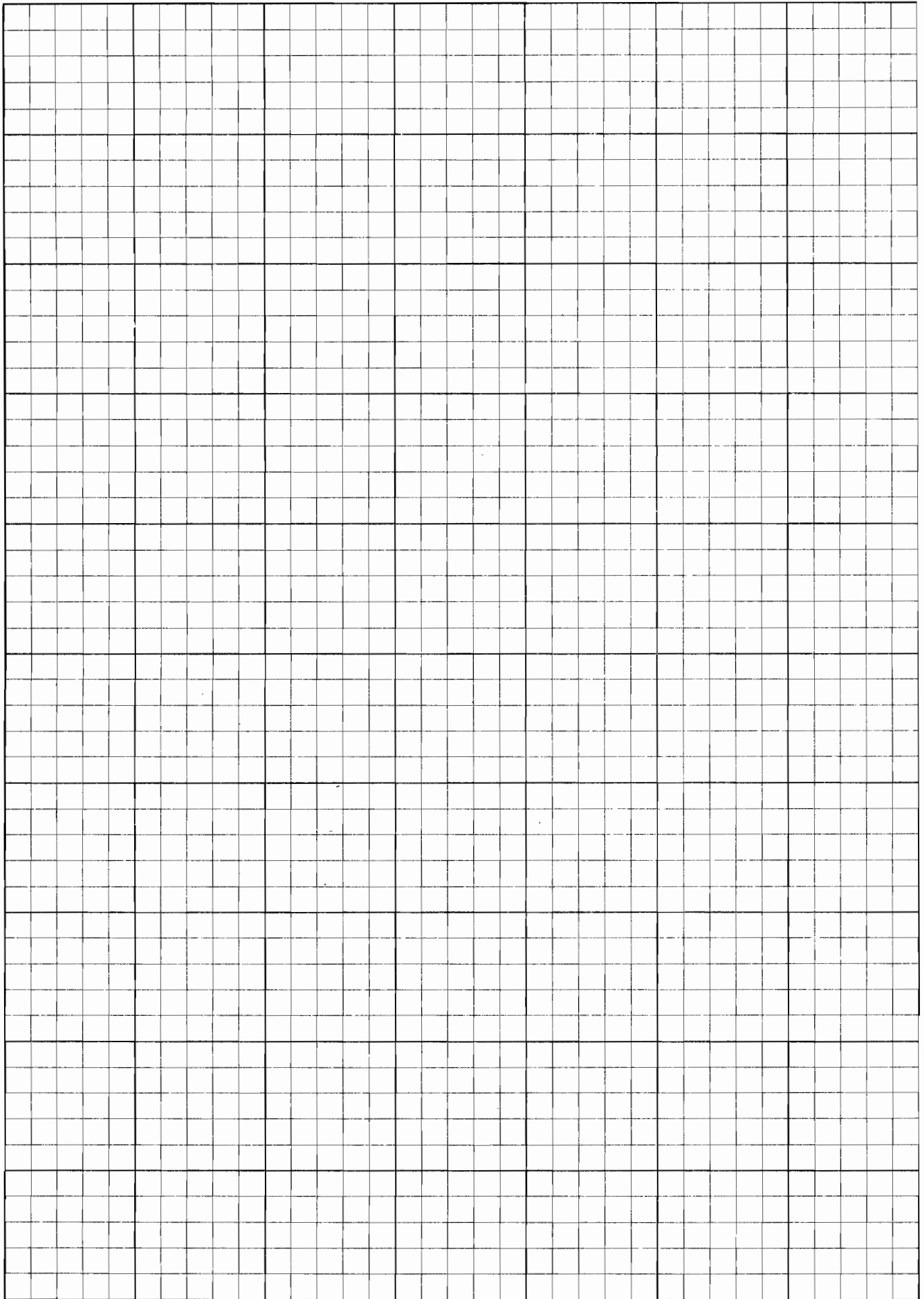
Frozen:

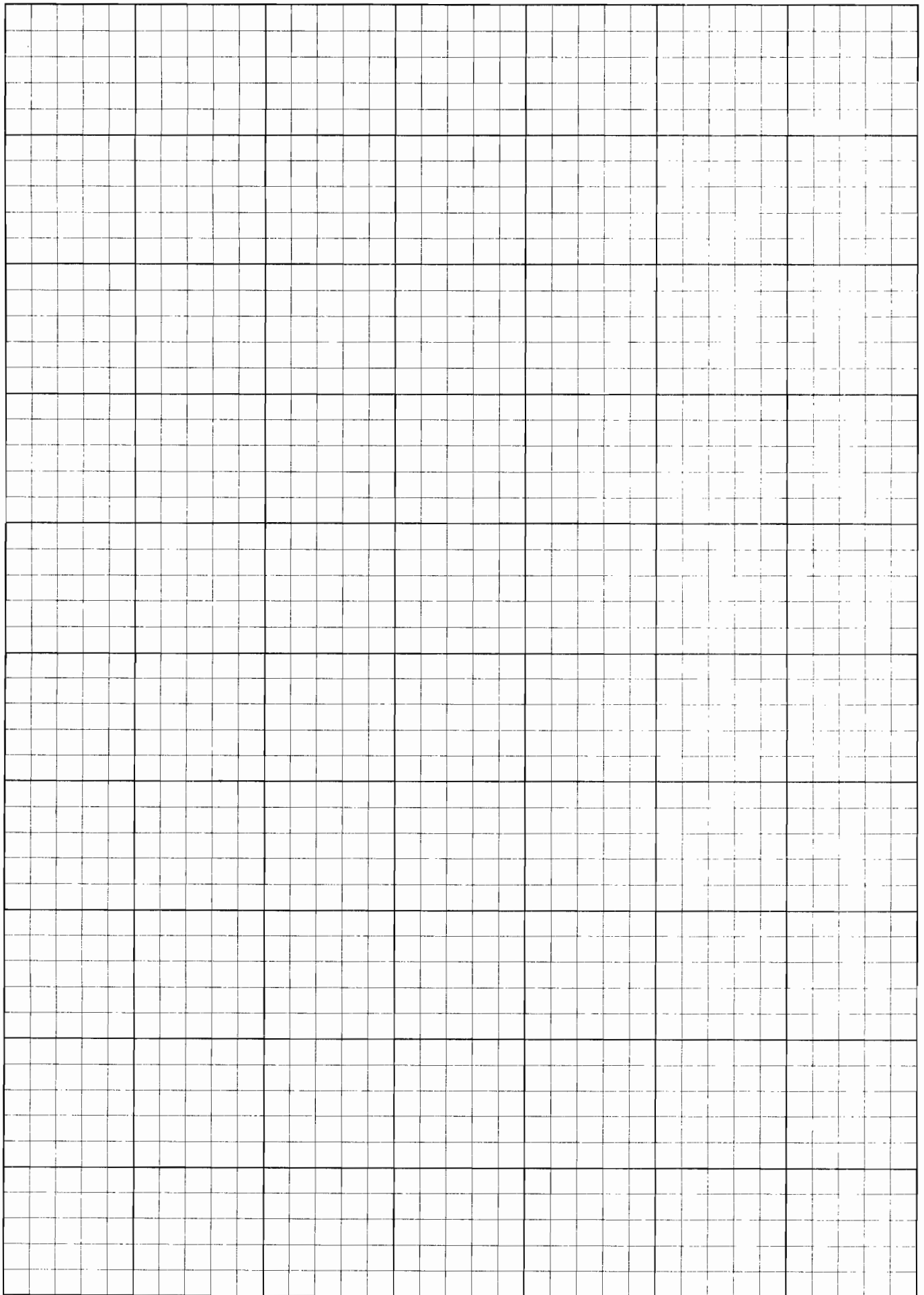
$$\frac{dx}{dx} = 0$$

$$a_f^2 = - \frac{h_p}{h_p - \frac{1}{\rho}}$$

$$= \frac{\frac{1}{A} \frac{dA}{dx}}{\frac{u^2}{a_f^2} - 1} \quad \checkmark$$







Where the complicated expression occurring in the denominator has already been replaced by a_e^2 from equation (6.17). Again, we see that the saddle point occurs at the nozzle throat and that either the flow speed has to be a_e or $du/dx = 0$. This is as it should be, since, for adiabatic equilibrium flow, $dp/d\rho = \left(\frac{\partial p}{\partial \rho}\right)_s = a_e^2$.

c) *Nonequilibrium flow.*

The situation is significantly different when nonequilibrium flow occurs in the region of the nozzle throat. The flow is no longer isentropic and $dp/d\rho$ is no longer $(\partial p/\partial \rho)_s$ and depends on du/dx . Hence, it may not be replaced by the square of some speed of sound, and, more important, the saddle point no longer occurs at the throat. Consider the case $du/dx > 0$. If du/dx is to be positive and finite, the numerator (N) and the denominator (D) must go to zero at the same value of x . For the IDG,

$$\frac{\partial h}{\partial \rho} < 0 \quad \text{and} \quad \frac{\partial h}{\partial \alpha} > 0$$

see p. 39. For $du/dx > 0$ the gas recombines in the flow direction i.e., $d\alpha/dx < 0$. Hence

$$\left(\frac{\partial h}{\partial \alpha} / \frac{\partial h}{\partial \rho}\right) \frac{1}{\rho} \cdot \frac{d\alpha}{dx} > 0.$$

Hence the numerator of (7.6)

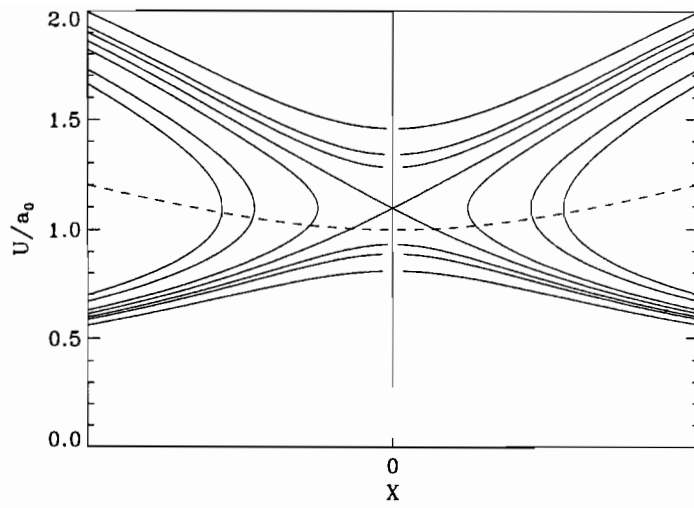
$$\frac{1}{A} \frac{dA}{dx} - \left(\frac{\partial h}{\partial \alpha} / \frac{\partial h}{\partial \rho}\right) \cdot \frac{1}{\rho} \frac{d\alpha}{dx}$$

goes to zero at a positive value of dA/dx , i.e., *downstream* of the nozzle throat. The position of the saddle point is particularly important for numerical computations. At the saddle it is necessary to take special measures to ensure that, when integrating through the saddle point, the solution follows the correct downstream branch. For example, the method of de l'Hôpital could be used to approximate the r.h.s. of (7.6) by

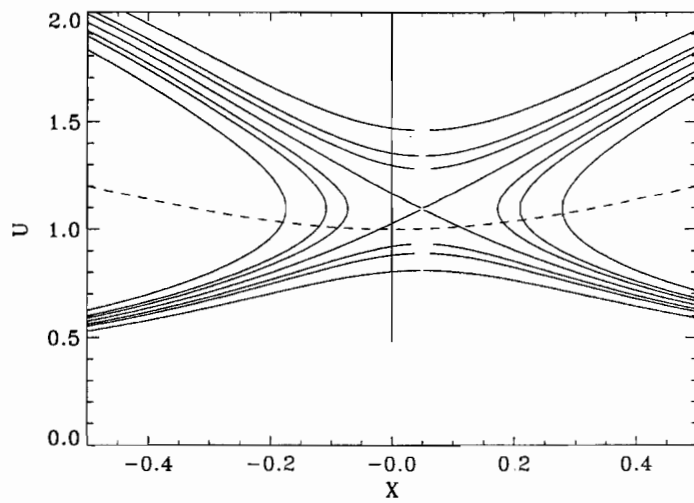
$$\frac{N}{D} = \frac{dN/dx}{dD/dx}$$

locally, and thus obtain a well-defined expression throughout.

Exercise 7.1 Use de l'Hôpital's rule to obtain a local solution for $\frac{1}{u} \frac{du}{dx}$ in the vicinity of the throat in the case of a perfect gas. Hence show that the singularity has saddle-point character.



Saddle point with frozen or equilibrium flow. Dashed: Area



Saddle point with non-equilibrium flow

Reference: Vincenti & Kruger

8 Nozzle Flow Freezing

In a large class of nozzle flows of practical importance the flow in the vicinity of the nozzle throat is in equilibrium. However, as $A(x)$ increases, the density falls, and the recombination rate (the negative term in $d\alpha/dx$), which is proportional to the square of the density,

$$u \frac{d\alpha}{dx} = C \rho T^\eta \left\{ (1 - \alpha) e^{\Theta_d/T} - \frac{\rho \alpha^2}{\rho_d} \right\}, \quad (8.1)$$

falls even more rapidly. At some stage, a point may be reached where the recombination rate can no longer keep up with the demands put on it by the rate of increase of $A(x)$. At that point a (smooth) transition from equilibrium to non-equilibrium flow occurs. Since the recombination rate falls rapidly with increasing $A(x)$, this transition is followed fairly closely by a second (smooth) transition to frozen flow, after which no significant changes of α occur anymore.

In numerical computations of such flows it is convenient to treat these three regions separately. We discuss them in terms of the above rate equation:

If the flow is in equilibrium the curly bracket is (very close to) zero. Since the change of conditions imposed on the gas with increasing $A(x)$ demands recombination, however, i.e., finite negative $d\alpha/dx$, the coefficient of $\{\}$ must be (very close to) infinity. For equilibrium flow, we determine α from the algebraic relation $\{\} = 0$.

In the numerical integration of the equations the equilibrium value of $d\alpha/dx$ is then compared at each step with $C \rho T^\eta \alpha^2 \rho / (u \rho_d)$. When a point is reached where

$$\left| \frac{C \rho^2 T^\eta \alpha^2}{u \rho_d \left(\frac{d\alpha}{dx} \right)_e} \right| \quad (8.2)$$

reaches $O(1)$ from above, a switch is made from the algebraic equation $\{\} = 0$ to the differential equation (8.1), i.e., to nonequilibrium flow. This strategy may be extended to more general problems in which many chemical reactions occur simultaneously. This avoids the numerical difficulties that arise in such situations from the possibly very different magnitude of different reaction rates, which cause the equations to be “stiff”. By separately switching each reaction from equilibrium to finite rate at the point where the l.h.s. of (8.2) for that reaction reaches a chosen threshold value, the “stiffness” is removed, see Rein.

The diagram shows the result of an IDG nozzle flow integration.

$$\alpha^* = 0.3, T^*/\theta_D = 0.10, \Lambda = 5.0E+02, \rho_D/\rho^* = 3.0E+03$$

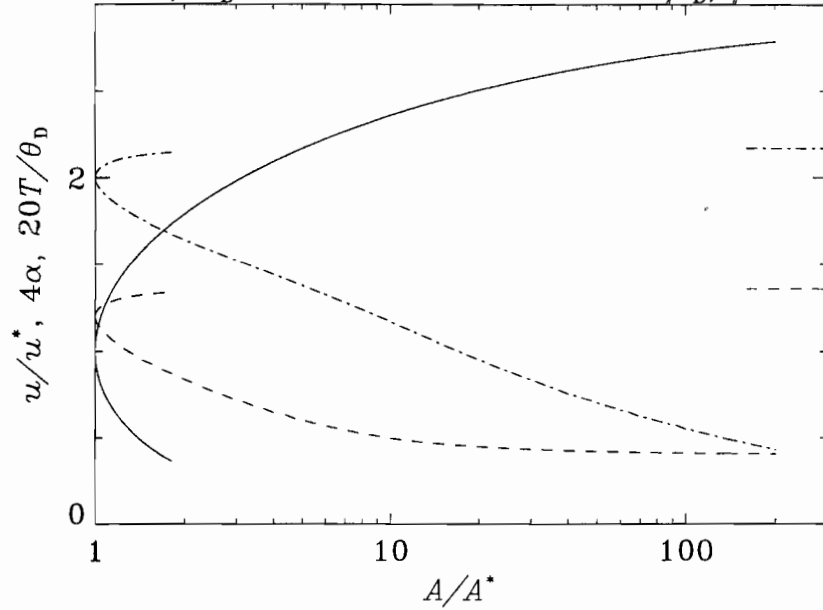


Figure 1. Calculated IDG nozzle flow. Λ is a reaction rate parameter to be defined later. The asterisks refer to values of a variable at the throat.

As may be seen, the change of α from the point where the nonequilibrium effects are significant to the point where α is constant (frozen flow) is not very large. This has led Bray (see V. & K.) to suggest the freezing criteria

$$\left| \frac{C\rho^2 T^\eta \alpha^2}{u\rho_d \left(\frac{d\alpha}{dx}\right)_e} \right| = 1 \quad (8.3)$$

to be used in conjunction with an equilibrium calculation. This leads to the result shown as a dashed line. Bray's procedure requires no nonequilibrium computations and therefore no integration since the nozzle flow equations for equilibrium may be written as algebraic equations only:

$$\begin{aligned} \rho u A &= \text{const.} \\ s &= s^*(p, \rho) = \text{const.}, \text{ see eqn. (3.14)} \\ h + \frac{u^2}{2} &= \text{const.} \\ \frac{p}{\rho} &= (1 + \alpha)T \frac{k}{2m} \end{aligned} \quad (8.4)$$

$$h = \frac{k}{2m} [(4 + \alpha)T + \alpha\Theta_d],$$

and the left hand side of equation (8.3) is completely determined by the equilibrium solution.

Since this is the case, one may also alternatively use a Mollier diagram. See procedure p. 185, Vincenti & Kruger.

Note that, as the speed approaches a constant with increasing A , the density and A become increasingly proportional to each other ($\rho A \sim \text{const.}$). Also, in the frozen limit, with $u \sim \text{const.}$, the pressure goes approximately as $p \sim A^{-\gamma}$ since $p \sim \rho^\gamma$. (For frozen flow the perfect gas model applies and $\gamma = c_p/c_v = \text{const.}$)

Features of nozzle-flow freezing

The fact that recombination can not keep up with the demands made by the rates of change imposed on the composition by the nozzle flow, leads to a nozzle-exit composition that is in a non-equilibrium state. For most applications it is important to know this composition. If the gas is subject to many different chemical reactions, and produces many different species, such as is the case for air flow, the problem appears at first sight to be very complex. It turns out, however, that there exists a very useful simplification, discovered by Harris and Warren.

For a given gas and a given nozzle geometry, the composition at which the gas eventually freezes in the nozzle expansion, depends only on the specific entropy in the reservoir. Hence the composition may be plotted against the specific reservoir entropy in a single diagram valid for all combinations of p_0 and T_0 . For example, a set of numerical computations of air flow in the T5 nozzle gives the result shown in the figures. Since the exit composition depends on the specific reservoir entropy, this can be translated by using a Mollier chart (lower part of figure) to give the dependence of exit composition on reservoir enthalpy and pressure. In T5 the maximum reservoir pressure is 100 MPa. It follows that, to obtain an exit composition of less than 1% by mass of atomic oxygen, the flow speed can not be increased to more than 4.2 km/s, and, at 6 km/s, the atomic oxygen concentration is 12% by mass. Also, the improvement achieved by increasing the reservoir pressure is slow. A tenfold increase to 1 GPa only increases these numbers to 5.2 km/s, and 5% by mass, respectively.

To explain why the reservoir-entropy-correlation works, introduce the characteristic length

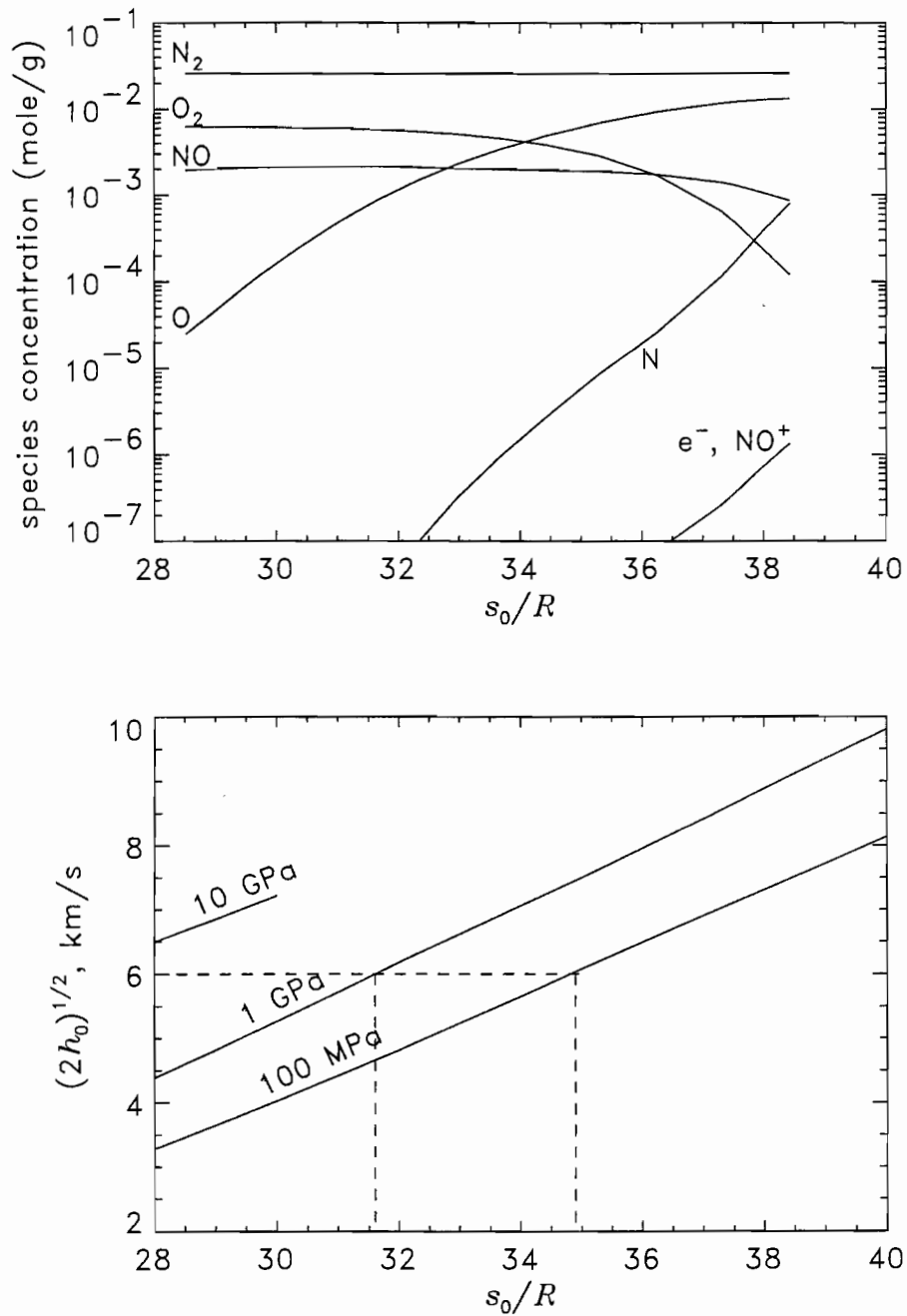


Figure 2. TOP: Calculated composition at the exit plane of the T5 nozzle as a function of specific reservoir entropy. BOTTOM: Mollier chart showing how the exit composition depends on the reservoir pressure and reservoir enthalpy.

$A/(dA/dx)$, of the nozzle. An approximate value for this is half the nozzle length, $L/2$, say.

The recombination reaction freezes when

$$\ell_r = \frac{u \rho_d}{\alpha^2 C \rho^2 T^\eta}$$

becomes comparable to $L/2$. ℓ_r increases extremely rapidly in a nozzle expansion. Assuming that the dominant variable in ℓ_r is ρ , we see that

$$\frac{\ell_{rx}}{\ell_r} \simeq -2 \frac{\rho_x}{\rho} \simeq 2 \frac{A_x}{A}.$$

Also, ℓ_r is determined essentially by state variables, provided that the gas is in equilibrium. Thus, the equilibrium value of ℓ_r may be represented in a Mollier chart. Since an equilibrium expansion is a vertical line in the Mollier chart, the point at which that line crosses the line

$$\ell_r = L/2$$

does not depend on the value of h_0 where that line starts, but only on s_0 . If ℓ_r increases sufficiently rapidly, freezing will occur suddenly at that point.

References:

Harris, C. J. and Warren, W. R., "Correlation of non-equilibrium expanding air flows", G.E. Document R64DS92, 1964.

Vincenti & Kruger

Rein, M. *Phys. Fluids* **4**, 873-886. (1992)

Bray K.N.C. *J. Fluid Mech.* **6** p.1 (1959)

Nozzle Flow Starting From Throat

6.1 Variables and Parameters

Write the variables in terms of the conditions at the throat as follows:

$$\begin{aligned}
 u &= u'/a_e'^* \\
 x &= x'/\sqrt{A'^*} \\
 \rho &= \rho'/\rho'^* \\
 T &= T'/\theta_d \\
 p &= p'/(\rho'^* a_e'^*{}^2) \\
 A(x) &= A'/A'^*,
 \end{aligned} \tag{6.1}$$

where the primed variables and θ_d are dimensional. The dissociation fraction is α , and the problem depends on the dimensionless parameters

$$K = \frac{a_e'^*{}^2}{2R\theta_d}, \quad \Lambda = \frac{C\rho'^*\theta_d^\eta\sqrt{A'^*}}{a_e'^*} = \frac{\sqrt{A'^*}}{l}, \quad \frac{T'^*}{\theta_d}, \quad \eta, \quad \text{and} \quad \frac{\rho_d}{\rho'^*}. \tag{6.2}$$

6.2 Equations for Equilibrium Flow

The equations then become:

*aim for 5 simultaneous d.e.'s
5 unknowns u, α, T, p, ρ*

$$\begin{aligned}
 C & \rho u A = 1 & \rho \frac{p_x}{p} + \frac{u_x}{u} + \frac{A_x}{A} = 0 \\
 M & u u_x + u A p_x = 0 \\
 E & 2K u u_x + (4 + \alpha) T_x + (1 + T) \alpha_x = 0 \\
 MA & \frac{2\alpha_x}{\alpha} - \frac{\alpha_x}{1 - \alpha} + \frac{\rho_x}{\rho} - \frac{T_x}{T^2} = 0 \\
 TS & \frac{p_x}{p} - \frac{\rho_x}{\rho} - \frac{\alpha_x}{1 + \alpha} - \frac{T_x}{T} = 0.
 \end{aligned} \tag{6.3}$$

~~$\frac{2Kp}{\rho} = \rho(1 + \alpha)T$~~

The third, fourth and last of these are obtained by differentiating the energy equation incorporating the caloric equation of state, the law of mass action and the thermal equation

$$\frac{2a^2}{\gamma-1}$$

$$\alpha = 0$$

$$\frac{u_x}{u} = \frac{A_x}{A} \frac{1}{\frac{2ku^2}{a^2} - 1}$$

~~$$\frac{T_x}{T} = -\frac{A_x}{A} \frac{1}{3} \frac{1}{\frac{2ku^2}{a^2} - 1}$$~~

$$\frac{T_x}{T} = -\frac{A_x}{A} \cdot \frac{1}{3} \frac{2ku^2}{\frac{2ku^2}{a^2} - 1}$$

$$= -\frac{2ku^2}{3} \frac{u_x}{u}$$

=

~~$$T_x = -\frac{uu_x}{c_p}$$~~

$$\frac{u^2}{2} + h = h_0$$

$$uu_x + h_x = 0$$

$$T_x = -\frac{uu_x}{c_p}$$

of state with respect to x . Using the second to replace p_x and the fifth to replace p in the last, and replacing ρ_x/ρ from the differentiated form of the first, *i. e.*,

$$\frac{\rho_x}{\rho} = -\frac{u_x}{u} - \frac{A_x}{A}, \quad (6.4)$$

we obtain the following three simultaneous differential equations in u , α , and T , with x as independent variable:

$$\begin{aligned} \frac{u_x}{u} \left[1 - \frac{2Ku^2}{(1+\alpha)T} \right] - \frac{\alpha_x}{1+\alpha} - \frac{T_x}{T} &= -\frac{A_x}{A} \\ \frac{u_x}{u} + \frac{2-\alpha}{\alpha(1-\alpha)}\alpha_x - \frac{T_x}{T} &= \frac{A_x}{A} \\ 2Kuu_x + (1+T)\alpha_x + (4+\alpha)T_x &= 0 \end{aligned} \quad (6.5)$$

These may be solved to give the derivatives explicitly in terms of the dependent variables and the area ratio:

$$\begin{aligned} u_x &= \frac{A_x}{A} \frac{a_e^2}{1 - a_e^2/(2Ku^2)} \frac{1}{2Ku} \\ \alpha_x &= -\frac{A_x}{A} \frac{T}{1 - a_e^2/(2Ku^2)} \frac{\alpha(1-\alpha)(1+\alpha-3T)}{\alpha(1-\alpha) + 3(2-\alpha)T^2} \\ T_x &= -\frac{A_x}{A} \frac{T^2}{1 - a_e^2/(2Ku^2)} \frac{(2-\alpha)(1+\alpha)T + \alpha(1-\alpha)}{\alpha(1-\alpha) + 3(2-\alpha)T^2}, \end{aligned} \quad (6.6)$$

$\frac{A_x}{A} \frac{u}{\frac{2Ku^2}{a_e^2} - 1}$

where

$$a_e^2 = T \frac{\alpha(1-\alpha^2)(1+2T) + (8+3\alpha-\alpha^3)T^2}{\alpha(1-\alpha) + 3(2-\alpha)T^2}, \quad (6.7)$$

is the square of the dimensionless equilibrium speed of sound. At an area minimum, or throat, where A_x is zero, u_x may be non-zero only if the denominator is also zero, *i. e.*, if the speed is equal to the equilibrium speed of sound. This means that, at the throat, the expressions for the derivatives become undefined. In the vicinity of this point it is therefore necessary to use de l'Hôpital's rule to specify the derivatives. By differentiating the numerators and denominators of the right hand sides in (6.6), and forming the quotient, we obtain three new differential equations for the neighborhood of the nozzle throat that involve the second derivative of A which is finite at the throat:



$$\begin{aligned}
u_x &= \sqrt{\frac{A_{xx}}{A} \frac{a_e^2 u}{4Ku + (G_1 F_1 + G_2 F_2)/G_3}} \\
\alpha_x &= -G_1 u_x \\
T_x &= -G_2 u_x,
\end{aligned} \tag{6.8}$$

where

$$\begin{aligned}
F_1 &= 3T^2(8 + 3\alpha - \alpha^3) + \alpha(3 + 2T)(1 - \alpha^2) - 6(2 - \alpha)T a_e^2 \\
F_2 &= 3T^2(1 - \alpha^2) + (1 + 2T)(1 - 3\alpha^2) - (1 - 2\alpha - 3T^2)a_e^2 \\
G_1 &= 2K \frac{\alpha(1 - \alpha)(1 + \alpha - 3T)}{\alpha(1 - \alpha^2)(1 + 2T) + (8 + 3\alpha - \alpha^3)T^2} \\
G_2 &= 2KuT \frac{(2 - \alpha)(1 + \alpha)T + \alpha(1 - \alpha)}{\alpha(1 - \alpha^2)(1 + 2T) + (8 + 3\alpha - \alpha^3)T^2} \\
G_3 &= \alpha(1 - \alpha) + 3(2 - \alpha)T^2.
\end{aligned} \tag{6.9}$$

The problem is most easily solved by integrating the initial-value problem in both directions starting from the throat, where the conditions are presumed known for a specified $A(x)$. Equations (6.8), derived using de l'Hôpital's rule, have to be used first, up to where A_x is no longer small, at which point a switch to equations (6.6) is in order. If it is necessary to solve the nozzle flow for a given reservoir condition, the equations are integrated in the upstream direction first, until u becomes small. This condition is then the reservoir state for the initially presumed throat condition. To get the desired reservoir condition, change the throat condition and iterate.

As the area increases with increasing x on the downstream side of the throat, it is possible that the recombination rate demanded by the area increase can not be supplied by the chemical reaction rate. At that point it is necessary to replace the law of mass action (or its derivative) with the reaction rate equation to give a non-equilibrium formulation. We assume here that the flow is always in equilibrium at the throat.

6.3 Non-equilibrium Flow

In the case of non-equilibrium flow it is necessary to replace the fourth of equations (6.3) with the rate equation

$$\alpha_x = \frac{\Lambda T^\eta}{u^2 A} \left[(1 - \alpha)e^{-1/T} - \frac{\alpha^2 \rho'^*}{u A \rho_d} \right]. \tag{6.10}$$

Thus, we obtain the set of equations that have to be solved in that case:

$$\alpha = 0$$

$$\begin{aligned} \frac{u_x}{u} &= \frac{4T \frac{A_x}{A}}{6ku^2 - 4T} \\ &= \frac{\frac{A_x}{A}}{\frac{3}{2}k \frac{u^2}{T} - 1} \\ &= \frac{\frac{A_x}{A}}{\frac{u^2}{a^2} - 1} \end{aligned}$$

because

$$\begin{aligned} a^2 &= \gamma R T' \\ &= \frac{4}{3} R \frac{T'}{\Theta_A} \end{aligned}$$

$$\begin{aligned} \frac{a^2}{a_e^2} &= \frac{4}{3} T \frac{R \Theta_A}{a_e^2} \\ &= \frac{2}{3} T \cdot \frac{1}{K} \end{aligned}$$

$$T_x = -\frac{2Kuu_x}{4}$$

$$\frac{T'_x}{\Theta_A} = -\frac{2a^2}{4R\Theta_A} \frac{u'u'_x}{a^2}$$

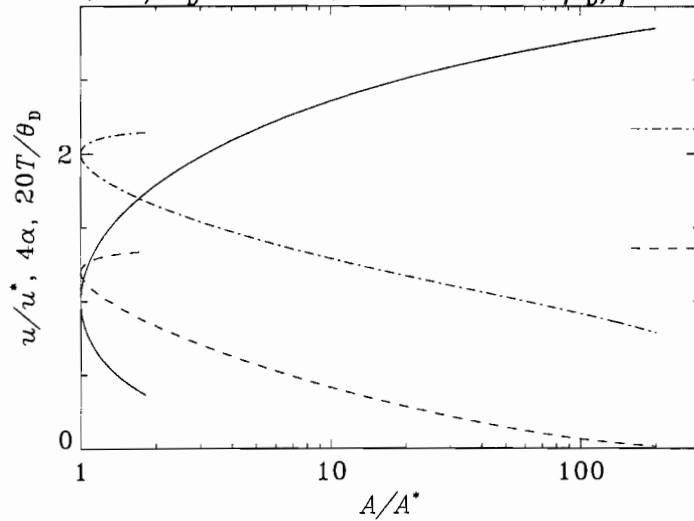
$$T'_x = -\frac{1}{4R} u'u'_x$$

$$\checkmark C_p = 4R$$

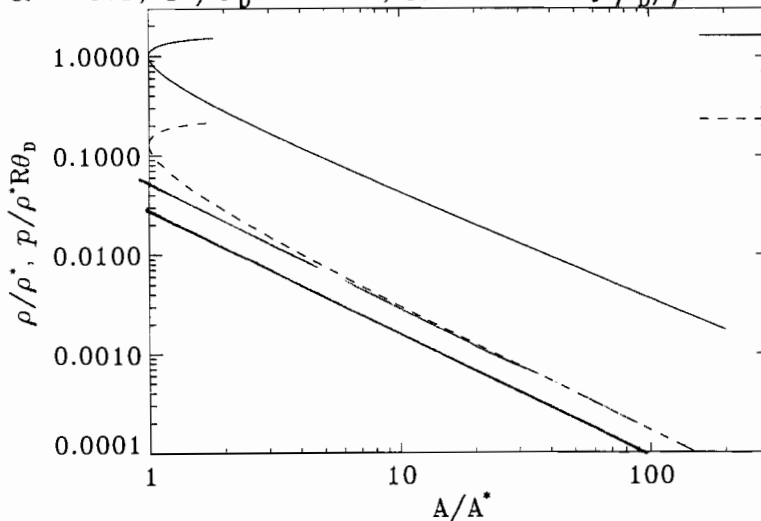
$$\begin{aligned}
 u_x &= \frac{u [(1 + \alpha)(4 + \alpha)T A_x/A + (1 + \alpha - 3T) \alpha_x]}{6Ku^2 - (1 + \alpha)(4 + \alpha)T} \\
 \alpha_x &= \frac{\Lambda T^\eta}{u^2 A} \left[(1 - \alpha)e^{-1/T} - \frac{\alpha^2 \rho'^*}{u A \rho_d} \right] \\
 T_x &= -\frac{2Kuu_x + (1 + T)\alpha_x}{4 + \alpha}.
 \end{aligned} \tag{6.11}$$

The following figures show two examples of solutions to the non-equilibrium flow problem, the first two being a case close to equilibrium ($\Lambda = 5E10$) and the next two a case where non-equilibrium effects are important, ($\Lambda = 500$).

$$\alpha^* = 0.3, T^*/\theta_D = 0.10, \Lambda = 5.0E+10, \rho_D/\rho^* = 3.0E+03$$



$$\alpha^* = 0.3, T^*/\theta_D = 0.10, \Lambda = 5.0E+01, \rho_D/\rho^* = 3.0E+03$$



$$\frac{2.5}{2} = 1.25$$

Large $\frac{A}{A^*}$

$$\rho u A = \text{const}$$

$$u \rightarrow \sqrt{2} a_0 = \text{const.}$$

$$\rho \sim \frac{1}{A}$$

if perfect gas $\frac{p}{\rho^\gamma} = \text{const}$

$$p \sim \rho^{+\gamma} \sim A^{-\gamma}$$

$$M \sim \frac{u}{\sqrt{p/\rho}}$$

$$\sim (\rho p^{1/\gamma})^{1/2}$$

$$\sim \rho^{1-\frac{\gamma}{2}}$$

$$\sim A^{\frac{\gamma-1}{2}}$$

eg. 10 fold A , $M_1 = 5$

$$\frac{M_2}{M_1} = \left(\frac{A_2}{A_1}\right)^{\frac{\gamma-1}{2}}$$

$$M_2 = 5 \times 10^{0.2}$$

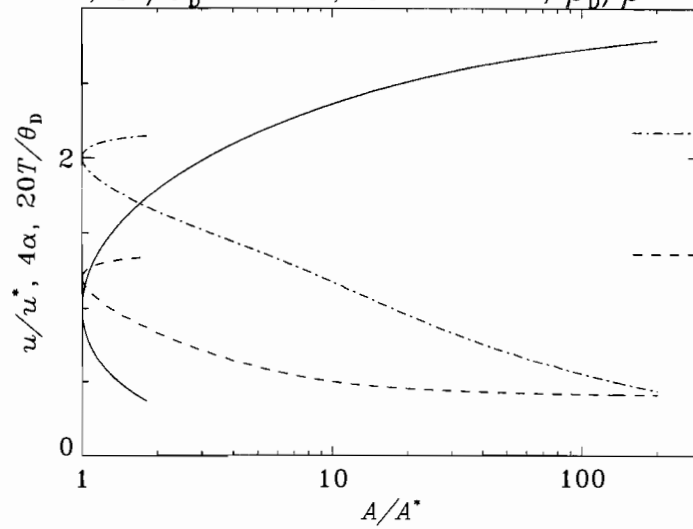
$$\log \frac{M_2}{M_1} = 0.2$$

$$\log 10 = 1$$

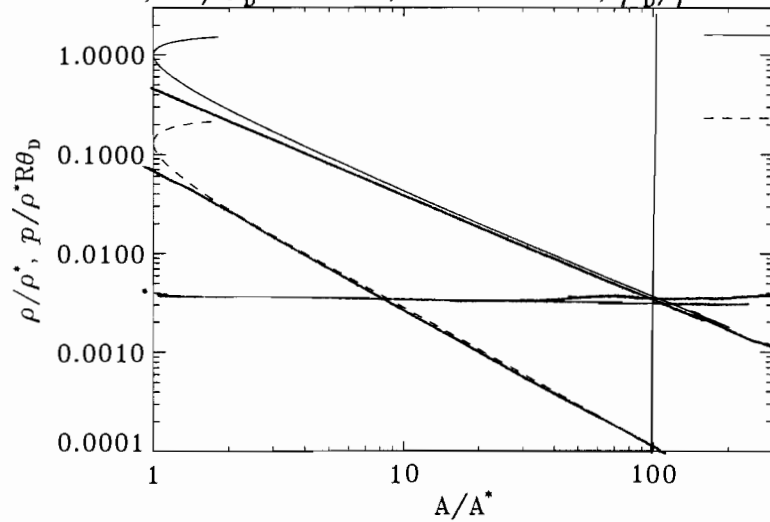
$$M_2 = 1.6 M_1$$

$$= 8$$

$$\alpha^* = 0.3, T^*/\theta_D = 0.10, \Lambda = 5.0E+02, \rho_D/\rho^* = 3.0E+03$$



$$\alpha^* = 0.3, T^*/\theta_D = 0.10, \Lambda = 5.0E+02, \rho_D/\rho^* = 3.0E+03$$



$$\frac{2.7}{2} \rightarrow 1.37 = \frac{4 + \alpha}{3}$$

$$\frac{4 + 0.1}{3} = 1.37 \times 2 = 2.74$$

9. Plane, oblique shock

Consider a plane shock making an angle β with an oncoming free stream at uniform condition 1. As the fluid crosses the shock, only its normal component of velocity, v , is changed, the tangential component u , remaining unaltered, i.e., $u_2 = u_1$.

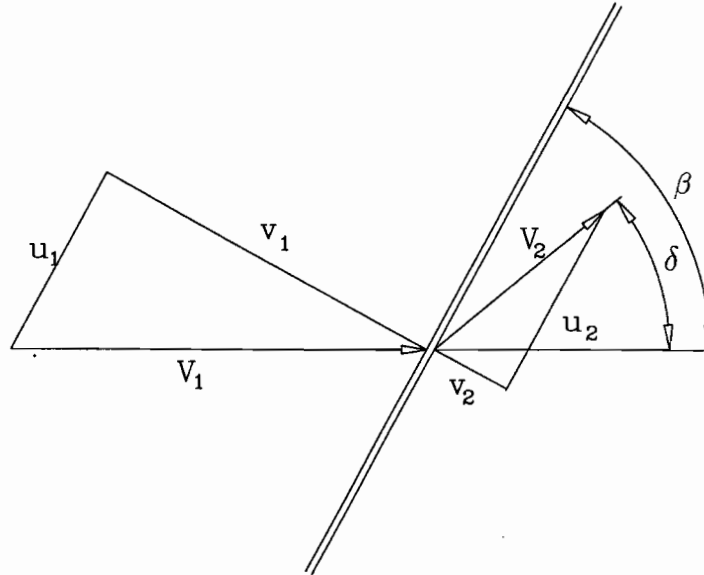


Figure 1. Sketch of oblique shock in perfect gas. Since this can be generated by a Galilean transformation from a normal shock, $u_1 = u_2$.

This result may be obtained by requiring Galilean invariance: An observer moving with velocity u_1 parallel to the shock would see the gas approaching only with the normal component of velocity v_1 . Hence he would see the situation of a normal shock in which the downstream value of u is also zero. It follows that if he moves at a velocity parallel to the shock but different from u_1 , the new shock-parallel velocity he sees is the same before and after the shock. The component of velocity parallel to the shock is thus uniform in the entire flow field.

We now use the results obtained for the normal shock with chemical nonequilibrium in order to obtain the flow through an oblique shock by superposition of a uniform velocity field parallel to the shock. To remind us of the features of nonequilibrium normal shock flow, the density and velocity profiles are sketched here again. A discontinuous reduction of the velocity at the translational shock is followed by a continuous further drop as the flow

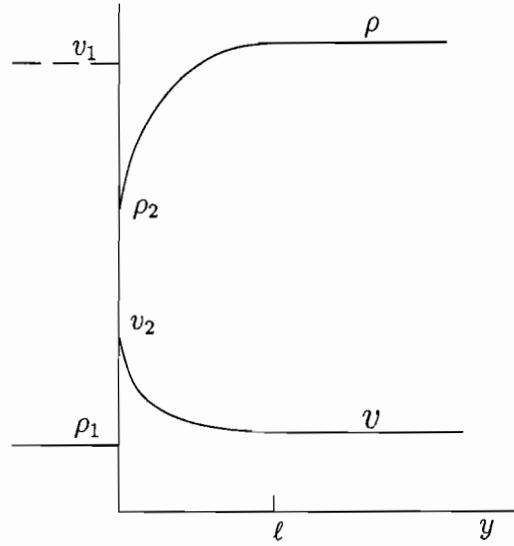


Figure 2. Sketch of density and velocity distribution in the flow downstream of a shock with dissociative relaxation.

approaches dissociative equilibrium. As may be seen from the Fig. 1, a reduction in v means an increase in δ . Thus, if we superpose a uniform velocity field parallel to the shock on a normal shock flow with nonequilibrium, the deflection angle increases with distance from the shock and the streamline downstream of the shock is curved. The deflection angle may be seen to be related to the shock angle and density ratio through

$$\frac{\rho}{\rho_1} = \frac{v_1}{v} = \frac{\tan\beta}{\tan(\beta - \delta)}, \quad (9.1)$$

as may be verified geometrically. The streamline is therefore curved in the relaxation zone and only becomes straight again when equilibrium is reached. If the relaxation is endothermic, as it is in the case of dissociation after a shock, the curvature is concave as shown in our sketch ($\delta_3 > \delta_2$). It is possible, however, to imagine a situation where the free stream is in a state of constrained equilibrium, such as, e.g., a mixture of hydrogen and oxygen at low temperature. If such a mixture flows through a sufficiently strong shock, the hydrogen may be caused to burn or detonate after the shock. This exothermic reaction would cause the behavior of the velocity in the relaxation region to be opposite to that shown in Fig. 2, and the streamline curvature would have opposite sign to that shown in Fig. 3. ($\delta_3 < \delta_2$). In the following we restrict discussion to the endothermic case.

An observer who cannot resolve the relaxation length ℓ sees only the straight parts of the streamline before the shock and downstream of $y = \ell$. For him the flow is in equilibrium in the complete field with the exception of a region within the thin shock, which he has to treat globally as a discontinuity.

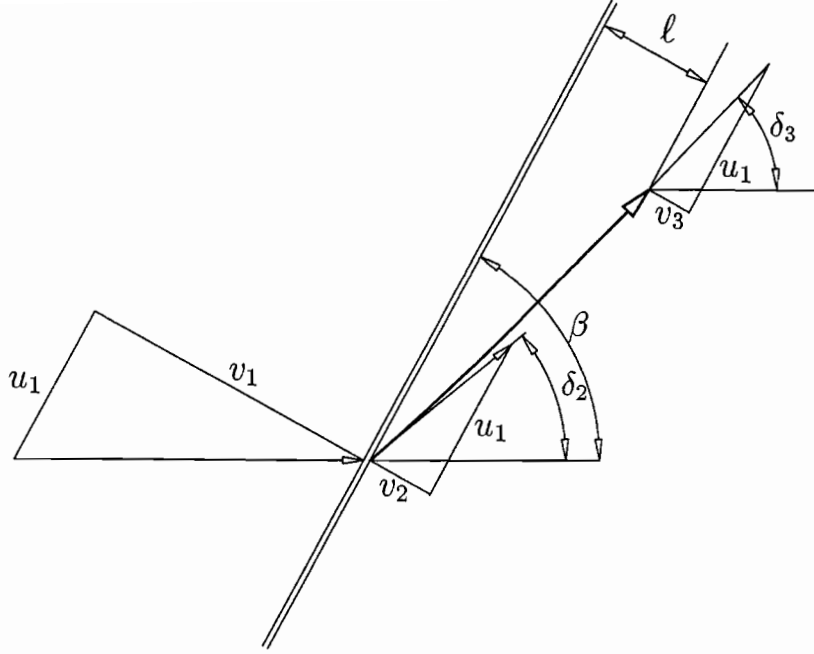


Figure 3. Sketch of streamline deflection in the flow downstream of a shock with dissociative relaxation.

We now vary the shock angle β and focus attention on the condition 2 after the shock and the final equilibrium condition 3 after the relaxation zone. It is convenient to plot these states in the $V - \delta$ plane. Two special cases give $\delta_2 = \delta_3 = 0$. They are the infinitely weak shock or sound wave

$$\beta = \arcsin (a_f/V_1), \quad (9.2)$$

and the normal shock

$$\beta = \pi/2. \quad (9.3)$$

In the latter case ($\beta = \pi/2$) it is necessary to distinguish between equilibrium and nonequilibrium flow. Since (for $\beta = \pi/2$) $V_2 = v_2 > v_3 = V_3$, the point representing the equilibrium normal shock (N_3) lies to the left of that for the frozen normal shock (N_2).

Varying the shock angle β from $\arcsin (a_f/V_1)$ to $\pi/2$ the condition 2 traverses the $V\delta$ -plane along the curve 2 and the condition 3 along the curve 3. As we know from perfect-gas dynamics the curve 2 passes through a maximum deflection point M_2 . Since (for endothermic reaction) $\delta_3 > \delta_2$, M_3 lies at a higher value δ than M_2 . Hence, *the maximum deflection angle is higher for equilibrium than for frozen flow.*

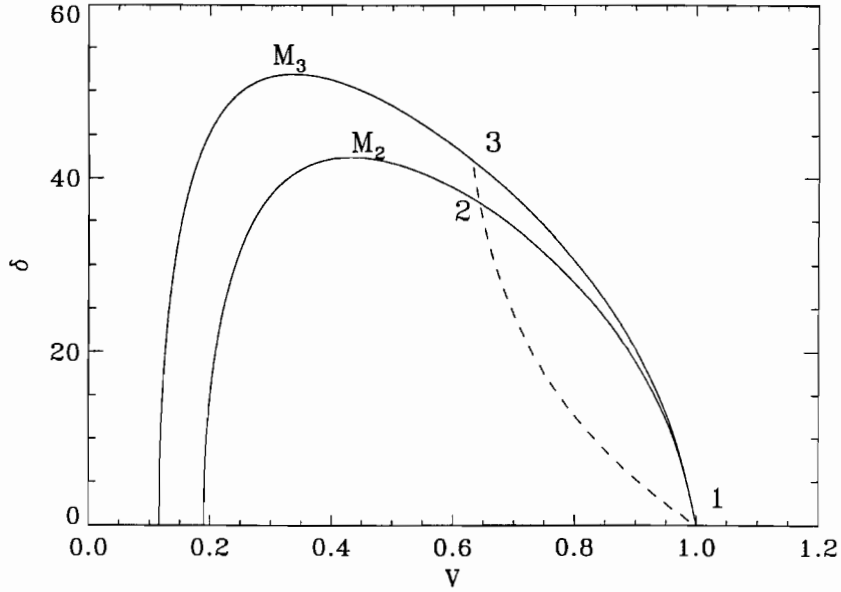


Figure 4. Oblique shock locus in the $V\delta$ -plane for frozen (lower curve) and equilibrium flow. Also shown is the locus of a streamline (dashed curve). Though there is a jump in δ and V across the shock from condition 1 (point(1,0)) to condition 2 on the lower curve, equation (9.4) describes the behavior of the streamline within this shock too. Of more interest to us is the behavior of the streamline between the condition 2 and condition 3.

We now seek the map of the streamline after an oblique shock that has a particular value of β in the $V\delta$ - plane. Evidently the condition jumps first of all from the state 1 on the V -axis to a state 2 whose position on the curve 2 is determined by β . Therefore, δ is given by

$$\delta = \beta - \arctan \frac{v}{u}, \quad (9.4)$$

as may easily be seen geometrically from Fig. 3. Replacing v by $\sqrt{V^2 - u^2}$ and differentiating δ w.r.t V at constant u and β (plane shock) we obtain

$$\frac{d\delta}{dV} = -\frac{u}{vV}. \quad (9.5)$$

since u, v and V are all positive, the streamline has negative slope in the $V\delta$ -plane. Since v decreases monotonically in the streamwise direction and so does V , while u remains constant, the map of the streamline in the $(V\delta)$ -plane is concave upward.

Note that all of this discussion does not make any assumptions about what happens in the

translational/rotational shock. In fact, (9.5) applies equally there. If the behavior of v through the translational shock is monotonic-decreasing, the dotted line between 1 and 2 indicates the map of the streamline within this thin shock.

Note that Fig. 4 applies for one free-stream condition and would be different if that is changed. The dimensionless parameters determining the diagram (in terms of IDG properties) are those of the normal shock flow, i.e., H_0 , K , α_1 , P , and ρ_d/ρ_1 .

Exercise 9.1:

Use the normal shock calculation you have made for a nonequilibrium normal shock flow to map out the streamline in the $V - \delta$ plane for a corresponding oblique shock.

Exercise 9.2:

Use the software you generated to solve the normal shock hydrogen flow to obtain the $\delta - V$ map for oblique shocks in nitrogen at a flow speed of 7 km/s and a free-stream density of 5×10^{-6} g cm $^{-3}$. Assume $\alpha_1 = 0 = P$, $H_0 = K$.



10. Sonic Line After Oblique Shock

In the last chapter we have tacitly assumed that shock waves of infinitesimal strength, i.e., sound waves, propagate at the frozen speed of sound a_f , see equation (6.13). This is the case because the relaxation length becomes infinite as the shock strength goes to zero. This is also the reason for the curves 2 and 3 in the $V\delta$ -plane to approach the point 1 with the same slope.

We now want to focus attention on that part of the $V\delta$ -plane where the downstream speed is near a_f and sketch that part of the $V\delta$ -plane. In this diagram we plot the maximum deflection points M_2 , M_3 , and the points S_{2f} and S_{3f} at which the speed V equals the local frozen speed of sound. At S_{2f} , $V_2 = a_{f2}$ and at S_{3f} , $V_3 = a_{f3}$. For a given free-stream, these two points correspond to two different shock angles β . In the limit of an infinitely strong

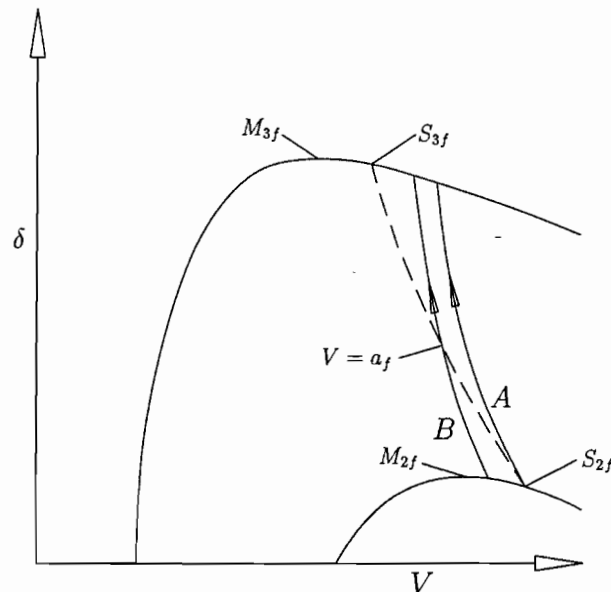


Figure 1. Sketch of $V\delta$ -plane for oblique shock with dissociation, showing the sonic line and two streamlines A and B.

shock ($V_1/a_f \rightarrow \infty$), the point S_{2f} coincides with the point M_2 .

Starting from the map of the streamline in the $V\delta$ -plane shown in section 9, we now increase the shock angle β . In that case both upstream and downstream flows are supersonic. By

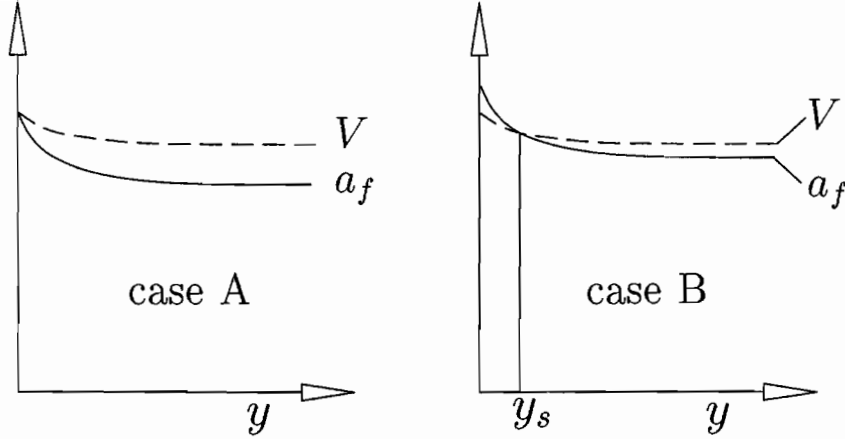


Figure 2. Profiles of V and a_f as functions of y for the two streamlines A and B.

increasing β , we reach a point where the point 2 coincides with S_{2f} . This case is shown in Fig. 1 as a streamline map A. The streamline A has been drawn in such a way that the intersection with 3 occurs to the right of S_{3f} .

We now examine whether this is correct. To do that we observe that for IDG

$$a_f^2 = \frac{4 + \alpha}{3} \frac{p}{\rho} \sim \frac{1}{\rho} \quad (10.1)$$

and

$$V^2 = V_1^2 \left(\cos^2 \beta + \frac{\rho_1^2}{\rho^2} \sin^2 \beta \right). \quad (10.2)$$

In the range of interest here, this means that a_f falls more quickly with distance from the shock than V . It follows that case A is as shown in the left sketch, i.e., supersonic everywhere except at the shock. However, if we increase the shock angle further, an entirely new phenomenon occurs: The intersection point between the curves $V(y)$ and $a_f(y)$ now moves downstream of the shock, thus opening up a *subsonic region of finite extent*, $y < y_s$, downstream of the shock. Beyond this region the flow remains supersonic. As we continue to increase β , y_s increases more and more rapidly until, as $y_s \rightarrow \ell$ it increases infinitely fast ($\frac{dy_s}{d\beta} \rightarrow \infty$) and at that point y_s becomes infinite, so that the whole of the downstream region becomes subsonic. This corresponds to the point at which the condition 3 maps onto the point S_{3f} in the $V\delta$ -plane.

It follows from the foregoing arguments that the sonic line is as sketched in the diagram Fig. 1 as a dashed line. The fact that a limited extent subsonic region may exist downstream

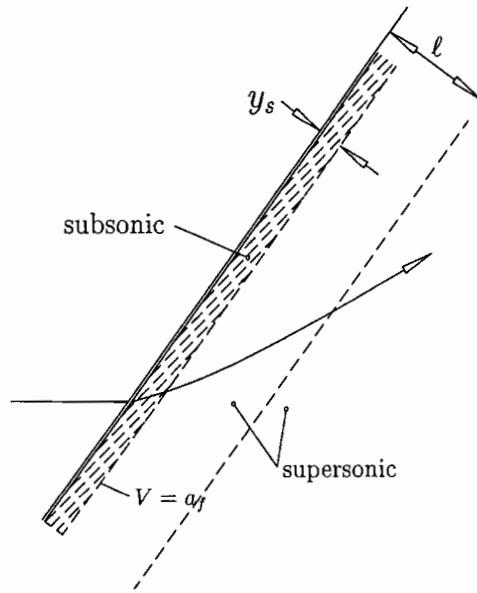


Figure 3. Physical picture for case B

of a plane oblique shock has important consequences as we shall see later. It also does not appear in any textbooks.

To show the quantitative extent of the subsonic region, the results of a numerical solution for the case $V_1 = 6 \text{ km/s}$, $\alpha_1 = 0$, $\rho_1/\rho_d = 10^{-6}$, $H_0 = K$, $IDG : N_2$ are reproduced here as a sketch y_s vs. β from [8].

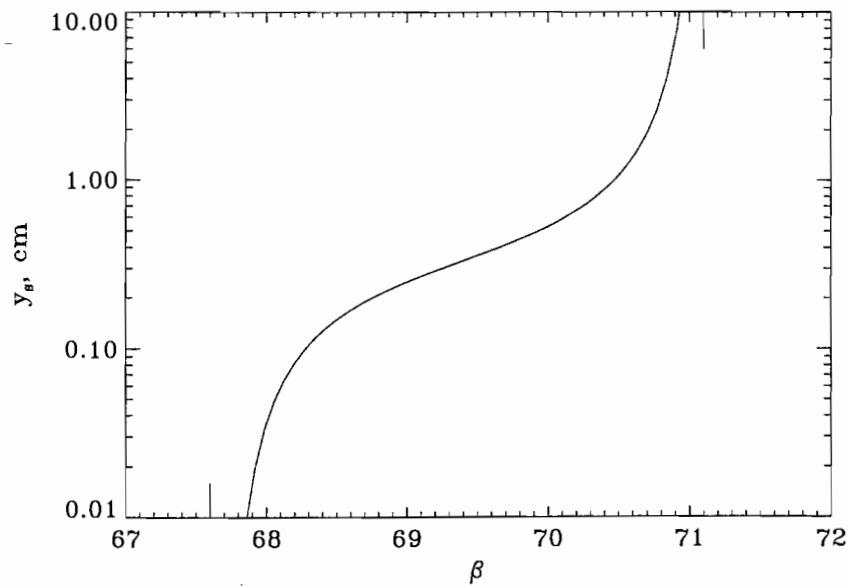


Figure 4. Sketch of variation of y_s with β

In this flow case A occurs as $\beta = 67.6^\circ$. This phenomenon, that a subsonic layer may follow a plane oblique shock, is of decisive significance for flow over a wedge. However, in order to understand it and other flows better, it is necessary to discuss the flow after a curved shock in more detail first (next chapter).

Exercise 10.1: Show that, as $V_1/a_{f1} \rightarrow \infty$ the point S_{2f} moves into the point M_2 in the $V\delta$ -plane. Is this also true for the corresponding points S_{3f} and M_3 ? If not, why not?

Reference:

[8] Hornung, H.G. & Smith G. H. *J. Fluid Mech.* 93, p.225-289, (1979).

11. Flow after a curved shock

To analyze the inviscid, adiabatic flow after a curved shock, we use the curvilinear coordinates whose origin lies in the point where the streamline to be considered pierces the shock. x is parallel to the shock, y normal to it. At the point $(x, y) = (0, 0)$ the radius of curvature of the shock is $1/k$, at the point where a streamline intersects the shock at right angles it is $1/k_0$.

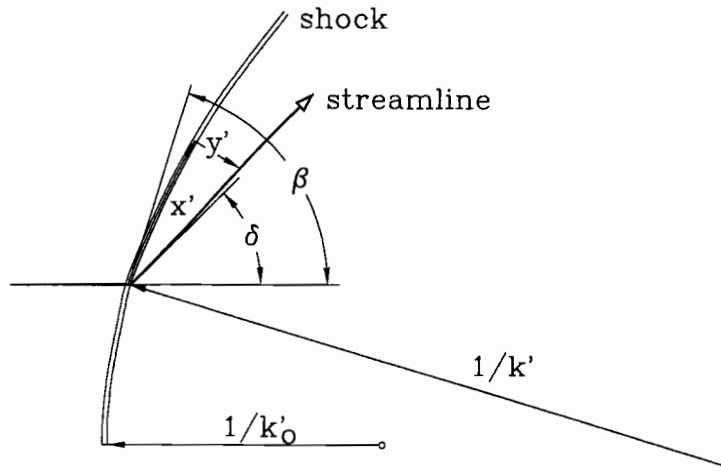


Figure 1. Notation.

In order to simplify the notation, introduce dimensionless variables as follows:

$$\begin{aligned} v &= \frac{v'}{V_1'}, & u &= \frac{u'}{V_1'}, & p &= \frac{p'}{\rho_1' V_1'^2}, & h &= \frac{h'}{V_1'^2}, \\ \rho &= \frac{\rho'}{\rho_1'}, & k &= \frac{k'}{k_0'}, & x &= x'k_0', & y &= y'k_0', & t &= t'V_1'k_0', \end{aligned} \quad (11.1)$$

where the primed variables are dimensional and the unprimed variables are dimensionless.

For the discussion in this chapter, we keep the gas general, as the conclusions to be drawn do not require a specific gas model. The conservation equations and caloric equation of state may be written in these coordinates

$$\begin{aligned} uu_x + (1 - ky)vu_y - kuv + \frac{1}{\rho} p_x &= 0 \\ uv_x + (1 - ky)vv_y + ku^2 + (1 - ky)p_y/\rho &= 0 \\ h(p, \rho, \alpha) + (u^2 + v^2)/2 &= h_0 \\ (\rho u)_x - k\rho v + (1 - ky)(\rho v)_y &= 0, \end{aligned} \quad (11.2)$$

where the indices denote partial differentiation w.r.t. the index variable. These equations, together with an equilibrium condition such as equation (2.14) or (alternatively) with an expression for $d\alpha/dt$ such as (4.18) specify the flow downstream of the shock. We are particularly interested in the nonequilibrium case. Here, we can introduce a more general reaction rate

$$h_\alpha \frac{d\alpha}{dt} = h_\alpha \left(v\alpha_y + \frac{u}{1-ky} \alpha_x \right) = r(p, \rho, \alpha), \quad (11.3)$$

which could be much more complex than the IDG model, involving many species and reactions, since the flow only cares about the rate at which enthalpy goes into and out of the chemical energy store. By differentiating the 3rd of (11.2) we can solve for the y -derivatives in terms of the flow variables and the x -derivatives. At the shock, the x -derivatives can be determined by differentiating the shock-jump relations w.r.t. x . This introduces the curvature $\beta_x = -k$. The x - and y -derivatives may then be combined to form the substantial derivatives with

$$\frac{d}{dt} = v \frac{\partial}{\partial y} + \frac{u}{1-ky} \frac{\partial}{\partial x}.$$

A great deal of algebra leads to the result

$$\begin{aligned} F \frac{dp}{dt} &= \rho r + k \frac{\rho^2 h_\rho}{v} G \\ F \frac{d\rho}{dt} &= \frac{\rho}{v^2} r - k \frac{\rho^2}{v} \left(h_p - \frac{1}{\rho} \right) G, \end{aligned} \quad (11.4)$$

where

$$\begin{aligned} F &= 1 - \rho [h_\rho/v^2 - h_p] \\ G &= \left\{ V^2 + \frac{uv_x}{k} - \frac{u}{\rho v} \frac{p_x}{k} - v \frac{u_x}{k} \right\} / (1-ky). \end{aligned} \quad (11.5)$$

(11.4) immediately yields the very interesting result

$$\frac{dp}{d\rho} = v^2 \frac{r + k \rho h_\rho G/v}{r - k \rho (h_p - \frac{1}{\rho})} Gv.$$

(11.6)

We use this equation to discuss the limiting cases of frozen flow ($r = 0$) and of the plane oblique shock ($k=0$)

a) *In frozen flow*, (11.6) degenerates to

$$\left(\frac{dp}{d\rho} \right)_{r=0} = - \frac{h_\rho}{h_p - \frac{1}{\rho}} = a_f^2. \quad (11.7)$$



In this expression we recognize the frozen sound-speed, as expected, since the flow is isentropic after the shock in frozen flow, and $(\partial p/\partial \rho)_s = a_f^2$. Note that this is *independent of G and k* .

b) For a straight shock, (11.6) degenerates to

$$\left(\frac{dp}{d\rho}\right)_{k=0} = v^2, \quad (11.8)$$

in agreement with our result for the plane shock; this may be checked by differentiating equation 5.21 which, in the dimensionless coordinates is

$$p = \sin^2 \beta (1 - 1/\rho)$$

giving

$$\frac{dp}{d\rho} = \frac{\sin^2 \beta}{\rho^2} = v^2.$$

Note that (11.8) is *independent of r* !

The equilibrium case is not covered by (11.6) because we would have had to use an algebraic equation of the form $\alpha = \alpha^*(p, \rho)$ instead of the differential equation (11.3).

For finite k and finite r , $dp/d\rho$ depends on both of these parameters. If one of them is zero, the dependence on the other also disappears.

In order to be able to draw conclusions about the $V\delta$ -map for reacting curved-shock flows, write the streamline component of the momentum equation as

$$V \frac{dV}{dt} = -\frac{1}{\rho} \frac{dp}{dt}. \quad (11.9)$$

Substantial differentiation of the equation

$$\delta = \beta - \arctan \frac{v}{u} \quad (11.10)$$

(with $\beta_x = -k$ and $\beta_y = 0$) then leads to

$$\frac{d\delta}{dV} = \frac{u}{Vv} \frac{\omega - G + \frac{uV^2}{u} \frac{p_z}{\rho k} \left(\frac{1}{a_f^2} - \frac{1}{v^2} \right)}{\omega - G}, \quad (11.11)$$

where

$$\omega \equiv -\frac{vr}{k\rho h_\rho} \quad (11.12)$$



is a local dimensionless reaction rate parameter. It relates the relaxation length to the radius of curvature of the shock. The limiting case $\omega = 0$ means frozen flow, and for it, equation (11.11) applies for arbitrary k :

$$\left(\frac{d\delta}{dV}\right)_{\omega=0} = -\frac{u}{Vv} \left[1 - \frac{vV^2}{uG} \frac{p_x}{\rho k} \left(\frac{1}{a_f^2} - \frac{1}{v^2} \right) \right] \quad (11.13)$$

It should be pointed out here that p_x/k is independent of k at the shock. Similarly G .

The limiting case $\omega = \infty$ means plane shock, since (11.11) only applies for finite r (the equilibrium case is excluded). We obtain

$$\left(\frac{d\delta}{dV}\right)_{\omega=\infty} = -\frac{u}{Vv}, \quad (11.14)$$

as expected (see eqn. 9.5).

Equations (11.13) and (11.14) thus show that the *direction of the streamline at the shock in the $V\delta$ -plane depends on ω* .

The right hand side of eqn. (11.13) has three zeros. Two of these occur at $\delta = 0$, namely because $u = 0$ both at $V = V_1$ and at the normal shock point N_2 . The third zero is $[] = 0$. It is the so-called Crocco-point C_2 , that lies between M_2 and S_2 . In the region between M_2 and N_2 , $(d\delta/dV)_{\omega=0}$ has a pole at the point I_2 .

The sketch shows as short full lines the direction in which the streamline leaves a curved shock in the case of frozen flow, while the dash-dotted short lines show the direction in which a reacting flow leaves a straight shock. For a curved shock with finite reaction rate, the direction of the streamline at the shock lies between these two extremes.

This map gives a useful means of drawing qualitative conclusions about reacting flows as we shall see. The physical plane can often be usefully mapped into the $V\delta$ -plane and vice versa.

Exercise (11.1): Find S_2 , C_2 , M_2 and I_2 for $V_1/a_f = \infty$. Give values of β .

References:

8. Hornung H.G. & Smith G.H., *J. Fluid Mech* 93 p.225-239 (1979)
9. Hornung H.G., 6th Australian Hydraulics & Fluid Mech. Conference, Proceedings, Adelaide (1977).

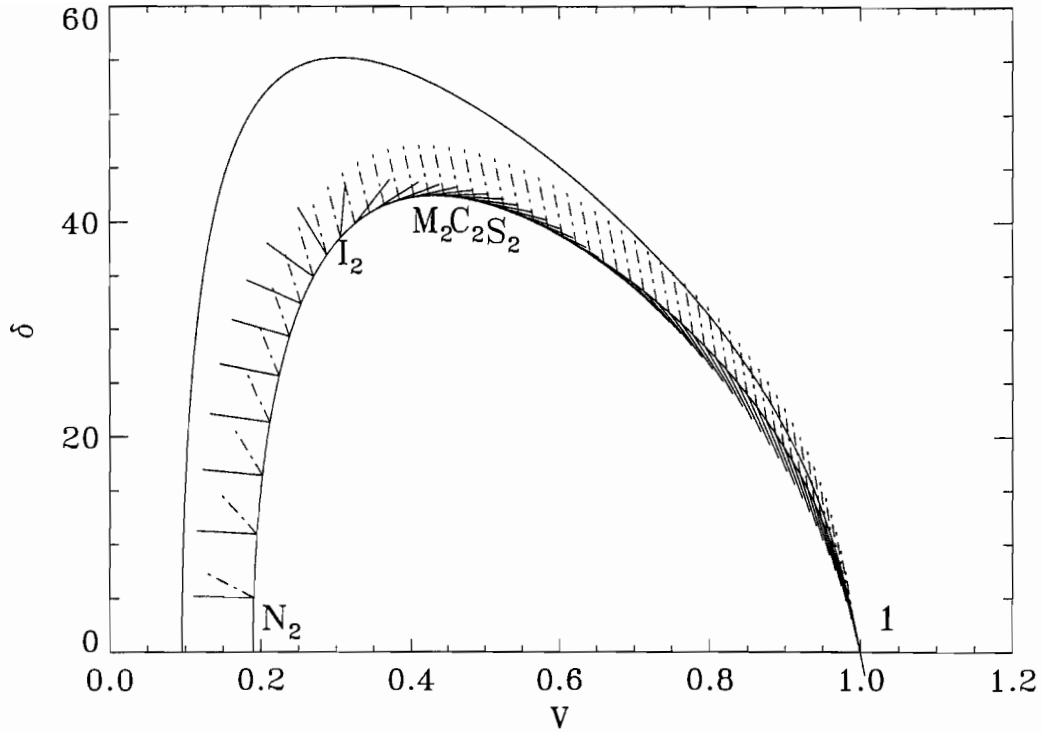


Figure 2. $V\delta$ -plane shock locus showing the directions in which streamlines have to leave the frozen shock locus when $\omega = 0$ (dash-dotted line) and when $\omega = \infty$ (full line). M_2 is the maximum-deflection point, S_2 the sonic point, and C_2 the Crocco point. At the Crocco point, the $d\delta/dV_{\omega=0} = 0$. I_2 is the point at which $d\delta/dV_{\omega=0} = \infty$.



Gradients at a curved shock in reacting flow

H. G. Hornung

Graduate Aeronautical Laboratories, California Institute of Technology, Pasadena, California 91125, USA

Received 12 February 1997 / Accepted 10 June 1997

Abstract. The inviscid equations of motion for the flow at the downstream side of a curved shock are solved for the shock-normal derivatives. Combining them with the shock-parallel derivatives yields gradients and substantial derivatives. In general these consist of two terms, one proportional to the rate of removal of specific enthalpy by the reaction, and one proportional to the shock curvature. Results about the streamline curvature show that, for sufficiently fast exothermic reaction, no Crocco point exists. This leads to a stability argument for sinusoidally perturbed normal shocks that relates to the formation of the structure of a detonation wave. Application to the deflection–pressure map of a streamline emerging from a triple shock point leads to the conclusion that, for non-reacting flow, the curvature of the Mach stem and reflected shock must be zero at the triple point, if the incident shock is straight. The direction and magnitude of the gradient at the shock of any flow quantity may be written down using the results. The sonic line slope in reacting flow serves as an example. Extension of the results — derived in the first place for plane flow — to three dimensions is straightforward.

Key words: Streamline curvature, Crocco point, Pressure–deflection map, Mach reflection, Detonation, Shock stability, Vorticity, Sonic line

1 Introduction

Physical shock waves, which always have finite thickness, may be modeled mathematically as infinitesimally thin entities across which physical properties change discontinuously. The relation between the two states at the discontinuity is supplied by the conservation equations. Thus, given the local and instantaneous velocity of propagation of a shock relative to the medium and the orientation of this velocity relative to the tangent–plane to the shock, the local and instantaneous conditions on the downstream side of the shock may be determined from the upstream state on the shock and the thermodynamic properties of the medium. This is true even if the shock is curved and accelerating, and if it

is propagating into a medium in which finite gradients exist. Such relations will be referred to in the following as the shock–jump relations.

When dealing with curved or accelerating shocks, or with non-uniform upstream media, it is sometimes useful to extend the shock–jump relations to include the connections between curvature or acceleration of the shock, and the gradients on the downstream side of the shock. The case considered here is that of a stationary curved shock with uniform upstream conditions in a steady flow of a perfect or a reacting gas. In this case the shock curvature and reaction rate determine the gradients on the downstream side of the shock.

A number of textbooks on gasdynamics partially cover this topic, *e. g.*, Hayes and Probstein (1959), Oswatitsch (1952), and several publications treat different aspects, *e. g.*, Lighthill (1949), Munk and Prim (1948), Clarke (1969), Mölder (1971). To present the problem coherently it is necessary to repeat the analyses of previous publications to some extent. In doing so the present approach begins with the analysis of Hornung (1976), in which the equations required for the present problem were used as a starting point for an asymptotic analysis of endothermic reacting flow downstream of a convex shock.

2 Definition of the problem

Consider a curved shock wave in a uniform free stream characterized by velocity V'_∞ , density ρ'_∞ . The origin of the shock-aligned curvilinear coordinates x', y' is chosen at the point where the streamline of interest crosses the shock wave. Let the shock curvature at this point be k' and the shock and deflection angles be β and δ as shown in Fig. 1. Introduce dimensionless variables defined by

$$\begin{aligned} h &= h' / V'_\infty{}^2, & p &= p' / \rho'_\infty V'_\infty{}^2, & v &= v' / V'_\infty, \\ \rho &= \rho' / \rho'_\infty, & y &= y' k'_0, & k &= k' / k'_0, \end{aligned}$$

where h, p, ρ, v are dimensionless specific enthalpy, pressure, density and y -velocity, and k'_0 is a convenient reference value of the shock curvature. The x -component of velocity u is made dimensionless in the same way as v .

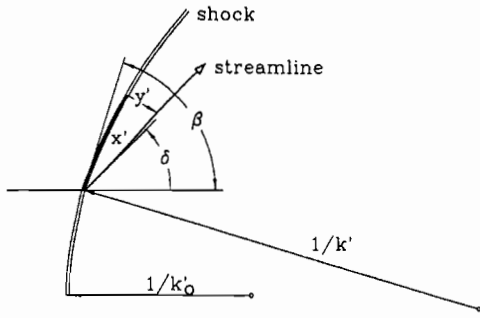


Fig. 1. Notation. Upstream of the curved shock wave, conditions are assumed to be uniform. The origin of coordinates is the point where the streamline of interest crosses the shock

The gas is supposed to obey caloric and thermal equations of state of the forms

$$h = h(p, \rho, c_i), \quad (1)$$

$$T = T(p, \rho, c_i), \quad (2)$$

in which T is the dimensionless absolute temperature $RT'/V_\infty'^2$, with the specific gas constant R , and the c_i are the mass fractions of the n constituent species of the gas, i taking values 1 through n .

Since the mass fractions must satisfy the identity

$$\sum_{i=1}^n c_i = 1,$$

the number of mass fractions that are independent is one less than the total number n of components present. It is usually convenient to choose c_1 as a dependent variable and the other c_i 's as independent variables. Thus,

$$dh = h_\rho d\rho + h_p dp + \sum_{i=2}^n h_{c_i} dc_i$$

where the subscripts denote partial differentiation.

In order to determine the gradients of physical properties of the flow at the shock wave, it is necessary to solve the differential equations of motion for the components of the gradients. To do this, consider the two components of the inviscid momentum equations, the y -differentiated energy equation and the continuity equation as follows:

$$uu_x + (1 - ky)vu_y - kuv + p_x/\rho = 0, \quad (3)$$

$$uv_x + (1 - ky)vv_y + ku^2 + (1 - ky)p_y/\rho = 0, \quad (4)$$

$$h_p p_y + h_\rho \rho_y + \sum_{i=2}^n h_{c_i} c_{iy} + vv_y + uu_y = 0, \quad (5)$$

$$(\rho u)_x - k\rho v + (1 - ky)(\rho v)_y = 0. \quad (6)$$

The case of interest here is $y = 0$, *i. e.*, the term $(1 - ky)$ that occurs in these equations may be written as 1 for our purposes. The x -differentiated form of the energy equation

$$\rho_x = -(uu_x + vv_x + h_p p_x)/h_p, \quad (7)$$

will also be needed, as will the shock-jump relations

$$p - p_\infty = \sin^2 \beta (1 - 1/\rho), \quad (8)$$

$$c_i = c_{i\infty}, \quad (9)$$

$$v = \sin \beta / \rho, \quad (10)$$

$$2(h - h_\infty) = \sin^2 \beta (1 - 1/\rho^2), \quad (11)$$

$$u = \cos \beta, \quad (12)$$

$$\rho = \frac{\gamma + 1}{\gamma - 1 + 2/(M^2 \sin^2 \beta)}, \quad (13)$$

where γ is the ratio of specific heats, and M is the free-stream Mach number. The expression for the density ratio across the shock, Eq. (13), is written for a constant- γ gas. This is permissible in a reacting flow situation if the shock-jump relations are taken to apply to the jump from the free-stream conditions to the conditions downstream of the shock before any reactions take place, *i. e.*, to a jump that does not involve a change of composition, as is made clear by Eq. (9).

The problem of determining the gradients of the flow variables at the shock consists of solving Eqs. (3 to 6) for the y -derivatives, and determining the x -derivatives (along the shock) by differentiating the shock-jump relations with respect to x .

So far it has been tacitly assumed that the flow is plane. As will be seen later, the extension to the general case is quite straightforward.

3 Partial and substantial derivatives at the shock

Differentiation of the shock-jump conditions with respect to x introduces the shock curvature $\beta_x = -k$:

$$\frac{u_x}{k} = \sin \beta \quad (14)$$

$$\frac{\rho_x}{k} = -\frac{4\rho^2 \cos \beta}{(\gamma + 1)M^2 \sin^3 \beta} \quad (15)$$

$$\frac{p_x}{k} = -2 \sin \beta \cos \beta \left(1 - \frac{1}{\rho}\right) + \frac{\sin^2 \beta}{\rho^2} \frac{\rho_x}{k} \quad (16)$$

$$\frac{v_x}{k} = -\frac{\cos \beta}{\rho} - \frac{\sin \beta}{\rho^2} \frac{\rho_x}{k}. \quad (17)$$

Solving Eqs. (3 to 6) for the y -derivatives yields:

$$p_y F = \rho \sum_{i=2}^n h_{c_i} c_{iy} - k\rho \left[u \left(1 - \frac{\rho h_p}{v^2}\right) K + \frac{u}{v} E + \rho \frac{h_p}{v} L \right] \quad (18)$$

$$u_y = -\frac{kE}{v} \quad (19)$$

$$vv_y F = -\sum_{i=2}^n h_{c_i} c_{iy} + k \left[\rho u h_p K + \frac{u}{v} E + \rho \frac{h_p}{v} L \right] \quad (20)$$

$$\rho_y F = \frac{\rho}{v^2} \sum_{i=2}^n h_{c_i} c_{iy} - \frac{k\rho}{v^2} \left[\rho u h_p K + \frac{u}{v} E + \left(1 - \rho h_p\right) L \right], \quad (21)$$

where

$$K = \frac{v_x}{k} + u, \quad (22)$$

$$L = \frac{(\rho u)_x}{\rho k} - v, \quad (23)$$

$$E = \frac{p_x}{\rho k} + u \frac{u_x}{k} - uv, \quad (24)$$

$$F = 1 - \rho \left(\frac{h_p}{v^2} + h_p \right). \quad (25)$$

The y -derivatives of the c_i have to be kept as components of a parameter, because they depend on the reaction rates, which are functions of state that have so far been left unspecified. As may be seen from Eqs. (14 to 17), any x -derivative is proportional to k , so that ratios like p_x/k are independent of the shock curvature, and all such ratios are known on the shock in terms of the free-stream conditions and β .

With both x - and y -derivatives known, it is now possible to form substantial derivatives according to

$$\frac{d}{dt} = \frac{u}{1-u} \frac{\partial}{\partial x} + v \frac{\partial}{\partial y}. \quad (26)$$

For example, noting that the deflection angle is

$$\delta = \beta - \arctan(v/u), \quad (27)$$

forming the derivatives of this function with respect to x and y , and writing

$$V = ds/dt = \sqrt{v^2 + u^2}, \quad (28)$$

where s is distance along the streamline measured from the origin, the streamline curvature at the shock, $d\delta/ds$ is obtained as

$$\frac{vV^3}{u} F \frac{d\delta}{ds} = \sum_{i=2}^n h_{c_i} \frac{dc_i}{dt} + \frac{k}{v} \left(\rho h_p G - \frac{vV^2}{\rho u} \frac{p_x}{k} F \right), \quad (29)$$

where

$$G = V^2 + \frac{uv_x}{k} - \frac{up_x}{\rho vk} - v \frac{u_x}{k}. \quad (30)$$

Similarly, other substantial derivatives may be formed:

$$F \frac{dp}{dt} = \rho \sum_{i=2}^n h_{c_i} \frac{dc_i}{dt} + kG \frac{\rho^2 h_p}{v}, \quad (31)$$

$$F \frac{d\rho}{dt} = \frac{\rho}{v^2} \sum_{i=2}^n h_{c_i} \frac{dc_i}{dt} - kG \frac{\rho^2}{v} \left(h_p - \frac{1}{\rho} \right), \quad (32)$$

$$V \frac{dV}{dt} = -\frac{1}{\rho} \frac{dp}{dt}. \quad (33)$$

At this point it is worth taking a closer look at these results. Note that the streamline curvature and the substantial time-derivatives all consist of two terms, one of which is proportional to the rate of change of specific enthalpy of the gas that is caused by chemical reaction, and the other is proportional to the shock curvature. (It is important to remember that the coefficients of these two parameters – reaction rate

and shock curvature – are all determined by the free-stream conditions and the shock-jump relations). It follows that, for non-reacting flow, all of these derivatives are proportional to the shock curvature, through a proportionality factor that depends on the free-stream conditions and the shock angle. Conversely, for chemically reacting flow through a straight shock, the streamline curvature and time derivatives are directly proportional to the rate of specific enthalpy removal by chemistry.

A special case of some interest warrants discussion: In inviscid chemically reacting flow over a plane wedge at an angle sufficiently small to give an attached shock, the streamline curvature at the tip of the wedge has to be zero (plane wedge) and Eq. (29) gives

$$\sum_{i=2}^n h_{c_i} \frac{dc_i}{dt} = -\frac{k}{v} \left(\rho h_p G - \frac{vV^2}{\rho u} \frac{p_x}{k} F \right), \quad (34)$$

i. e., the reaction-rate parameter is proportional to the shock curvature at the tip, as has been pointed out by Clarke (1969), Becker (1972) and others. This has also been used to determine reaction rates experimentally by Smith and Wegener (see Becker, 1972) and by Kewley and Hornung (1974).

Another interesting observation may be made by forming the ratio of Eqs. (31) and (32). This gives

$$\frac{dp}{d\rho} = v^2 \frac{\sum_{i=2}^n h_{c_i} dc_i/dt + kG \rho h_p / v}{\sum_{i=2}^n h_{c_i} dc_i/dt - kG \rho v (h_p - 1/\rho)}. \quad (35)$$

Both the numerator and the denominator obviously contain two terms, one from shock curvature and one from reaction rate. Again consider the limiting cases of non-reacting flow and straight shock: In the case of non-reacting flow, the first terms in the numerator and in the denominator vanish. This has the interesting consequence that the curvature terms also cancel, so that the derivative of p with respect to ρ along the streamline also becomes independent of the shock curvature! The equation reduces to

$$\frac{dp}{d\rho} = -\frac{h_p}{h_p - 1/\rho}. \quad (36)$$

This is just the expression for the value of this derivative at constant entropy (the square of the frozen speed of sound) for a gas with a general caloric equation of state. This is as it should be, since the entropy will be constant along a streamline in non-reacting flow.

In the other limit, that of reacting flow through a plane shock, omitting the curvature terms again causes the other parameter to cancel as well, and gives the well-known result

$$\frac{dp}{d\rho} = v^2. \quad (37)$$

4 Streamline curvature

Many interesting features of flows may be understood better by studying the streamline curvature at a shock. This is, of course, only one case where the results of the previous section about gradients at the shock can be used to advantage. However, it serves the purpose of demonstrating how the jump conditions may be extended by considering gradients.

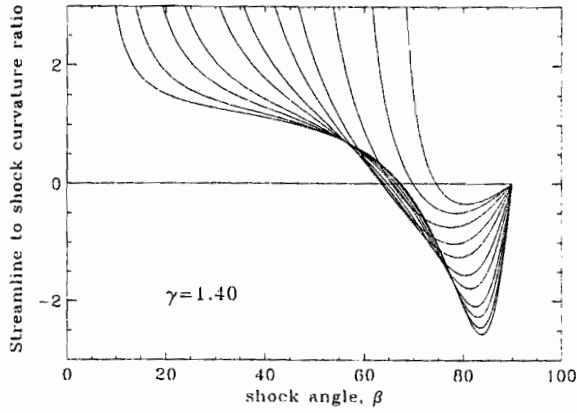


Fig. 2. Ratio of streamline to shock curvature for perfect-gas flows with $\gamma = 1.4$ and for free-stream Mach numbers 1.1 (uppermost curve), 1.2, 1.4, 1.7, 2.0, 2.5, 3.4, 5, 7, 10, 20. The ratio becomes singular at the Mach angle, and goes to zero at the normal-shock point. A zero crossing occurs again at the Crocco point (zero crossing) which always occurs between the sonic and maximum-deflection point

4.1 Perfect-gas flows

With non-reacting flow, G , F , E , K , and L reduce to relatively simple functions of M , γ and β :

$$G = \left[3 \cos^2 \beta - \frac{\sin^2 \beta}{\rho^2} \right] \left(1 - \frac{1}{\rho} \right) + \frac{8 \cot^2 \beta}{(\gamma + 1) M^2}, \quad (38)$$

$$F = -\frac{1}{\gamma - 1} \left(1 - \frac{\gamma p \rho}{\sin^2 \beta} \right), \quad (39)$$

$$E = -\frac{\cos \beta \sin \beta}{\rho} \left[\left(3 - \frac{1}{\rho} \right) + \frac{4}{\rho (\gamma + 1) M^2 \sin^2 \beta} \right], \quad (40)$$

$$K = \cos \beta \left[1 - \frac{1}{\rho} + \frac{4}{(\gamma + 1) M^2 \sin^2 \beta} \right], \quad (41)$$

$$L = \sin \beta \left(1 - \frac{1}{\rho} \right) - \frac{4 \rho \cos^2 \beta}{(\gamma + 1) M^2 \sin^3 \beta}. \quad (42)$$

Evaluating the ratio of streamline to shock curvature gives the result shown in Fig. 2 for $\gamma = 1.4$. The features of the streamline-to-shock curvature ratio may be described in terms of a convex shock such as is shown in Fig. 1. At the normal-shock point the streamline curvature has to be zero, of course. It is of opposite sign to that of the shock at values of β smaller than and close to 90° , but reaches a minimum before increasing again to positive values, and finally becomes singular at the Mach angle. The zero-crossing occurs at the so-called Crocco point, at which the streamline curvature is zero for all values of the shock curvature. For perfect-gas flows, the Crocco point always lies between the point where the Mach number at the shock is unity – the sonic point – and the maximum-deflection point. Thus, for the convex shock, the streamline curvature is concave-up near the normal-shock point, and goes to convex-up at small shock angles. The singularity at the Mach angle does not mean that the streamline curvature becomes infinite, but rather that the shock curvature is identically zero there.

The dependence of the streamline to shock curvature ratio on γ may be illustrated by plotting the same graphs for

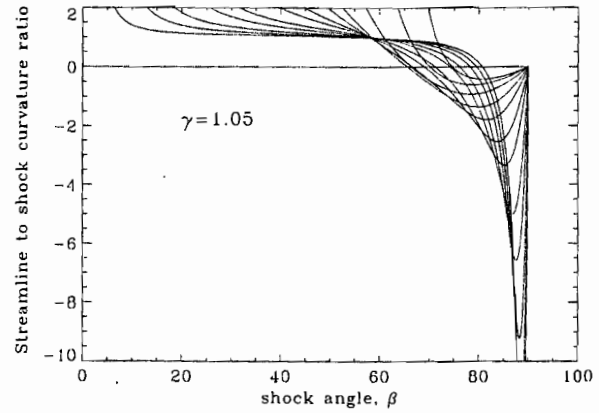


Fig. 3. Ratio of streamline to shock curvature for perfect-gas flows with $\gamma = 1.05$ and for free-stream Mach numbers 1.1, 1.2, 1.4, 1.7, 2.0, 2.5, 3, 4, 5, 7, 10, 20. Note how the high-Mach-number cases hug the ratio 1. This is close to the Newtonian limit, where the streamlines lie close to the shock for a large range of shock angles

$\gamma = 1.05$, see Fig. 3. At low Mach numbers the curves behave in much the same manner as for higher γ , but at higher Mach numbers the minimum is much lower, the Crocco point is pushed closer to the normal-shock point, and, as the Mach number becomes very high, the curvature ratio hugs the value 1 more and more closely and for a larger range of shock angles. This is the behavior expected as conditions approach the Newtonian limit ($M \rightarrow \infty$, $\gamma \rightarrow 1$), where streamline and shock become almost congruent, since the density ratio across the shock approaches infinity.

4.2 Reacting flow

In order to calculate explicit values of gradients in the case of reacting flow, it is necessary to introduce a model for the caloric equation of state and for the reaction rate. For this purpose, the rate equation is written in the simple form

$$\sum_{i=2}^n h_{ci} \frac{dc_i}{dt} = \frac{\theta}{\varepsilon} \exp(-\theta \rho / p), \quad (43)$$

so that a representative variation of the dependence of reaction rate on shock angle is maintained by using the Arrhenius form. The differential form of the caloric equation of state becomes

$$dh = -\frac{\gamma}{\gamma - 1} \frac{p}{\rho^2} d\rho + \frac{\gamma}{\gamma - 1} \frac{1}{\rho} dp + \frac{\theta}{\varepsilon} \exp(-\theta \rho / p) dt. \quad (44)$$

With this form of the reaction rate, the streamline curvature may be calculated explicitly for given values of θ and ε . The result of such a computation is plotted in Fig. 4. With the sign convention chosen in Eqs. (43) and (44), positive values of θ and ε mean that the reaction is endothermic. Thus, Fig. 4 shows the remarkable fact that, for a given set of parameters M , γ , and θ , there exists a particular reaction rate parameter ε , below which the streamline-to-shock curvature ratio is positive for all shock angles, and no Crocco point exists. The reaction rate at this point is always exothermic, *i. e.*, ε is negative at this point. For the parameters chosen in Fig. 4, the special value of ε is approximately $-1/119$.



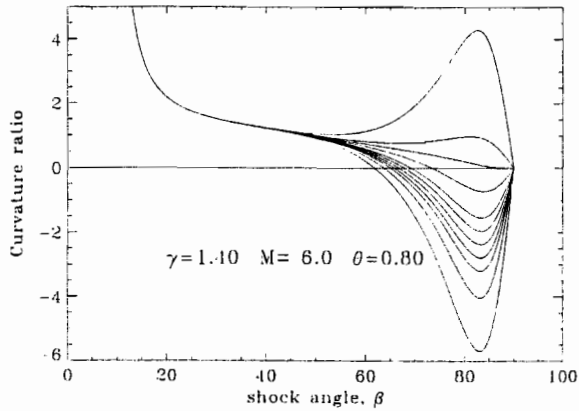


Fig. 4. Streamline to shock curvature ratio in reacting flow for $\gamma = 1.4$, $M = 6$ and $\theta = 0.8$. The values of the reaction rate parameter are $1/\epsilon = 160$ (lowest curve), 80, 40, 20, 0.1, -20, -40, -80, -119, -160, -320

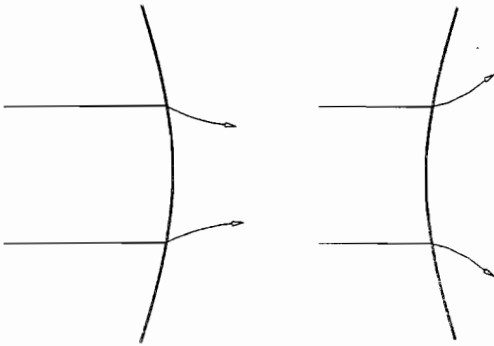


Fig. 5. Schematic sketch of a convex and concave near-normal shocks with associated streamlines, for a perfect gas. Both the concave and the convex shocks produce streamline curvatures that can exist stably in steady flow

4.3 Application to geometrically perturbed normal shock

The fact that the curvature ratio is positive near the normal-shock point, if the rate of an exothermic reaction is sufficiently fast, has interesting consequences. In order to understand this, consider first the case of a sinusoidally perturbed normal shock in a perfect gas. Figures 2 and 3 show that, for small negative perturbations of the shock angle from 90° , the streamline-to-shock curvature ratio is negative for a perfect gas. Similarly, for positive perturbations of β from 90° , the ratio will be positive. Consequently, a concave-upstream shock, which is associated with streamline convergence toward the symmetry plane of the shock, will cause the streamline curvature to be such that streamlines merge into the direction of the symmetry plane, see Fig. 5, left. A convex-upstream shock, for which the deflection is away from the symmetry plane, produces streamlines that bend away from the symmetry plane, see Fig. 5, right. This is very different in the case of a sufficiently fast exothermic reaction, of the type where no Crocco point exists, or where the streamline-to-shock curvature ratio is positive in the range $0 < \beta < 90^\circ$. In that case, the situation is as illustrated in Fig. 6. The convex-upstream shock with deflection away from the symmetry plane is also associated with a streamline curvature away from the symmetry plane, see Fig. 6, left. On the other hand, the concave-upstream shock, with deflections

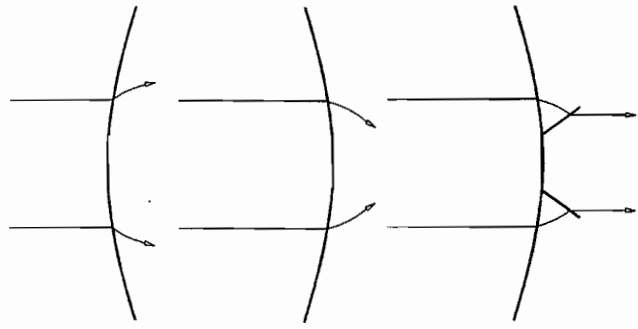


Fig. 6. Schematic sketch of a convex and concave near-normal shocks with associated streamlines, for a gas with fast exothermic reaction rate. The convex-upstream shock on the left can exist with stable steady flow. However, the concave-upstream shock shown in the center requires a pair of unsteady shocks to deflect the flow parallel to the symmetry plane (right)

toward the symmetry plane, also produces a streamline curvature toward the symmetry plane. On the symmetry plane, this causes a clash between the two convergent streamlines that will necessarily result in the production of two unsteady shock waves traveling outward from the symmetry plane, see Fig. 6, right.

Thus, it is evident that a concave-upstream shock can not give a steady solution if an exothermic reaction of sufficiently fast rate occurs at the shock. This is clearly related to the unsteady waves that occur in detonations and that form the cellular structure observed in such waves.

5 Shock and streamline in the $V\delta$ -plane

Many gasdynamical problems are simplified by mapping the flow into the hodograph or uv -plane. It is sometimes more convenient to choose other variables for this mapping, such as the $V\delta$ -plane, or the $p\delta$ -plane. The condition after a straight shock in non-reacting flow maps into the $V\delta$ shock locus shown in Fig. 7 as the continuous curve, starting at the infinitesimally weak shock point $(1,0)$, moving smoothly through the maximum-deflection point and back to $\delta = 0$ at the normal-shock point. This curve is the same for flows with finite reaction rate, of course, since it just represents the shock-jump conditions, which we have taken to be the same, by choosing the composition to be unchanged across the shock.

The additional information that is brought into this picture by knowing the gradients at the shock, is that it permits curved and reacting shocks to be treated in this way as well. It is therefore convenient to treat perfect-gas and reacting flows separately.

In particular, the derivative $d\delta/dV$ may be formed by using the general results for the gradients at the shock. Thus,

$$\frac{d\delta}{dV} = \frac{d\delta}{ds} \frac{ds}{dV} = \frac{d\delta}{ds} \frac{ds}{dt} \frac{dt}{dV} = \frac{d\delta}{ds} (-\rho V^2) \frac{dt}{dp} \quad (45)$$

Substituting from Eqs. (29) and (31), this gives

$$\frac{d\delta}{dV} = -\frac{u}{Vv} \frac{\sum_{i=2}^n h_{c_i} \frac{dc_i}{dt} + \frac{k}{v} \left(\rho h_p G - \frac{vV^2}{\rho u} \frac{p_z}{k} F \right)}{\sum_{i=2}^n h_{c_i} \frac{dc_i}{dt} + kG \frac{\rho h_p}{v}} \quad (46)$$

This derivative indicates the direction in which the streamline departs from the shock in the $V\delta$ -plane.



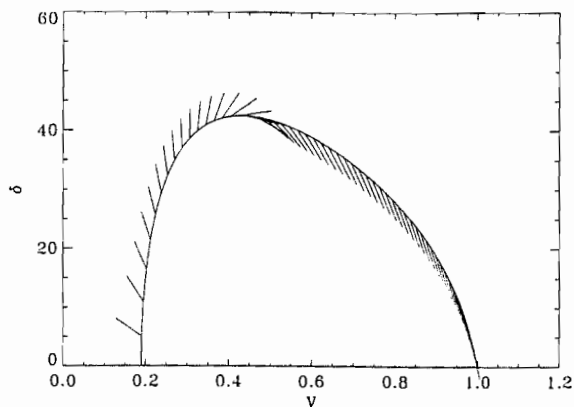


Fig. 7. $V\delta$ -plane map of a curved shock in non-reacting flow with $M = 6$ and $\gamma = 1.4$. The short straight lines indicate the direction in which the streamline leaves the shock in the case of a convex-upstream shock. Note how the direction is parallel to the shock locus at the weak-shock point, becomes horizontal at the Crocco point, then vertical at the zero- G point, and finally horizontal again at the normal-shock point

5.1 Perfect-gas flows

For the special case of non-reacting flow, the streamline slope in the $V\delta$ -plane becomes

$$\frac{d\delta}{dV} = \frac{-u}{Vv} \left[1 - \frac{vV^2}{\rho^2 h_\rho u} \frac{p_x}{k} \frac{F}{G} \right]. \quad (47)$$

In Fig. 7 this direction is indicated by a short straight line starting at the shock locus. Although the *slope* of the streamline in the $V\delta$ -plane is independent of the shock curvature, its *direction* is opposite to the one shown, for a shock wave curvature of opposite sign. The direction of the streamline shown in Fig. 7 is that for a convex-upstream shock.

The streamline direction in the $V\delta$ -plane undergoes several changes as we proceed from the weak-shock point to the normal-shock point. At the former, the streamline direction is parallel to the shock locus. No dramatic change occurs up to the vicinity of the Crocco point. In that vicinity, the slope changes rapidly from negative to zero at the Crocco point, and subsequently to infinite, where it changes sign to minus infinity, and then approaches zero from below at the normal-shock point. For non-reacting flow, the point at which the slope becomes infinite is easily identified as the zero- G point, see Eq. (47).

This kind of diagram was used extensively by Guderley in the hodograph plane. He called it the hedgehog or porcupine diagram. Figure 7 is a funny-looking porcupine, with some of the "spines" pointing inward. However, it becomes obvious why the term porcupine seemed appropriate to Guderley, when it is remembered that he was concerned particularly with flows in the vicinity of $M = 1$. Thus, Fig. 8 shows the same plot for the case $M = 1.5$ in which all the spines are seen to point outward.

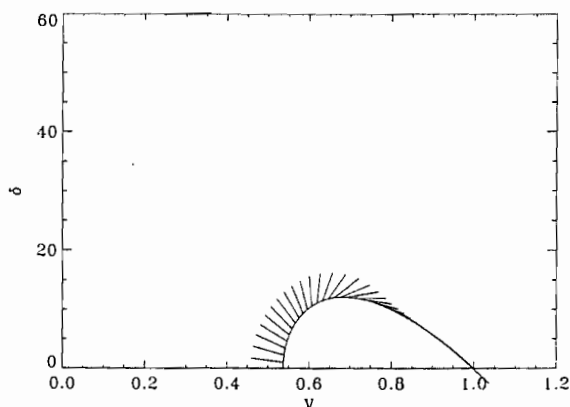


Fig. 8. For $M = 1.5$, $\gamma = 1.4$, the streamline direction at the convex-upstream shock is everywhere outward from the shock locus

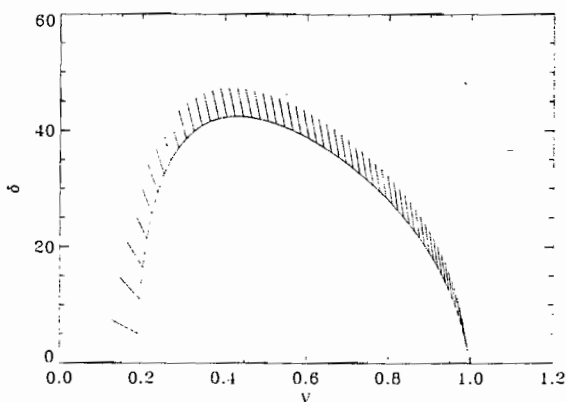


Fig. 9. Plane shock with endothermic chemical reaction. $M = 6$, $\gamma = 1.4$. Note the difference between the streamline slopes of this diagram and those of Fig. 7

5.2 Reacting flow

In the other extreme case of a straight shock with finite chemical reaction rate the streamline slope in the $V\delta$ -plane becomes particularly simple:

$$\frac{d\delta}{dV} = -\frac{u}{Vv}. \quad (48)$$

It is clear that this slope is negative throughout the range $0 < \beta < 90$, and the spines point outward for an endothermic reaction and inward for exothermic reaction. Figure 9 shows that case with $M = 6$ and $\gamma = 1.4$ for endothermic reaction.

The streamline slopes in Figs. 7 and 9 are very different, especially in the weak and medium shock strength regime. Both are extreme cases, of course, and the general case of finite reaction, Eq. (46), will give slopes anywhere between the two extremes depending on the relative importance of chemical reaction and shock curvature. It is also possible to obtain the asymptotic behaviors of Eq. (46), both in the fast and slow reaction limits. To do this, introduce the parameter

$$\omega = -\frac{v \sum_{i=2}^n h_{ci} \frac{dc_i}{dt}}{k\rho h_\rho} = \sin\beta \frac{\gamma - 1}{\gamma} \frac{\theta}{\varepsilon k} \exp(-\theta\rho/p), \quad (49)$$



where the last expression applies for the gas model of Eq. (43). This variable measures the relative importance of reaction rate and shock curvature. It is positive for endothermic reaction and convex-upstream shocks. With this definition of ω , Eq. (46) becomes

$$\frac{d\delta}{dV} = -\frac{u}{Vv} \frac{\omega - G + \frac{vV^2}{\rho^2 h_\rho u} \frac{p_x}{k} F}{\omega - G}. \quad (50)$$

Expanding this for $\omega \rightarrow 0$, the slope becomes

$$\left(\frac{d\delta}{dV}\right)_{\omega \rightarrow 0} = -\frac{u}{Vv} \left[1 - \left(\frac{vV^2}{\rho^2 h_\rho u} \frac{p_x}{k} F \right) \frac{1}{G} \left(1 + \frac{\omega}{G} \right) \right] + O(\omega^2). \quad (51)$$

In the other limit, we obtain

$$\left(\frac{d\delta}{dV}\right)_{\omega \rightarrow \infty} = -\frac{u}{Vv} \left[1 + \frac{1}{\omega} \left(\frac{vV^2}{\rho^2 h_\rho u} \frac{p_x}{k} F \right) \right] + O\left(\frac{1}{\omega^2}\right). \quad (52)$$

It is opportune here to stress again that the functions on the right of 50 to 52 may all be expressed in terms of the free-stream conditions, β and ω .

The manner in which $d\delta/dV$ changes with reaction rate is shown for $M = 6$, $\gamma = 1.4$ and $\theta = 0.8$ in Fig. 10, using the reaction rate model of Eqs. (43) and (44). Consider first the full lines in this graph: In the weak-shock limit, the slope has a finite negative value. For a given value of $k\varepsilon$, as β is increased from the weak-shock limit, the slope increases and becomes infinite at a particular value of β , then rises from negative infinity, toward zero at the normal-shock point. This rise occurs almost exactly along the straight-shock curve, which is the lower convergence line in the graph. Note that, for straight shocks, *i. e.*, infinite ω the slope is negative everywhere except at the normal-shock point, independently of whether ω is positive or negative. This is the reason why this line is a convergence line between the dashed and full curves. In the $V\delta$ -plane the difference between endothermic and exothermic reactions would be that the streamlines would leave the shock (at the same slope) in opposite directions. The upper convergence line is the value for a curved shock in non-reacting flow, the curve labeled $k\varepsilon = \pm 1$.

It is interesting to consider a particular shock angle, say 55° and fixed shock curvature, and changing ε from ∞ (non-reacting flow) to 0 (fast reaction rate). The slope starts on the upper convergence line ($k\varepsilon = \pm 1$), where $d\delta/dV$ is approximately -1.8 , then increases rapidly to ∞ at $\varepsilon \simeq 10^{-3}$, where it flips to $-\infty$ and then approaches the lower convergence line from below. For a convex-upstream shock, these changes represent a smooth anticlockwise rotation of the "spine" of the porcupine from the direction in Fig. 7 to that in Fig. 9.

6 Three-shock points

Across the streamline coming out of an intersection of three shock waves in inviscid, steady flow the velocity is discontinuous, but the deflection and pressure are continuous. This

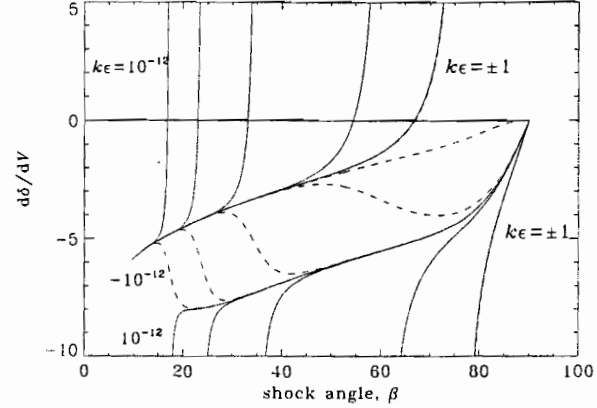


Fig. 10. Effect of reaction rate on $d\delta/dV$ as a function of shock angle, for $M = 6$, $\gamma = 1.4$ and $\theta = 0.8$. The values of the reaction rate parameter are $k\varepsilon = 1, 10^{-3}, 10^{-6}, 10^{-9}, 10^{-12}, -1, -0.0084, -10^{-3}, -10^{-6}, -10^{-9},$ and -10^{-12} . The dashed lines indicate the cases where the reaction is exothermic. The lower convergence line corresponds to the straight-shock solution shown in Fig. 9. The non-reacting curved-shock case is the upper convergence line at low shock angles, and - at larger shock angles - may be identified as the lines for $k\varepsilon = \pm 1$ that are practically congruent

makes representation of the flow in the δp -plane very attractive. With the knowledge of the gradients, it is relatively simple to extend arguments about triple points of straight shocks to include cases where the shocks are curved. To this end, the derivative $d\delta/dp$ at a curved shock may be evaluated quite straightforwardly as:

$$\frac{d\delta}{dp} = \frac{d\delta}{ds} \frac{ds}{dp} = \frac{d\delta}{ds} \frac{ds}{dt} \frac{dt}{dp} = \frac{d\delta}{ds} V \frac{dt}{dp}. \quad (53)$$

Substituting from Eqs. (29) and (31),

$$\frac{d\delta}{dp} = \frac{u}{\rho V^2 v} \frac{\sum_{i=2}^n h_{c_i} \frac{dc_i}{dt} + \frac{k}{v} \left(\rho h_\rho G - \frac{vV^2}{\rho u} \frac{p_x}{k} F \right)}{\sum_{i=2}^n h_{c_i} \frac{dc_i}{dt} + kG \frac{\rho h_\rho}{v}}, \quad (54)$$

which is just $(-1/\rho V)d\delta/dV$. This means that the qualitative behavior of $d\delta/dp$ is like $-d\delta/dV$.

An example of the occurrence of a triple point is the Mach reflection of a straight shock from a wall, as shown schematically in the upper part of Fig. 11. The lower part of Fig. 11 shows a map of non-reacting flow of this kind in the δp -plane. The regions labeled 1 through 5 in the physical space are labeled similarly at the corresponding points in the δp -space. Now suppose that, at the triple point, the Mach stem is curved, the incident shock is plane, and the reflected shock is curved. Since δ and p must be continuous across the slip line not only at the triple point, but also at ds from the triple point, $d\delta/dp$ has to be continuous across the slip line at the triple point.

The value of $d\delta/dp$, for non-reacting flow and a concave-upstream shock, gives the slopes and directions shown in Fig. 11 for the chosen parameters. It is clear from Fig. 11 that, with a straight incident shock, the slope in δp -space of the slip line issuing from the Mach stem is *not* the same as that issuing from the reflected shock at the point 3,4. Since the slopes are independent of the shock curvatures, there is no possibility for the curvatures to adjust to meet the constraint. The only possible conclusion to be drawn from

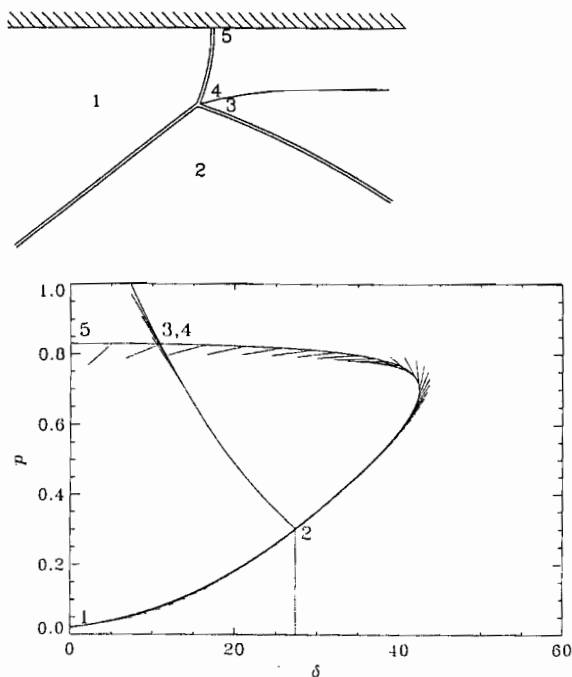


Fig. 11. Mach reflection. Top: Schematic sketch of the shock configuration, with labels identifying regions and points of the flow in physical space. Bottom: δp -map of this flow, showing the incident shock (1-2), the reflected shock (2-3) and the Mach stem (4-5), as determined from the shock-jump relations. $M = 6$, $\gamma = 1.4$, non-reacting steady flow. Also shown are the streamline directions from the reflected shock and the Mach stem. Note that the two streamline directions coming from 3 and 4 are not the same, leading to the conclusion that these two shocks must have zero curvature at the triple point

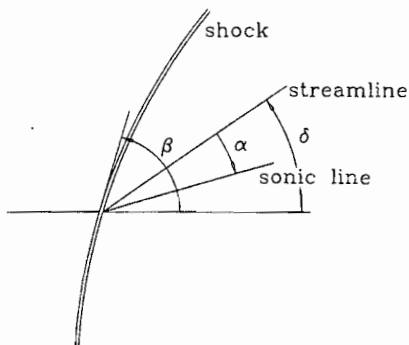


Fig. 12. Definition of angles

this result is that – in non-reacting flow – the curvatures of both the Mach stem and the reflected shock must be zero at the triple point (except in very special cases). This is not to say that these two shocks can not be curved at other locations, but rather that – at the triple point – both have a point of inflection. (In the more general case of a curved incident shock, Mölder (1972) shows that the curvature of the other shocks need not be zero.)

It is interesting that this result may be different for the case of reacting flow. This is because, with finite reaction rate, $d\delta/dp$ is no longer independent of the shock curvature. The reaction therefore provides an additional degree of freedom that may permit the shocks to assume the finite

curvatures that correspond to the local reaction rates and the streamline curvature constraint at the triple point.

7 Some other derivatives

The derivatives of the flow quantities at the shock obtained in Sect. 3 permit a number of other interesting quantities to be determined. In this section the vorticity at a shock is used as an example, and an illustration of how the results may be used generally is given.

7.1 Vorticity at the shock

In the curvilinear coordinates chosen, the vorticity at the shock is given by

$$\zeta = u_y - v_x + ku. \quad (55)$$

Substituting for u_y from Eqs. (19) and (24), this becomes

$$\zeta = -\frac{k}{v} \left(\frac{p_x}{\rho k} + u \frac{u_x}{k} - uv - v \frac{v_x}{k} + uv \right). \quad (56)$$

In this expression, the terms with explicit Mach-number and γ dependence in the p - and v -derivative terms cancel when using Eqs. (8-17), and only the β - and ρ -dependence remains. The result is

$$\zeta = -k\rho \cos\beta \left(1 - \frac{1}{\rho} \right)^2. \quad (57)$$

This is the well-known expression for the vorticity at a curved shock, see *e. g.*, Hayes and Probstein (1959). Clearly, the vorticity *at the shock* is independent of the reaction rate. Note that this is because the problem considered here is that where the composition is constant across the shock and contributions from the reaction occur only after the shock, rather than that of equilibrium shocks.

7.2 Gradients at the shock, sonic line direction

The results of Sect. 3 may be used to determine the magnitude and direction of the gradient of any flow quantity. For example, the pressure gradient direction and magnitude will be

$$\arctan(p_y/p_x), \quad \sqrt{p_y^2 + p_x^2}. \quad (58)$$

Since reactions strongly affect the direction of the density gradient, knowledge of this direction is very valuable, for example, in the interpretation of interferograms of reacting flow. Other gradients are of interest. For example, the slope of the sonic line, for which a closed-form solution exists in the case of plane flow of a perfect gas (see Hayes and Probstein, 1959), is also affected by the reaction rate.

In order to determine the sonic line slope, consider the energy equation for our isoenergetic flow and the model gas in the form

$$\frac{V^2}{2} + \frac{a^2}{\gamma - 1} + h_{\text{chem.}} = h_0, \quad (59)$$

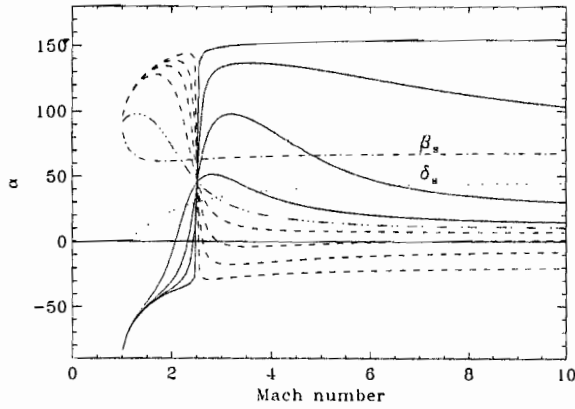


Fig. 13. Top: Dependence of sonic line angle on Mach number and reaction rate, plane flow, $\gamma = 1.4$, $\theta = 0.8$. The deflection and shock angles at the sonic condition are also shown as a dotted and a chain-dotted line. The chain-dotted line with three dots is for the non-reacting case, in agreement with the solution given by Hayes and Probstein. Continuous lines and dashed lines represent endothermic and exothermic reaction rate cases respectively, for $k\varepsilon = -0.0001, -0.001, -0.003, -0.01, 0.01, 0.003, 0.001, 0.0001$. Bottom: Schematic sketch of shapes of subsonic pocket behind a plane convex shock in near-sonic flow

where h_{chem} is chemically stored specific energy and a is the frozen speed of sound. $V = a$ along the sonic line, for which we can therefore write

$$\frac{\gamma + 1}{2(\gamma - 1)} V^2 + h_{\text{chem}} = h_0. \quad (60)$$

Differentiating this along the sonic line, and recalling that $c_{ix} = 0$,

$$V_x \cos \phi + V_y \sin \phi + \sin \phi \frac{\gamma - 1}{\gamma + 1} \frac{1}{V} \sum_{i=2}^n h_{c_i} c_{iy} = 0. \quad (61)$$

Here, ϕ is the angle between the sonic line and the shock. It is related to the angle α between the sonic line and the streamline through

$$\alpha = \phi - \beta + \delta,$$

see Fig. 12 for notation. Thus,

$$\tan \phi = \frac{-V_x}{V_y + \frac{\gamma - 1}{\gamma + 1} \frac{1}{V} \sum_{i=2}^n h_{c_i} c_{iy}}. \quad (62)$$

Figure 13 shows that, at high Mach number, endothermic reactions cause α to increase, and *vice versa*, but these trends are reversed at low Mach number. The reversal occurs at a particular Mach number, which, for the value of γ chosen,

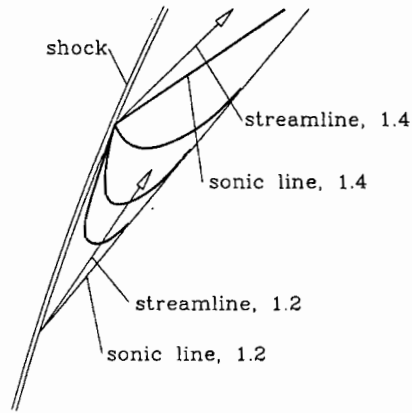


Fig. 14. Sketch of sonic lines for $M = 10$, $\gamma = 1.4$ with endothermic reaction. The equilibrium situation is modeled by a $\gamma = 1.2$ flow to provide the asymptotic sonic-line direction. The sonic lines for three reacting-flow cases and the frozen case are shown as heavy lines

is approximately 2.5. This is the point where the reaction rate term in V_y just cancels the one that occurs explicitly in the denominator of (62). This condition occurs at

$$\frac{p}{\rho v^2} = \frac{\gamma^2 - \gamma + 2}{\gamma^2 - 1}.$$

Using (8), (10) and (13) to express p , v and ρ in terms of M , γ and β then leads — for the particular value of $\beta = \beta_s(\gamma, M)$ at the sonic point — to a particular value of $M(\gamma)$ at which the reaction rate does not influence the sonic line slope.

For very fast reactions, ϕ switches from -90° to $+90^\circ$ at this critical Mach number, so that, at large Mach number, the limiting sonic line direction for very fast reaction is along the shock. In endothermic flow it is at $\phi = +90^\circ$ and in exothermic flow at -90° .

The response of the sonic line to reaction rate at high Mach number has been observed by Hornung and Smith (1979), who used it to make an argument about the influence of non-equilibrium dissociation on the shock detachment process in flow over a wedge. This behavior was also observed in recent numerical computations of these wedge flows by Candler (unpublished work). In endothermic flow near the shock, at high Mach number, streamlines cross the sonic line from a subsonic region, while, for sufficiently fast exothermic reactions, the opposite holds (negative α).

In the low Mach number range, the sonic line direction is very sensitive to slight heat removal by endothermic reaction. Near $M = 1$, a change from non-reacting to slow endothermic reaction switches α from $+90^\circ$ to -90° , while exothermic reactions have a weaker effect. This will cause the subsonic pocket behind a convex shock to change as shown in the sketch of Fig. 13. (bottom).

The effect of chemical reaction on the sonic line may be illustrated by considering frozen and equilibrium flow limits. In the endothermic case, the equilibrium limit is displaced, relative to the non-reacting limit, toward the direction of smaller γ . For smaller γ the sonic point is displaced to larger β . This is shown with the correct values of β_s in Fig. 14 for the example of a circular-arc shock at $M = 10$ with $\gamma = 1.4$ and 1.2. Also plotted are the correct streamline



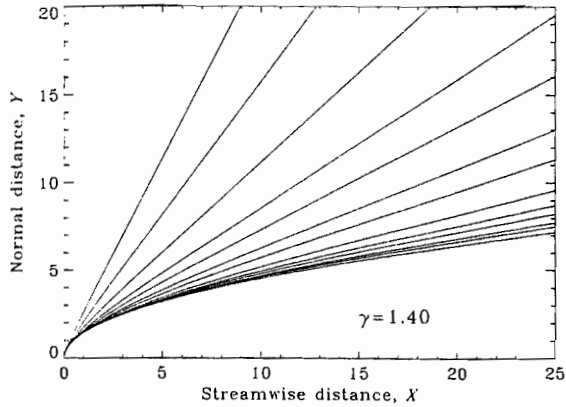


Fig. 15. Hyperbolic shock shapes, with finite curvature at the normal-shock point and asymptoting to a Mach wave at large X . Mach numbers are: 1.1, 1.2, 1.4, 1.7, 2, 2.5, 3, 4, 5, 6, 8, 10, 20

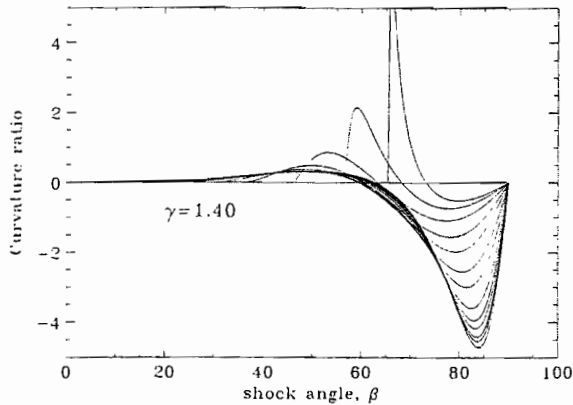


Fig. 16. Streamline-to-shock curvature ratio for axisymmetric shocks as shown in Fig. 15. Perfect gas, $\gamma = 1.4$, Mach numbers as in Fig. 15. The ratio is the streamline curvature divided by the shock curvature k in the xy -plane

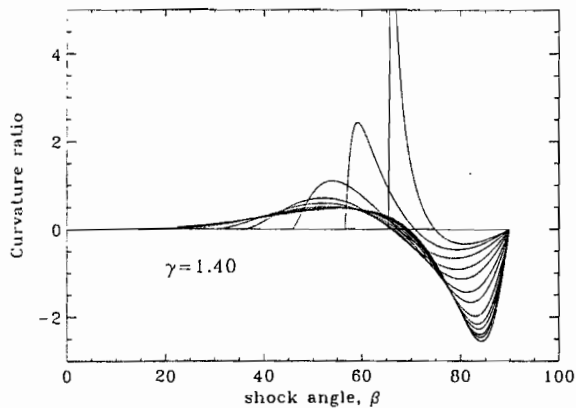


Fig. 17. Streamline-to-shock curvature ratio for plane shocks of the shape shown in Fig. 15. Perfect gas, $\gamma = 1.4$, Mach numbers as in Fig. 15

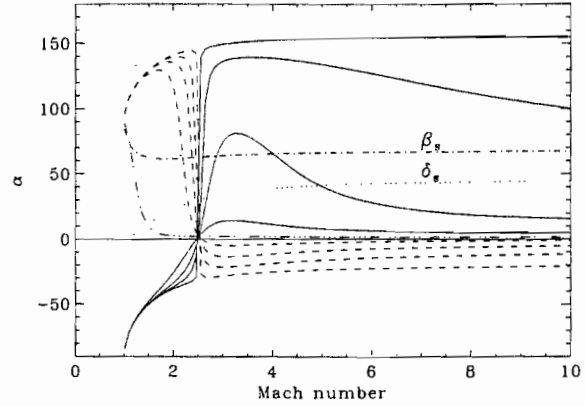


Fig. 18. Sonic line angle in axisymmetric flow. Shock shape as in Fig. 15, notation as in Fig. 13. $\gamma = 1.4$, $\theta = 0.8$, $k\epsilon = -0.0001, -0.001, -0.003, -0.01, 0.01, 0.003, 0.001, 0.0001$

and sonic line directions for the two cases. In flow with endothermic reaction, the sonic lines depart from the $\gamma = 1.4$ sonic point at angles α that increase with reaction rate. If the reaction is completed to equilibrium over a distance that is small compared with the shock radius of curvature, all the directions at equilibrium should be something like that for $\gamma = 1.2$ in this crude model. Thus, the sonic line for finite reaction rate leaves the $\gamma = 1.4$ sonic point at a finite angle relative to that of non-reacting flow and asymptotically blends into the $\gamma = 1.2$ sonic line. In the sketch, sonic lines for three finite rates are shown to illustrate how the transition from frozen flow to larger and larger rates proceeds.

The situation is reversed for exothermic flow. It is easily seen from Fig. 14 that the streamline always crosses the sonic line from the subsonic to the supersonic side with endothermic flow at these conditions, while both directions are possible with exothermic flow, as has been pointed out earlier.

8 Three-dimensional flows

Finally, consider the extension of these results to the more general case of three-dimensional flow. To this end, choose the xy -plane to be the plane of the free-stream direction and the local normal to the shock wave at the point of interest. With this choice, the velocity component in the third (z) direction and its gradients in the xy -plane are zero. Thus a suitable name for this plane is the "flow plane". By choosing x and y to lie in the flow plane, the derivatives of p , ρ and u with respect to z (the dimensionless coordinate normal to the flow plane) are zero, and the only non-zero gradient normal to the flow plane is

$$w_z = l,$$

where w is the dimensionless z -component of velocity and l is the shock curvature in the yz -plane. $k+l$ is the Gaussian curvature of the shock at the point considered.

If we write Eqs. (3 to 6) for $y = 0$, the only changes to these equations are that the term $-k\rho v$ in the continuity equation becomes $-(k+l)\rho v$, and a new term $-\rho l$ is added. The equation (at $y = 0$) becomes



$$(\rho u)_x - (k + l)\rho v + \rho l + (\rho v)_y = 0. \quad (63)$$

This causes additional terms proportional to l to appear in Eqs. (18), (20) and (21), for the y -derivatives of p , v , and ρ as follows:

$$p_y F = \dots + l\rho h_p(1/v - 1), \quad (64)$$

$$vv_y F = \dots + l\rho h_p(1/v - 1), \quad (65)$$

$$\rho_y F = \dots + l(1 - 1/\rho + \rho/v). \quad (66)$$

Equation 19 for u_y remains unchanged.

A relatively simple example is that of axisymmetric flow. In this case, the flow plane is the meridional plane. Consider an axisymmetric shock wave of hyperbolic shape in the flow plane, such that the normal-shock point has finite curvature equal in both directions, and the shock is asymptotically conical with half-angle equal to the Mach angle far from this point. Defining the distance along the axis of symmetry, normalized by the radius of the shock at the nose, to be X , and the normal to it (similarly normalized) as Y , the shock shapes for a set of Mach number values are as shown in Fig. 15. The equation of the shock shape is

$$Y = \tan \mu \sqrt{X \left(X + \frac{2}{\tan^2 \mu} \right)} \quad (67)$$

where μ is the Mach angle $\arcsin(1/M)$. This gives a shock angle β that can be determined from

$$\tan \beta = \frac{\tan \mu}{\sqrt{X}} \frac{1 + 1/(X \tan^2 \mu)}{\sqrt{1 + 2/(X \tan^2 \mu)}}. \quad (68)$$

Solving this for X ,

$$X \tan^2 \mu = \sqrt{\frac{\tan^2 \beta}{\tan^2 \beta - \tan^2 \mu}} - 1. \quad (69)$$

With this, the shock curvature in the meridional plane becomes

$$k = (1 + 2X \cos^2 \mu + X^2 \sin^2 \mu)^{-3/2}. \quad (70)$$

This gives an explicit relation between k and β with Mach number as a parameter. For an axisymmetric shock, the transverse curvature in the yz -plane is $l = \cos \beta / Y$. The shape of the shock now permits the streamline to shock

curvature ratio to be determined for the axisymmetric and the plane case as functions of the shock angle β . The results are shown in Figures 16 and 17. These exhibit no qualitative differences. Quantitative changes include slight changes in the Crocco points and a greater negative value of the curvature ratio for axisymmetric flow.

It is interesting to find the effect of the third dimension on the sonic line slope at the shock. This is not new in non-reacting flow (see Hayes and Probstein), but our results permit it to be obtained directly for reacting flow also. Figure 18 shows how α behaves in an axisymmetric flow with the same shock shapes as in Fig. 15. The effect of reactions is very similar to that for plane flow.

Acknowledgements. Some of the work presented here has been part of various courses I have taught over the last 20 years at the Australian National University, at the University of Göttingen, and at Caltech. Many of my students have contributed in the form of discussions that have helped correct some mistakes. At Caltech, Professor J. E. Shepherd, in numerous discussions, contributed many ideas and important corrections, and he encouraged me to put this material together in a publication. My sincere thanks to them all.

References

- Becker E (1972) Chemically reacting flows. *Ann. Rev. Fluid Mech.* 6:155
 Clarke JF (1969) in Wegener PP: *Non-equilibrium flows*, Part II. Marcel Dekker
 Hayes WD, Probstein RF (1959) *Hypersonic Flow Theory*. Academic press
 Hornung HG (1976) Non-equilibrium ideal-gas dissociation after a curved shock wave. *J. Fluid Mech.* 74:143
 Hornung HG, Smith GH (1979) The influence of relaxation on shock detachment. *J. Fluid Mech.* 3:225
 Kewley DJ, Hornung HG (1974) Non-equilibrium nitrogen flow over a wedge 64:725
 Lighthill MJ (1949) The flow behind a stationary shock. *Phil. Mag.* 40:214
 Mölder S (1971) Reflection of curved shock waves in steady supersonic flow. *CASI Trans.* 40:73-80
 Mölder S (1972) Polar streamline directions at the triple point of Mach interaction of shock waves. *CASI Trans.* 5:88-89
 Munk MM, Prim RC (1948) Surface-pressure gradient and shock-front curvature at the edge of a plane ogive with attached shock front. *J. aeron. Sci.* 15:691
 Oswatitsch K (1952) *Gasdynamik*. Springer



Curved shock waves and chemical reactions

H. G. Hornung

Graduate Aeronautical Laboratories, California Institute of Technology, Pasadena, CA 91125, USA

Abstract: The features of steady flows with chemical reactions initiated by curved shocks are described by using examples of results in which endothermic or exothermic reactions take place. The dramatic effects of shock curvature are highlighted. Attention is then focused on the immediate vicinity of the shock in order to show that gradients at a curved shock always contain two terms: one proportional to reaction rate and one proportional to shock curvature. Numerous results are derived for endo- and exothermic flows with convex and concave shocks.

Key words: Dissociation quenching, streamline curvature, sonic line, Mach reflection, detonation

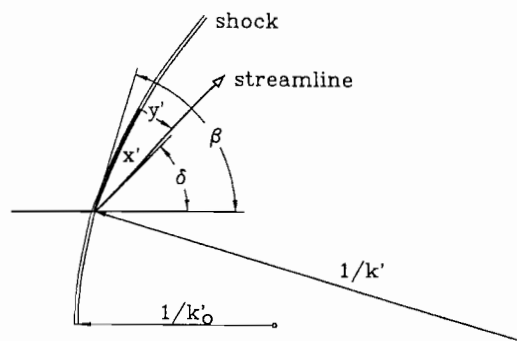


Figure 1. Notation. Upstream of the curved shock wave, conditions are assumed to be uniform. The origin of coordinates is the point where the streamline of interest crosses the shock.

1. Introduction

The phenomena that occur in steady flows with shock-initiated chemical reactions are particularly interesting if the shock is curved. They may be characterized by two dimensionless parameters. One is a measure of the ratio Ω of the radius of curvature of the shock to the characteristic reaction length, and the second is a measure of the ratio Φ of the energy going into the reaction to the kinetic energy of the free stream. The richness of the flow features that may occur is increased significantly by the fact that Ω and Φ can be positive or negative. (They change sign together). A sign change corresponds to a change from an endothermic to an exothermic chemical reaction, *i. e.*, from energy absorption into (as in the case of dissociation) to energy release from the chemical energy store (as in the case of shock-initiated combustion).

In a first, descriptive part of this paper, experimental and theoretical results are used to illustrate phenomena with endothermic reactions where the flow features depend on both of these parameters, as well as cases where only the first one plays a role. Experimental results are then used to illustrate phenomena that occur with exothermic reactions.

In the second part, attention is focused on the point at the downstream side of a curved shock, where the rate of exchange of thermal and chemical energy competes with the curvature-induced temperature change. Restriction to this region permits the gradients of flow quantities to be determined

explicitly, from which many flow features may be derived. This restriction limits the quantitative results to those dependent on Ω alone, but qualitative features that depend on both parameters may be deduced by extrapolation.

Throughout the paper the discussion is restricted to steady flows with uniform free stream.

2. Definition of variables

Consider a curved shock wave in a uniform free stream characterized by velocity V'_∞ , density ρ'_∞ . The origin of the shock-aligned curvilinear coordinates x', y' is chosen at the point where the streamline of interest crosses the shock wave. Let the shock curvature at this point be k' and the shock and deflection angles be β and δ as shown in Fig. 1. Introduce dimensionless variables defined by

$$\begin{aligned} h &= h'/V'_\infty{}^2, & p &= p'/\rho'_\infty V'^2_\infty, & v &= v'/V'_\infty, \\ \rho &= \rho'/\rho'_\infty, & y &= y'k'_0, & k &= k'/k'_0, \end{aligned}$$

where h, p, ρ, v are dimensionless specific enthalpy, pressure, density and y -velocity, and k'_0 is a convenient reference value of the shock curvature. The x -component of velocity u is made dimensionless in the same way as v . The caloric equation of state for a reacting gas mixture is

$$h = h(p, \rho, c_i), \quad (1)$$

where the c_i are the mass fractions of the n reacting



species. Since the sum of the mass fractions has to equal unity, one of the c_i may be expressed as a function of the others, and the differential form of the caloric equation of state becomes

$$dh = h_p d\rho + h_p dp + \sum_{i=2}^n h_{c_i} \frac{dc_i}{dt} dt. \quad (2)$$

Here, the subscripts denote partial differentiation, and the reaction rates and dimensionless time (measured from when the fluid element has crossed the shock) have been introduced in the last term. It is convenient to rewrite this as

$$dh = h_p d\rho + h_p dp + h_{it} dt, \quad (3)$$

thus defining h_{it} . The last term measures the enthalpy change caused by the reaction.

3. Endothermic flows

3.1. Straight, oblique shock

At a straight oblique shock the temperature jumps to a high value, so that (in cases of interest here) the gas begins to dissociate, and the third term in equation 3 is negative. This causes the temperature to decrease at a finite rate determined by the dissociation rate at the local conditions, until eventually the new post-shock equilibrium condition is reached. This process is plotted against t as a dotted line in Fig 4, which also shows as a second dotted line the density change. In this case the density increases monotonically, so that the shock-normal component of velocity will decrease monotonically with time, and a streamline will have a concave-up curvature. Such a streamline is sketched into the finite-fringe interferogram of Fig. 2 showing dissociating carbon-dioxide flow over a wedge, with a nearly straight shock. The fringes in such an interferogram approximately correspond to density profiles across the flow, so that the density change following a streamline such as the one superimposed on the photograph in white can be seen to be monotonically increasing.

3.2. Curved shock, dissociation quenching

In non-reacting flow, a temperature change along a streamline after a shock may be brought about by shock curvature. For example, a temperature decrease occurs along a streamline after a convex-upstream oblique shock. The initial temperature gradient along a streamline is then proportional to the shock curvature. If both effects (shock curvature and chemical reaction) are present, we may therefore expect interesting phenomena to result

from competition between them. Such competition is at the heart of many important steady flows. Further complications occur if the flow is unsteady, as may be seen from the contribution by Eckett et al. (1997). Only steady flows will be discussed here.

To illustrate one such phenomenon and to define the scope of this presentation, consider high-speed dissociating flow of nitrogen over a circular cylinder as in the interferogram by Sanderson (1995) shown in Fig. 3. In this interferogram the fringes approximate lines of constant density which show a maximum density at the stagnation point. The fringe pattern is typical of a non-equilibrium flow with a significant density rise between the shock and the body on the stagnation streamline.

A streamline is sketched in this interferogram as a thick white line with an arrowhead. As in the straight-shock case, the density increases along the streamline at first, but reaches a maximum value approximately at the point where the streamline is tangent to the fringes, and then decreases again. If many such streamlines were plotted in this flow, their points of tangency with the fringes would trace out a line approximately like the thin white line sketched in the interferogram, starting from the stagnation point and intersecting the shock near the top of the picture. Comparing the two flows of Fig. 2 and Fig. 3 thus shows that shock curva-



Figure 2. Finite-fringe interferogram of CO_2 flow over a wedge, $V'_\infty = 4.1 \text{ km/s}$, $\rho'_\infty = 0.005 \text{ kg/m}^3$. Since fringe shift is approximately proportional to density change, it may be seen that the density increases monotonically to equilibrium along streamlines such as the one sketched in white. Taken by Ebrahim (1975), T3 run 678.



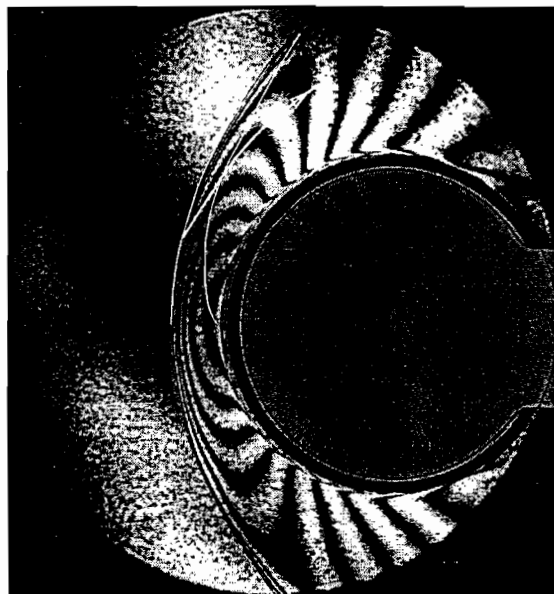


Figure 3. Infinite-fringe interferogram taken by Sanderson (1995) of dissociating nitrogen flow over a circular cylinder of 1.6 in. diameter, aspect ratio 4.5, T5 run 824. Free stream conditions: Velocity, 5.4 km/s, density, 0.016 kg/m³. The heavy white line sketches a streamline. A density maximum is reached along this streamline approximately where it is tangent to the fringes. The locus of such streamline-fringe tangent points is sketched as a light white line. The shock is also emphasized by a sketched thin white line.

ture causes the initial increase of density associated with the dissociation to be reversed further downstream. This behavior is typical of the regime where the characteristic dissociation distance is small compared with the local shock curvature radius.

The strong influence of curvature in dissociating flow may best be illustrated by a plot of the flow properties along a streamline such as the one highlighted in Fig. 3. Such a plot is shown, for conditions corresponding closely to the chosen streamline in Fig. 4, calculated from the asymptotic theory of Hornung (1976). This plot shows density ratio, temperature and dimensionless pressure plotted against dimensionless time along the streamline. Dotted lines show straight-shock results and full lines correspond to the curved shock. Note the close correspondence of the two sets of curves in the immediate vicinity of the shock.

The tiny additional drop in temperature caused by the shock curvature a little further downstream makes a dramatic difference to the flow. In fact, it causes the dissociation to stop altogether very shortly after the maximum-density point. This is because of the strong temperature dependence of the dissociation rate. Stalker, in 1972, was the

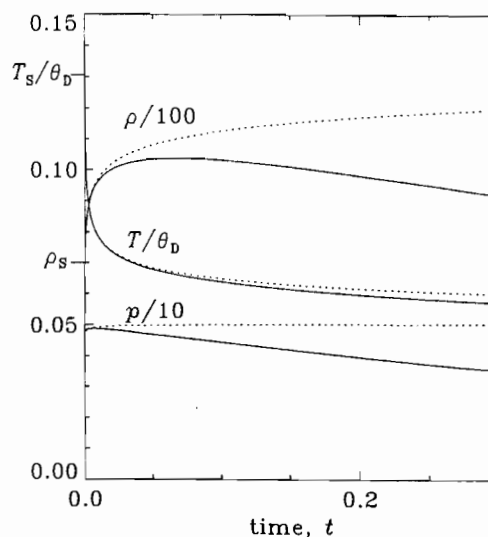


Figure 4. Temperature, density and pressure distributions along a streamline such as the one sketched in Fig. 3 (full line) as calculated from the asymptotic theory of Hornung (1976). The dotted lines show the corresponding straight-shock solutions. The values at the shock are marked with labels with subscript *s*.

first to recognize this, and he called it “dissociation quenching”. It is appropriate to choose a different name than “freezing”, because the latter term is generally used for the termination of recombination, whereas here, the reaction is terminated while proceeding in the dissociating direction.

In many flows of this nature the recombination rate is very much smaller than the dissociation rate, so that a good approximation is to consider the composition to be constant after quenching, albeit different on different streamlines. (The effect of recombination was considered by Wen (1994)). Thus, the flow downstream of the thin white line in Fig. 4 (quenching line) is practically non-reacting and the reaction is restricted to the region upstream of it.

For fast reactions, such as in the case shown in Fig. 3, the quenching line lies close to the shock, so that it is tempting to define effective shock jump conditions, appropriate for the flow downstream of the quenching line, that depend not only on free-stream conditions and shock angle, but in addition on dissociation rate and shock curvature. Such jump conditions have been derived by Hornung (1976). As had been suggested by Stalker, these new conditions give shock temperatures that are approximately independent of shock angle β and shock densities that are approximately proportional to $\sin^2\beta$, exactly opposite to perfect-gas behavior.



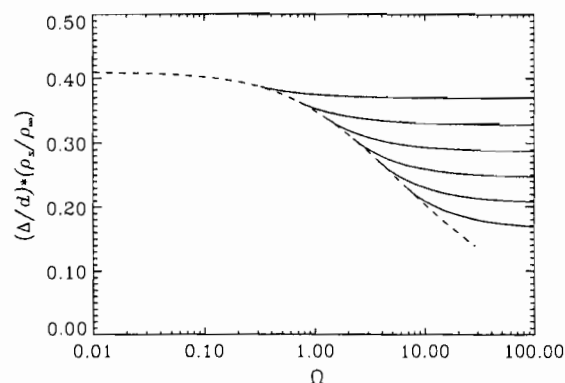


Figure 5. Plot of dimensionless shock stand-off distance on a sphere against reaction-rate parameter according to Wen and Hornung's integral theory for values of $\rho_s/\rho_e = 0.4, 0.5, 0.6, 0.7, 0.8, 0.9$. The uppermost full line corresponds to the value 0.9. The subscripts denote shock and equilibrium values. ρ_e increases monotonically with Φ .

Dissociation quenching is an example of a flow that does not reach equilibrium, and in which the chemical activity is confined to a half-moon shaped region where the shock angle is large. The amount of energy that goes into dissociation to equilibrium therefore does not enter the problem and the influence of chemistry is subject to the parameter Ω alone. It is necessary to treat this statement with care, however, because the asymptotic theory that leads to the quenching concept breaks down in the immediate vicinity of the stagnation point.

3.3. Stagnation region

In the stagnation region the recombination rate and the energy to equilibrium may not be ignored when the reaction rate is sufficiently large. This is brought out by the simple integral method used by Wen and Hornung (1995) for the shock stand-off distance Δ on a sphere of diameter d , shown in Fig. 5. This figure shows that the higher the value of Φ , the larger is the range in which the dimensionless stand-off distance depends only on Ω (dashed curve). This integral theory agrees well with experiments as is shown by Fig. 6.

4. Exothermic flows

Exothermic flows exhibit much more dramatic phenomena. This is because endothermic nonequilibrium flows generally start from an equilibrium state that is perturbed by the shock, and a final equilibrium state is approached smoothly in an energy-absorbing process. Exothermic flows start from a state of constrained equilibrium containing stored chemical energy that is suddenly made available by

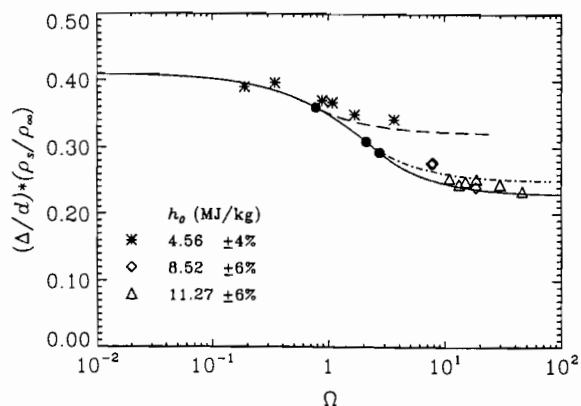


Figure 6. Measured dimensionless stand-off distance in carbon dioxide flows over a sphere at three specific reservoir enthalpies, for which the theoretical curves are plotted as the dashed, dash-dot and full line. The black circles mark the points where each curve departs from the dashed line of Fig. 5.

the shock wave. The structure of the flow field can be significantly affected, depending on how rapidly the chemistry can give this energy to the flow.

To observe this, consider the shadowgraphs shown in Fig's. 7 and 8 taken by Kaneshige, see Bélanger et al. (1995) and Kaneshige and Shepherd (1996). Fig. 7 shows a shadowgraph in which a spherical projectile travels through a combustible mixture of hydrogen, oxygen and nitrogen at 2730 m/s. The pressure of the mixture is approximately half an atmosphere, which is high enough to make the bow shock on the projectile ignite the mixture in the region where the shock angle β is sufficiently large. Downstream of a cut-off value of β , however, no reaction occurs. Most of the combustion occurs in a region close to the shock, just as in the case of dissociation quenching, see Fig. 3. The region filled with combustion products is thus bordered by a turbulent reacting interface that corresponds approximately to a streamsurface, outside of which the flow is smooth and completely non-reacting. The shadowgraph makes the region inside this interface appear turbulent too, but remember that this is an axisymmetric flow visualized by a line-of-sight integrating method.

Just how small an extra kick the gas needs to make it burn outside the interface is shown by the fact that the bow shock on a small piece of diaphragm (see arrow in photo) suffices to start the reaction again. In this flow, the estimated reaction distance (equivalent Chapman-Jouguet detonation cell size) is 11 mm, approximately the same as the the projectile radius of 12.7 mm. The ratio of radius to cell size is a measure of $-\Omega$.

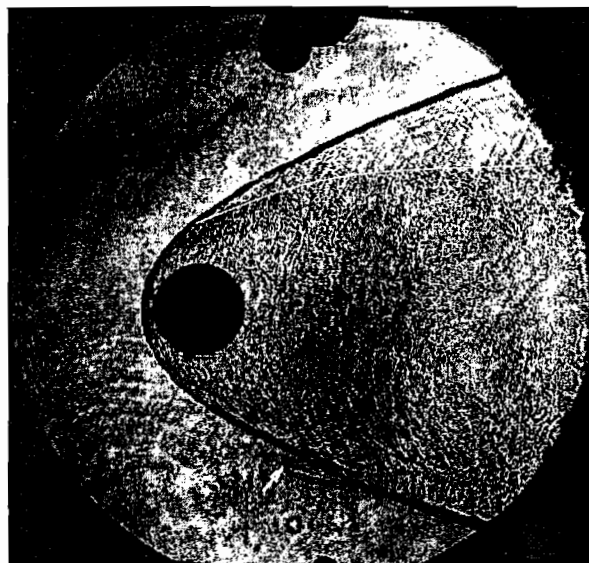


Figure 7. Shadowgraph of a spherical projectile of 25.4 mm diameter traveling at a speed of 2730 m/s through a mixture of $(2\text{H}_2 + \text{O}_2 + 3.76\text{N}_2)$ at a pressure of 42.1 kPa. The Chapman-Jouguet speed at this condition is 1950 m/s. Up to the point where the sketched light white line intersects the shock wave, the shock is steep enough to ignite the gas mixture, as indicated by the turbulent nature of the region of combustion products. The white line is sketched in to indicate the edge of this region. Note the weak shock on the piece of diaphragm (arrow) just upstream of the shock on the lower side (see text). T5 run 1015.

If the pressure of the mixture is increased to 2.5 atmospheres, the reaction rate is increased so much that the heat release is sufficiently rapid to support an oblique, overdriven detonation wave, see Fig. 8. In this flow the axisymmetric detonation wave is reflected in a weak Mach reflection off the walls of the square test section.

5. Gradients at a curved shock

It would be desirable, of course, to obtain theoretical descriptions of general curved-shock flows with chemical reactions. Unfortunately, it has only been possible to solve special cases such as that of dissociation quenching. However, it is possible to find general expressions for the gradients of flow quantities at a curved shock. A remarkable number of interesting results may be derived from such information.

5.1. Outline of derivation

In this section, the results derived in Horning (1997) will be used without giving a detailed derivation, but rather describing it only in broad terms. The inviscid equations of motion may be

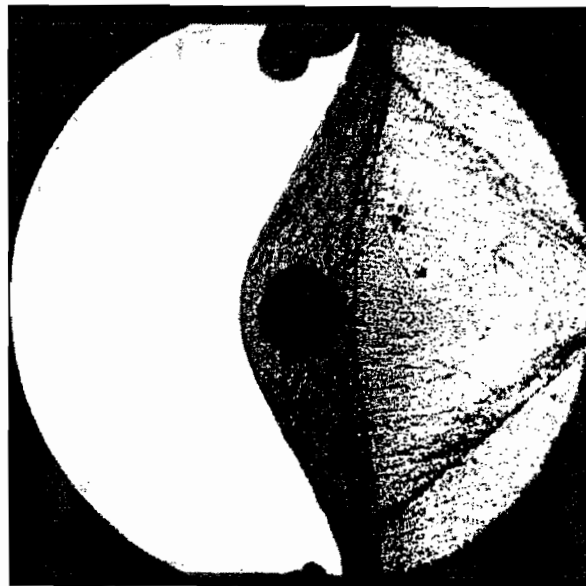


Figure 8. Shadowgraph of same projectile traveling at a speed of 2560 m/s through same mixture at a pressure of 256 kPa. At these conditions the CJ-speed is 1990 m/s. The pressure is now sufficiently high to make the reaction length so small as to cause the combustion to couple into the shock and produce an overdriven oblique detonation wave at 60° , CJ-angle= 51° . T5 run 1020.

written in the curvilinear coordinates of Fig. 1 as

$$\begin{aligned} uu_x + (1 - ky)vu_y - kuv + p_x/\rho &= 0, \\ uv_x + (1 - ky)vv_y + ku^2 + (1 - ky)p_y/\rho &= 0, \\ h_p p_y + h_\rho \rho_y + \sum_{i=2}^n h_{c_i} c_{i_y} + vv_y + uu_y &= 0, \\ (\rho u)_x - k\rho v + (1 - ky)(\rho v)_y &= 0. \end{aligned}$$

At the shock, $y = 0$, and the resulting equations may be solved for the shock-normal derivatives p_y , u_y , v_y , ρ_y in terms of the other variables. The shock-parallel derivatives may be obtained by differentiating the shock-jump conditions, which introduces the shock curvature $\beta_x = -k$. For this purpose, perfect-gas behavior is assumed up to the point where the chemical reaction begins, i. e., the downstream point on the shock. The resulting x - and y -derivatives may then be combined to form the substantial time derivative

$$\frac{d}{dt} = u \frac{\partial}{\partial x} + v \frac{\partial}{\partial y}. \quad (4)$$

Noting that the deflection angle is

$$\delta = \beta - \arctan(v/u), \quad (5)$$

forming the derivatives of this function with respect to x and y , and writing

$$V = ds/dt = \sqrt{v^2 + u^2}, \quad (6)$$



where s is distance along the streamline measured from the origin, the streamline curvature at the shock, $d\delta/ds$ is obtained in the form

$$\frac{d\delta}{ds} = h_{it}f_1 + kf_2, \quad (7)$$

where the functions f_1 and f_2 are known functions of β , the free-stream Mach number M and the ratio of specific heats γ . Similarly, other substantial derivatives are obtained:

$$\frac{dp}{dt} = h_{it}f_3 + kf_4, \quad (8)$$

$$\frac{d\rho}{dt} = h_{it}f_5 + kf_6, \quad (9)$$

$$V \frac{dV}{dt} = -\frac{1}{\rho} \frac{dp}{dt}. \quad (10)$$

Again the functions f_3 to f_6 are known in terms of β , M , and γ .

All of these derivatives thus have two contributions: one from shock curvature and one from reaction rate, and the ratio of these contributions is proportional to the reaction rate parameter $\Omega = h_{it}/k$. In order to compute numerical values it is necessary to introduce a model for the reaction rate. This is assumed to be of the form

$$h_{it} = \frac{\theta}{\varepsilon} \exp(-\theta\rho/p). \quad (11)$$

5.2. Streamline curvature

Calculating the streamline-to-shock curvature ratio by dividing equation 7 by k results in the plots shown in Fig. 9 for given values of γ , M , and θ , and with ε as a parameter. The dashed curve is the non-reacting case. As β decreases, it shows the typical transition from zero at the normal-shock point to negative at large shock angles, a zero crossing at the Crocco point, and a positive range with singularity at the Mach angle, where the shock curvature must be zero. With endothermic reaction (lowest four curves), nothing changes qualitatively, except that the shock angle at the Crocco point decreases with increasing reaction rate. Similarly, negative reaction rates (negative $1/\varepsilon$) that correspond to exothermic reaction continue this trend in the opposite direction. The interesting thing is, however, that when the reaction rate exceeds a particular threshold, the region of negative curvature ratio ceases to exist. This has interesting consequences for a nearly-normal curved shock as sketched in Fig. 10.

Since shock and streamline curvature now have the same sign in the near-normal shock region, a

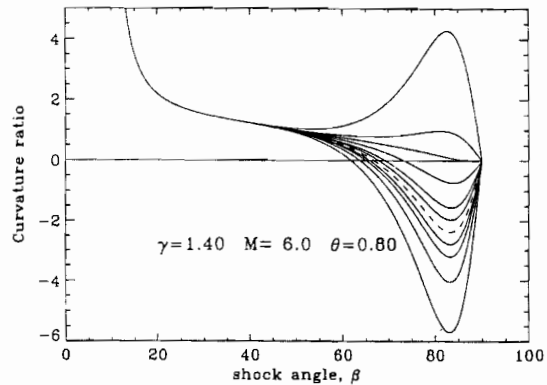


Figure 9. Streamline to shock curvature ratio in reacting flow for $\gamma = 1.4$, $M = 6$ and $\theta = 0.8$. The values of the reaction rate parameter are $1/\varepsilon = 160$ (lowest curve), 80, 40, 20, 0 (dashed curve), -20, -40, -80, -119, -160, -320.

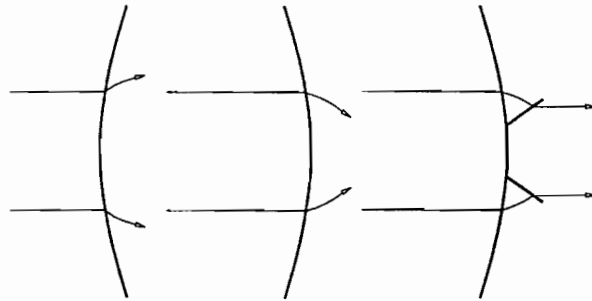


Figure 10. Schematic sketch of convex and concave near-normal shocks with associated streamlines, for a gas with fast exothermic reaction rate. The convex-upstream shock on the left can exist with stable steady flow. However, the concave-upstream shock shown in the center requires a pair of unsteady shocks to deflect the flow parallel to the symmetry plane (right).

convex shock produces streamlines as shown in the leftmost sketch of Fig. 10. If the shock is concave, the streamlines curve inward, so they will clash on the symmetry plane and require two unsteady shocks to deflect the flow into the symmetry-plane direction. It is this instability that leads to the weak transverse waves behind a shock, which generate the characteristic cellular structure in detonations.

5.3. Triple-shock points

The results may be combined to form the derivative

$$\frac{d\delta}{dp} = f_7 \frac{h_{it} + kf_8}{h_{it} + kf_9}, \quad (12)$$

or

$$\frac{d\delta}{dp} = f_7 \frac{\Omega + f_8}{\Omega + f_9}, \quad (13)$$

where the f are again known functions of β , M , and γ . This is a very useful result for arguments relating to triple shock points, where the δp -plane



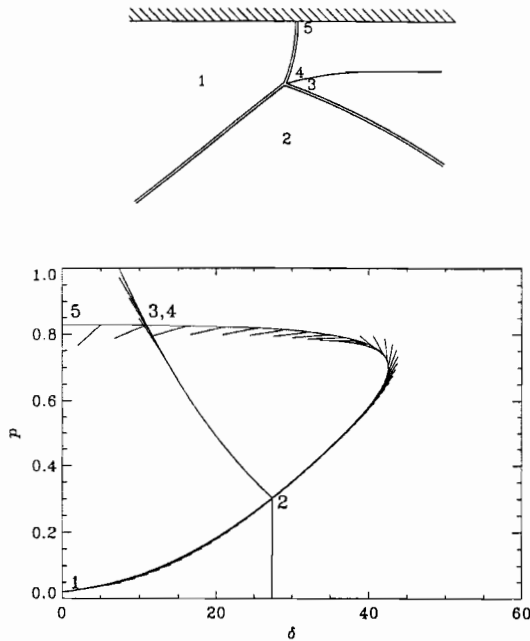


Figure 11. Mach reflection. Top: Schematic sketch of the shock configuration, with labels identifying regions and points of the flow in physical space. Bottom: δp -map of this flow, showing the incident shock (1-2), the reflected shock (2-3) and the Mach stem (4-5), as determined from the shock-jump relations. $M = 6$, $\gamma = 1.4$, non-reacting steady flow. Also shown are the streamline directions from the reflected shock and the Mach stem. Note that the two streamline directions coming from 3 and 4 are not the same, leading to the conclusion that these two shocks must have zero curvature at the triple point.

is a powerful simplifying device. Fig. 11 shows the usual picture of a Mach reflection in steady flow that may be mapped into the δp -plane as shown, with the numbers in corresponding places according to the mapping. At the triple point the pressures and streamline directions (inviscid flow) on either side of the slip line have to match. However, the streamline curvatures also have to match at that point for inviscid flow. This is where equation 12 can help us. Consider this equation in the non-reacting case $h_{it} = 0$. Note that then, $d\delta/dp$ reduces to a known function of β , M and γ , and is independent of the shock curvature. The direction in which the streamline leaves the shock in the δp -plane therefore does not depend on the shock curvature and may be indicated by short straight lines as shown in Fig. 11. Thus, we see that the directions in which streamlines leave the reflected shock and the Mach stem are not matched! The only way in which this problem can be resolved in non-reacting flow with a straight shock and uniform upstream conditions is if the Mach stem and the reflected shock both have zero curvature at the

triple point ($d\delta = dp = 0$).

It is interesting that an additional degree of freedom is introduced if either the incident shock is not straight, or the free stream is non-uniform, or both, as has been shown by Mölder (1972). Such cases therefore permit the shocks to be curved at the triple point. However, it is also possible to give the flow this additional degree of freedom if the shocks start a chemical reaction, as equation 13 shows.

5.4. Sonic line direction

The sonic line plays a very important role in gas-dynamics, because it is a boundary of information-transfer. Call the shock angle at the sonic point $\beta_s(M, \gamma)$, and let the direction of the sonic line relative to the shock be ϕ . Analysis results in

$$\cot \phi = f_{10} h_{it}/k + f_{11}, \quad (14)$$

where the f are again known functions of β , M and γ . For a particular γ , Fig. 12 shows plots of ϕ for different values of $\Omega = 1/(k\epsilon)$. The chain-dotted curve with three dots shows the non-reacting case. At high Mach numbers, above approximately 2.5, the endothermically reacting flows give values higher and the exothermically reacting flows give lower ϕ than the non-reacting case. At $M \simeq 2.5$, f_{10} changes sign, so that this trend is reversed.

Consider $M = 6$ and let the reaction rate change from very fast exothermic to non-reacting to very fast endothermic. This takes ϕ from 0 to 35° and then rapidly to 180°. This allows us to make an intelligent extrapolation to sketch the behavior of the sonic line in physical space. If we know Φ , which measures the energy that goes into the reaction to equilibrium, we can locate the sonic points on a curved shock not only for frozen, but also for equilibrium flow. In Fig. 13 this has been done quantitatively correctly on a circular-arc piece of shock. The corresponding streamline directions at the sonic points are also shown. The exothermic equilibrium sonic point lies above (smaller β), and the endothermic equilibrium sonic point below the frozen sonic point.

Now consider $\Omega \rightarrow -\infty$, for which $\phi \simeq 0$, so that the initial direction of the sonic line hugs the shock on the upper side. In the limit when the reaction rate is infinitely fast, one may consider the sonic line to start at the frozen sonic point, follow the shock and leave it at the equilibrium sonic point in the appropriate direction. Thus, the uppermost thick line that asymptotically approaches the equilibrium sonic line illustrates the likely behavior of



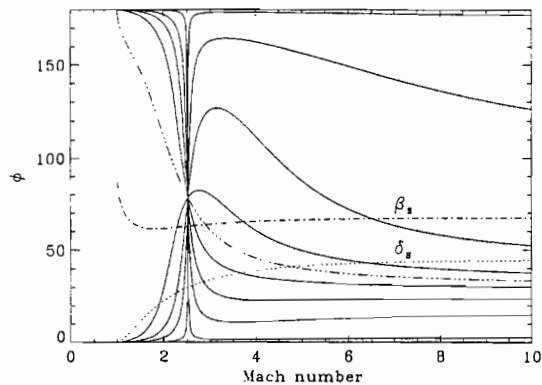


Figure 12. Dependence of sonic line angle on Mach number and reaction rate, plane flow, $\gamma = 1.4$, $\theta = 0.8$. The deflection and shock angles at the sonic condition are also shown as a dotted and a chain-dotted line. The chain-dotted line with three dots gives ϕ for the non-reacting case, in agreement with the solution given by Hayes and Probst. Continuous lines and dashed lines represent endothermic and exothermic reaction rate cases respectively, for $k\epsilon = -0.0001$ (lowest curve at high Mach number), -0.001 , -0.003 , -0.01 , ∞ (chain-dotted with three dots), 0.01 , 0.003 , 0.001 , 0.0001 .

the sonic line for fast exothermic reaction. Similarly, the lowest thick line shows the behavior of the sonic line for fast endothermic flow. Between them, a smooth transition occurs, something like the sketched thick lines for different values of Ω . A conclusion that may be drawn from this behavior is that streamlines that cross the shock between the frozen and endothermic equilibrium sonic points cross the sonic line from subsonic to supersonic conditions, while the opposite is true for exothermic flow. If the shock is nearly straight, the separation of the frozen and equilibrium sonic points can be large. In the endothermic case, this can lead to a slender subsonic sliver near the shock, which has a profound influence on the shock detachment process on a wedge, as has been shown experimentally and theoretically by Hornung and Smith (1979).

Studying the effects of chemical reactions in this way takes no account of the intricacies of rate processes, but it opens up a new view on the subject. An interesting next step would be to repeat the asymptotic analysis for exothermic flows.

Acknowledgement. The work leading to Sanderson (1995), Wen (1994) and Wen and Hornung (1995) was supported by the AFOSR URI grant F49620-93-1-0338 (Dr. J. Tishkoff). I wish to thank Joe Shepherd for many useful discussions and important corrections.

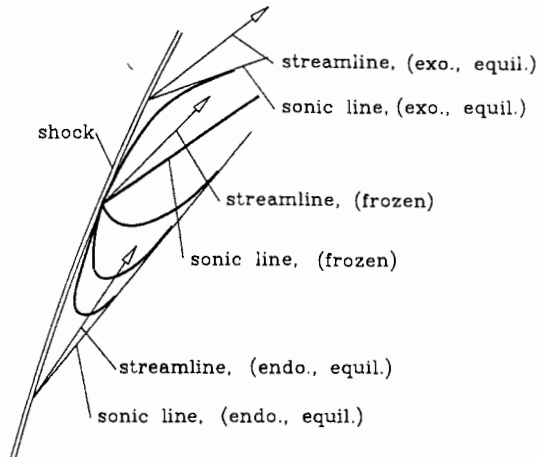


Figure 13. Sketch of the sonic line for different reaction rates (thick lines). The uppermost curve is the sonic line for a fast exothermic reaction, the lowest for a fast endothermic one, see text.

References

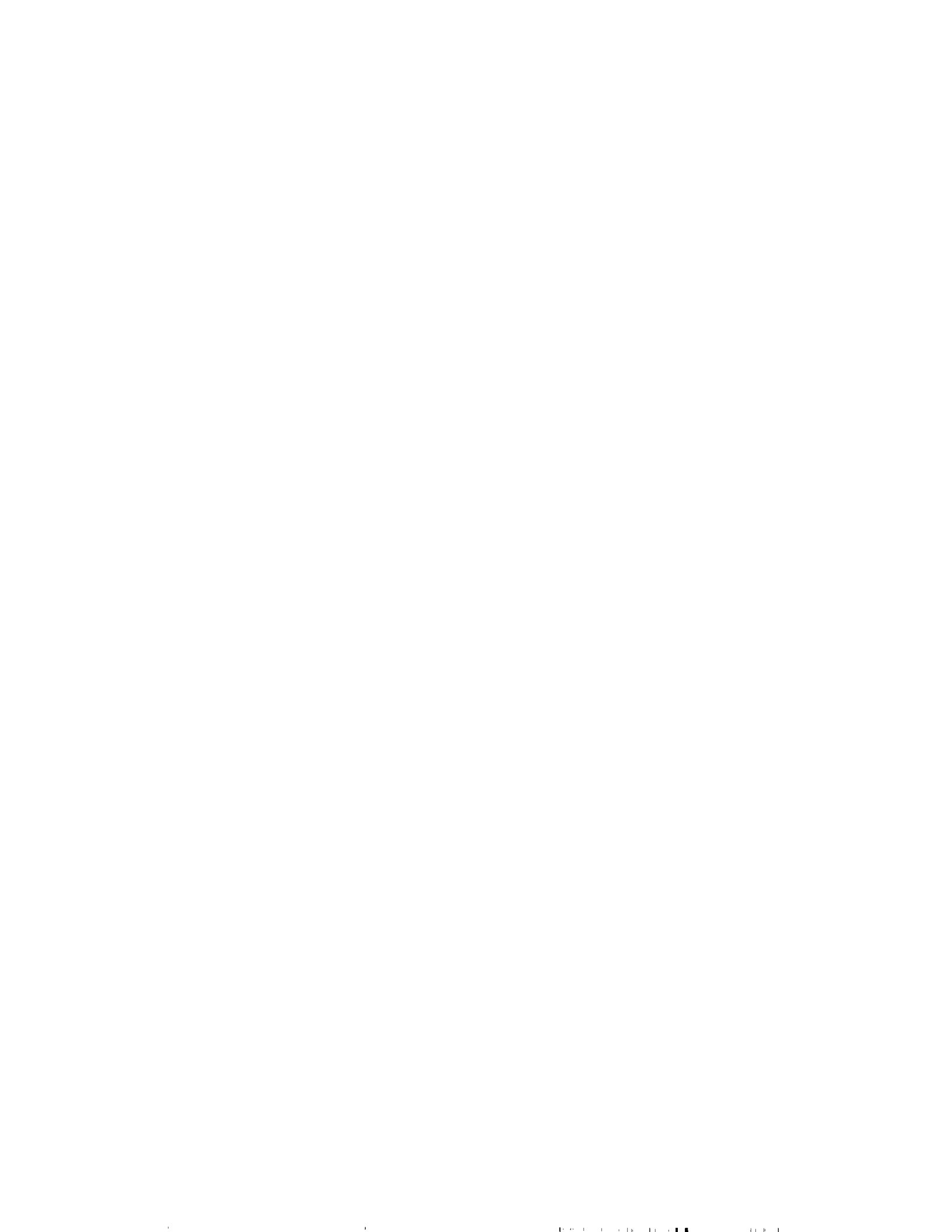
- Bélanger J, Kaneshige MJ, Shepherd JE (1995) Detonation initiation by hypervelocity projectiles. *Shock Waves*, World Scientific Press, 1119.
- Ebrahim N (1975) Nonequilibrium in high-enthalpy carbon dioxide flows. PhD thesis, Australian National University.
- Eckett C, Quirk JJ, Shepherd JE (1997) A new model for direct initiation of gaseous detonations, 21st ISSW, Great Keppel, Australia.
- Hornung HG (1976) Non-equilibrium ideal-gas dissociation after a curved shock wave. *J. Fluid Mech* 74:143-159.
- Hornung HG (1997) Gradients at a curved shock in reacting flow (to be published in *Shock Waves*)
- Hornung HG, Smith GH (1976) The influence of relaxation on shock detachment. *J. Fluid Mech.* 93:225-239.
- Kaneshige MJ, Shepherd JE (1996) Oblique Detonation Stabilized on a Hypervelocity Projectile. 26th International Symposium on Combustion, 3015-3022.
- Mölder S (1972) Polar streamline directions at the triple point of Mach interaction of shock waves. *CASI Trans.* 5:88-89.
- Sanderson SR (1995) Shock wave interaction in hypervelocity flow. PhD thesis, Caltech.
- Stalker RJ (1972) Unpublished, discussions in the T3 laboratory. Australian National University.
- Wen CY (1994) Hypervelocity flow over spheres. PhD thesis, Caltech.
- Wen CY, Hornung HG (1995) Non-equilibrium dissociating flow over spheres. *J. Fluid Mech.* 299:389-405



Ae234 Assignment No. 2, due 30 April, 2002

QUESTION 1

Calculate the relaxation zone after a shock propagating at 16 km/s into undissociated hydrogen at a density of 10^{-5} kg/m³. Neglect the enthalpy and pressure of the free stream, *i. e.*, take $H_0 = K$, $P = 0$. Use $C = 6 \times 10^{18}$ cm³g⁻¹s⁻¹K, $\eta = -1$. Plot α , density, velocity, temperature and pressure as a function of distance from the shock. Use the values of ρ_d and θ_d that you determined in assignment no. 1.



12. $V\delta$ -PLANE for $\omega \rightarrow 0$ And $\omega \rightarrow \infty$

To complete the picture of the streamline direction at the frozen shock in the $V\delta$ -plane consider the cases $\omega \rightarrow 0$ and $\omega \rightarrow \infty$. Equation (11.11) gives

$$\frac{d\delta}{dV} = -\frac{u}{Vv} \cdot \frac{\omega - G + \left[\frac{p_x}{\rho k} \frac{vV^2}{u} \left(\frac{1}{a_f^2} - \frac{1}{v^2} \right) \right]}{\omega - G}$$

For $\omega \rightarrow 0$,

$$\begin{aligned} \left(\frac{d\delta}{dV} \right)_{\omega \rightarrow 0} &= -\frac{u}{Vv} \left\{ 1 + \frac{[]}{\omega - G} \right\} \\ &= -\frac{u}{Vv} \left\{ 1 - [] \frac{1}{G} \left(1 + \frac{\omega}{G} \right) \right\} + O(\omega^2) \end{aligned} \quad (12.1)$$

As ω is increased from zero, it changes according to

$$\begin{aligned} \left[\frac{\partial}{\partial \omega} \left(\frac{d\delta}{dV} \right) \right]_{\omega \rightarrow 0} &= \frac{u}{Vv} \frac{[]}{G^2} \\ &= \frac{V}{\rho} \frac{p_x}{k} \left(\frac{1}{a_f^2} - \frac{1}{v^2} \right) \cdot \frac{1}{G^2} \end{aligned} \quad (12.2)$$

$\frac{p_x}{k}$ is negative for a convex shock and, since $v < a_f$ (normal component of velocity is subsonic after the shock) the bracket is also negative. All the other variables in (12.2) are positive.

Hence

$$\left[\frac{\partial}{\partial \omega} \left(\frac{d\delta}{dV} \right) \right]_{\omega \rightarrow 0} > 0. \quad (12.3)$$

For $\omega \rightarrow \infty$

$$\begin{aligned} \left(\frac{d\delta}{dV} \right)_{\omega \rightarrow \infty} &= -\frac{u}{Vv} \left\{ \frac{\omega \left(1 - \frac{G}{\omega} + \frac{[]}{\omega} \right)}{\omega \left(1 - \frac{G}{\omega} \right)} \right\} \\ &= -\frac{u}{Vv} \left\{ 1 + \frac{[]}{\omega} \right\} + O\left(\frac{1}{\omega^2} \right) \end{aligned} \quad (12.4)$$

We see that, not only is the limiting value of $d\delta/dV$ at $\omega = \infty$ independent of G , but the dependency drops out already in the first order of $\frac{1}{\omega}$. The rate at which $d\delta/dV$ changes with ω is now

$$\left[\frac{\partial}{\partial \omega} \left(\frac{d\delta}{dV} \right) \right]_{\omega \rightarrow \infty} = \frac{V}{\rho \omega^2} \frac{p_x}{k} \left(\frac{1}{a_f^2} - \frac{1}{v^2} \right). \quad (12.5)$$

This is again positive, so that

$$\left[\frac{\partial}{\partial \omega} \left(\frac{d\delta}{dV} \right) \right]_{\omega \rightarrow \infty} > 0. \quad (12.6)$$

Thus, in both cases, the streamline leaves the shock in the $V\delta$ -plane at an angle that lies between the two angles for the frozen and straight-shock limits. Monotonic changes of the angle with ω may be expected throughout the range.

In order to compute the values of the terms in the equations derived in chapters 11 and 12, one may proceed as follows: Put

$$m = \sin \beta \quad (12.7)$$

Then the shock-jump relations are

$$\begin{aligned} u &= \sqrt{1 - m^2} \\ v &= m/\rho \\ V^2 &= 1 - m^2 + \frac{m^2}{\rho^2} \\ p &= m^2 \left(1 - \frac{1}{\rho}\right) + p_1 \\ \rho &= \frac{\gamma + 1}{\gamma - 1 + \frac{2\gamma p_1}{m^2}} \\ a_f^2 &= \frac{\gamma p}{\rho} \end{aligned} \quad (12.8)$$

Also, by differentiating these w.r.t. x , we obtain,

$$\begin{aligned} u_x &= m k \\ \frac{p_x}{k} &= -2m\sqrt{1 - m^2} \left(1 - \frac{1}{\rho}\right) + \frac{m^2}{\rho^2} \frac{\rho_x}{k} \\ \frac{v_x}{k} &= -\frac{1}{\rho} (\sqrt{1 - m^2}) - \frac{m}{\rho^2} \frac{\rho_x}{k} \\ \frac{\rho_x}{k} &= -\frac{\rho\sqrt{1 - m^2}}{m} \frac{4\gamma(\gamma - 1) \left(\frac{p_1}{m^2}\right)}{1 + 2\gamma(\gamma - 1) \left(\frac{p_1}{m^2}\right)} \end{aligned} \quad (12.9)$$

For example,

$$G = \left[3(1 - m^2) - \frac{m^2}{\rho}\right] \left(1 - \frac{1}{\rho}\right) - \frac{2m\sqrt{1 - m^2}}{\rho^2} \frac{\rho_x}{k}. \quad (12.10)$$

Since the free-stream Mach number is

$$M_1^2 = \frac{\rho_1' V_1'^2}{\gamma p_1'} = \frac{1}{\gamma p_1'}$$

$p_1 \rightarrow 0$ as $M_1^2 \rightarrow \infty$

and the above formulae are somewhat simplified.

Example: Maximum deflection point

$$\begin{aligned}
 \delta &= \beta - \arctan \frac{v}{u} \\
 \delta_x &= \beta_x - \frac{\partial}{\partial x} \left(\arctan \frac{v}{u} \right) \\
 &= -k - \frac{k}{1 + \frac{v^2}{u^2}} \left(u^{-1} \frac{v}{k} - \frac{v}{u^2} \frac{u_x}{k} \right) \\
 \delta_x &= 0 \text{ when r.h.s.} = 0, \text{ i.e., when}
 \end{aligned}
 \tag{12.11}$$

$$1 + \frac{1}{V^2} \left[u \frac{v_x}{k} - v \frac{u_x}{k} \right] = 0.$$

Substitute:

$$1 + \frac{1}{1 - m^2 + \frac{m^2}{\rho^2}} \left\{ \sqrt{1 - m^2} \left[-\frac{\sqrt{1 - m^2}}{\rho} + \frac{\sqrt{1 - m^2}}{\rho} \cdot \frac{4\gamma(\gamma - 1) \frac{P_1}{m^2}}{1 + 2\gamma(\gamma - 1) \frac{P_1}{m^2}} \right] - \frac{m^2}{\rho} \right\} = 0$$

$$1 - m^2 + \frac{m^2}{\rho^2} = \frac{1 - m^2}{\rho} \left(1 - \frac{2P}{1 + P} \right) + \frac{m^2}{\rho}$$

$$(1 - m^2) \left(1 - \frac{1}{\rho} + \frac{2P}{1 + P} \right) = \frac{m^2}{\rho} \left(1 - \frac{1}{\rho} \right)$$

$$\frac{m^2}{1 - m^2} = \rho \frac{\rho - 1 + 2P/(1 + P)}{\rho - 1}.$$

(12.11)

This is a general expression for the maximum-deflection point of a perfect gas in terms of M_1 , γ and m , since

$$P = \frac{2(\gamma - 1)}{M_1^2 m^2}.$$

For $M^2 \rightarrow \infty$, $P \rightarrow 0$, so for

$$M^2 = \infty \quad \frac{m^2}{1 - m^2} = \rho = \frac{\gamma + 1}{\gamma - 1}$$

for $\gamma = \frac{7}{5}$ this gives $\frac{m^2}{1 - m^2} = 6$ or $\beta = 67.79^\circ$.

13. Flow Over A Wedge. Constrained Shock Points

In chapters 11 and 12 the equations of motion were applied to the problem of finding gradients right *at* the downstream side of the frozen shock only. They are, of course, valid also at finite values of y .

In this chapter we extend the streamline map to regions of $y \neq 0$ for the region

$$y \ll \frac{1}{k}$$

close to the shock wave in terms of the radius of curvature. This restriction allows us to neglect ky in comparison with 1. In addition, the x -derivatives may be assumed to be independent of y . The last assumption is a thin-layer type of assumption similar to the boundary layer assumptions.

Consider a streamline that intersects a curved shock at a particular value of β . Let this correspond to the point P in the (ψ, δ) map on the frozen shock locus 2. Let the value of (w) at the shock be (w_2) . As the streamline leaves the shock, in the direction corresponding to this value of w , the dissociation rate decreases rapidly, just as in the flow after a normal shock. If equation (11.11)

$$\frac{d\delta}{dV} = -\frac{u}{vV} \frac{\omega - G + \frac{vV^2}{u} \left(\frac{p_x}{\rho k}\right) \left(\frac{1}{a_f^2} - \frac{1}{v^2}\right)}{\omega - G} \quad (11.11)$$

applies in the region $y \ll \frac{1}{k}$, as it should, if the above assumptions hold, then the direction of the streamline map changes towards the frozen direction ($\omega = 0$) with increasing distance from the shock along the streamline as shown. The final direction of the streamline depends on the composition of the gas at the point where $d\alpha/dt$ has become zero. The sketch shows how the streamline map changes as (w_2) is increased from 0 to ∞ .

At this point it is interesting to consider the entropy change along the streamline as it traverses the relaxation region. To do this, recall that

$$Tds = dh - \frac{1}{\rho} dp + (\mu_{N_2} - \mu_N) d\alpha.$$

Along a streamline, starting from the point 2 after a frozen shock, the energy and momentum equations may be written as

$$\begin{aligned} dh + VdV &= 0 \\ dp + \rho VdV &= 0. \end{aligned}$$

derivative

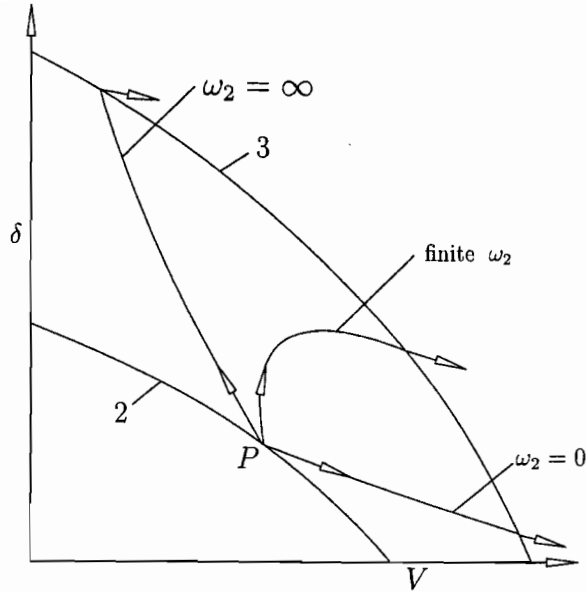


Figure 1. Behavior of streamlines in the relaxation region (between conditions 2 and 3) when $\ell \ll 1/k'$ for different values of ω .

It follows that

$$dh - \frac{1}{\rho} dp = 0.$$

Therefore

$$T ds = (\mu_{N_2} - \mu_N) d\alpha.$$

In the case of the IDG,

$$2m ds = k \ln \left[\frac{\rho_a (1 - \alpha) e^{-\theta_a/T}}{\rho \alpha^2} \right] d\alpha.$$

(In this equation k is Boltzmann's constant). Recall that the square bracket is equal to one for equilibrium flow, so that no entropy change occurs downstream of the shock for equilibrium flow, as required. Trivially we also recognize that $ds = 0$ for $d\alpha = 0$. The square bracket is the ratio of the dissociation rate to the recombination rate. Depending on whether this is greater or smaller than one, the logarithm is positive or negative. However, $d\alpha$ also changes sign when the square bracket does, so that their product (ds) is always positive, as required by the second law of thermodynamics.

It is interesting to consider the limiting case of equilibrium flow as that when the dissociation rate becomes infinite. In that case we might consider the extremely thin relaxation region as part of the shock wave. Thus, the difference between the two ways of looking at the problem: frozen shock followed by a thin relaxation zone on one hand, and equilibrium shock followed by isentropic equilibrium flow on the other, is just the difference of whether one considers the entropy rise associated with the dissociation as occurring within the equilibrium shock, or in a thin relaxation region after the frozen shock.

Fig. 1 shows the situation after an unconstrained shock point. A constraint is applied, for example, if the streamline direction is fixed by the presence of a solid boundary. An example is the flow near the tip of a wedge as shown. Along the wedge surface, the

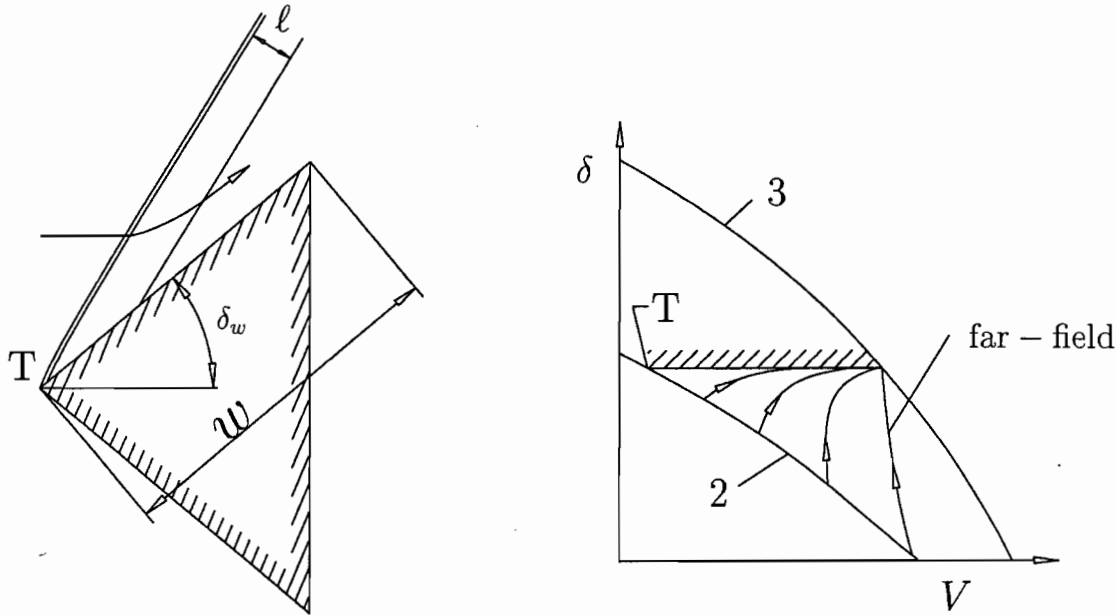


Figure 2. LEFT: Physical plane, showing an attached shock in flow over a symmetrical wedge. RIGHT: $V\delta$ -map of this flow for the case when $w \ll l$, in which the far-field streamline passes through a straight shock.

deflection is constant, $\delta = \delta_w$. In the $V\delta$ -plane, this streamline therefore maps into a horizontal line. The apparent contradiction of this with the diagram at the top of the page is resolved if the curvature of the shock at the wedge tip takes on that special value which enables this.

Equation (11.11) shows that this is the case if

$$\frac{d\delta}{dV} = 0 : \omega_{2T} = G - \frac{vV^2}{u} \frac{p_x}{\rho k} \left(\frac{1}{a_f^2} - \frac{1}{v^2} \right). \quad (13.1)$$

It follows that the shock curvature at the wedge tip is a measure of the dissociation rate. It has been attempted by several authors to use this as a method of measuring dissociation rates. However, in a practical flow, the displacement effect of the viscous boundary layer always causes the method to be inaccurate, and curvature is difficult to measure accurately in any case. If the wedge extends infinitely far downstream the shock becomes straight asymptotically, and the streamlines there map into the straight-shock curve for $\omega_2 = \infty$.

Between the tip and the far field, there is a continuous transition from $\omega_2 = \omega_{2T}$ to $\omega_2 = \infty$. This occurs at constant r by virtue of a continuous change of shock curvature.

$$\omega = -\frac{r}{k} \cdot \frac{v}{\rho h_\rho V^2}. \quad (11.12)$$

The extent of the region where the shock is significantly curved is thus scaled by ℓ .

Constraints may be applied at a shock in other ways too, of course; for example, at a point where two shock waves intersect such as in the regular shock reflection shown on the next page. If this occurs in a perfect gas, both incident and reflected shock are straight, and the $V\delta$ map of the region downstream of the reflected shock is a single point C . For relaxing flow the incident shock encounters a nonuniform free stream, and further dissociation may occur after the reflected shock. The flow after the incident shock maps into the straight-shock solution AB , and the region downstream of the reflected shock into the region $GHCFE$, with all arrows asymptotically approaching the V axis ($\delta = 0$). In this flow it is not possible to draw any conclusions about the sign of the curvature of the reflected shock without knowing details about the two relaxation processes.



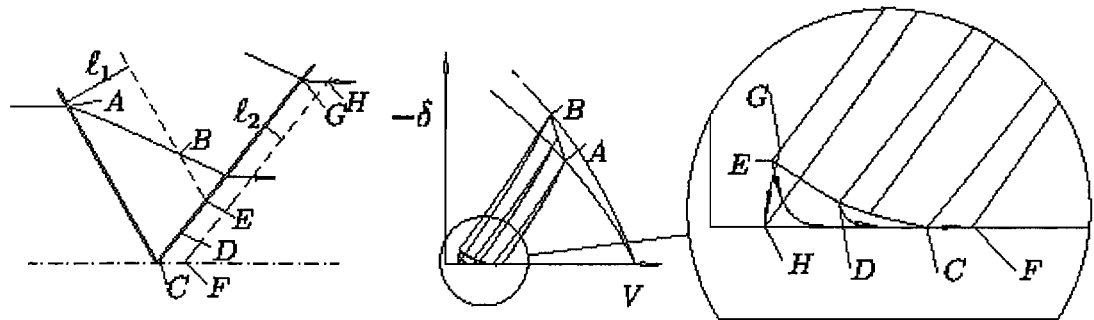


Figure 3. LEFT: Regular reflection of a plane oblique shock from a plane of symmetry. The incident and reflected shock have different relaxation lengths. RIGHT: $V\delta$ map of this flow. The inflow conditions for the reflected shock now lie on the streamline AB through the relaxation zone of the incident shock. From each point on this streamline we have to draw a new shock locus pair to find the locus of conditions GEDC on the downstream side of the frozen reflected shock. The subsequent streamlines all have to finish up with zero δ . This happens through a straight shock in the far field (GH) and along the axis for the streamline CF. To achieve the latter, the reflected shock has to curve appropriately.



Ae234 Assignment No. 3, due 7 May, 2002

QUESTION 1

Use the software you generated to calculate a normal shock in an IDG with appropriate changes to calculate an oblique shock. Use this to plot the $V - \delta$ map of a frozen and an equilibrium shock in nitrogen with free-stream at 7 km/s, 0.004 kg/m³ and 500 K. Choosing a few particular shock angles, plot (in the same diagram) the path followed by a streamline from the frozen to the equilibrium shock.

QUESTION 2

Use the results from Question 1 and suitable additional calculations to plot a graph of the distance (measured normal to the shock) from the shock to the point where $V = a_f$ as a function of shock angle, in the range where this distance is finite.

The influence of relaxation on shock detachment

By H. G. HORNUNG AND G. H. SMITH

Department of Physics, Australian National University, Canberra, Australia

(Received 12 July 1978)

By establishing that the length scale governing the detachment of a shock wave from a wedge is the distance from the leading edge to the sonic line, and by considering the view of observers with different length scales, it is predicted that the detachment distance increases gradually with wedge angle for relaxing flow and more rapidly in a perfect gas. Both of these features are confirmed by experiments in the free-piston shock tunnel. The influence of other length scales is discussed. The phenomenon is related to a relaxation effect in which a subsonic layer grows from the translational-rotational shock as the wedge inclination is increased beyond the frozen sonic point.

1. Introduction

A two-dimensional wedge placed symmetrically in a uniform supersonic flow supports an oblique shock wave which is attached to the leading edge if the wedge is sufficiently slender. In the vicinity of the leading edge, the oblique shock on a slender wedge is straight if the fluid is in thermodynamic equilibrium before and immediately after the shock and if the shock itself is thin compared with the observer's length scale. Under such circumstances the conditions throughout region B (see figure 1*a*) are uniform and may be determined from the shock jump conditions, that is, from the conservation and state equations. Take the flow speed, V_B , to be a representative property of region B . For a given deflexion δ of the flow through the shock the shock jump conditions give two possible solutions for V_B , of which the 'stronger', with smaller V_B , is usually only realized in practice when the shock is curved. It is convenient to map the flow into the velocity-deflexion plane (see figure 1*b*). The whole of region A maps into the point $A'(V_\infty, 0)$ and point $B'(V_B, \delta)$ represents the whole of region B . When the shock front segment bordering region B is straight, the flow deflexion angle, δ , at the shock is constant throughout B , and equal to the angle of inclination, δ_w , of the wedge face relative to the freestream direction. The curve in figure 1(*b*) is called a shock locus and represents all possible states which may be reached from state A via an oblique shock. As the wedge angle δ_w is increased from zero, the point B' moves from A' along the shock locus towards the sonic point S at which V_B has decreased to the local speed of sound. At this point an important change occurs. Whereas, before, conditions in B were supersonic, so that signals from the trailing edge of the wedge were unable to travel upstream, and the flow pattern near the leading edge was devoid of a length scale, information about the finiteness of the wedge, that is about the length w , can now be communicated to the leading edge. The flow pattern responds to this situation by exhibiting a curved attached shock when B' lies slightly to the left of S . The region B is then no longer uniform, and B' only represents the post-shock flow at

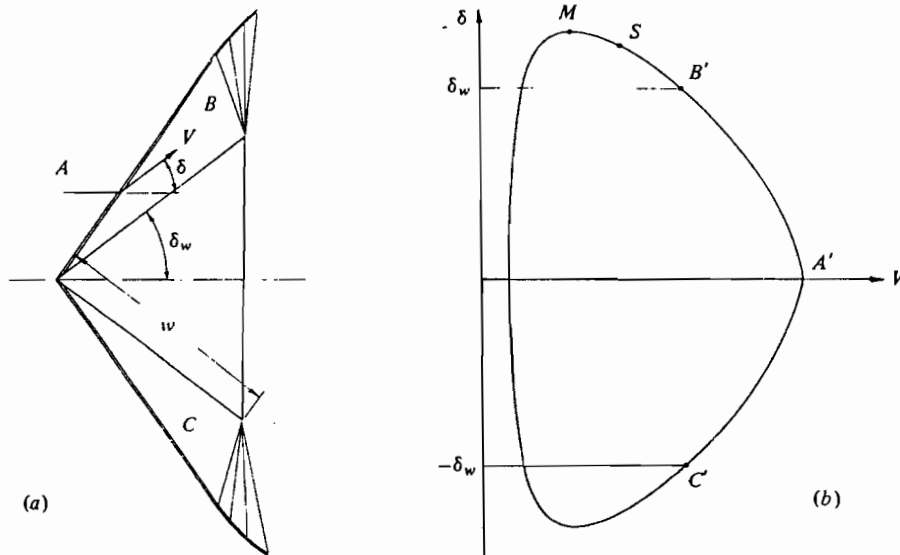


FIGURE 1. Attached shock wave and supersonic post-shock flow. (a) Physical plane. (b) V, δ plane. A , free stream; B, C , post-shock flow upstream of corner expansion; M , maximum deflexion point; S , sonic point. The flow near the leading edge is devoid of a length scale.

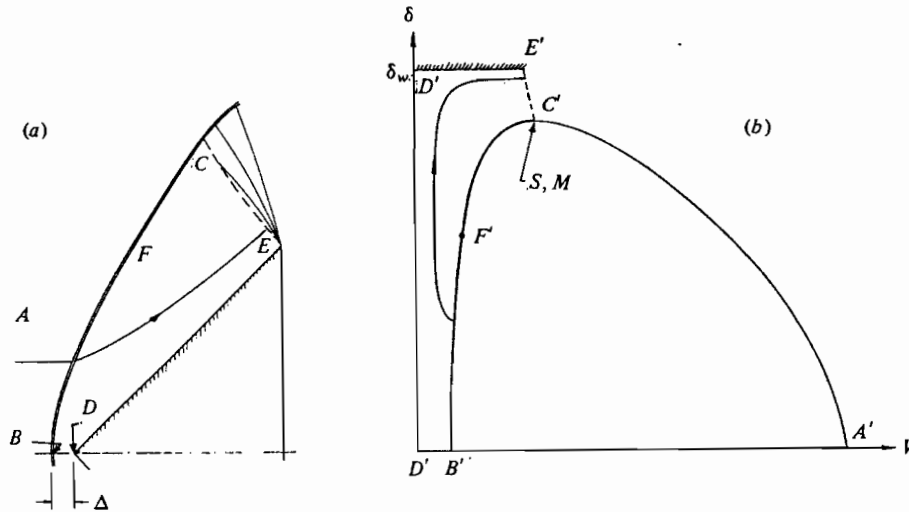


FIGURE 2. Detached shock wave and subsonic post-shock flow up to the sonic line at the trailing edge. (a) Physical plane. (b) V, δ plane. Information about the length scale w can reach the leading edge. S and M are effectively coincident at high free stream Mach number.

the leading edge, the remaining part of the shock being mapped into the portion of the shock locus between B' and S . For very large free stream Mach number, the case of present interest, the point S practically coincides with the maximum deflexion point M . When the wedge angle is increased beyond δ_M a significant change occurs in the flow pattern: The shock wave detaches from the leading edge of the wedge to form the flow pattern shown in figure 2(a) with the corresponding V, δ map of figure 2(b).

If S and M are considered to be coincident, a particular wedge angle $\delta = \delta_M$ sharply divides the two flow patterns of figures 1(a) and 2(a). In the former, the flow in region B is supersonic and 'knows' nothing about the extent of the wedge face; this results in the absence of a length scale in the flow pattern. In the latter case, the post-shock flow is subsonic, so that the length w communicates itself to all of the flow field over the wedge. For a given free stream and wedge angle the length scale of the flow pattern, as manifested for example by the stand-off distance Δ , is then proportional to w .

In the present investigation we inquire how the detachment process is modified when the approach to thermodynamic equilibrium at the shock occurs over a finite length, so that the equilibrium shock may no longer be considered thin. In the discussion of situations encountered in relaxation gas-dynamics it is convenient to introduce the smallest resolvable and largest viewable lengths of the observer, λ and Λ , say. The ratio Λ/λ is a measure of the range or power of observation. Let the relaxation lengths for translational, rotational, vibrational and dissociative relaxation be l_t , l_r , l_v and l_d respectively. In the following, vibration and dissociation will be regarded as a single relaxation process with characteristic length l . Similarly, translation and rotation may both be conveniently described by the length scale l_t . This is appropriate to the experimental conditions of §3. The situation to be considered by an observer who cannot resolve any relaxation, is specified by the set of conditions

$$l_t < l < \lambda < w < \Lambda. \quad (1)$$

The shock observed by this observer will be referred to as 'equilibrium shock' for which the post-shock flow is everywhere seen to be in thermodynamic equilibrium. The case of present interest, in which the observer can resolve the dissociative relaxation, may then be specified by

$$l_t < \lambda < l < w < \Lambda. \quad (2)$$

Since our observer would regard as zero all lengths smaller than λ , (2) specifies a situation in which the translational shock thickness is zero. However, he can resolve dissociative relaxation, so that (chemical) equilibrium is reached within his window.

By restricting his field of view, Λ , the observer may reduce his power of observation and thereby change the nature of the problem he has to study, for example to

$$l_t < \lambda < \Lambda \ll l, \quad \Lambda \ll w. \quad (3a)$$

This corresponds to the case of a perfect or chemically frozen continuum gas in which the translational shock thickness is again zero. It is a set of assumptions appropriate for describing the conditions in the immediate vicinity of the frozen shock, before any appreciable dissociation has occurred. The gas may effectively be considered to be in a state of constrained equilibrium. For the observer (3) the post-shock equation of state is different from that for the observer (1), and consequently the shock jump condition and shock locus are also different; this is illustrated in figure 3. The region B , in a sufficiently small window $\Lambda(3)$, maps into the point B' on the 'frozen' shock locus (3) while the eventual equilibrium point C [well outside $\Lambda(3)$] maps into C' on the shock locus (1); this describes the flow when it has eventually attained chemical equilibrium; it may be thought of as the equilibrium shock locus.

The relative positions of the shock loci (1) and (3) are always as shown in figure 3 if the free stream is in unconstrained thermodynamic equilibrium, and the streamlines

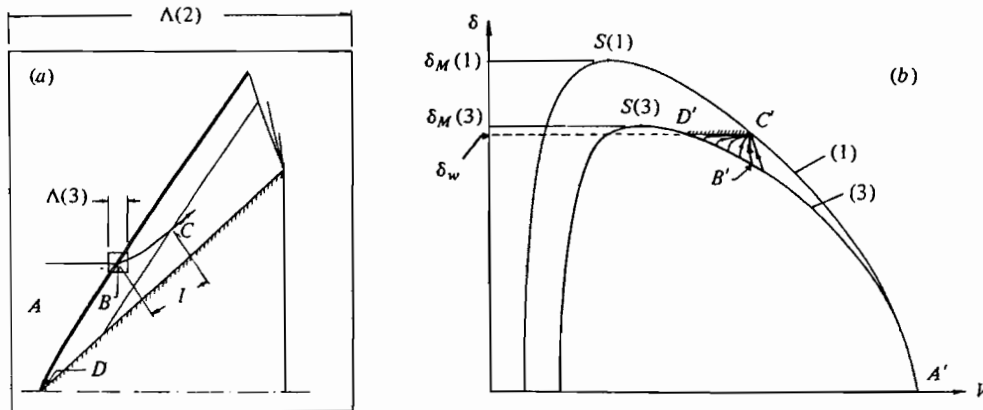


FIGURE 3. Flow over a wedge with resolvable relaxation length and an attached shock wave. (a) Physical plane. (b) V, δ plane. The shock loci seen by observers (1) and (3) do not coincide.

are drawn in the V, δ map according to the rules derived for relaxing flow by Hornung (1977). In the case illustrated in figure 3, the flow is supersonic everywhere.

In the above discussion the transition to observer (3) is made by holding the geometric length scale constant and varying the observer's length scale. This leads to observer (3) viewing a small part of a large experiment, the extent of which lies outside his window. He is therefore unable to measure w and cannot make any statements about the flow as a whole. If, on the other hand, the transition to observer (3) is made by increasing the relaxation length until it is much larger than Λ while maintaining the inequality $\Lambda > w$, he can view the perfect gas flow problem as a whole. His situation is then specified by

$$l_t < \lambda < w < \Lambda \ll l. \quad (3b)$$

It corresponds to the continuum, perfect gas situation commonly treated in gas dynamics text books.

It can now be demonstrated that detachment is a more complex process when the relaxation can be resolved by the observer. Consider the case when δ_w lies between the maximum deflexion angles $\delta_M(1)$ and $\delta_M(3)$ (see figure 4b). According to observer (1) who cannot resolve l , the equilibrium shock is straight and attached. However, according to observer (2), who can resolve details within the relaxation length l , the frozen shock is detached. The two observers can only be simultaneously right if the detachment occurs on such a small length scale that observer (1) cannot resolve it, but observer (2) can. The same conclusion is reached when it is recognized that a small subsonic region starts to grow from the frozen shock as the shock angle is increased beyond that corresponding to $\delta_M(3)$; a more detailed discussion follows in § 2.2. The distance to the sonic point is the determining length scale for the stand-off distance Δ .

On the basis of the above arguments it may be expected that the observer (2), who can resolve l , will see the following as he increases δ_w . At $\delta_M(3)$ the frozen shock becomes strongly curved near the tip and, as δ_w increases further, begins to detach gradually, Δ being approximately proportional to the smoothly increasing distance to the sonic line, until the sonic line reaches the end of the relaxation zone. This point corresponds to $\delta_w = \delta_M(1)$, and a further increase in δ_w results in a very rapid move-

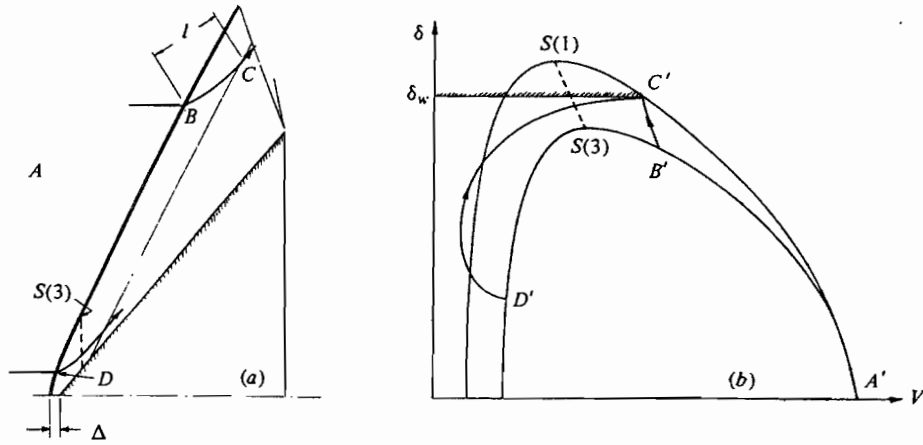


FIGURE 4. When $\delta_M(3) < \delta_w < \delta_M(1)$, observer (3) sees a detached shock, but observer (1) sees an attached shock. This can occur only if Δ is so small that observer (1) cannot resolve it. Note that the equilibrium shock locus (1) applies only if the shock curvature is small compared with $1/l$. (a) Physical plane. (b) V, δ plane.

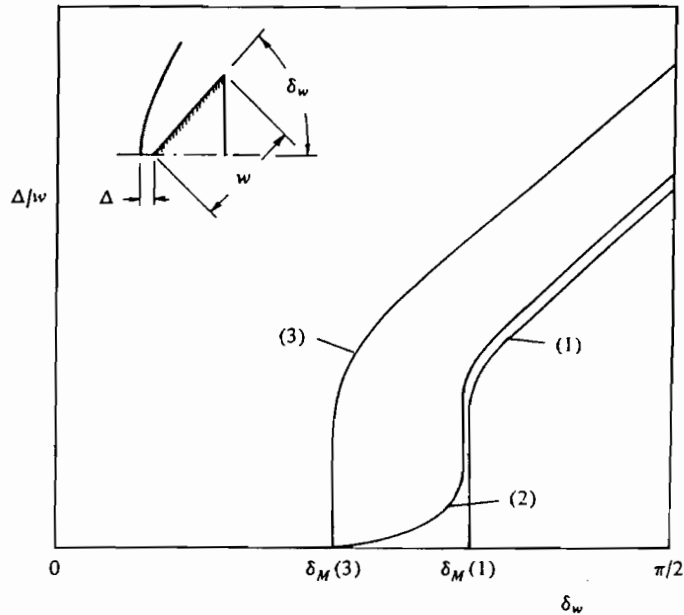


FIGURE 5. Behaviour of stand-off distance with wedge angle as predicted for observers (1), (2) and (3).

ment of the sonic line to the trailing edge of the wedge (see also figure 8b), and a consequent rapid increase in Δ . This corresponds to the detachment of the equilibrium shock. Figure 5 illustrates the variation of the stand-off distance with δ_w expected by observers (1), (2) and (3). The behaviour of the curves as $\delta_w \rightarrow \frac{1}{2}\pi$ is sketched in according to the expectation that the stand-off distance, measured not from the tip but from the line joining the trailing edges of the wedge, becomes insensitive to δ_w as $\delta_w \rightarrow \frac{1}{2}\pi$ (see Cabannes 1960).

The aim of the present investigation is to test these predictions for observers (2) and (3) experimentally in the free-piston-driven shock tunnel with dissociating nitrogen and carbon dioxide flows, for which this facility is able to reproduce the conditions of observer (2) around the detachment angle. As a check, perfect gas argon flows should reproduce the conditions of observer (3) reasonably well.

2. Theoretical considerations

2.1. Dimensional analysis

In the dynamics of an inviscid perfect gas (frozen flow) with a uniform free stream the variables governing the flow over a body are the free stream speed, pressure and density, $V_\infty, p_\infty, \rho_\infty$, the ratio of specific heats, γ , the size of the model, w , say, and additional parameters describing the shape, such as the wedge angle δ_w in our problem. Thus, the shock stand-off distance Δ may be written in dimensionless form

$$\Delta/w = f_3(M_\infty, \gamma, \delta_w). \quad (4)$$

These are the variables that are important to observer (3) when w is within his window. M_∞ is the free stream Mach number $V_\infty \rho_\infty^{1/2} / (\gamma p_\infty)^{1/2}$.

For observer (1) the chemical composition changes (in zero distance after the shock), so that an additional variable is required to specify the flow completely. This may be conveniently chosen to be the amount of energy per unit mass, E , to bring the gas to its new equilibrium state at some representative condition, say after a normal shock. Hence, for observer (1),

$$\Delta/w = f_1(M_\infty, \gamma_\infty, \delta_w, \mu), \quad (5)$$

where $\mu = V_\infty^2 / 2E$, and γ_∞ is the ratio of specific heats in the free stream.

Observer (2) sees the composition change over a finite distance and therefore requires yet another variable to specify his picture completely, namely the relaxation length l . For him,

$$\Delta/w = f_2(M_\infty, \gamma_\infty, \delta_w, \mu, l/w). \quad (6)$$

The transition from the flow seen by observer (1) to that of observer (3) proceeds via that seen by observer (2) and may be described by

$$f_1 \rightarrow f_2 \rightarrow f_3 \quad (7)$$

corresponding to the change

$$0 \rightarrow l/w \rightarrow \infty. \quad (8)$$

For constant free stream conditions, the parameters M_∞, γ_∞ and μ are constant and may be omitted from f_1, f_2 and f_3 . The problem of observer (2) then reduces to

$$\Delta/w = f(\delta_w, l/w), \quad (9)$$

the dependence on l/w disappearing for the other two observers, for whom only δ_w matters.

2.2. The position of the sonic line

Our motivation to study the detachment process in relaxing flow came about through our discovery that in relaxing flow through an oblique shock there exists a range of

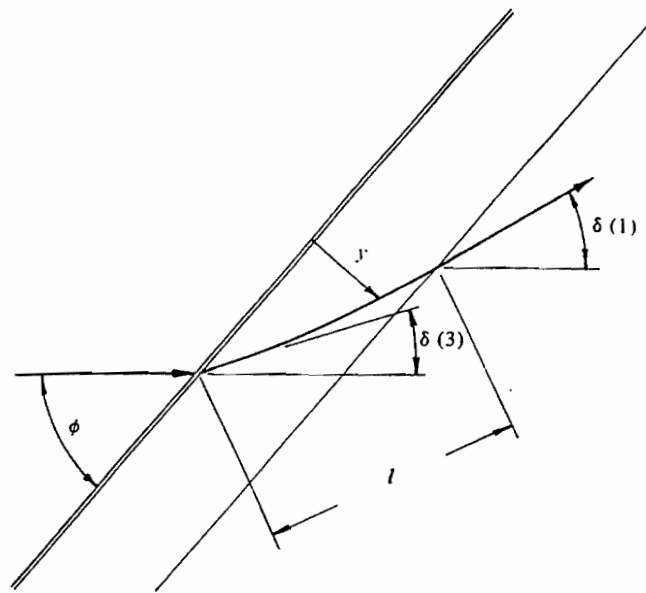


FIGURE 6. Notation for flow through a straight, oblique shock with relaxation.

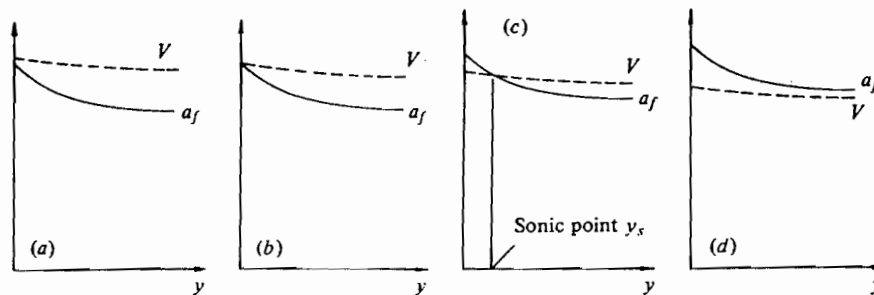


FIGURE 7. The growth of a subsonic layer after a straight, oblique shock making an angle ϕ with the free stream. (a) $\phi < \phi_s(3)$. (b) $\phi = \phi_s(3)$. (c) $\phi > \phi_s(3)$. (d) $\phi > \phi_{s*}$. Relaxation causes the frozen speed of sound, a_f , to decrease more rapidly than the flow speed, V , with distance from the shock.

shock angles within which the flow after the translational shock is first subsonic and then becomes supersonic again within the relaxation zone. This is an effect which is of dominant importance to the detachment process. It comes about essentially because the frozen speed of sound, a_f , falls more rapidly than the flow speed, along a streamline within the relaxation zone.

In order to illustrate the effect it is convenient to consider a straight, oblique shock making an angle ϕ with the free stream, as shown in figure 6. The streamline is deflected by the translational shock to the frozen deflexion angle $\delta(3)$, and within the relaxation zone it suffers a further deflexion to the equilibrium deflexion angle $\delta(1)$. Let the distance measured at right angles to the shock be y . As ϕ is increased from a point where the flow is everywhere supersonic, the sequence of sketches of figure 7 illustrates the process by which a subsonic region grows from the translational shock to cover the

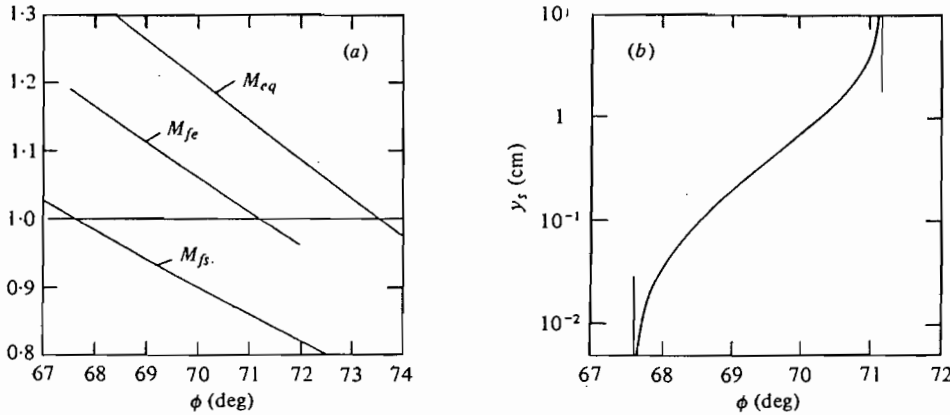


FIGURE 8. (a) Numerical calculations of dissociative relaxation of nitrogen after a straight oblique shock at a freestream speed of 6 km/s, showing the frozen Mach number at the shock, M_{fs} , and at the end of the relaxation zone, M_{fe} , as well as the equilibrium Mach number as functions of the shock angle ϕ . (b) The corresponding movement of the frozen sonic point away from the shock.

whole region downstream of the shock. The sequence relates ϕ to two of its possible values, one when the frozen shock becomes sonic, $\phi_s(3)$, and the other when the flow becomes sonic at the end of the relaxation zone, ϕ_{se} .

To substantiate this idea quantitatively, numerical calculations were made for a series of straight oblique shocks in a dissociatively relaxing nitrogen flow at fixed freestream conditions. (These conditions were chosen arbitrarily and do not represent those of the experiments in section 3 exactly.) The results are presented in figure 8. Figure 8(a) shows the frozen Mach number $M_f = V/a_f$, calculated at the translational shock (subscript s) and at the end of the relaxation zone, i.e. at the equilibrium composition (subscript e), plotted against the shock angle ϕ . As may be seen, the flow becomes sonic at the translational shock when $\phi = 67.6^\circ$ but becomes supersonic again within the relaxation zone for shock angles up to $\phi = 71.2^\circ$. At the former condition, $\delta(3) = 45^\circ$ and, at the latter, $\delta(1) = 56^\circ$, a change of 11° in the relevant wedge deflexion angle.

The corresponding distance to the sonic point, y_s , is shown in figure 8(b). The implication to the detachment process of the variation of y_s with ϕ is that signals from downstream of $y = y_s$ cannot reach the shock. It follows that the region of the flow field which is able to influence the flow near the tip of a wedge is the subsonic region of dimension y_s . The latter must therefore be the determining length scale for the stand-off distance Δ . As ϕ is increased through $\phi_s(3)$, observer (2) may therefore expect to see Δ increase smoothly like y_s . This behaviour is in agreement with that expected from the argument in the introduction and outlined in figure 5.

Figure 8(a) also shows the equilibrium Mach number $M_{eq} = V/a_{eq}$, where a_{eq} is the equilibrium speed of sound; a_{eq} is the speed at which disturbances of a wavelength much larger than l propagate and is smaller than the frozen speed of sound a_f , relevant for short wavelengths. Observer (1) cannot detect wavelengths shorter than l so that a_{eq} is the sound speed relevant to his observations. Both observers (3) and (2) must consider disturbances propagated at a_f , however, since they can resolve wavelengths shorter than l . The region downstream of the shock must therefore be considered to be

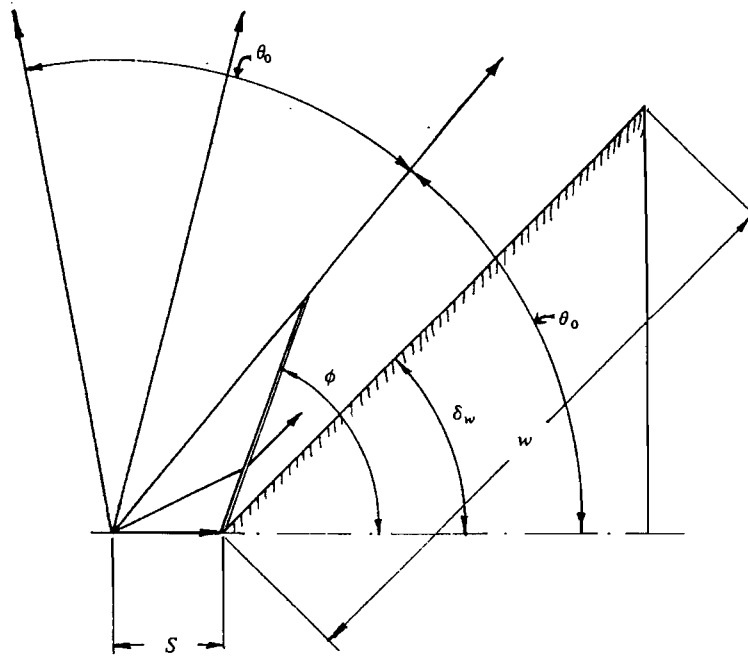


FIGURE 9. The source flow effect.

wholly subsonic above $\phi = 71.2^\circ$ in the example of figure 8, since we identify ourselves with observer (2).

2.3. Other length scales

Experience with the interpretation of interferograms of relaxing flows has shown that the presence of other length scales can produce phenomena which manifest themselves in a manner similar to relaxation. Care must therefore be taken to avoid such effects. To illustrate how they may come about in the flow over a wedge, two specific additional lengths are considered in detail. These are the transverse length of the wedge, L , and the distance to the source point in a divergent free stream, S . The latter is important if, as is often the case, a conical nozzle is used to generate the flow.

The presence of these two additional lengths would alter (9) to the form

$$\Delta/w = f'(\delta_w, l/w, S/w, L/w). \quad (10)$$

These additional two parameters could make interpretation of experimental results much more difficult, so that it is desirable to produce a situation with $L/w = S/w = \infty$. The manner in which these two parameters affect our experiment may best be studied by considering the extreme cases $L/w \rightarrow 0$ and $S/w \rightarrow 0$.

Take $S/w \rightarrow 0$ first. For simplicity let the source flow have plane symmetry and consider a wedge of large flank length w , placed with its tip a small distance S from the source (see figure 9). Within a distance from the tip which is small compared with S , the flow is like that for a parallel free stream, producing a shock at an angle ϕ , say. Assuming this shock to be straight (for simplicity) and proceeding along it away from the tip, the streamlines cross it at smaller and smaller angles, so that the shock becomes progressively weaker, until, at $\theta = \theta_0$, it ceases to deflect the streamline. The mass

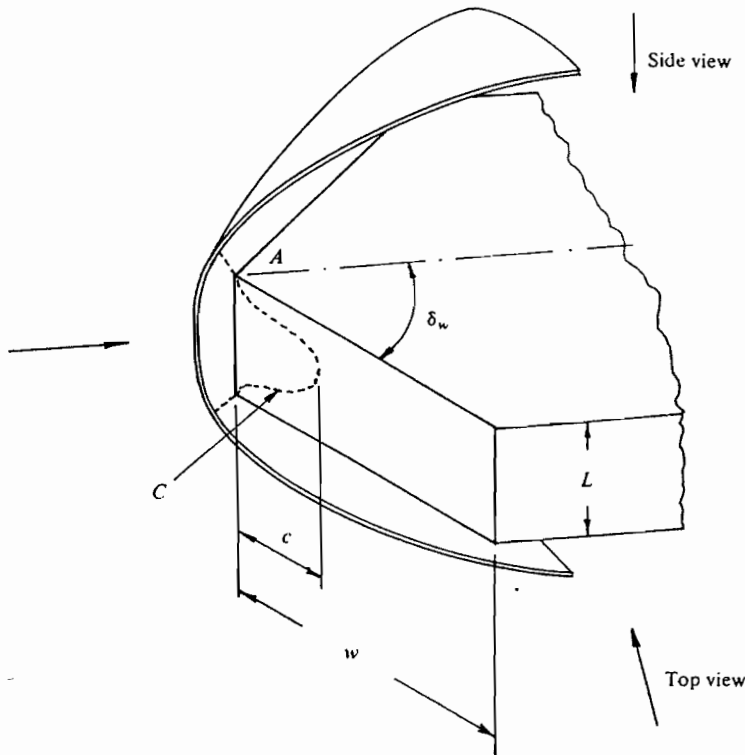


FIGURE 10. The effect of finite transverse length. Perspective view of model and cut-away shock.

flux between the wedge and $\theta = \theta_0$ is the same as that between $\theta = \theta_0$ and $\theta = 2\theta_0$, however the rate of increase of cross-sectional area in the latter sector is much larger. Consequently the pressure drops more quickly along the streamline in the sector $\theta_0 < \theta < 2\theta_0$ than near the wedge, and pressure-equalizing expansion waves cause the flow near the wedge to be accelerated. If the shock at the tip is detached, followed by subsonic flow, this acceleration can cause the flow to become supersonic before it encounters the trailing edge of the wedge. The sonic point may therefore reside on the face of the wedge rather than at the trailing edge. It is not necessary for the situation to be as extreme as that in figure 9 for the effect to be noticeable, as even a slight weakening of the shock at distances small compared with S can cause the necessary slight acceleration of the flow.

A similar effect may occur when the experiment is performed in an open jet. The wedge shock is reflected as an expansion wave from the edge of the jet. This expansion wave may impinge on the wedge face and cause the flow to be accelerated if the jet diameter, yet another length scale, is too small.

Finite L/w also causes the sonic line to move forward by a similar mechanism, with the accelerating expansion coming in from the side of the model. It may be illustrated by considering a wedge of finite width L in the extreme case $L/w \rightarrow 0$ when $\delta_w > \delta_M$, see figure 10. By considering the flow in the immediate vicinity of the tip, within a radius small compared with L , the shock is seen to be detached. However, when viewing the flow from the 'top', the symmetry plane containing the leading edge of the wedge

intersects the sonic surface in a line emanating from the end point A of the leading edge. The expansion propagating inwards from the sides accelerates the flow and causes the sonic surface to intersect the wedge face in a curve C , whose maximum extent c from the leading edge is smaller than w .

Other effects such as the displacement due to a viscous boundary layer can cause the wedge face to be effectively convex. This too would bring the sonic point closer to the leading edge.

The above discussion shows that many finite lengths, some of which are unavoidable in an experiment, produce effects similar to those of relaxation. It is therefore essential that any experiment examining the effect of relaxation must be complemented by a control experiment in which the relaxation effect is removed (e.g. by making $l/w \rightarrow \infty$) while the other finite length scales are retained.

3. Experiment

3.1. Facility, model and instrumentation

Much of the discussion in the preceding section about length scales other than l and w arose in the first place because a pilot experiment for this project had been performed in the small free-piston shock tunnel at A.N.U. (known as T2). In these experiments the nozzle was conical ($S/w \simeq 4$), the wedge face length was comparable to the free jet diameter, and the transverse length of the model was such that $L/w \simeq 1$. An asymmetric wedge was used, consisting of a flat plate whose incidence was adjusted to change δ_w . The experiment measured the stand-off distance as a function of δ_w for reacting nitrogen and carbon dioxide as well as perfect gas argon flows.

In view of the importance of L/w and S/w in this experiment, it is not surprising in hindsight that the results were inconclusive, inasmuch as the behaviour of Δ/w with δ_w had essentially the same features for the perfect gas argon flow as for the dissociating flows, all of which showed a gradual increase of Δ/w with δ_w .

In order to reduce the undesirable effects of finite L/w and S/w , the experiment was performed again in the large free-piston shock tunnel, T3 (see Hornung & Stalker 1978) with a contoured nozzle and also with a symmetrical wedge. This contoured nozzle was originally designed for use with air at a specific reservoir enthalpy of $3 \times 10^7 \text{ m}^2/\text{s}^2$ and a reservoir pressure of 200 atm. However, it also gives good quality parallel, uniform flows ($S/w = \infty$) with specific reservoir enthalpies in nitrogen of $2.2 \times 10^7 \text{ m}^2/\text{s}^2$, carbon dioxide of $1.6 \times 10^7 \text{ m}^2/\text{s}^2$ and argon of $2.5 \times 10^6 \text{ m}^2/\text{s}^2$. The former two gases are partially dissociated in the reservoir and recombine rapidly as they cool upon flowing through the throat, while their composition is frozen by the rapid drop in density through the nozzle flow. The effective specific heat ratios, and therefore the exit Mach numbers, are different for the two gases. At the low enthalpy chosen for the argon, it behaves like a perfect gas. Though the nominal exit Mach number is 16 for the argon flow, the displacement thickness of the nozzle wall boundary layer is quite large at this condition, so that the exit Mach number may be significantly reduced. The test section conditions for the three gases are obtained by numerical computation of the nozzle flow from the measured reservoir conditions and are given in table 1.

The new model consisted of two sharp wedges whose position and incidence could be

	Nitrogen	Carbon dioxide	Argon
Specific reservoir enthalpy (m^2/s^2)	2.2×10^7	1.6×10^7	0.25×10^7
Reservoir temperature (K)	9070	5750	5000
Reservoir pressure (atm)	180	180	180
Exit velocity (km/s)	5.5	4.1	2.2
Exit density (g/cm^3)	2.6×10^{-6}	4.6×10^{-6}	2.2×10^{-6}
Exit temperature (K)	1100	1960	57
Exit Mach number	7.5	6.0	16
Exit composition (mole/g)	N_2 0.0319 N 0.0077 $e^- < 10^{-6}$ $\text{N}^+ < 10^{-6}$	C $< 10^{-10}$ O 0.0044 CO_2 0.0074 O ₂ 0.0055 CO 0.0153	Ar 0.025

TABLE 1. Calculated tunnel conditions.

adjusted separately so that they could be arranged in the form of a single symmetrical wedge with variable δ_w by making their leading edges touch. Small nonuniformities in the leading edges caused a gap of no more than 0.2 mm width to appear between the leading edges. This was sealed from behind the wedges with a pliable vacuum-sealing compound. The width of the model was $L = 15.2$ cm and w was 5.1 cm giving $L/w = 3$. This is still quite finite and should ideally be much larger. However, at the chosen conditions the relaxation length is approximately 1–2 cm, and the exit diameter of the nozzle is 25 cm. In order to stay well clear of the edge of the free jet it is necessary to have L sufficiently small compared with 25 cm ($L = 15.2$ cm chosen). To produce a behaviour significantly different from the frozen flow of observer (3) it is desirable to make l comparable to w . This led to the compromise $w = 5.1$ cm, i.e. $l/w \doteq \frac{1}{3}$, $L/w = 3$.

The flow was investigated by Mach-Zehnder interferometry, the light source being an exploding wire. This produces a sufficiently short ($\sim 50 \mu\text{s}$) intense light pulse, bright enough to overcome the self-luminosity of the gas in the shock layer, which is also partially eliminated by a stop at the exit focus of the interferometer and by an interference filter passing wavelengths of 510 ± 5 nm. The main purpose of the filter is to facilitate quantitative interpretation of the interferograms.

3.2. Results

As an example of the experimental results obtained with a relaxing flow, a set of interferograms of dissociating carbon dioxide flow over the wedge is presented in figure 11. These show an attached shock in figure 11(a), and gradually increasing stand-off distance with increasing δ_w through to figure 11(e). Figure 11(a) shows a curved attached shock followed by strong relaxation as indicated by the decrease of fringe shift gradient with distance from the shock. The sharp rise in fringe shift at the wedge surface is due to the boundary layer and gives an indication of its thickness.

Two examples of detached shocks in argon are presented in figure 12. In these interferograms the trailing edge of the wedge is obscured by a support bracket on the side of the wedge which does not significantly affect the flow over the wedge. Notice the

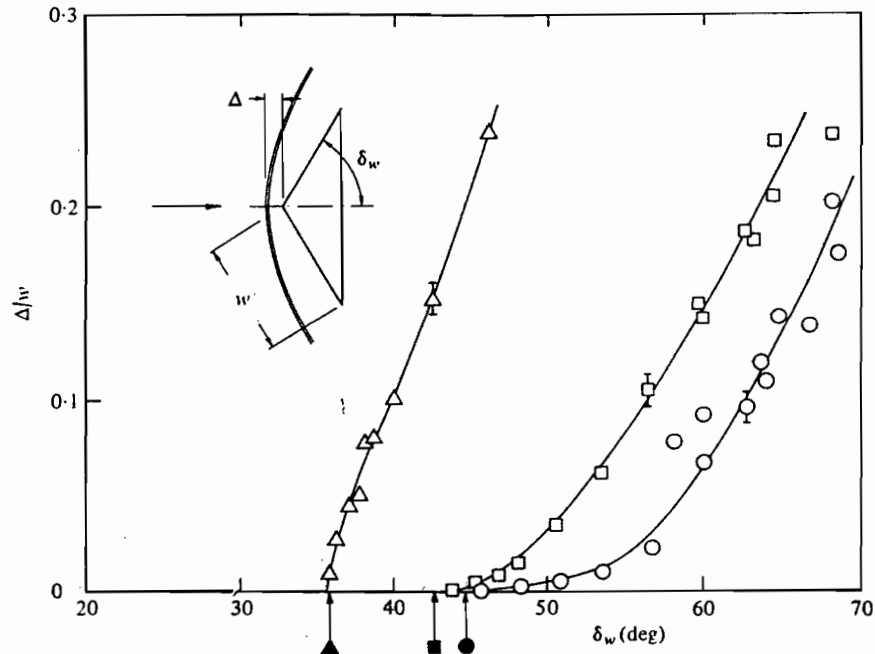


FIGURE 14. Measured stand-off distance for: Δ , the perfect gas argon; \square , dissociating nitrogen; \circ , dissociating carbon dioxide. For freestream conditions see table 1. The filled symbols indicate the calculated frozen detachment angle. The curves are mean lines through the experimental results.

more nearly constant fringe shift in the shock layer, indicating a more uniform density field. Also, the boundary layer on the wedge surface is noticeably thicker than in the carbon dioxide flows. Figure 12(a) shows a situation with δ_w barely above the incipient detachment angle and figure 12(b) shows a case with Δ so large that it can be appreciated that finite L/w and finite open jet diameter will affect the results.

Incipient detachment and a small Δ are shown for dissociating nitrogen flow in figures 13(a) and (b). Again a considerable change in δ_w is necessary to change Δ relatively slightly.

The features of the interferograms taken at the three conditions of table 1 are presented in figure 14, which is a graph of Δ/w against δ_w . Estimated error bars for the measurement of Δ are indicated on a few representative points, while the error in δ_w is smaller than the size of the symbols. There are a few points showing a significant discrepancy from the main trend in the carbon dioxide data, which we are unable to explain. The value of $\delta_M(3)$, the frozen detachment angle, as calculated from the free-stream conditions is also shown in figure 14, and may be seen to agree well with the observed incipient detachment point in all three cases.

It is shown in figure 14 that the trend at small values of Δ/w is as expected from the argument in the introduction. The relaxing flows give a very slow rise of Δ/w with increase of δ_w , whereas the perfect gas flow gives a rapid increase.

4. Discussion

The perfect gas detachment process has been examined by a number of authors whose results indicate that Δ/w increases gradually with δ_w even in the absence of relaxation. Guderley (1962) obtains this result on theoretical grounds; Frank (1972) from measurements in transonic flows; Zierep (1968) from similarity arguments; and Johnston (1953) from measurements at $M_\infty = 2.5$. The former three are concerned with the transonic situation in which the sonic and maximum deflexion points on the shock locus (S and M) are significantly separated. In Johnston's results the gradient $d\Delta/d\delta_w$ at incipient detachment is comparable with that of the present experiments at $\Delta/w \approx 0.1$ in argon. However, following the argument presented in the introduction, we observe that, in parallel, frozen flow with $L/w = \infty$, no length scale is available to the flow at the tip of the wedge until the flow becomes subsonic after the shock. At high Mach number, M and S effectively coincide, so that, at incipient detachment, the length scale governing the stand-off distance jumps from zero to w . It is probable that, in the absence of relaxation, any smoothing of the effect of this discontinuity in the length scale on the behaviour of Δ with δ_w occurs because of finite L/w . The importance of this effect may be expected to increase as Δ/L increases. It is supported by the argon curve in figure 14. A possible way of testing this explanation is to repeat the experiment in frozen flow with a smaller w . This would reduce the importance of L/w in the frozen case.

5. Conclusions

The discussion of relaxing flows in terms of the phenomena seen by observers with different smallest resolvable and largest viewable length scales has been shown to give correct predictions in the case of detachment of a shock from a wedge. The mapping of the flow into the speed-deflexion plane has been shown to be a useful tool for obtaining the principal features of relaxing gas flows. The determining length scale for the detachment distance is the distance to the sonic line which has been shown to grow with increasing shock angle, even for a straight shock. The detachment distance therefore grows gradually as the wedge angle is increased for relaxing gases and more steeply for a perfect gas. Both features have been confirmed by experiment. The effect of finite transverse extent of the wedge and of a divergent free stream have been discussed and shown to produce similar effects as those due to relaxation.

The facility used in this project was financially supported by the Australian Research Grants Committee. The project has benefited greatly from discussions with Professor E. Becker during his visit to A.N.U.

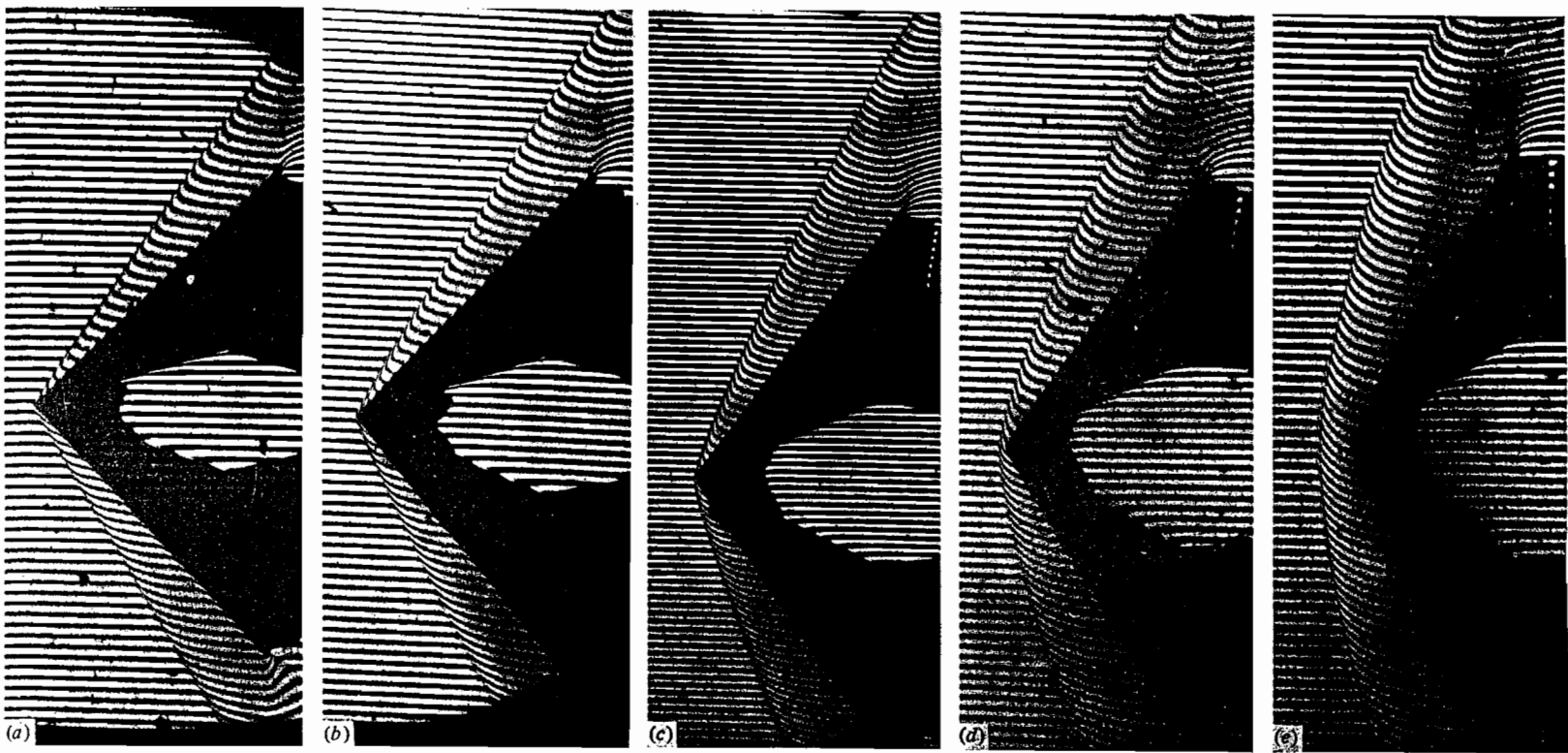


FIGURE 11. Interferograms of dissociating carbon dioxide flow over a wedge. (a)–(e) show progressively larger wedge angles with increasing detachment distance. For freestream conditions see table 1.

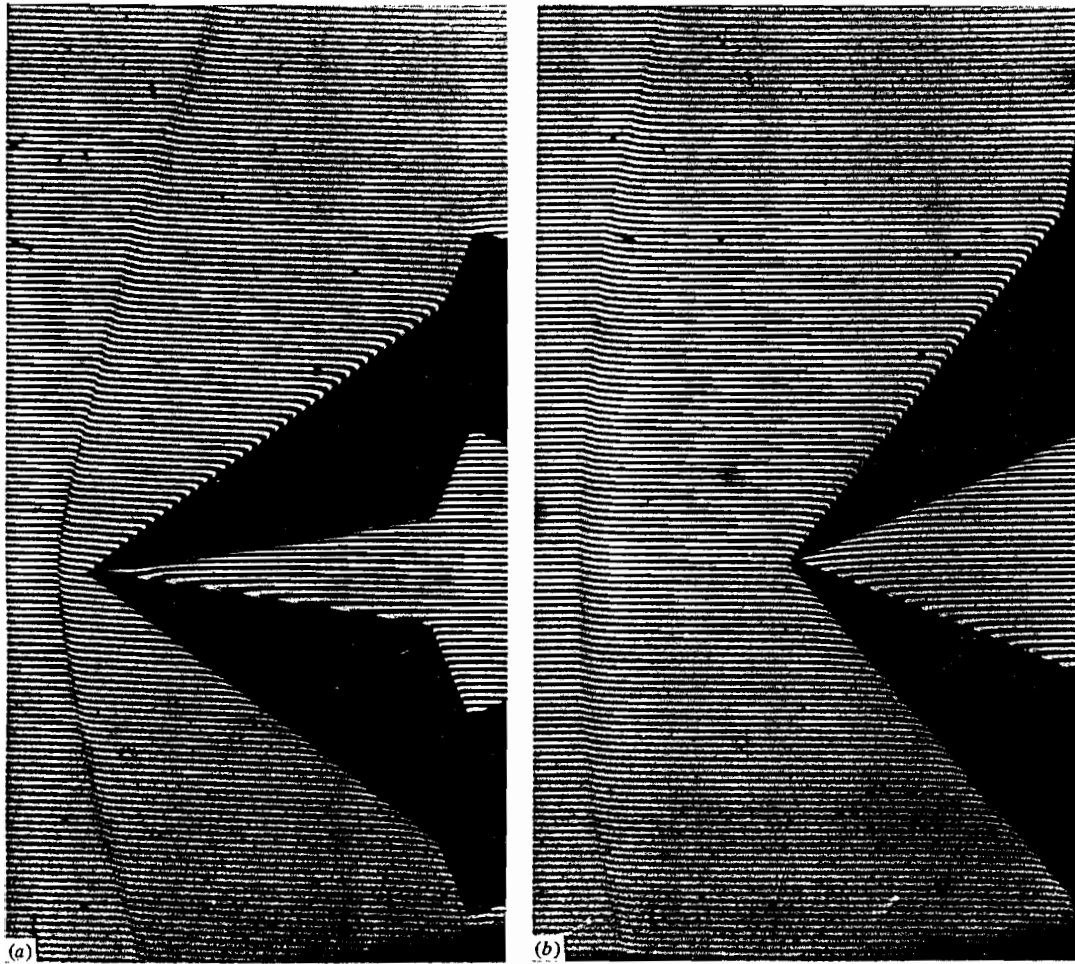


FIGURE 12. Interferograms of perfect gas flow (argon) over a wedge. (a) Just detached shock.
(b) Large stand-off distance. For freestream conditions see table 1.

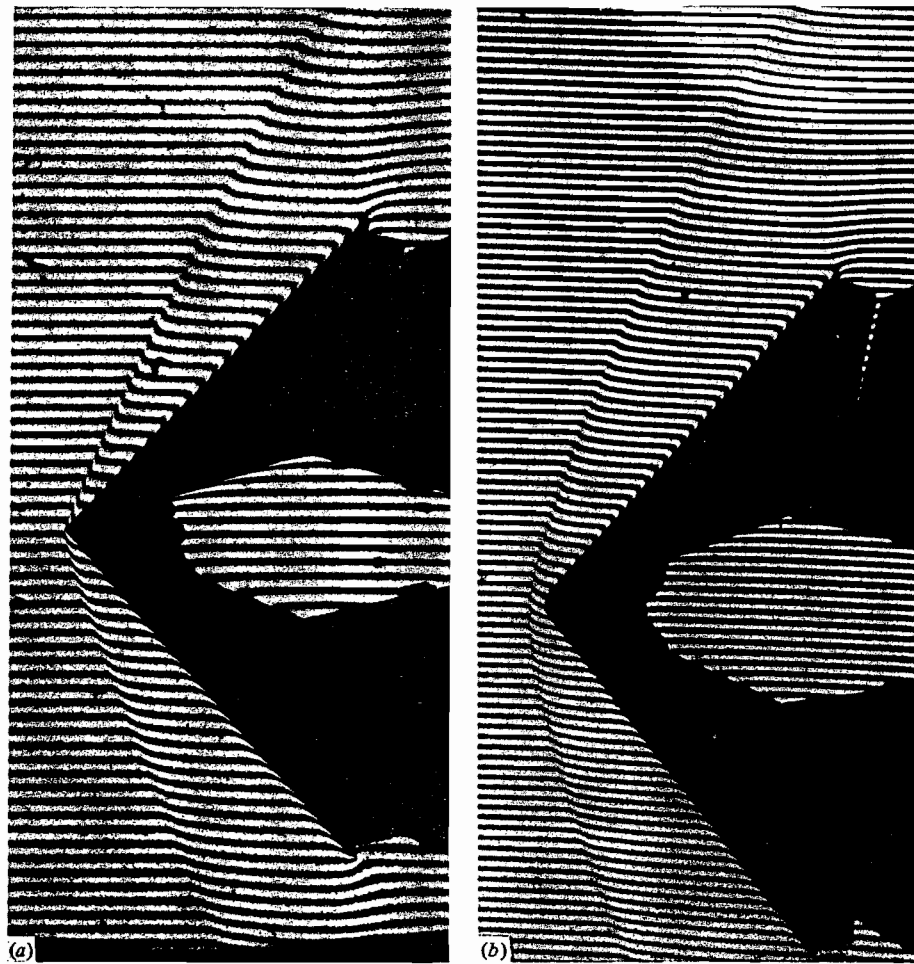


FIGURE 13. Interferograms of dissociating nitrogen flow over a wedge. (a) Curved attached shock. (b) Small stand-off distance. For freestream conditions see table 1.

REFERENCES

- CABANNES, H. 1960 In *Handbuch der Physik*, vol. 9, p. 162. Springer.
- FRANK, W. 1972 Dissertation, Karlsruhe.
- GUDERLEY, K. G. 1962 *Theory of Transonic Flow*. Pergamon.
- HORNUNG, H. G. 1977 *Proc. 6th Austral. Hydr. Fluid Mech. Conf. Adelaide*, pp. 217-220.
- HORNUNG, H. G. & STALKER, R. J. 1978 In *Applied Fluid Mechanics* (ed. H. Oertel), Karlsruhe University.
- JOHNSTON, G. W. 1953 *J. Aeron. Sci.* **20**, 378-382.
- ZIEREP, J. 1968 *Acta Mechanica* **5**, 204-208.

Shock detachment from cones in a relaxing gas

By H. G. HORNING† AND A. F. P. HOUWING

Department of Physics, Australian National University, Canberra, Australia

(Received 8 November 1979)

Measurements of the shock stand-off distance on cones of various base diameters in carbon dioxide and nitrogen flows with dissociative relaxation show that the detachment process occurs more gradually with relaxation than in a perfect gas, as the cone semi-angle is increased. This is in agreement with a prediction which is made on the basis of the behaviour of the sonic surface in the flow field. The phenomenon is similar to that observed previously with wedge flow but shows interesting effects peculiar to the cone flow. The cone experiments also eliminate the end effect and permit easy variation of the relaxation rate parameter without changing the gas. Perfect-gas argon experiments provide a convenient check.

1. Introduction

This paper is concerned with the inviscid, high-Mach-number flow of a relaxing gas over cones at zero incidence with semi-angles in the range around the value at which the shock wave detaches from the cone tip. The shock is taken to be partly dispersed, the situation of particular interest being that in which a translational-rotational subshock of unresolvably small thickness is followed by a region of vibrational and dissociative relaxation, the extent of which is characterized by a single relaxation length, l .

Whether an observer sees such a flow to be in thermodynamic equilibrium or not depends on the relative magnitudes of his smallest resolvable length scale λ , his largest viewable length Λ , and the relaxation length l . If he cannot resolve l , or if

an equilibrium ^{situation} exists, while, if $l < \lambda < \Lambda$, (1)

$$\lambda < l < \Lambda, \quad (2)$$

the relaxation is resolvable and must therefore be taken into account. At the other extreme, when

$$\lambda < \Lambda \ll l, \quad (3)$$

a 'frozen' situation exists. The gas may be considered to be in a constrained state of equilibrium, which differs from the unconstrained equilibrium state indicated by (1). Hence the equation of state is different for case (3) than for case (1). Since the conditions after a plane oblique shock are determined from the free-stream conditions by the conservation and state equations, they will be different for (1) and (3), and, in case (2) the conditions after the translational shock are as for (3) while they asymptotically approach those specified by (1) further from the shock.

The conditions achievable from a free-stream state, A , by a plane, oblique shock may be conveniently presented in the speed-deflexion (V - δ) plane, see figure 1. The two

† Present address: DFVLR-AVA, 34 Göttingen, Bunsenstr. 10, W. Germany.

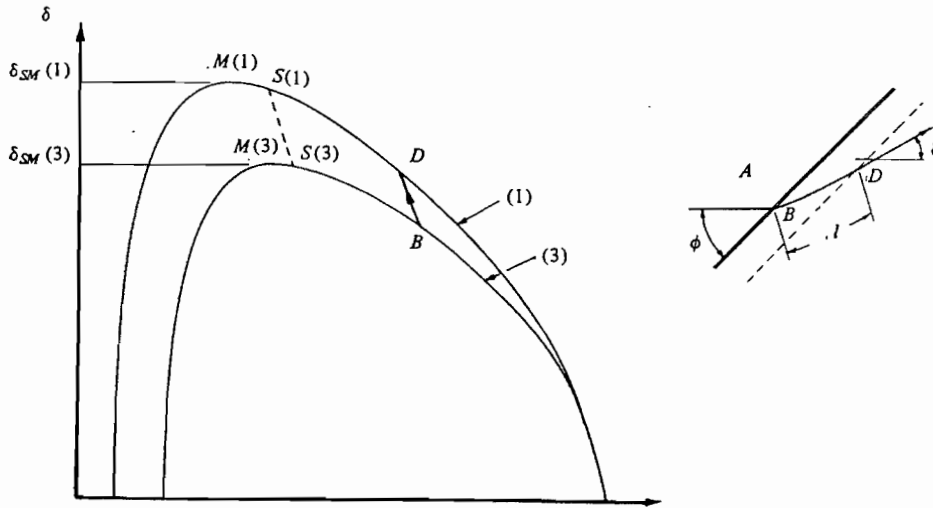


FIGURE 1. Shock loci in the speed-deflexion plane for equilibrium (1) and frozen (3) flow.
 - - - -, sonic line relative to frozen speed of sound.

curves represent the loci of conditions after the shock as observed in cases (1) and (3) respectively as the shock strength is increased from zero at point A . The maximum deflexion points $M(3)$ and $M(1)$ represent the largest angles of a wedge at which an attached shock can be observed in the respective situations. For high free-stream Mach number, the point $S(3)$ at which the flow is sonic (flow speed = frozen speed of sound) at the sub-shock practically coincides with $M(3)$.

By considering the flow over a wedge of angle δ_w such that

$$\delta_{SM}(3) < \delta_w < \delta_{SM}(1), \quad (4)$$

Hornung & Smith (1979) showed that, in this range, the shock stand-off distance, Δ , is $O(l)$, and that Δ increases more gradually with relaxation than for a perfect gas. They related this behaviour to the phenomenon that, as ϕ is increased beyond a certain value, a subsonic layer starts to grow from the subshock into the relaxation layer while the flow further downstream is still supersonic. Their experiments with dissociating nitrogen and carbon dioxide flows substantiated these predictions and were given additional weight by being contrasted with a perfect-gas argon experiment.

One of the weaknesses of wedge flow experiments is that the transverse length of the wedge is finite. The end effects influence results in a similar way as relaxation does, and a null-experiment with a perfect gas becomes essential. One of the motivations for repeating the experiments with cones was that the end effect is automatically removed in axisymmetric flow. The relative ease of making cones also allows the important parameter l/d to be varied without changing the gas by making cones of different base diameter, d .

2. Relaxing cone flow

2.1. Weak and strong relaxation

The flow over cones is more complex than wedge flow, as the condition at the body, characterized for example by the cone semi-angle δ_C , is not the same as that at the

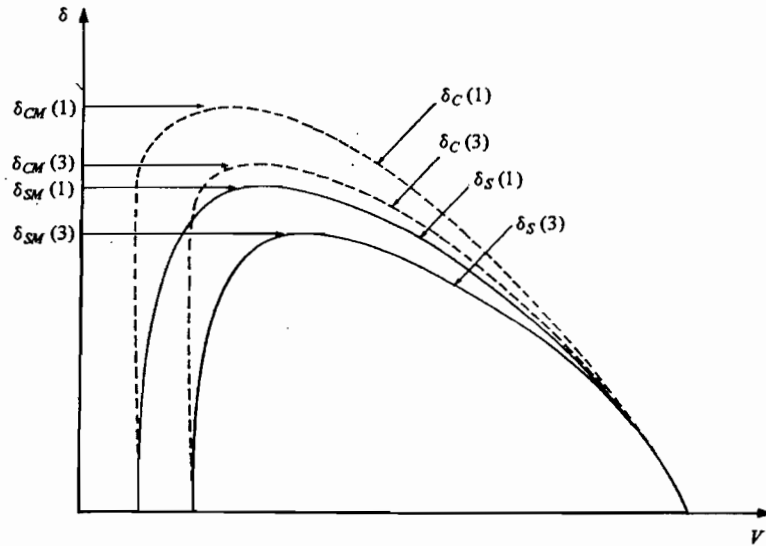


FIGURE 2. Shock and body loci for frozen (3) and equilibrium (1) cone flow in the case of weak relaxation, $\delta_{SM}(1) < \delta_{CM}(3)$.

shock, δ_S , even in equilibrium or frozen flow. The conditions at the body map into a body locus in the V - δ plane, the shock detachment condition being given by

$$\delta_C = \delta_{CM}, \quad (5)$$

where δ_{CM} is the extreme value of δ_C . Again, the body locus for the frozen situation (3) is different from that for the equilibrium situation (1), as is the case for the shock locus. One may now distinguish between two cases according to the relative magnitude of the extreme deflexion angles at the shock and cone in the frozen and equilibrium situations. We denote by 'strong' and 'weak' relaxation the cases when $\delta_{SM}(1)$ is greater or less than $\delta_{CM}(3)$ respectively. The V - δ map of the case of weak relaxation is shown in figure 2.

This is the case relevant to the present discussion and, indeed, strong relaxation may be expected to be quite rare in a laboratory environment. This can be demonstrated by the following simple estimate. Numerical solutions of the equations of perfect gas cone flow give δ_{CM} as a function of γ , the ratio of specific heats. The values of δ_{CM} and the corresponding maximum deflexion at the shock are shown in figure 3 for infinite free-stream Mach number. Taking the case of a free stream of diatomic molecules, $\gamma = 1.4$, and figure 3 gives $\delta_{CM}(3) \simeq 57^\circ$. The curve for δ_{SM} has this value at $\gamma = 1.18$. For $\delta_{CM}(3) = \delta_{SM}(1)$, the internal degrees of freedom of the equilibrium flow would have to use up enough energy to make the effective ratio of specific heats equal to 1.18, corresponding to a hypersonic density ratio across the shock of 12.1. While this is possible in free flight, it is unusual in wind-tunnel experiments, because freezing of the internal degrees of freedom in the nozzle flow invariably causes the free stream to remain partially dissociated. In the free-piston shock tunnel a density ratio of 12 in nitrogen has only been achieved across a normal shock. In the following, we shall therefore restrict discussion to the case of weak relaxation.

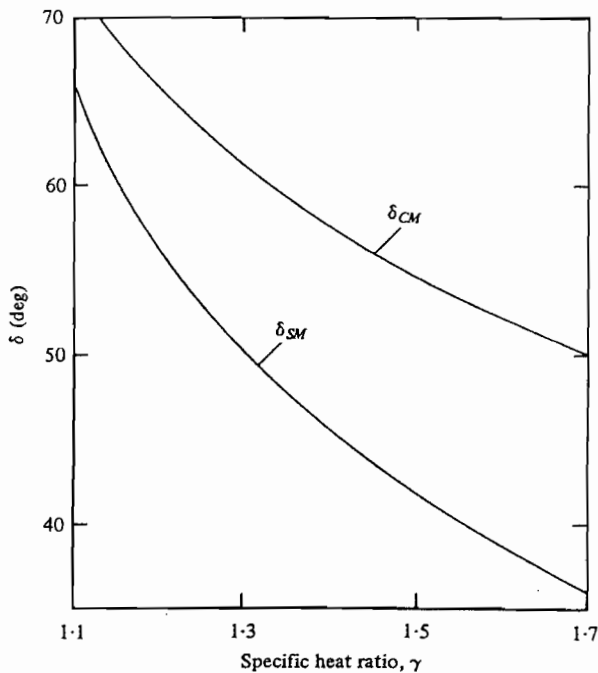


FIGURE 3. Calculated maximum deflection angles at the shock and at the cone in perfect-gas flow at infinite free-stream Mach number.

2.2. The V - δ map of cone flow with an attached shock

When the cone angle is sufficiently small, the shock is attached to the cone tip and the flow is everywhere supersonic. Within a distance $\Lambda(3)$ of the cone tip, such that $\Lambda(3) \ll l$, the frozen conditions apply. Consider first the streamline that passes through the shock very close to the tip. It suffers an initial discontinuous deflexion to $\delta_S(3)$ at the shock, followed by a further deflexion asymptotically approaching the cone semi-angle δ_C . During this second continuous deflexion the velocity decreases along the streamline according to a relation $\delta(V)$ which can be determined from numerical solutions of frozen cone flow. Since $\Lambda(3) \ll l$, no appreciable relaxation takes place along this streamline until it has reached the cone semi-angle δ_C on the body locus $\delta_C(3)$. The subsequent relaxation along this streamline occurs at constant deflexion and is accompanied by an increase in velocity, so that the conditions on it finally approach a point close to $\delta_C = \delta_C(1)$ in the V - δ plane. This streamline is shown in figure 4(b) in the physical plane as BC , and its corresponding V - δ map is $BB'C$ in figure 4(a). Note that the point B in the physical plane maps into the line BB' in the V - δ plane.

The streamline that passes through the shock at a distance from the tip much larger than the relaxation length, l , must approach the point $\delta_C = \delta_C(1)$ eventually. It is shown as DEF in figure 4(b). The distance measured along this streamline to the point where the flow deflexion approaches the body deflexion δ_C is large compared with l . The deflexion of the streamline due to relaxation is therefore completed before any significant turning due to the cone flow occurs. The V - δ map of this equilibrium streamline is also shown in figure 4(a). Clearly, the curves BB' and EF represent the frozen and equilibrium cone flow solutions respectively for a cone of semiangle δ_C .

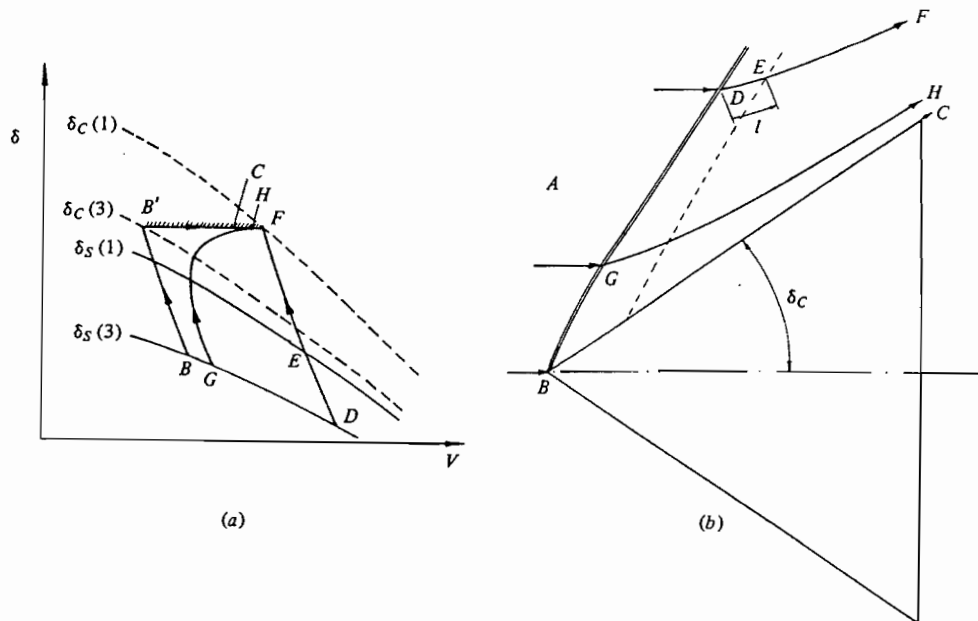


FIGURE 4. Relaxing flow over a cone with attached shock and supersonic conditions throughout. (a) V - δ plane; (b) physical plane.

The V - δ map now shows that the translational subshock must be curved between B and D . Since the body loci $\delta_C(3)$, $\delta_C(1)$ as well as the equilibrium shock locus $\delta_S(1)$ only apply for straight shocks, they can only be used for the frozen and equilibrium extremes in the cone flow. However, the qualitative behaviour of the V - δ map of a streamline through a curved shock has been determined by Hornung (1977) for the plane case, and the results may be easily extended to axisymmetric flows. Applied to the present problem they yield the qualitative shape of the V - δ map of the general streamline BH shown in figure 4. Note, that the intersections of this streamline with the lines $\delta_S(1)$ and $\delta_C(3)$ have lost their significance because the shock radius of curvature at G is neither very large nor very small compared with l . The separation of the asymptotic points C and F in the V - δ plane also arises from the fact that the shock angles at B and D are not the same so that, though the asymptotic pressures at C and F are the same, the streamline near the body has a higher entropy and therefore a lower velocity.

2.3. The sonic line

Since we have only considered the supersonic problem so far, the size of the cone was not important. As the cone semiangle δ_C is increased, however, the flow becomes locally subsonic. The existence of subsonic regions provides the mechanism by which the detachment process derives its length scale either from the relaxation length or from the size of the cone. The latter may conveniently be specified by the base diameter, d .

Consider first the case of perfect-gas (frozen) flow. The equations of cone flow admit conical solutions in which both subsonic and supersonic regions occur, the conical sonic surface separating a subsonic region near the body from a supersonic one near the shock. If the cone is finite, this provides a path by which the trailing edge of the cone

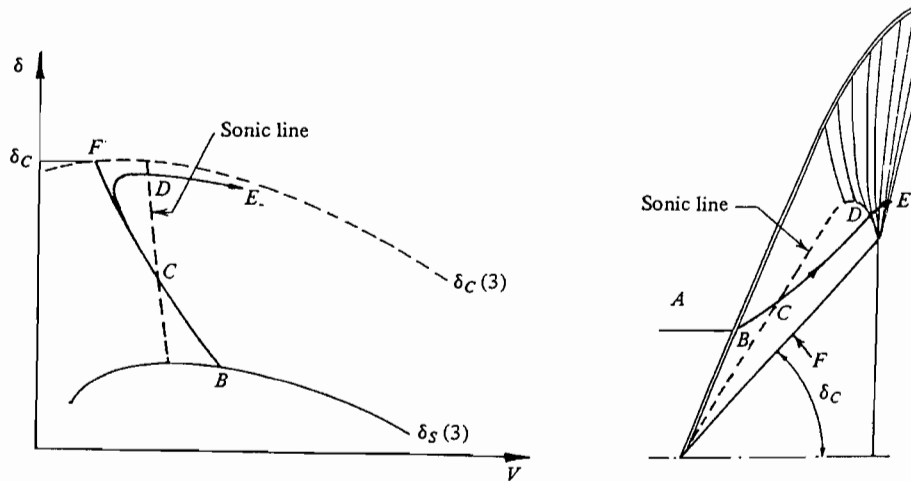


FIGURE 5. Mixed (supersonic and subsonic) cone flow of a perfect gas.

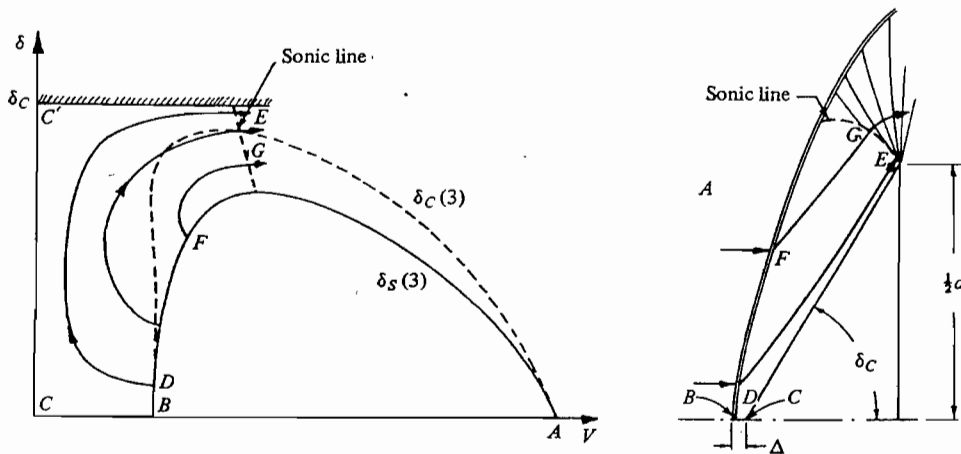


FIGURE 6. Detached shock in perfect-gas flow over a cone.

can influence the flow near the tip. However, it appears that, at least for a small range of angles, this is not enough to cause the shock to be influenced (see Solomon 1955). The sonic line has to meet the trailing edge where the flow is accelerated by the corner. The mixed case for perfect gas flow over a finite cone with its V - δ map is shown schematically in figure 5.

The cone angle for maximum deflexion is somewhat larger than that for a sonic shock. Thus when the cone semiangle has reached $\delta_{CM}(3)$ conditions behind the shock are already subsonic. The trailing edge of the cone, and therefore the length scale d , can influence the shock, so that the shock is curved. For cone angles larger than $\delta_{CM}(3)$ the shock detaches. The detachment distance, Δ , increases approximately linearly with $\delta_C - \delta_{CM}(3)$ (see Ward & Pugh 1968). The detached flow and its V - δ map are shown in figure 6. Clearly, the body locus in the V - δ plane no longer has any significance in this case because the shock is curved. Similarly, the shape of the sonic line in the V - δ plane depends on the shock shape in the physical plane, though its end point on the shock is fixed.

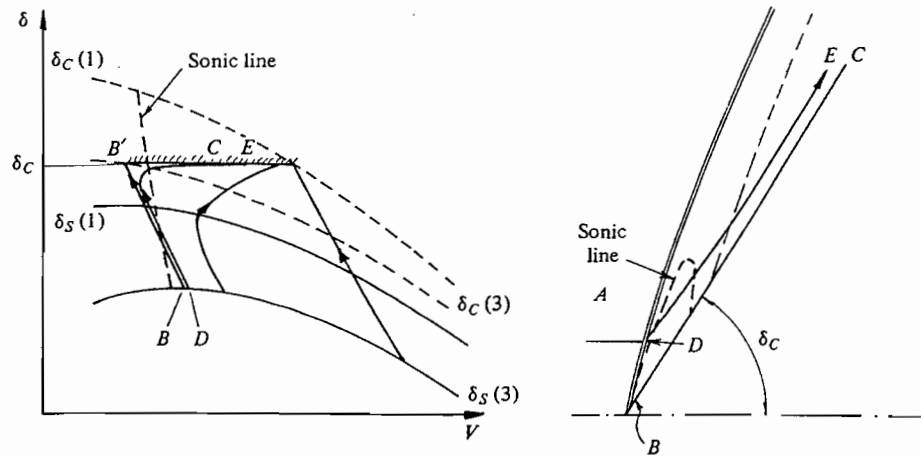


FIGURE 7. Relaxing cone flow. Attached shock, subsonic region embedded in relaxation region.

Now introduce relaxation and, for simplicity, take the case $d \gg l$ first. Consider the attached shock of figure 4 and let δ_C be increased, so that the 'quadrilateral' enclosing the flow field in the V - δ plane slides up and to the left, its corners being constrained to lie on $\delta_C(1)$, $\delta_C(3)$ and $\delta_S(3)$. As δ_C is increased, there comes a point at which B' crosses the sonic line. However, the Mach number on the streamlines entering the subsonic region is increased again by the relaxation, so that the complete flow picture is as shown in figure 7.

As δ_C is increased to a point where $\delta_C > \delta_{CM}(3)$, the frozen shock detaches, but the detachment distance remains so small that it cannot be resolved by an observer for whom the inequalities (1) apply. This is consistent with the form of the corresponding V - δ map of the flow, see figure 8. It shows that the extent of the subsonic region from which the detachment distance derives its scale is less than the relaxation length l .

Further increase of δ_C causes the extent of the subsonic region to increase further, until it exceeds the relaxation length. This occurs when $\delta_C \simeq \delta_{CM}(1)$. Thereafter the point where the sonic line meets the body lies at the trailing edge of the cone, and the flow picture is qualitatively very similar to that of figure 6. The length scale governing Δ is then the cone size d . The shock stand-off distance Δ may be expected to increase more slowly with δ_C when $\delta_{CM}(3) < \delta_C < \delta_{CM}(1)$ than when $\delta_C > \delta_{CM}(1)$, since the length scale governing Δ is l in the former range while it is d in the latter.

Now let $d \simeq l$. Consider the case $\delta_{CM}(3) < \delta_C < \delta_{CM}(1)$. The subsonic region may now be terminated by the expansion around the trailing edge and not by the relaxation. The governing length scale for the detachment distance is then d , so that one may expect only a slight departure from the frozen flow behaviour. If $d \ll l$, figure 6 applies, and Δ is always governed by d . The expected behaviour of Δ/d with δ_C can now be sketched for different values of l/d , see figure 9. This diagram incorporates the linear behaviour of Δ/d with δ_C observed by Ward & Pugh (1968) in the frozen case and assumes that it also occurs at equilibrium. Ward & Pugh's measurements resolve δ_C more finely in the immediate vicinity of detachment than the otherwise more extensive measurements of Emunds (1976).

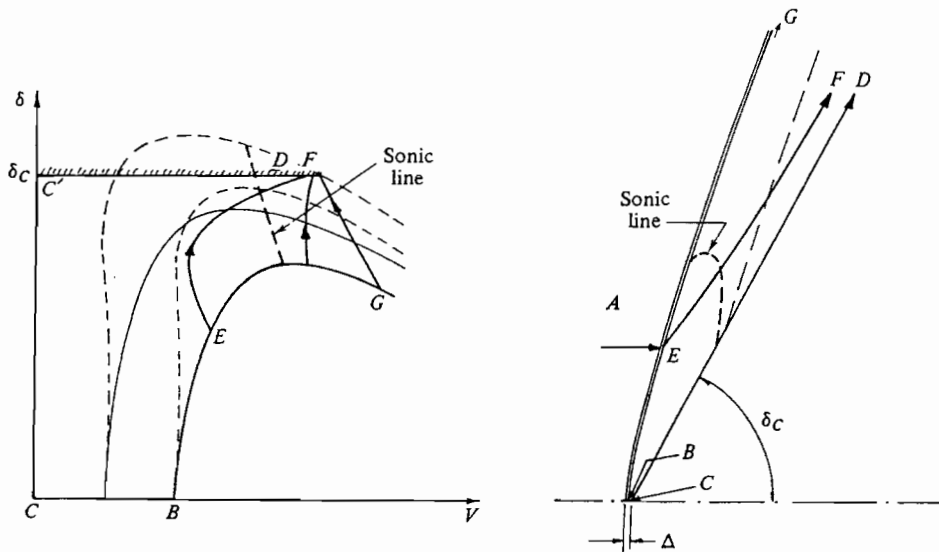


FIGURE 8. Relaxing cone flow. Detached shock, stand-off distance controlled by relaxation length. $\delta_{CM}(3) < \delta_c < \delta_{CM}(1)$. Subsonic region has reached shock.

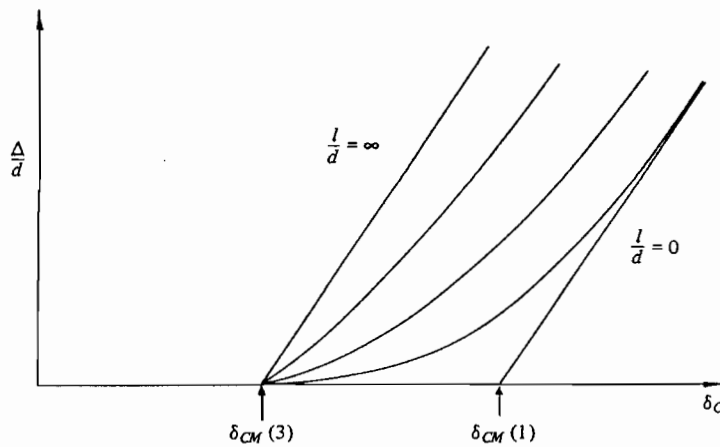


FIGURE 9. Expected behaviour of shock stand-off distance for cones of different sizes relative to the relaxation length.

3. Experiment

3.1. Facility and free-stream conditions

The large free-piston shock tunnel was used for all the experiments in the same configuration as in the wedge flow experiments of Hornung & Smith (1979). Mach-Zehnder interferograms were taken of dissociating nitrogen and carbon dioxide flows, and of perfect-gas argon flows. The free-stream conditions of the contoured nozzle flow, calculated numerically from measured reservoir conditions, are given in table 1. The free-stream density in the carbon dioxide and nitrogen flows was increased by a factor of 1.7 over those of the wedge flow experiments in order to reduce the viscous length scale. This has the consequence that the gas composition is slightly changed in favour of the molecular constituents.

	Nitrogen	Carbon dioxide	Argon
Velocity (km s ⁻¹)	5.2	4.0	2.2
Mach number	7.8	5.9	16
Density (g cm ⁻³)	4.3 × 10 ⁻⁶	7.8 × 10 ⁻⁶	2.2 × 10 ⁻⁶
Temperature (K)	1040	1900	57
Composition (mole g ⁻¹)	N ₂ 3.37 × 10 ⁻² N 4.0 × 10 ⁻³	CO ₂ 9.1 × 10 ⁻³ CO 1.34 × 10 ⁻² O ₂ 6.2 × 10 ⁻³ O 1.0 × 10 ⁻³	Ar 0.025

TABLE 1. Free-stream conditions.

3.2. Range of parameters

For each of the experimental conditions in table 1, a relation of the form implied by figure 9,

$$\Delta/d = f(l/d, \delta_C) \quad (6)$$

exists for inviscid flow. In the experiment, however, the Reynolds number is finite and is likely to affect the experiment in the case of the smallest cones ($d = 1$ cm), so that the boundary-layer thickness has to be estimated. The case of most interest in the present context is that of incipient detachment of the shock when the Mach number outside the boundary layer, but behind the attached shock, is approximately 1, and conditions outside the boundary layer are uniform. For the small cones, the flow may be assumed to be frozen throughout for the purposes of estimating the boundary-layer displacement thickness, δ^* . For the case of an insulated wall (giving an overestimate of δ^*) the results of van Driest (1952) may be used to obtain

$$\frac{\delta^*}{L} \approx \frac{2}{\sqrt{Re}} \quad (7)$$

for a flat plate at zero incidence, at sonic conditions outside the boundary layer, for a Prandtl number of 0.75 and a specific heat ratio of 1.4. Though the last two conditions are not exactly satisfied in our experiments, δ^* is not sufficiently sensitive to these parameters to cause concern in our crude estimation. Applying a Mangler transformation to this result to account for the axial symmetry (see, for example, Walz 1966, p. 174), yields

$$\frac{\delta^*}{L} \approx \frac{2}{\sqrt{3}\sqrt{Re}} \quad (8)$$

In (7) and (8) L is the length of the generator of the cone, δ^* is the displacement thickness at the trailing edge of the cone, and Re is the Reynolds number outside the boundary layer, based on L .

In both of the dissociating gases the temperature after a frozen shock of 60° incidence to the free stream is approximately 10000 K. Since the wall temperature remains at 300 K during the short test time, the effect of heat transfer to the wall must be considered. This may be estimated by assuming the Prandtl and Lewis numbers to be unity and using equation (8.3.3) of Hayes & Probstein (1959) in a linear velocity

	Nitrogen	Carbon dioxide	Argon
Reynolds number			
$L = 1$ cm	5 000	5 000	1 500
$L = 10$ cm	50 000	50 000	15 000
Displacement thickness (cm)			
$L = 1$ cm	0.005	0.005	0.007
$L = 10$ cm	0.01	0.01	0.02
Relaxation length l (cm)	1.2	0.4	∞

TABLE 2. Range of boundary-layer displacement thickness at incipient detachment.

profile. In this manner, the effect of wall cooling may be shown to reduce δ^* by a factor of 4. The viscosity may be estimated from data given by Dorrance (1962) to be $(3 \pm 1) \times 10^{-3} \text{ g cm}^{-1} \text{ s}^{-1}$ for nitrogen at 10 000 K and is assumed to be the same for the carbon-dioxide flow, which consists in a large part of CO. The resulting values of the Reynolds number and estimates of displacement thickness are given in table 2. Clearly, δ^* is near or below the resolution limit. This is in agreement with observation (see, for example, figure 12*d*, near trailing edge).

In the present experiments the parameter l/d was varied both by changing l and by varying the model size d . The dissociation rate is very sensitive to temperature and varies approximately linearly with the density. For a given set of free-stream conditions, the relaxation length is therefore sensitive to the shock angle. Since the range of shock angles of interest to the detachment problem lies in a narrow range around incipient detachment, l may be considered to be constant for each gas. Calculated values of the relaxation length after a normal shock (to where the density change due to relaxation reaches 95% of its maximum value) are given in the last row of table 2. However, changing l by changing the gas changes the functional form of equation (6) (for example, it changes the values of $\delta_{CM}(1)$ and $\delta_{CM}(3)$) so that this does not help in examining the detailed behaviour predicted by figure 9. It is more profitable to change d . For this purpose a large number of cones was made with a range of semi-angles δ_C and with $d = 7.5, 3$ and 1 cm. A few very large ($d = 15$ cm) and very small ($d = 0.5$ cm) cones were also made, but the limits of the facility size and resolution in interferometry caused results obtained with those to be only of restricted value.

4. Results and discussion

The results of the argon experiments are presented in figure 10. These were all obtained on cones with $d = 3$ cm. The error bars on the measurement of Δ represent approximately ± 0.15 mm. Though the photographs permit considerably better resolution, the relatively low density of the argon flow causes the shock in the interferograms to be poorly defined. The behaviour of Δ/d with δ_C can be seen to follow approximately that observed by Ward & Pugh (1968), though there appears to be a slight departure from linearity of the curve in our experiment. As can be seen, the results also agree with the calculated value of δ_{CM} , within the error, though they indicate a slightly higher value.

The results obtained in nitrogen with cones of $d = 1, 3$ and 7.5 cm are shown in figure 11. It is clear that the error bars on Δ/d , particularly for the small cones, is too large to be able to separate the curve obtained for $d = 7.5$ cm from that for $d = 1$ cm

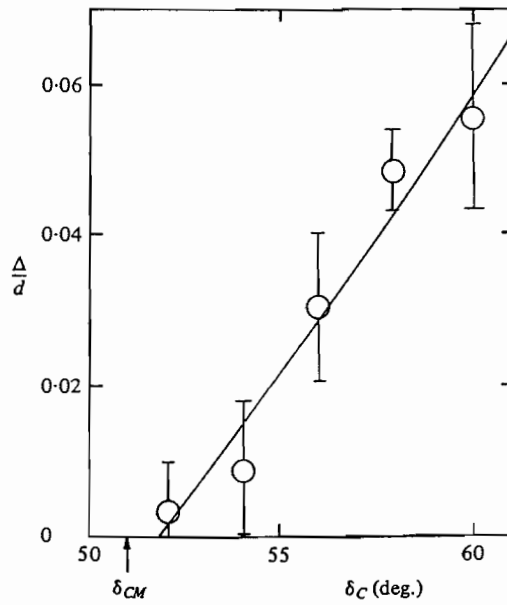


FIGURE 10. Results of perfect-gas argon experiments, $d = 3$ cm. The arrow shows the calculated value of δ_{CM} .

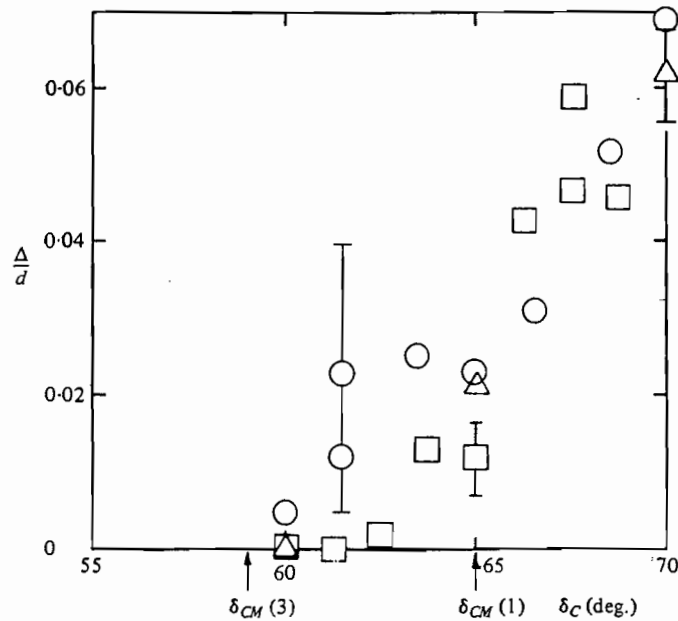


FIGURE 11. Results of dissociating nitrogen experiments. \circ , $d = 1$ cm; \triangle , $d = 3$ cm; \square , $d = 7.5$ cm. The effect of model size is barely significant in view of the measurement errors. Arrows show calculated angles.

with any significance above $\delta_C = 64^\circ$, and it is barely possible to detect the trend predicted by figure 9 below this angle. The calculated values of $\delta_{CM}(1)$ and $\delta_{CM}(3)$ are again shown by arrows.

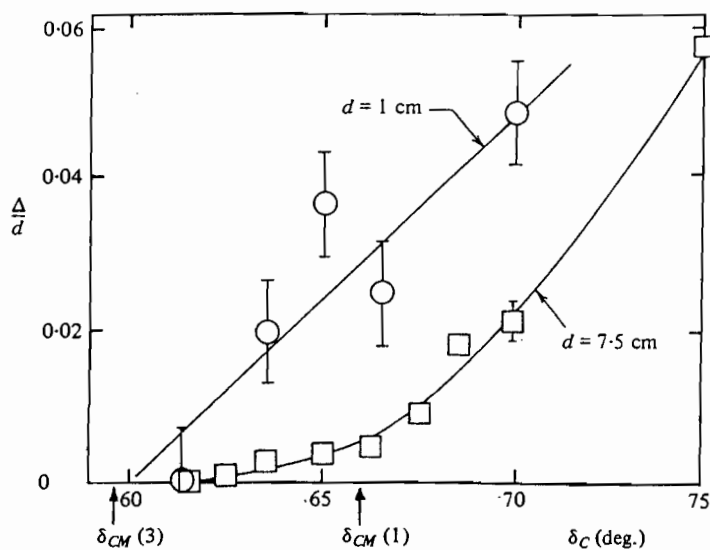


FIGURE 13. Results of dissociating carbon dioxide flows.
 \circ , $d = 1$ cm; \square , $d = 7.5$ cm.

The higher density and refractive index of the gas in the carbon dioxide flow makes it possible to resolve the shock much more sharply. With care in the adjustment of the interferometer it was even possible to see the shock on cones with $d = 0.5$ cm provided that it was detached. Examples of the interferograms taken in carbon dioxide flows are shown in figure 12 (plate 1).

The results obtained with carbon dioxide are shown in figure 13, in which the points for $d = 1$ cm and $d = 7.5$ cm only have been selected. Here, the separation of the two curves is clearly in the same direction as that in figure 9 and the qualitative behaviour is generally as predicted. The points for $d = 3$ cm fall between the two curves. It can be seen from figure 13 that the position of the two curves in relation to the two arrows ($\delta_{CM}(1)$ and $\delta_{CM}(3)$) is closer to the equilibrium side than in the case of nitrogen (see figure 11). This is as it should be in view of the difference in the relaxation lengths. For example, the case $d = 3$ cm in nitrogen gives the same l/d as the case $d = 1$ cm in carbon dioxide. This is part of the reason for the small separation of the curves in figure 11.

5. Conclusions

Experiments to examine shock detachment in relaxing flow with wedge models had the unavoidable problem that end effects are difficult to separate from relaxation effects. The present experiments were successful in eliminating this difficulty by performing the experiments with cones. The results clearly show that the effect, observed by Hornung & Smith (1979) on wedges, that shock detachment occurs more gradually in a relaxing gas than in equilibrium or frozen flow, is also observed in cone flow.

Considerations of a map of the flow into the speed-deflexion plane again allow the effect to be predicted. However, this mapping is considerably more complex in cone flow, because the conditions after a conical shock are not uniform even in frozen or



(a) $\delta_C = 65^\circ$; (b) $d = 7.5$ cm, $\delta_C = 68.8^\circ$; (c) $d = 7.5$ cm, $\delta_C = 68.5^\circ$; (d) $d = 1$ cm, $\delta_C = 70^\circ$.

equilibrium flow. The speed-deflexion plane map gives a good explanation of the qualitative behaviour of the sonic surface in the flow field as the cone semi-angle is increased.

The experiments were performed with sets of cones of various base diameters, thus varying the parameter l/d without changing the gas. Though the predicted effect was clearly observed in carbon dioxide flows, the limits of resolution of optical interferometry caused the results obtained in nitrogen to be barely significant. As a check, a perfect-gas argon experiment showed the effect to be absent in frozen flow.

The facility used in this project received support from the Australian Research Grants Committee.

REFERENCES

- DORRANCE, W. H. 1962 *Viscous Hypersonic Flow*. McGraw-Hill.
EMUNDS, H. 1976 *Deutsche Luft- und Raumfahrt*, DLR-FB 76-26.
HAYES, W. D. & PROBSTEIN, R. F. 1959 *Hypersonic Flow Theory*. Academic.
HORNUNG, H. G. & SMITH, G. H. 1979 *J. Fluid Mech.* **93**, 225.
HORNUNG, H. G. 1977 *Proc. 6th Austral. Hydr. Fluid Mech. Conf. Adelaide*, p. 217.
SOLOMON, G. E. 1955 *N.A.C.A. Rep.* 1242.
VAN DRIEST, E. R. 1952 *N.A.C.A. Tech. Note* 2597.
WALZ, A. 1966 *Strömungs- und Temperaturgrenzschichten*. Braun.
WARD, L. C. & PUGH, P. G. 1968 *A.I.A.A. J.* **6**, 2018.

Shock Detachment Process in Hypervelocity Flow over a Cone

I.A. Leyva, H.G. Hornung

Graduate Aeronautical Laboratories, California Institute of Technology, Pasadena, CA 91125, USA

Abstract: A comprehensive experimental and computational study of the shock detachment process in hypervelocity flow over cones is presented. The experiments are carried out in the T5 hypervelocity shock tunnel. The computations are mostly done with a code for axisymmetric thermo-chemical nonequilibrium flow. The data obtained confirm a previous theoretical model that predicts lower growth rate of the detachment distance with increasing cone half-angle for nonequilibrium flows than for frozen and equilibrium flows. The lower growth rate is related to the behavior of the sonic line in relaxing flows. The growth of the subsonic region is studied in detail from attached to detached conditions. A comparison between measured and computed interferograms is also made. Measured and computed heat flux distributions are compared, and differences between flows with attached and detached shocks are discussed.

Key words: Shock detachment, Hypervelocity flow, High enthalpy, Nonequilibrium cone flows

1. Introduction

The flow over cones at hypervelocity conditions is one of the most sensitive flows to thermo-chemical nonequilibrium. For certain combinations of free-stream conditions and cone half-angles, the shock can be detached if the flow is frozen but attached if the flow is in equilibrium. The rate of increase of the detachment distance with cone half-angle is strongly affected by the relaxation rate. Features of special interest are the conditions for incipient shock detachment, the important parameters of the body geometry and free-stream conditions that determine the detachment process, and the effect of shock detachment on heat loads and surface pressure. This knowledge can be applied to the design of inlets or any other sharp large-half-angle conical structure in a hypersonic vehicle.

The objective of the present study is to explain the effects of nonequilibrium on the shock detachment distance and its growth rate with increasing cone half-angle in hypervelocity flows. This work extends the

study by Hornung and Houwing (1980) which showed that the growth rate of the detachment distance with increasing cone half angle is smaller for nonequilibrium than for frozen or equilibrium flows, and related this effect to the behavior of the sonic surface. The results were, however, only marginally conclusive because of the relatively large measurement uncertainties. With a greater range of free-stream conditions, coupled numerical investigation, higher resolution interferograms, and heat flux and surface pressure measurements, the present study has been able to yield conclusive results.

2. Experiments

About 170 shots have been performed in the T5 hypervelocity shock tunnel at Caltech, which is described in Hornung (1992). A total of 24 stainless steel cones have been tested, ranging in base diameter d from 2 cm to 16 cm and cone half-angles from 55° to 75° . Figure 1 shows a schematic diagram of a model in the test section of T5. The variable d_{ep} is the distance from the tip of the cone to the nozzle exit plane during the test time.

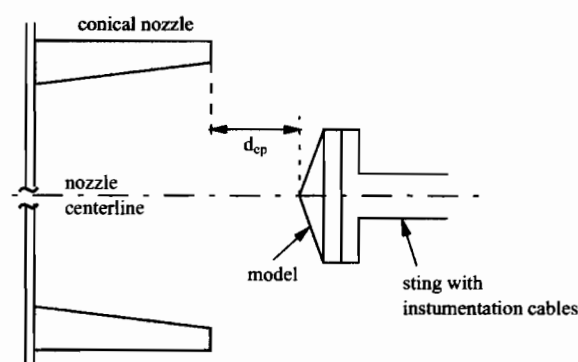
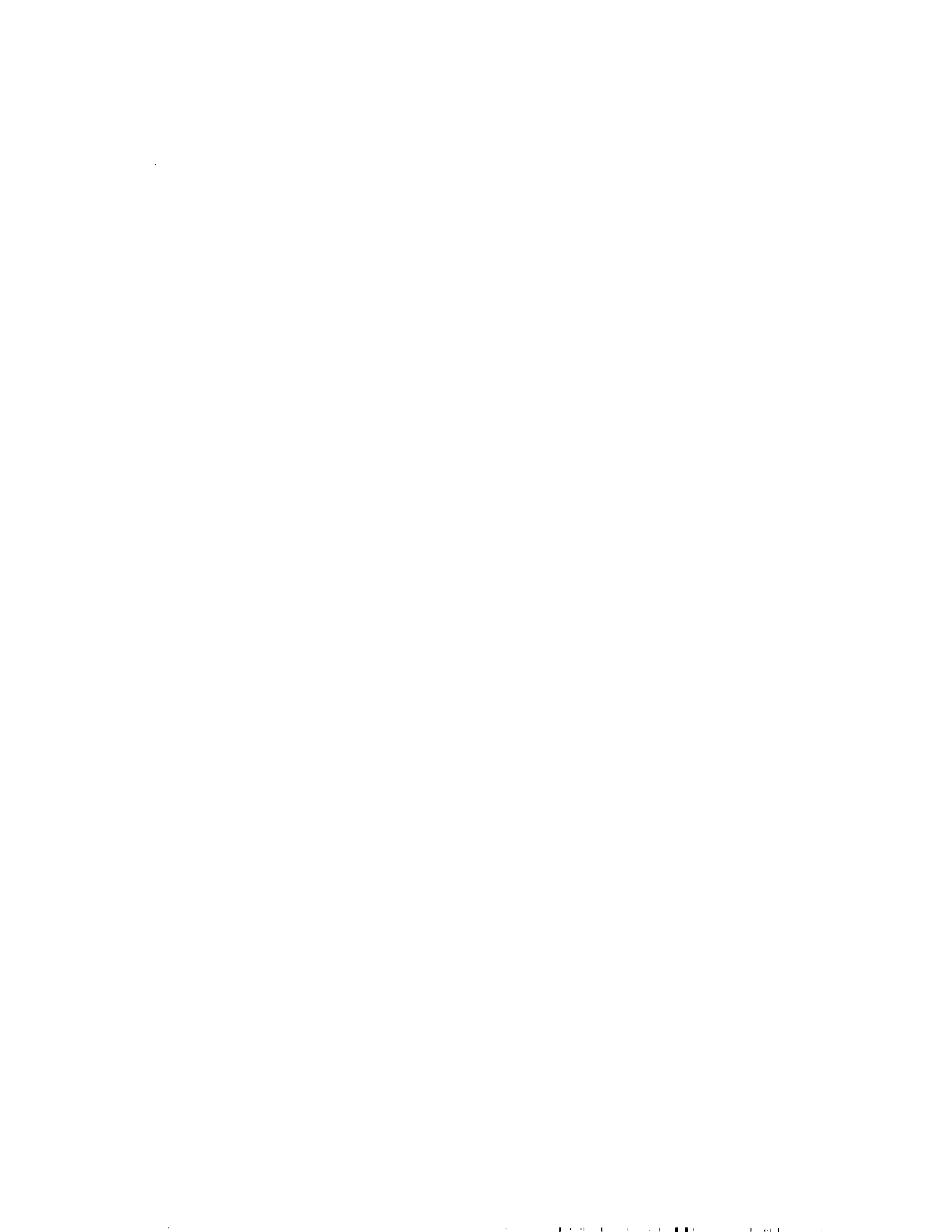


Figure 1. Schematic diagram of model in test section of T5.

The cones with $d = 8$ cm and $d = 16$ cm are instrumented with coaxial thermocouples and the largest cones also have recessed pressure transducers. Flow visualization by holographic interferometry gives quantitative field information and, in particular, the detach-



ment distance. Each cone is tested in six free-stream conditions (see tables 1 and 2) which span the available ranges of stagnation pressure and enthalpy of T5. The values of h_o and P_o represent the mean and standard deviation calculated from all the shots obtained for a given free-stream condition. All the shots are performed using a 7° half-angle conical nozzle.

Table 1. Free-stream conditions used.

Condition	N ₂ 1	N ₂ 2	N ₂ 3
h_o (MJ/kg)	18.2 ± 0.7	10.3 ± 0.9	16.3 ± 1.1
P_o (MPa)	53.6 ± 1.5	53.9 ± 2.8	20.3 ± 1.3

Table 2. Free-stream conditions used. (Cont'd.)

Condition	N ₂ 4	CO ₂ 2	CO ₂ 3
h_o (MJ/kg)	$9.20 \pm .38$	6.62 ± 0.39	$9.13 \pm .46$
P_o (MPa)	28.2 ± 1.5	24.5 ± 1.2	64.7 ± 1.8

3. Computations

The reservoir conditions in T5 are calculated using the computational tool STANJAN, see Reynolds (1986). For N₂ flows, the conical conditions at the nozzle exit are computed using the code SURF, see Rein (1989), for the conditions just downstream of the throat, and a modified version of the code by Olejniczak (1997) for the nozzle exit results. For CO₂ flows, the quasi-one-dimensional code NENZF, see Lordi et al. (1966), is used to calculate the nozzle exit conditions.

The main numerical code used to simulate cone flows was originally written by Candler (1988) and improved by Olejniczak (1997). It uses a finite-volume approximation to solve either the Navier–Stokes equations or the Euler equations for 2-D or axisymmetric flows with thermo-chemical nonequilibrium. The code can also be used for frozen flows. For the spatial differencing it uses a flux-splitting method, see Candler and MacCormack (1991), based on the Steger and Warming approach. The code marches in time using the implicit and iterative Gauss–Seidel line relaxation method. For this study, the vibrational modes are modeled as harmonic oscillators and the Park model is used for the vibration–dissociation coupling. The dissociation rates for N₂ are taken from Park (1985) and those for CO₂ flows are taken from Park et al. (1994). Almost all the grids for cones with $d=8$ cm or smaller have 100×200 cell points. The grids for the biggest cones have 200×200 points.

In a few cases, the computational system Amrita, see Quirk (1998), is also used to compute inviscid, frozen flows. This system provides the advantage of adaptive mesh refinement. For the cases run here, a

flux-limited, operator split, Roe solver is used. The grids used have 120×200 cells, and two tiers of refinement by a factor of 3 are applied, giving an effective grid resolution of 1080×1800 .

4. Theoretical considerations

On the basis of a simple scaling argument, Hornung and Houwing (1980) are able to deduce that the detachment distance Δ is scaled by the cone diameter (for a given free-stream condition and cone half-angle) for frozen and equilibrium flows. Nonequilibrium flows introduce a new length scale, the relaxation length l , which in this case is taken as an overall characteristic length for the vibrational and chemical relaxation processes. In the range of cone angles between the frozen and the equilibrium detachment angle, the detachment distance Δ is scaled by the relaxation length l . The ratio l/d is zero for equilibrium flows and infinite for frozen flows. The growth rate is expected to be smaller when the detachment distance is controlled by l than when it is controlled by d . This is related to the difference in the growth rate of the subsonic region inside and outside the relaxation zone. Hornung and Smith (1979) show that, within the relaxation zone, the frozen speed of sound decreases more rapidly than the flow speed with distance along a streamline. This means that, in this range of angles, a subsonic region is embedded in the relaxation zone, and the extent of this subsonic zone scales the detachment distance. The rate at which the detachment distance grows with angle in this range is therefore determined by the relaxation process.

5. Results and discussion

5.1. Sonic line from attached to detached conditions in frozen flows

If we start with a given free-stream condition and cone diameter, as we increase the cone half-angle, the flow will be supersonic throughout the shock layer up to a certain critical angle. A subsonic region then starts to grow from the cone surface and from near the cone tip. With further angle increase, the subsonic region grows toward the cone corner and toward the shock. Figure 2 left shows a numerical simulation of frozen flow with an attached shock and mixed supersonic–subsonic conditions. This simulation was performed with Amrita. The white line represents the sonic line. In order for the shock to detach, the sonic line has to reach the corner of the cone at its downstream end and the shock along its upstream face like in figure 2 right. It is then that the size of the cone can be communicated back to the tip of the cone and the detachment distance is scaled by d , as argued by Hornung and Houwing (1980). In these computa-



tions, it was found that the transition from attached to detached conditions is not abrupt. For the case studied here it took about 2.5° for the shock to detach after the sonic line had met the two conditions mentioned above.

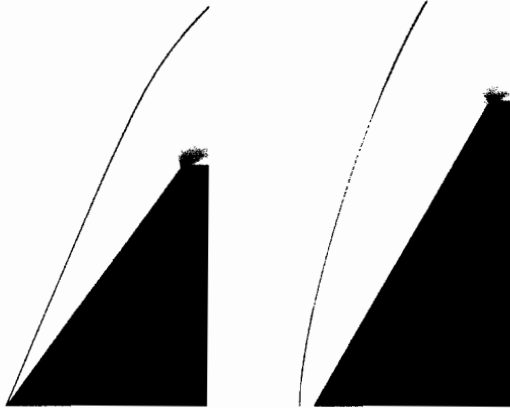


Figure 2. Left: Frozen flow with attached shock and mixed supersonic-subsonic conditions: $\theta = 53.8^\circ$ $M = 5.89$ $\gamma = 1.4$. Right: Frozen flow with detached shock. The sonic line has reached the corner of the cone on the downstream end and the shock in the upstream face: $\theta = 60.0^\circ$ $M = 5.89$ $\gamma = 1.4$

5.2. Experimental and computed interferograms

Figures 3 and 4 present a comparison between an experimental and a computed interferogram. Notice that the fringe distribution in the experimental interferogram is asymmetric, with more dark fringes on the upper side. This asymmetry was a recurrent feature in those experimental interferograms for which the infinite-fringe condition was not achieved, so that fringes were evident in the free stream. Without taking into account the free-stream fringes, the computed interferograms show symmetric flow fields, as one would expect, since both the free stream and the cone flow are symmetric about the same axis. When the free-stream fringe distribution is taken into account in the computed interferogram, see figure 4, the flow field becomes asymmetric and the agreement in the number of fringes is also improved.

5.3. Dependence of detachment distance on relaxation rate

For given free-stream conditions, the relaxation length is approximately constant for the range of angles considered here. Thus, one way to vary the ratio l/d is by varying the diameter of the cone. Changing the cone diameter can make the flow go from near the frozen limit to near the equilibrium limit. Figure 5 shows a compilation of the normalized detachment distance for the free-stream condition N_2 4 and four cone

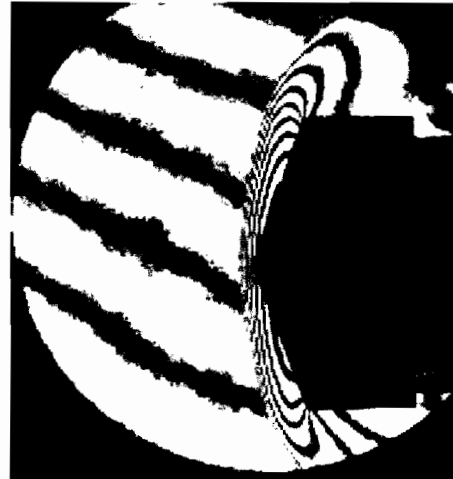


Figure 3. Experimental interferogram for condition N_2 2: $\theta = 70^\circ$ $d = 4$ cm.

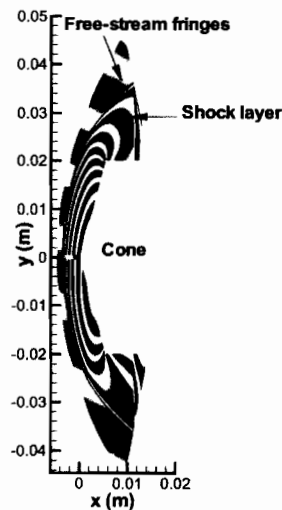


Figure 4. Computational interferogram for condition N_2 2: $\theta = 70^\circ$ $d = 4$ cm.

diameters. The results are plotted against the cone half-angle θ . The only data available for the frozen and equilibrium limits come from numerical simulations. The data labeled "f" are obtained from the code by Olejniczak (1997) run in its frozen inviscid mode. The data "f a" are also for the frozen limit but obtained with the Roe code under Amrita. The discrepancy between the two data sets is attributed to the uncertainty in the value of the effective γ for the free-stream condition. Both data sets are well fitted by straight lines confirming the experimental data of Ward and Pugh (1968). The data set "e" is obtained from numerical calculations for the equilibrium limit obtained with the code by Olejniczak (1997) by adjusting the reaction and relaxation rates appropri-

ately. The good linear fit to the frozen and equilibrium results confirm the features expected from the theory of Hornung and Houwing (1980). The points θ_f and θ_e are the critical detachment angles for frozen and equilibrium flow, respectively. The difference between these values increases with the fraction of the total energy of the flow that is absorbed by the relaxation, and therefore also increases with reservoir enthalpy. The curve "2cm" shows the experimen-

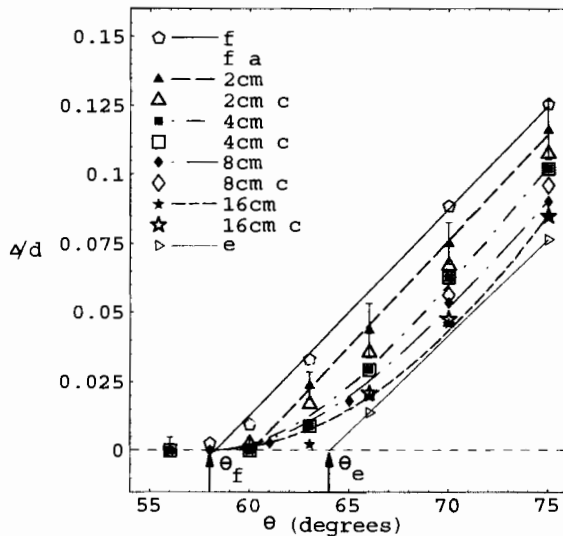


Figure 5. Non-dimensional detachment distance for condition N_2 4. The filled symbols indicate experimental results. The straight lines are linear fits to the numerical data "f", "fa", and "e", and to the experimental data set "2cm". The rest of the curves are cubic fits to the experimental data presented to aid the eye. The letter "c" at the end stands for computations.

tal data obtained for the smallest diameter cones. As expected, this data set is closest to the frozen limit. In fact, this flow is almost frozen as revealed by the linear behavior of the curve and by the fact that the linear fit is good nearly all the way to incipient detachment. As the cone diameter increases, the curves shift toward the equilibrium limit. Notice that the dimensionless detachment distance grows more slowly for the relaxing flows than for the frozen and equilibrium flows as expected. Also note that all the curves start to detach from the same point (θ_f) as predicted by Hornung and Houwing (1980). The error bars represent the uncertainty in reading the detachment distance off the interferograms and the effect of the uncertainties in the free-stream on the detachment distance. For most of the N_2 conditions studied here, the discrepancy in Δ/d between experimental and numerical data is between 6 and 10%, with the computational data falling fairly consistently below the experimental

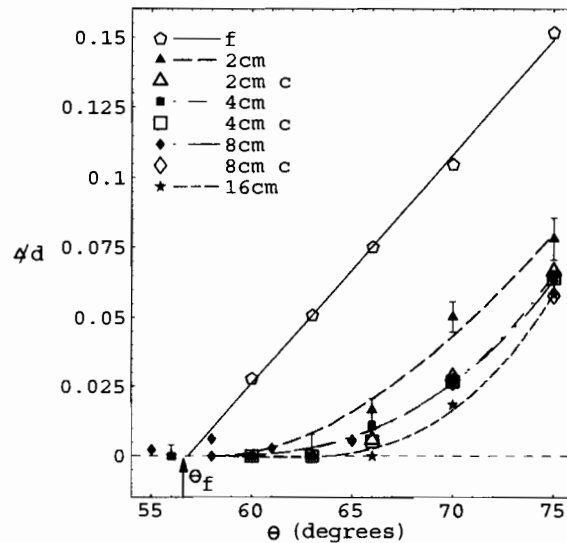


Figure 6. Non-dimensional detachment distance for condition CO_2 2. The filled symbols indicate experimental results. The straight line is a linear fit to the numerical data "f" while the rest of the curves are cubic fits to the experimental data presented to aid the eye. The letter "c" at the end stands for computations.

values, however, the difference is too small to attach significance to it. Figure 6 is an example of the results obtained for CO_2 flows. The frozen data are again well fitted by a straight line as expected since the linear behavior is independent of the gas used. Notice how all the curves are closer to the equilibrium limit than for the N_2 example. Also note the larger separation between θ_f and θ_e . This is to be expected since the separation depends on the amount of energy absorbed by relaxation, which is greater for the CO_2 flows treated here than for the N_2 flows. The numerical simulations for CO_2 were not as successful as those for N_2 . A more detailed model for the different vibrational modes in CO_2 is needed along with more accurate reaction rates and a nozzle code to take into account the conical nature of the free-stream flow.

5.4. Normalized detachment distance from the frozen to equilibrium limits

In this section, we try to collapse the normalized detachment distance obtained for different N_2 conditions, from the frozen to the equilibrium limits, for a given cone half-angle. Using the ideas of Wen and Hornung (1995), who studied nonequilibrium flow over spheres, we now scale the dimensionless detachment distance by the density ratio across the frozen normal shock:

$$\Delta_m \equiv \frac{\Delta}{d} \frac{\rho_s}{\rho_\infty}, \quad (1)$$



where the subscript s denotes conditions immediately after the shock and ρ_∞ is the free-stream density. We plot this variable against the reaction rate parameter Ω which quantifies the rate of energy absorption by relaxation. In this sense it is similar to the ratio l/d used previously. For N_2 flows Ω reduces to

$$\Omega \sim \frac{\rho_s d \left(\frac{\partial h}{\partial \alpha} \frac{d\alpha}{dt} \right)_s}{\rho_\infty u_\infty^3}, \quad (2)$$

where α is the mass fraction of atomic nitrogen (N), h is the specific enthalpy, and u_∞ is the free-stream speed. This expression is evaluated assuming nitrogen to be well approximated by the ideal dissociating gas model. The results are presented in figure 7. In this case, $\Omega = 0$ represents the frozen limit and $\Omega = \infty$ represents the equilibrium limit. The different curves obtained for the same condition are the results of using different baseline diameters to numerically reach the frozen and the equilibrium limits as explained in Leyva (1999). If this flow followed binary scaling, as expected since the ratio of the dissociation to the recombination reaction rates varies from 500-5000 for the cases studied here, all the curves for a given condition would collapse into a single curve. We would have three curves instead of four. The differences between

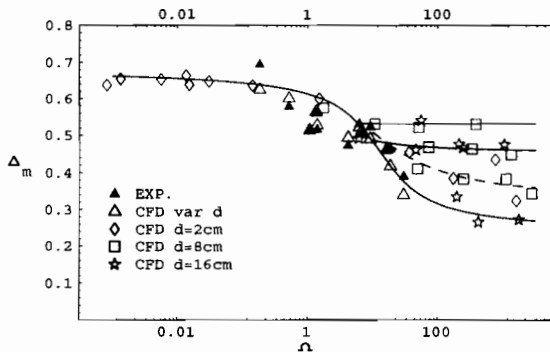


Figure 7. Modified non-dimensional detachment distance from frozen to equilibrium limits. The red color corresponds to condition N_2 3, green to condition N_2 4, and blue to condition N_2 2. The curves shown are fits of the form $y = A + B \arctan(cx + d)$ for the numerical data. For all of these cases the cone half-angle is 75°

the data sets for different diameters for a particular condition, as the equilibrium limit is approached, can be explained in terms of the experimental error, except for the difference between the curve “CFD $d=16\text{cm}$ ” and the curve for “CFD $d=8\text{cm}$ ” and “CFD $d=2\text{cm}$ ” for condition N_2 3. This difference is most probably due to vibrational non-equilibrium which is ignored while deriving the significant scaling parameters for binary scaling. We do observe, however, a collapse of the curves for different conditions in the frozen limit. Also observe that the detachment distance changes

most rapidly for the range of cone diameters used in this study. This dramatic change means that we have captured the most sensitive regime for the effects of nonequilibrium on the detachment distance. The offset along the Ω -axis, in the fast-changing region, from one condition to another can be accounted for in terms of the error in Ω which is about 80%. Finally, the difference between the frozen and the equilibrium plateaus for each condition is proportional to the stagnation enthalpy of the condition as mentioned before.

5.5. Dimensionless heat flux and pressure distributions

Heat flux measurement are made to determine whether the heat flux is a sensitive indicator of shock detachment. The results are also compared with results from computations using the code by Olejniczak (1997) in its viscous mode. To non-dimensionalize the results, we form the Stanton number St , and the Reynolds number Re_x ,

$$St = \frac{\dot{q}}{\rho_\infty u_\infty h_o}, \quad (3)$$

$$Re_x = \frac{\rho_{eq} u_{eq} x}{\mu_{eq}}, \quad (4)$$

where \dot{q} is the dimensional heat flux, μ is the viscosity of the flow, and the subscript “eq” denotes properties evaluated in the stagnation streamline after the shock when the vibrational and translational temperature are in equilibrium. Figure 8 is a logarithmic plot of typical results obtained for a given N_2 condition for different cone diameters. The CFD data are fitted to straight lines in their linear part in the low Re limit. For attached shocks the slope of this line should be $-1/2$, following the formula,

$$St = \frac{A}{\sqrt{Re}}, \quad (5)$$

which applies for attached shocks, see Leyva (1999). In this case the slopes are 0.48 and 0.47 for the CFD data, even though equation 5 does not strictly apply anymore. If the heat flux were sensitive to the chemistry, we would see the effects in this graph, where the cone diameter changes by a factor of four. What we have instead are very similar curves in terms of the slope in the low Re limit and their general shape. The corner of the cone manifests itself in two ways, the most evident one is the heat flux peak near the corner. This peak is due to the thinning of the boundary layer as it approaches the expansion around the corner. The more subtle one is the “peel-off” of each curve from the linear behavior. As the size of the cone increases, the range of Re covered by the cone is larger and the heat flux follows the linear part of the curve longer before “feeling” the effects of the corner. Therefore,



the heat flux measured close to the end of the cone (before the corner peak) gets lower and lower as the cone diameter increases.

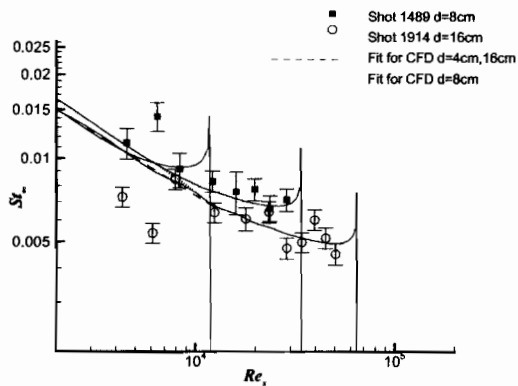


Figure 8. Comparison of non-dimensional heat flux for condition N₂ 4.

The results obtained from the surface pressure measurements confirm the theoretical predictions that surface pressure is not sensitive to nonequilibrium effects. It was found that the numerical results slightly underpredict (less than 10%) the surface pressure measurements.

6. Conclusions

The shock detachment process on cones in hypervelocity flows has been studied experimentally and computationally. It has been confirmed that the detachment distance grows more slowly for relaxing flows than for frozen and equilibrium flows. The difference is due to the behavior of the sonic line inside and outside the relaxation zone behind the shock wave. The growth of the sonic line has been characterized from attached to detached conditions in the frozen case. It has been found that the transition from incipient to full detachment is not abrupt but takes a few degrees to be completed. The behavior of the detachment distance has also been characterized from the frozen to the equilibrium limits. A new modified detachment distance is correlated to the reaction rate parameter. The correlation is not perfect because of the effects of vibrational nonequilibrium. Measured and computed interferograms have also been compared. The heat flux distribution is found to be insensitive to shock detachment. The changes seen in the heat flux as the shock detaches can be attributed to the conditions at the edge of the boundary layer, the pressure field outside the boundary layer, and to the Reynolds number, rather than to nonequilibrium effects.

Acknowledgement. The authors would like to thank T5 members for helping to set up and run the experiments and Joe Olejniczak for providing the nonequilibrium code and endless help on its use.

References

- Candler G (1988) The computation of weakly ionized hypersonic flows in thermo-chemical nonequilibrium. Ph. D. thesis, Stanford Univ
- Candler GV, MacCormack (1991) Computation of weakly ionized hypersonic flows in thermo-chemical nonequilibrium. *Journal of Thermophysics and Heat Transfer* 5(3):266–273
- Hornung, HG (1992) Performance data of the new free-piston shock tunnel at GALCIT. *AIAA Paper* 92-3943
- Hornung HG, Houwing AFP (1996) Shock detachment from cones in a relaxing gas. *Journal of Fluid Mechanics*, 101:307–319
- Hornung HG, Smith GH (1979) The influence of relaxation on shock detachment. *Journal of Fluid Mechanics* 93: 225–239
- Leyva IA (1999) Shock detachment process on cones in hypervelocity flows. Ph. D. thesis, California Institute of Technology
- Lordi JA, Mates RE, Moselle JR (1966) Computer program for solution of nonequilibrium expansions for reacting gas mixtures. *NASA CR* 472
- Olejniczak J (1997) Computational and experimental study of nonequilibrium chemistry in hypersonic flows. Ph. D. thesis, University of Minnesota
- Park C (1985) On convergence of computations of chemically reacting flows. *AIAA paper* 85-0247.
- Park C, Howe JT, Jaffe RL, Candler GV (1994) Review of chemical-kinetic problems for future NASA missions, ii: Mars entries. *AIAA Journal of Thermophysics and Heat Transfer*, 8(1)
- Quirk J (1998) Amrita—a computational facility (for CFD modelling). vonKarman Institute 29th CFD Lecture Series, ISSN 0377-8312
- Rein M (1989) Surf: a program for calculating inviscid supersonic reacting flows in nozzles. California Institute of Technology, GALCIT FM 89-1
- Reynolds WC (1986) The element potential method for chemical equilibrium analysis: implementation in the interactive program STANJAN. Stanford Univ Dept. of Mechanical Engineering Report
- Ward C, Pugh PG (1968) Shock standoff distance of blunt and sharp cones. *AIAA Journal*, 6(10):2018–2019
- Wen C-Y, Hornung HG (1995) Non-equilibrium dissociating flow over spheres. *Journal of Fluid Mechanics* 299:389–405

Non-equilibrium dissociating flow over spheres

By C.-Y. WEN¹ AND H. G. HORNUNG²

¹ Department of Mechanical Engineering, Da-Yeh Institute of Technology, Taiwan.

² Graduate Aeronautical Laboratories, California Institute of Technology, Pasadena, CA 91125, USA

(Received 27 May 1994 and in revised form 10 May 1995)

Previous work on the correlation of dissociative non-equilibrium effects on the flow field in front of blunt bodies considered the dependence of the dimensionless shock stand-off distance on the dimensionless dissociation rate immediately after the normal shock in the simple case of a diatomic gas with only one reaction. In this paper, the correlation is corrected to take into account the additional parameter of the dimensionless free-stream kinetic energy, and extended to the case of complex gas mixtures with many species and many reactions, by introducing a new reaction rate parameter that has a clear physical meaning, and leads to an approximate theory for the stand-off distance. Extensive new experimental results and numerical computations of air, nitrogen and carbon dioxide flow over spheres were obtained over a large range of total enthalpy. The results comprise surface heat flux measurements and differential interferograms. Both experimental results and numerical computations substantiate the approximate theory.

1. Introduction

When a sphere is placed in a flow at high Mach number and at such high velocity that the ordered kinetic energy of the uniform free stream is comparable with the dissociation energy of the gas, two new parameters (in addition to those of perfect-gas flows) enter the problem. In the simplest case of dissociation of a single diatomic gas, a dimensionless number of the form $K \equiv u_\infty^2/(2D)$ measures the free-stream kinetic energy in terms of the dissociation energy of the gas. Here, u_∞ is the free-stream speed and D is the specific dissociation energy of the gas.

If the gas density is sufficiently large, the collision frequency between the molecules is high and produces a dissociation rate that is fast enough to cause significant dissociation over distances that are comparable with the diameter of the sphere. In the simplest case of dissociation of a single diatomic gas, where the composition may be characterized by a single variable, e.g. the dissociation fraction α , this means that a dimensionless number of the form

$$\Omega \equiv \left(\frac{d\alpha}{dt} \right)_s \frac{d}{2u_\infty}$$

is $O(1)$. Here, the time derivative is the dissociation rate at a representative point, e.g. just after the normal shock wave, and d is the diameter of the sphere. High density is required to satisfy this condition because the dissociation rate is directly proportional to the density. Clearly, this means that the product of density and body size has to be sufficiently large. Hence, the Reynolds number of the flow is also large, and for

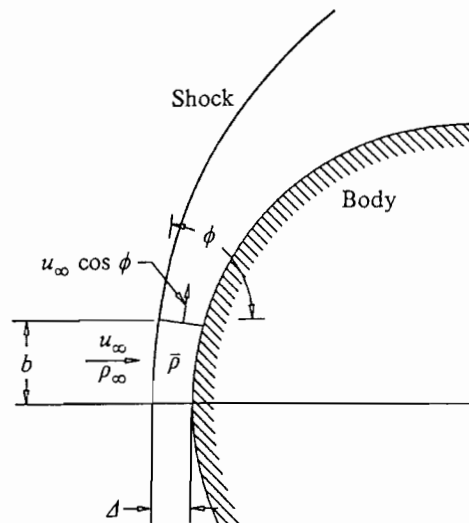


FIGURE 1. Schematic of control volume, and notation.

many purposes the flow may be considered to be inviscid to very good approximation. Infinite Ω corresponds to such a fast reaction that the flow may be considered to be in equilibrium, while zero Ω corresponds to no dissociation, or the frozen limit. For given free-stream conditions, Ω can be varied by changing the size of the body.

A well-known feature of hypervelocity blunt-body flows is that the shock wave stand-off distance Δ is inversely proportional to the average density on the stagnation streamline. This follows from a very simple argument which is presented here because it determines the right dimensionless numbers to choose for the problem. Consider the control volume shown in figure 1. Apply continuity to this control volume. At the left, the rate at which mass enters the control volume is $u_\infty \rho_\infty b$, or $\pi u_\infty \rho_\infty b^2$, depending on whether the flow is plane or axisymmetric. For small b , the rate at which mass leaves the control volume is $u_b \bar{\rho} \Delta$ or $2\pi u_b b \bar{\rho} \Delta$, respectively, where $\bar{\rho}$ is the average density in the shock layer. With $u_b \approx u_\infty \cos \phi$ and $b = r_s \cos \phi$, mass balance gives

$$\frac{1}{2} \frac{\Delta}{r_s} \frac{\bar{\rho}}{\rho_\infty} = \frac{1}{4} \quad \text{and} \quad = \frac{1}{2}$$

respectively, for axisymmetric and plane flow. Here, r_s is the radius of curvature of the shock. Since the stand-off distance is small compared to the body radius, $d/2 \approx r_s$ and the dimensionless parameter on the left may be formed with the body radius instead of the shock radius. The importance of this simple argument is not in the numbers on the right, but in the fact that it brings out the importance of the average density in the shock layer.

This topic was studied theoretically and experimentally in some detail by Hornung (1972). By examining a large number of numerical computations of dissociating flow over cylinders, it was found that the dimensionless stand-off distance, in the form

$$\tilde{\Delta} \equiv \frac{\Delta}{d} \frac{\rho_s}{\rho_\infty},$$

could be correlated by plotting it against the parameter Ω . Here, ρ_s is the density immediately after the normal shock. The computed density fields in the shock layer were also shown to be correlated approximately by Ω . However, the experimental

results of that study, obtained in the free-piston shock tunnel T3, at the Australian National University, did not corroborate the numerical correlation very well.

This earlier study suffered from two main problems. First, the theory was limited to a single diatomic gas, and did not account for the effect of K on $\tilde{\Delta}$. No derivation of the correlation of $\tilde{\Delta}$ with Ω was given. Second, the unavoidable end-effects in experimental studies of flow over cylinders manifest themselves in just the same manner as non-equilibrium dissociation effects, so that the latter were obscured by them. Also, the facility employed probably suffered from driver-gas contamination at the highest specific enthalpies tested.

Therefore, in the present study, we have the following three aims: to perform a theoretical study to relate the stand-off distance to both Ω and K ; to seek a more general reaction rate parameter, that allows the gas to consist of many species with many reactions; and to test the results experimentally and numerically. In the experiments, the new facility T5, at GALCIT, in which the density is significantly larger than was possible in T3 so that interferograms of flow over spheres give sufficient resolution, permitted the bothersome problems associated with flow over cylinders to be avoided. In the numerical investigation, the code developed by Candler (1988) was employed.

2. Conditions along the stagnation streamline

2.1. Effect of chemical reactions

Consider the stagnation streamline along the symmetry axis between the shock and the stagnation point. The momentum and energy equations for inviscid adiabatic flow take the simple forms

$$dp + \rho u du = 0 = dh + u du,$$

where p , ρ , u , and h are pressure, density, velocity and specific enthalpy respectively. Thus,

$$dp = \rho dh.$$

This equation does not mean that the entropy is constant along the stagnation streamline, but rather that the only entropy change that occurs is that associated with the chemical reaction:

$$T ds = \sum \hat{\mu}_i dc_i,$$

where T , s are temperature and specific entropy, and the $\hat{\mu}_i$ and c_i are the chemical potentials and mass fractions of the constituents. Let the caloric equation of state be given in the form

$$h = h(p, \rho, c_i).$$

Since the mass fractions must satisfy the identity

$$\sum_{i=1}^n c_i = 1,$$

the number of mass fractions that are independent is one less than the total number n of components present. It is usually convenient to choose c_1 as a dependent variable

and the other c_i as independent variables. Thus,

$$dh = h_\rho d\rho + h_p dp + \sum_{i=2}^n h_{c_i} dc_i = h_\rho d\rho + \rho h_p dh + \sum_{i=2}^n h_{c_i} dc_i,$$

where the subscripts denote partial differentiation. Solving for $d\rho$,

$$d\rho = \frac{1 - \rho h_p}{h_\rho} dh - \frac{1}{h_\rho} \sum_{i=2}^n h_{c_i} dc_i.$$

Note that the coefficient of dh is related to the frozen speed of sound a_f , and that dh may be replaced by $-u du$. Rewriting the first term on the right of this equation accordingly, it becomes

$$\frac{d\rho}{\rho} = -\frac{u^2}{a_f^2} \frac{du}{u} - \frac{1}{\rho h_p} \sum_{i=2}^n h_{c_i} dc_i,$$

where

$$a_f^2 = \frac{-h_p}{h_\rho - 1/\rho}.$$

The frozen Mach number u/a_f after the normal shock is typically 0.2 or less. This means that, in the absence of dissociation, the density is practically constant along the stagnation streamline, and, with dissociation, the density change along the stagnation streamline is essentially controlled by the chemistry:

$$(d\rho)_s \approx - \left(\frac{1}{h_p} \sum_{i=2}^n h_{c_i} dc_i \right)_s.$$

This approximation makes it possible to relate the average density on the stagnation streamline to the rate at which energy is absorbed by the chemical reactions at the shock. This then appears to be the right quantity to incorporate in a new reaction rate parameter

$$\tilde{\Omega} \equiv - \frac{d}{\rho_s u_\infty} \left(\frac{1}{h_p} \sum_{i=2}^n h_{c_i} \frac{dc_i}{dt} \right)_s.$$

For a given gas mixture,

$$\tilde{\Omega} \sim \rho_s d \left(\sum_{i=2}^n h_{c_i} \frac{dc_i}{dt} \right)_s / (\rho_\infty u_\infty^3),$$

which has the physical significance of

$$\tilde{\Omega} = \frac{\text{Energy absorption rate by chemistry}}{\text{Input rate of free-stream kinetic energy}}.$$

In order to determine the value of $\tilde{\Omega}$ it is necessary to express h_p in terms of the conditions at the shock. This may be done by assuming that the gas mixture obeys the thermal equation of state

$$T = T(p, \rho, c_i) = \frac{p}{\rho R \Gamma},$$

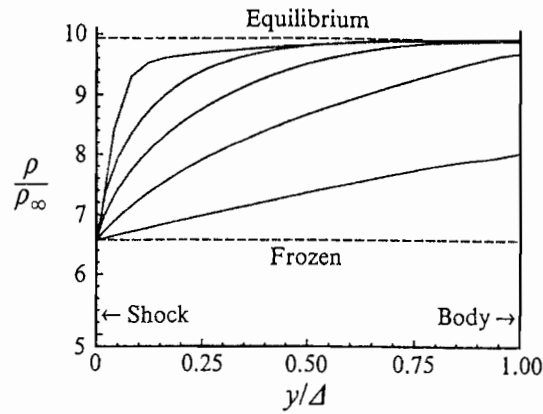


FIGURE 2. Density profile along the stagnation streamline from numerical computations for different values of the reaction rate parameter.

where

$$\Gamma = \sum_{i=1}^n \frac{c_i}{W_i} = \frac{1}{W},$$

and W_i and W are the molecular weights of species i and of the dissociated gas mixture, respectively. This leads to

$$h_p = -\frac{c_p p}{\rho^2 R \Gamma},$$

where

$$c_p = \sum_{i=1}^n c_i c_{pi},$$

and the c_{pi} are the specific heats at constant pressure of the constituents. The value of h_p at the shock can be estimated by approximating the value of p_s with $\rho_\infty u_\infty^2$, so that

$$(h_p)_s = -\frac{c_{ps} \rho_\infty u_\infty^2}{\rho_s^2 R \Gamma}.$$

2.2. Density profile

Figure 2 shows seven density profiles along the stagnation streamline obtained using an inviscid version of Candler's code plotted against y/Δ , where y is the distance from the shock. The free-stream conditions for these different profiles were the same, and the changes are brought about by successively increasing the sphere diameter. As may be seen, the profile changes in a monotonic fashion from the frozen-flow profile, with virtually constant density, to the equilibrium profile, in which all the dissociation, and therefore all the density change, occurs in the shock, and the density is again virtually constant thereafter.

Recall that the quantity that determines the stand-off distance is the average density. In fact, numerous correlations of stand-off distance with average density have been made for non-reacting flow. Upon interpretation into our variables, these give the following result:

$$\frac{\Delta}{d} \frac{\bar{\rho}}{\rho_\infty} = \tilde{\Delta} \frac{\bar{\rho}}{\rho_s} = L,$$

where $L = 0.41$ for spheres.

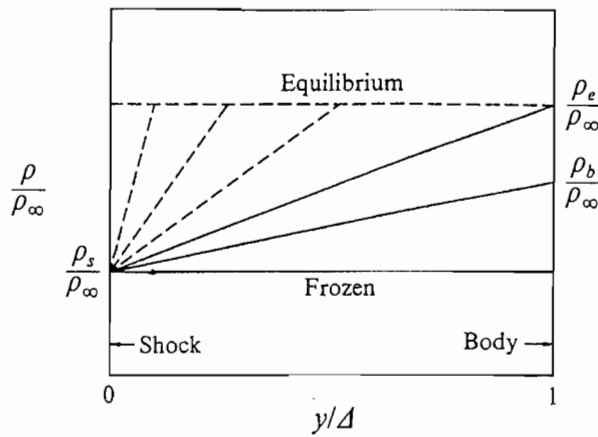


FIGURE 3. Simplified density profiles for the purpose of determining an approximate average value of the density along the stagnation streamline. ρ_b and ρ_e denote the stagnation-point density and the equilibrium density, respectively. By comparing with Fig. 2, it is clear that using this linear approximation will overestimate the average density slightly, because the actual profiles are always convex up.

Because the stand-off distance is related to the average density, the exact details of the density profile are not important and we can proceed in an approximate Kármán-Pohlhausen-type analysis by assuming linear density profiles between the shock and the body, provided that the density on the body ρ_b is smaller than the equilibrium density ρ_e . If the linear profile reaches ρ_e before the stagnation point, the density is taken to be constant thereafter at ρ_e . This clearly requires the equilibrium density to be determined and is evidently the place where the dependence of $\tilde{\Delta}$ on K (and therefore the recombination reaction) enters.

To proceed with the analysis, distinguish the cases where $\rho_b < \rho_e$ from those in which the body density is ρ_e . The slope of the density profile at the shock is determined from the dissociation rate just downstream of the shock. Figure 3 shows the simplified linear profiles.

3. Analytic solution for the stand-off distance

3.1. The case when $\rho_b < \rho_e$

When $\rho_b < \rho_e$, the linear profiles give

$$\left(\frac{d\rho}{dy}\right)_s = \frac{\rho_b - \rho_s}{\Delta} \quad \text{and} \quad \bar{\rho} = \frac{1}{2}(\rho_b + \rho_s) ;$$

$(d\rho/dt)_s$ can then be approximated as

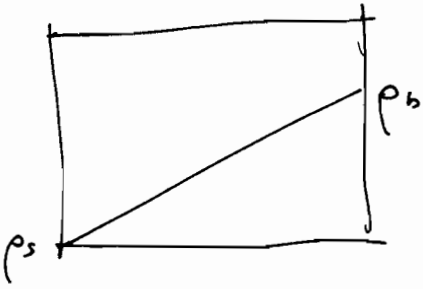
$$\left(\frac{d\rho}{dt}\right)_s = u_s \left(\frac{d\rho}{dy}\right)_s = (\rho_b - \rho_s) \left(\frac{\rho_\infty}{\rho_s} \frac{d}{\Delta}\right) \left(\frac{u_\infty}{d}\right) .$$

Using the definition of $\tilde{\Omega}$ to replace $(d\rho/dt)_s$ leads to the quadratic equation for $\tilde{\Delta}$

$$\tilde{\Delta}^2 - (L - \tilde{\Delta}) \frac{2}{\tilde{\Omega}} = 0 .$$

Only one of the two roots of this equation is physically meaningful. It is

$$\tilde{\Delta} = \frac{1}{\tilde{\Omega}} \left[-1 + \left(1 + 2L\tilde{\Omega} \right)^{1/2} \right] . \tag{3.1}$$



$$\bar{p} = \frac{1}{2}(p_b + p_s)$$

$$\tilde{\Delta} \frac{\bar{p}}{\rho_s} = L$$

$$p_b = 2\bar{p} - p_s$$

$$\left(\frac{dp}{dt}\right)_s = u_s \left(\frac{dp}{dx}\right)_s = u_s \frac{p_b - p_s}{\Delta} = \frac{\rho_\infty u_\infty}{\rho_s} \frac{p_b - p_s}{\Delta}$$

now $\left(\frac{dp}{dt}\right)_s = \rho_s u_\infty \tilde{\Omega}$

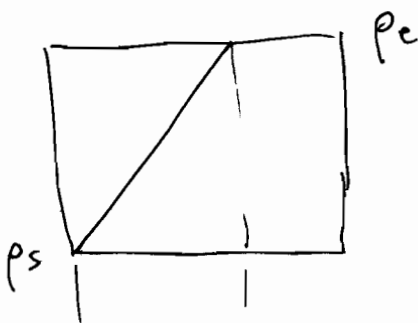
$$\therefore \tilde{\Omega} = \frac{p_b - p_s}{\rho_s} \cdot \frac{\rho_\infty}{\rho_s} \frac{d}{\Delta}$$

$$= 2\left(\frac{\bar{p}}{\rho_s} - 1\right) \cdot \frac{1}{\Delta}$$

$$\tilde{\Omega} = 2\left(\frac{L}{\Delta} - 1\right) \frac{1}{\Delta}$$

$$\tilde{\Delta}^2 - \frac{2}{\tilde{\Omega}}(L - \tilde{\Delta}) = 0$$

$$\tilde{\Delta} = \frac{1}{\tilde{\Omega}} \left[\sqrt{1 + 2L\tilde{\Omega}} - 1 \right]$$

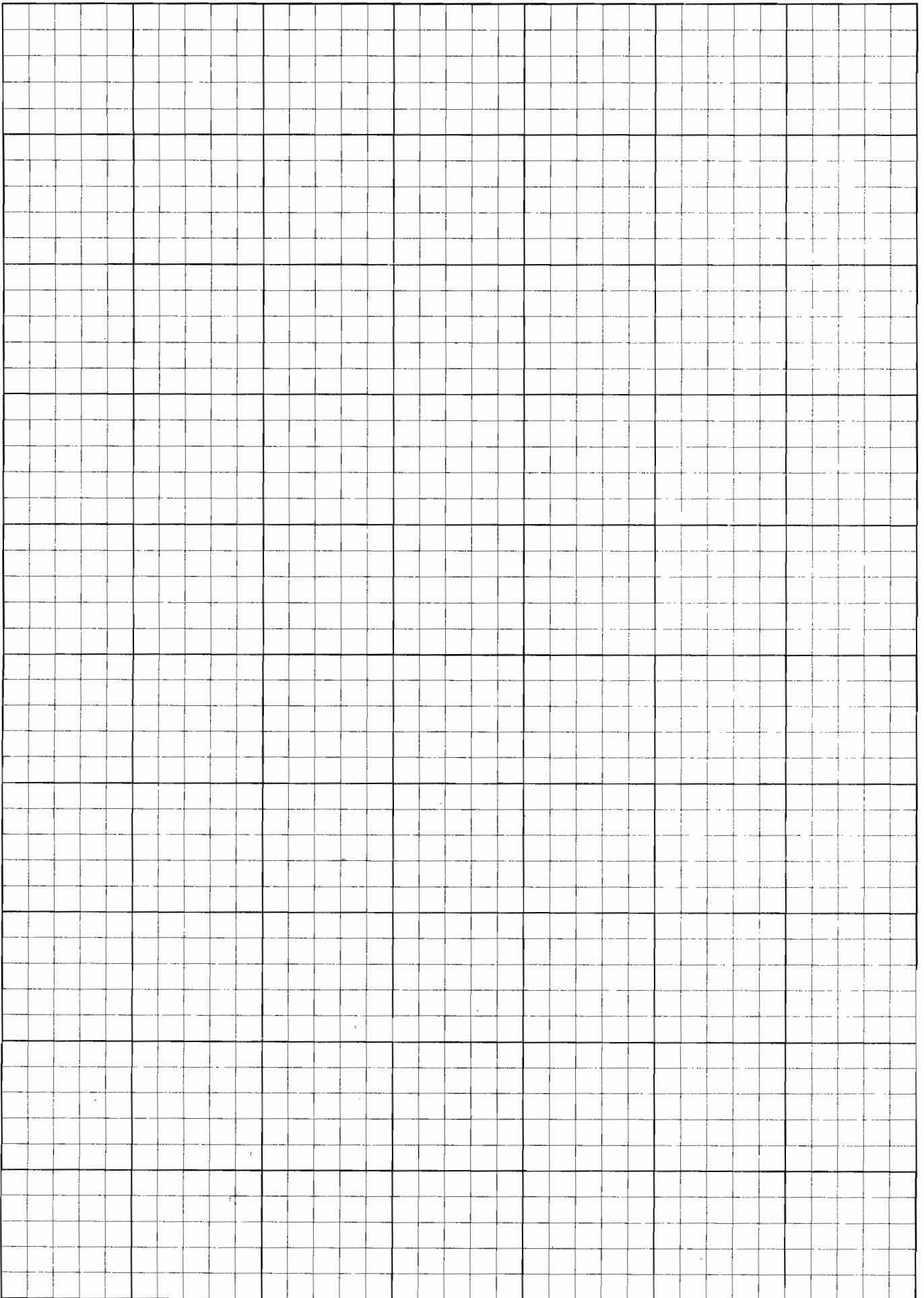


$$\left(\frac{dp}{dt}\right)_s = \rho_s u_\infty \tilde{\Omega}$$

$$\left(\frac{dp}{dx}\right)_s = \frac{\rho_s u_\infty}{d u_s} \tilde{\Omega} = \frac{p_e - p_s}{l}$$

$$\therefore \frac{l}{\Delta} = \frac{p_e - p_s}{\rho_s} \frac{d \rho_\infty}{\tilde{\Omega} \rho_s \Delta} = \frac{p_e - p_s}{\rho_s} \cdot \frac{1}{\tilde{\Omega} \Delta}$$

$$\therefore \bar{p} = \frac{l}{2\Delta}(p_s + p_e) + \frac{(l - \Delta)}{\Delta} p_e$$



$$\bar{p} = \frac{(p_e p_s - 1)}{2 \Omega \Delta} (p_s + p_e) + \left(1 - \frac{p_e - p_s}{2 \Omega p_s}\right) \frac{1}{\Omega} \frac{p_e}{p_s}$$

$$L \bar{\Omega} = \frac{p_e}{2 p_s} \left(1 - \frac{p_e}{p_s}\right) - \left(\frac{p_e}{p_s}\right)^2$$

$$= \frac{p_e}{2 p_s} - \frac{3}{2} \left(\frac{p_e}{p_s}\right)^2$$

$$\frac{L}{\Delta} = \frac{p_e}{p_s} + \frac{1}{2 \Omega \Delta} \left[\frac{p_e - 1}{p_s} \left(1 + \frac{p_e}{p_s}\right) - 2 \frac{p_e}{p_s} \left(\frac{p_e}{p_s} - 1\right) \right]$$

$$= \frac{p_e}{p_s} + \frac{1}{2 \Omega \Delta} \left(\frac{p_e}{p_s} - 1\right) \left(1 + \frac{p_e}{p_s} - 2 \frac{p_e}{p_s}\right)$$

$$\boxed{\frac{L}{\Delta} = \frac{p_e}{p_s} - \frac{1}{2 \Omega \Delta} \left(\frac{p_e}{p_s} - 1\right)^2}$$

$$\frac{p_e}{p_s} \Delta^2 - \frac{1}{2 \Omega} \left(\frac{p_e}{p_s} - 1\right)^2 - L \Delta = 0$$

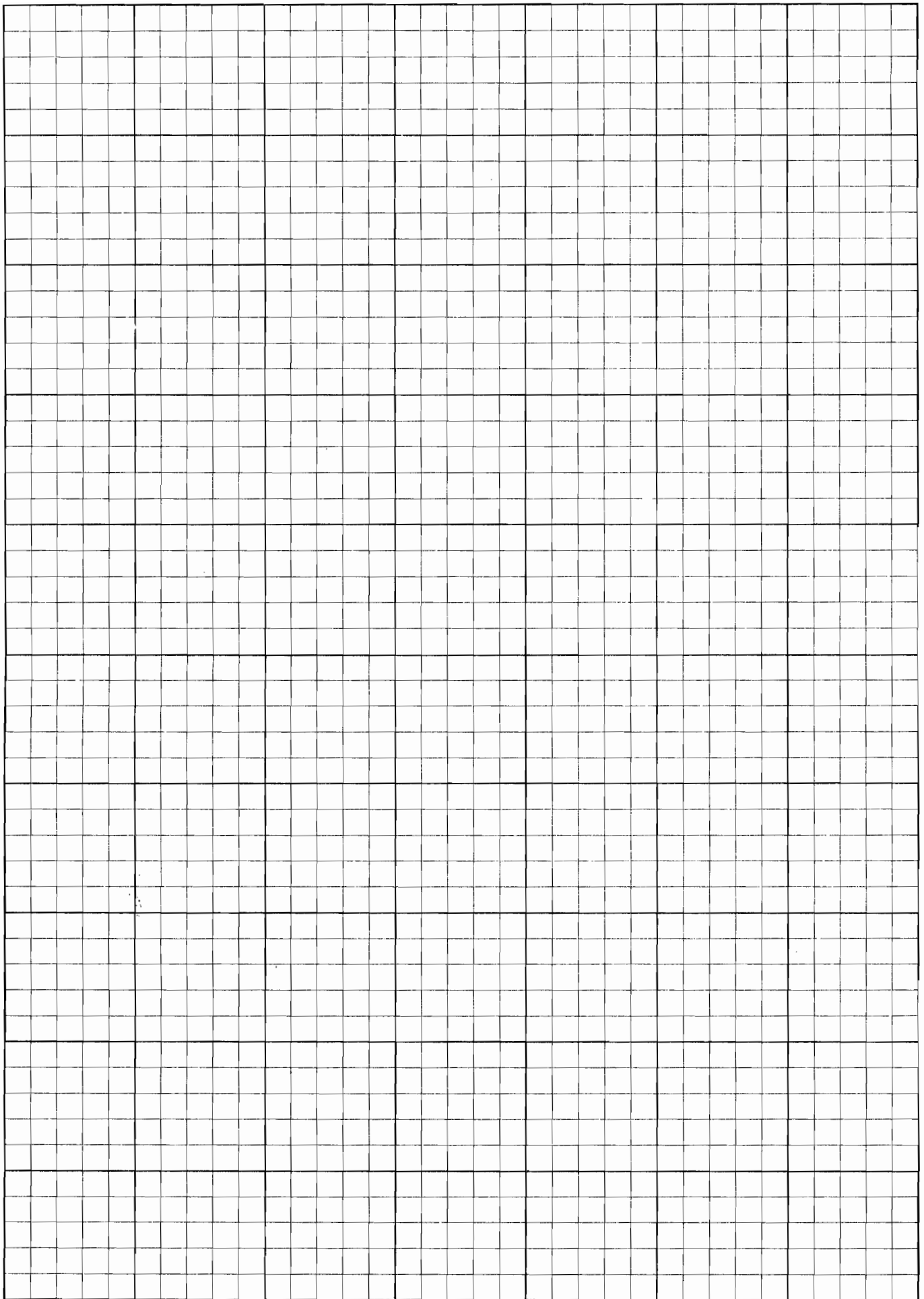
$$\Delta = \frac{L \pm \sqrt{L^2 - \frac{2 p_e}{\Omega p_s} \left(\frac{p_e}{p_s} - 1\right)}}{2 \frac{p_e}{p_s}}$$

$$= \frac{L p_s}{2 p_e} \left[1 \pm \sqrt{1 - \frac{2 p_e}{\Omega p_s} \left(\frac{p_e}{p_s} - 1\right)} \right]$$

$$= \frac{1}{\Omega} \frac{\left(\frac{p_e}{p_s} - 1\right)^2}{4 \frac{p_e}{p_s}} \left[1 \pm \sqrt{1 + 16 \frac{p_e}{p_s} \cdot \frac{1}{\left(\frac{p_e}{p_s} - 1\right)^4} \frac{L^2}{\Omega^2}} \right]$$

$$\Omega \rightarrow \Delta = L \frac{p_s}{p_e} \sqrt{\dots}$$

13,782
42,381
42,382
42,383
42,384
42,385
42,386
42,387
42,388
42,389
42,390
42,391
42,392
42,393
42,394
42,395
42,396
42,397
42,398
42,399
42,400
42,401
42,402
42,403
42,404
42,405
42,406
42,407
42,408
42,409
42,410
42,411
42,412
42,413
42,414
42,415
42,416
42,417
42,418
42,419
42,420
42,421
42,422
42,423
42,424
42,425
42,426
42,427
42,428
42,429
42,430
42,431
42,432
42,433
42,434
42,435
42,436
42,437
42,438
42,439
42,440
42,441
42,442
42,443
42,444
42,445
42,446
42,447
42,448
42,449
42,450
42,451
42,452
42,453
42,454
42,455
42,456
42,457
42,458
42,459
42,460
42,461
42,462
42,463
42,464
42,465
42,466
42,467
42,468
42,469
42,470
42,471
42,472
42,473
42,474
42,475
42,476
42,477
42,478
42,479
42,480
42,481
42,482
42,483
42,484
42,485
42,486
42,487
42,488
42,489
42,490
42,491
42,492
42,493
42,494
42,495
42,496
42,497
42,498
42,499
42,500
42,501
42,502
42,503
42,504
42,505
42,506
42,507
42,508
42,509
42,510
42,511
42,512
42,513
42,514
42,515
42,516
42,517
42,518
42,519
42,520
42,521
42,522
42,523
42,524
42,525
42,526
42,527
42,528
42,529
42,530
42,531
42,532
42,533
42,534
42,535
42,536
42,537
42,538
42,539
42,540
42,541
42,542
42,543
42,544
42,545
42,546
42,547
42,548
42,549
42,550
42,551
42,552
42,553
42,554
42,555
42,556
42,557
42,558
42,559
42,560
42,561
42,562
42,563
42,564
42,565
42,566
42,567
42,568
42,569
42,570
42,571
42,572
42,573
42,574
42,575
42,576
42,577
42,578
42,579
42,580
42,581
42,582
42,583
42,584
42,585
42,586
42,587
42,588
42,589
42,590
42,591
42,592
42,593
42,594
42,595
42,596
42,597
42,598
42,599
42,600
42,601
42,602
42,603
42,604
42,605
42,606
42,607
42,608
42,609
42,610
42,611
42,612
42,613
42,614
42,615
42,616
42,617
42,618
42,619
42,620
42,621
42,622
42,623
42,624
42,625
42,626
42,627
42,628
42,629
42,630
42,631
42,632
42,633
42,634
42,635
42,636
42,637
42,638
42,639
42,640
42,641
42,642
42,643
42,644
42,645
42,646
42,647
42,648
42,649
42,650
42,651
42,652
42,653
42,654
42,655
42,656
42,657
42,658
42,659
42,660
42,661
42,662
42,663
42,664
42,665
42,666
42,667
42,668
42,669
42,670
42,671
42,672
42,673
42,674
42,675
42,676
42,677
42,678
42,679
42,680
42,681
42,682
42,683
42,684
42,685
42,686
42,687
42,688
42,689
42,690
42,691
42,692
42,693
42,694
42,695
42,696
42,697
42,698
42,699
42,700
42,701
42,702
42,703
42,704
42,705
42,706
42,707
42,708
42,709
42,710
42,711
42,712
42,713
42,714
42,715
42,716
42,717
42,718
42,719
42,720
42,721
42,722
42,723
42,724
42,725
42,726
42,727
42,728
42,729
42,730
42,731
42,732
42,733
42,734
42,735
42,736
42,737
42,738
42,739
42,740
42,741
42,742
42,743
42,744
42,745
42,746
42,747
42,748
42,749
42,750
42,751
42,752
42,753
42,754
42,755
42,756
42,757
42,758
42,759
42,760
42,761
42,762
42,763
42,764
42,765
42,766
42,767
42,768
42,769
42,770
42,771
42,772
42,773
42,774
42,775
42,776
42,777
42,778
42,779
42,780
42,781
42,782
42,783
42,784
42,785
42,786
42,787
42,788
42,789
42,790
42,791
42,792
42,793
42,794
42,795
42,796
42,797
42,798
42,799
42,800
42,801
42,802
42,803
42,804
42,805
42,806
42,807
42,808
42,809
42,810
42,811
42,812
42,813
42,814
42,815
42,816
42,817
42,818
42,819
42,820
42,821
42,822
42,823
42,824
42,825
42,826
42,827
42,828
42,829
42,830
42,831
42,832
42,833
42,834
42,835
42,836
42,837
42,838
42,839
42,840
42,841
42,842
42,843
42,844
42,845
42,846
42,847
42,848
42,849
42,850
42,851
42,852
42,853
42,854
42,855
42,856
42,857
42,858
42,859
42,860
42,861
42,862
42,863
42,864
42,865
42,866
42,867
42,868
42,869
42,870
42,871
42,872
42,873
42,874
42,875
42,876
42,877
42,878
42,879
42,880
42,881
42,882
42,883
42,884
42,885
42,886
42,887
42,888
42,889
42,890
42,891
42,892
42,893
42,894
42,895
42,896
42,897
42,898
42,899
42,900
42,901
42,902
42,903
42,904
42,905
42,906
42,907
42,908
42,909
42,910
42,911
42,912
42,913
42,914
42,915
42,916
42,917
42,918
42,919
42,920
42,921
42,922
42,923
42,924
42,925
42,926
42,927
42,928
42,929
42,930
42,931
42,932
42,933
42,934
42,935
42,936
42,937
42,938
42,939
42,940
42,941
42,942
42,943
42,944
42,945
42,946
42,947
42,948
42,949
42,950
42,951
42,952
42,953
42,954
42,955
42,956
42,957
42,958
42,959
42,960
42,961
42,962
42,963
42,964
42,965
42,966
42,967
42,968
42,969
42,970
42,971
42,972
42,973
42,974
42,975
42,976
42,977
42,978
42,979
42,980
42,981
42,982
42,983
42,984
42,985
42,986
42,987
42,988
42,989
42,990
42,991
42,992
42,993
42,994
42,995
42,996
42,997
42,998
42,999
43,000



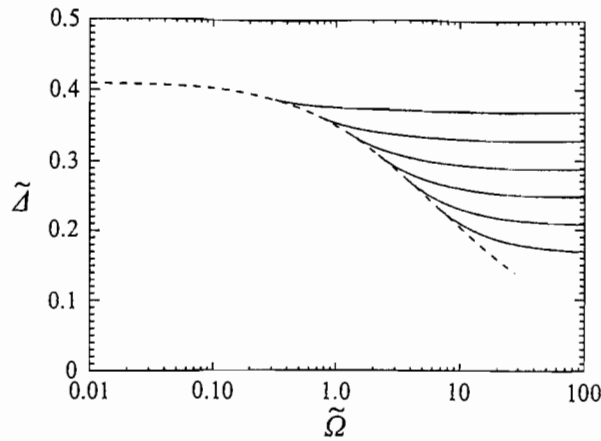


FIGURE 4. Plot of equations (3.1) (dashed line), and (3.2) (full lines) for $\rho_s/\rho_e = 0.4, 0.5, 0.6, 0.7, 0.8$ and 0.9 .

This has the correct limit $\tilde{A} = L$ at $\tilde{\Omega} = 0$, but will clearly fail at large $\tilde{\Omega}$, because we have to proceed differently in calculating $\bar{\rho}$ when the linear profile reaches the equilibrium density within the shock layer.

3.2. The case when $\rho_b = \rho_e$

For values of $\tilde{\Omega}$ that are sufficiently small, so that $\rho_b < \rho_e$, the previous section shows that \tilde{A} depends only on $\tilde{\Omega}$. When $\rho_b = \rho_e$, however, this is no longer true, since the equilibrium value of the density now enters the calculation of $\bar{\rho}$. Thus, a critical value of $\tilde{\Omega}$ exists for each free-stream condition, beyond which \tilde{A} depends on two parameters, changing in form

$$\text{from } \tilde{A} = f(\tilde{\Omega}) \text{ to } \tilde{A} = g(\tilde{\Omega}, \rho_e/\rho_s).$$

By proceeding as in the previous section, but this time forming the average density from the linear profile up to the point where ρ reaches ρ_e and a constant-density part with $\rho = \rho_e$ thereafter, the average density becomes

$$\frac{\bar{\rho}}{\rho_s} = \frac{\rho_e}{\rho_s} - \frac{1}{2\tilde{\Omega}\tilde{A}} \left(1 - \frac{\rho_e}{\rho_s}\right)^2.$$

By using the relation between the average density and the stand-off distance, and solving for \tilde{A} , we obtain

$$\tilde{A} = \frac{\rho_s}{\rho_e} \left[L + \frac{1}{2\tilde{\Omega}} \left(\frac{\rho_e}{\rho_s} - 1 \right)^2 \right]. \quad (3.2)$$

Again, this may be seen to have the correct limiting value $L\rho_s/\rho_e$ when $\tilde{\Omega} = \infty$.

Equations (3.1) and (3.2) are plotted in figure 4. The curves of the two-parameter family of equation (3.2), valid for large $\tilde{\Omega}$, are nearly tangent to the single curve of equation (3.1), valid for small $\tilde{\Omega}$ at the transition point, which is different for different ρ_s/ρ_e .

The coordinates of the transition point $(\tilde{\Omega}_0, \tilde{A}_0)$, can be determined explicitly as

$$\tilde{\Omega}_0 = \frac{(\rho_e/\rho_s)^2 - 1}{2L},$$

and

$$\tilde{\Delta}_0 = \frac{2L}{\rho_e/\rho_s + 1}.$$

The slopes of the two curves are not quite the same at this point. This may be seen from the fact that the average density increases less rapidly with $\tilde{\Omega}$ when the equilibrium density is reached before the stagnation point than if $\rho_e > \rho_b$ (see figure 3).

3.3. Discussion

The approximate theory leading to equations (3.1) and (3.2) takes account of the free-stream kinetic energy K through the appearance of the equilibrium density ρ_e . This is therefore the place where the effect of the recombination reactions enters the picture. For higher values of K , i.e. higher values of the total enthalpy h_0 , the amount of energy absorbed by dissociation to equilibrium is increased, so that ρ_e/ρ_s is increased, and $\tilde{\Delta}$ is decreased. The approximate theory takes all of these effects into account in the simplest approximation. The two-part approximation of the density profile (linear plus constant) makes it necessary to distinguish between the regimes of low and high $\tilde{\Omega}$ with the two equations (3.1) and (3.2).

The two-part approximation also overestimates the average density and therefore underestimates the stand-off distance, as will be seen later. This error may be reduced significantly if the approximation for the density profile is improved, for example, by writing it as

$$\frac{\rho - \rho_s}{\rho_e - \rho_s} = 1 - \exp \left[-\frac{2\tilde{\Omega}\rho_s}{\rho_e - \rho_s} \frac{y}{\tilde{\Delta}} \right].$$

Integrating this to determine the average leads to

$$\frac{\bar{\rho} - \rho_s}{\rho_e - \rho_s} = 1 + \frac{1}{2\tilde{\Omega}\tilde{\Delta}} \left(\frac{\rho_e}{\rho_s} - 1 \right) \left(\exp \left[-\frac{2\tilde{\Omega}\tilde{\Delta}\rho_s}{\rho_e - \rho_s} \right] - 1 \right).$$

This is now a single equation for the average density, from which a single equation for $\tilde{\Delta}$ can be obtained by substituting in

$$\tilde{\Delta} = L \frac{\rho_s}{\bar{\rho}},$$

and solving the resulting equation for $\tilde{\Delta}$. In this case, an explicit solution is not possible, except in the two limiting cases, where the results are, of course, the same as equations (3.1) and (3.2). This refined theory is more accurate in the mid-range of $\tilde{\Omega}$. However, the simple forms of equations (3.1) and (3.2) are surprisingly accurate and the theory is much more transparent in this simpler form.

The manner in which the stand-off distance may be described in terms of the two parameters K and $\tilde{\Omega}$ is, of course, also of wider significance. It may be expected, for example, that, for a given gas, the density field in the shock layer of a blunt body will be the same for all flows in which these two parameters take the same value. The stand-off distance just serves as a convenient variable to test this concept. The success of the simple correlation stems from the fact that the influence of the chemistry on the fluid motion acts through the removal or addition of energy to or from the chemical energy store represented by the dissociated species. Thus, the important step in the

analysis is to express $\tilde{\Omega}$ in terms of the dimensionless chemical energy absorption rate.

4. Computational method

The code developed by Candler (1988) was used to compute the inviscid reacting flow over a sphere. The flow field is described by coupled partial differential equations for the conservation of species, mass, mass-averaged momentum, vibrational energy of each diatomic species and total energy. A finite-volume method using modified Steger–Warming flux-vector splitting is used to obtain the steady-state solution to these fully coupled equations for different gases. Park's semi-empirical two-temperature model and chemical kinetics model (Park 1988, 1989) was used to calculate the reaction rates for different reactions of air and nitrogen. For carbon dioxide, the chemical kinetics model of Park *et al.* (1991) was used. The scheme is implicit, using Gauss–Seidel line relaxation and is second-order accurate in the tangential direction. A compromise between efficiency in computational time and accuracy led to the use of a (56×100) grid throughout the present work. Extensive documentation of successful examples exists in reproducing experimental results in great detail, see e.g. Candler (1988), Rock, Candler & Hornung (1992), Wen & Hornung (1993), and Hornung *et al.* (1994). Since the shock values of temperature, vibrational temperatures, and density are not accessible during the experiment, the computational method provides a good way to obtain partial information about them.

The stand-off distance and the shock values of the reaction rate and density for the numerical calculation are determined from the point where the vibrational temperature reaches a maximum.

5. Experiment

5.1. Facility

The facility used for all the experiments described here was the free-piston shock tunnel T5 at GALCIT. The facility uses the principle of free-piston adiabatic compression of the driver gas of a shock tunnel to achieve the high shock speeds and densities required to generate high enthalpy and reaction scaling. It is capable of producing flows of air or nitrogen up to specific reservoir enthalpy h_0 of 25 MJ kg⁻¹ at reservoir pressure p_0 up to 100 MPa. The shock tunnel has two additional important features. One is that the test duration is sufficiently short to avoid destruction of the machine by melting, yet long enough to provide good measurements during the steady-flow period. The other is that the gas is partially dissociated at the nozzle exit, especially in the cases of air and carbon dioxide at high specific reservoir enthalpies, where these gases also contain, respectively, some nitric oxide and carbon monoxide. A more detailed description of T5 and its performance envelope, flow quality and repeatability may be found in Hornung (1992).

5.2. Free-stream conditions

For the experiments, the flow was generated through a contoured nozzle of 300 mm exit diameter and 30 mm throat diameter. Using an equilibrium calculation, the specific reservoir enthalpy can be determined from the measured shock speed and the measured reservoir pressure. The nozzle flow is then computed by using an axisymmetric inviscid non-equilibrium flow code developed by Rein (1989). The calibration

	p_0 (MPa)	h_0 (MJ kg ⁻¹)	u_∞ (km s ⁻¹)	T_∞ (K)	ρ_∞ (kg m ⁻³)	
Nitrogen	from	30	10.58	4.2	1390	0.0175
	to	90	21.06	5.5	2760	0.0561
Air	from	30	9.81	3.9	1340	0.0152
	to	90	22.15	5.6	2930	0.0627
Carbon dioxide	from	30	4.5	2.5	1130	0.0326
	to	90	11.95	3.6	2400	0.162

TABLE 1. Range of reservoir and free-stream conditions

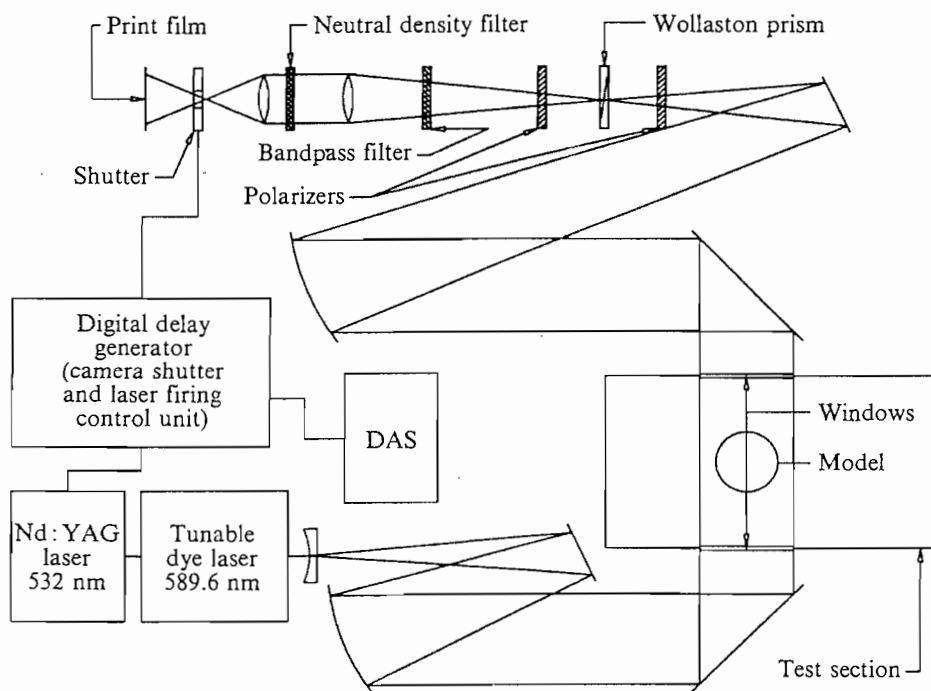


FIGURE 5. Schematic diagram of the optical arrangement. Bandpass and spatial filters are used to reduce the luminosity emitted from the test gas. The bandwidth of the bandpass filter is 10 nm centred at 590 nm for the dye laser and 10 nm centred at 532 nm for the neodymium-YAG laser.

of the free-stream conditions obtained by this method has been accomplished by measuring test section Pitot pressure distribution, see Rousset (1994) and stagnation-point heat flux, see Wen (1994).

Table 1 gives the ranges of values of the reservoir and test section conditions chosen for the present investigation. The Mach number of the free stream is about 5.5 for nitrogen, 5.3 for air and 4.6 for carbon dioxide.

5.3. Models and flow visualization

The models were spheres with diameters 1, 2, 3, 4 and 6 in. in order to vary the reaction rate parameter at a given tunnel condition. This has an upper limit of 6 in.

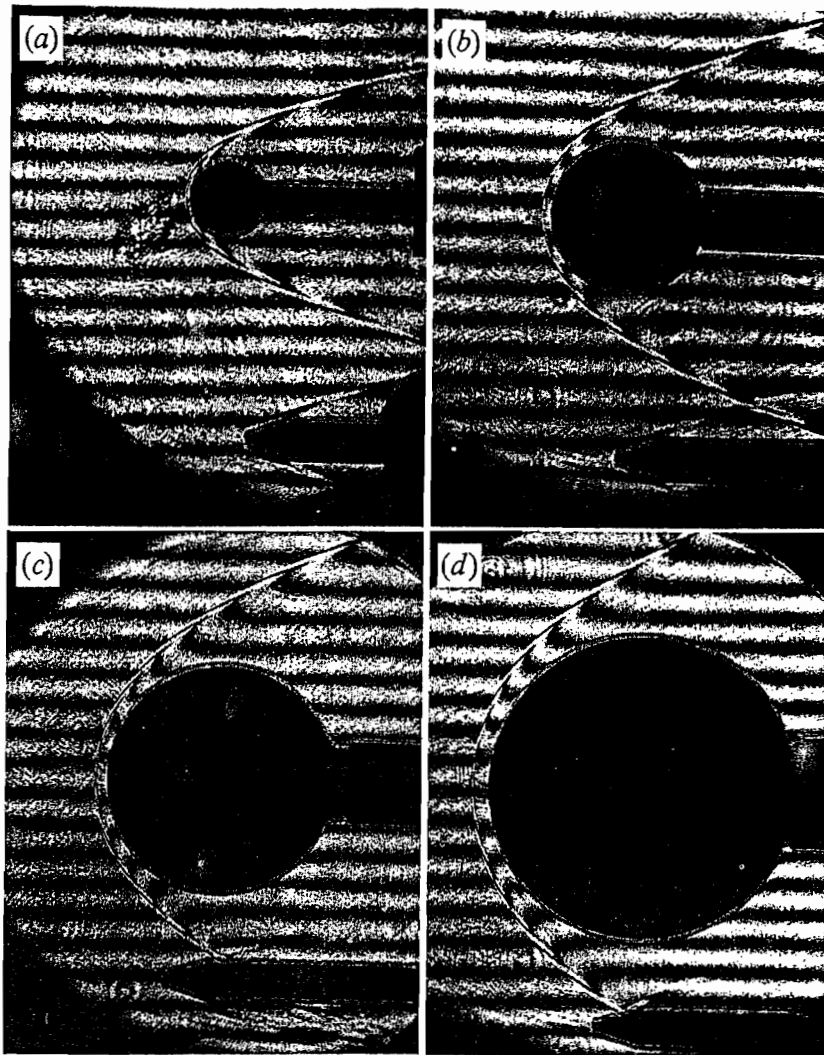


FIGURE 6. Finite fringe differential interferograms of air flow over 1, 2, 3 and 4 in. diameter spheres. $\lambda = 589$ nm. (a) $p_0 = 58$ MPa, $h_0 = 10.7$ MJ kg⁻¹. (b) $p_0 = 25$ MPa, $h_0 = 9.8$ MJ kg⁻¹. (c) $p_0 = 28$ MPa, $h_0 = 10$ MJ kg⁻¹. (d) $p_0 = 27.5$ MPa, $h_0 = 16$ MJ kg⁻¹. The blemish ahead of the bow shock wave in interferograms (a) and (b) is due to a flaw in the optical window.

because of the useful diameter of the flow, and a lower limit of 1 in. because of the resolution of the optical system. The spheres were instrumented with thermocouples to measure the surface temperature history and thus the surface heat flux, in particular at the stagnation point.

The optical system used for flow visualization is a differential interferometer shown schematically in figure 5. This instrument uses a Wollaston prism in a conventional schlieren setup and was used in the finite-fringe mode with a dye laser producing 5 mJ pulses of 6 ns duration.

6. Results

6.1. Density field

As an example of the interferometric results obtained, figure 6 shows a set of four finite-fringe differential interferograms of air flow over four different-size spheres, and figure 7 shows five cases of carbon dioxide flow. A large number of such measurements

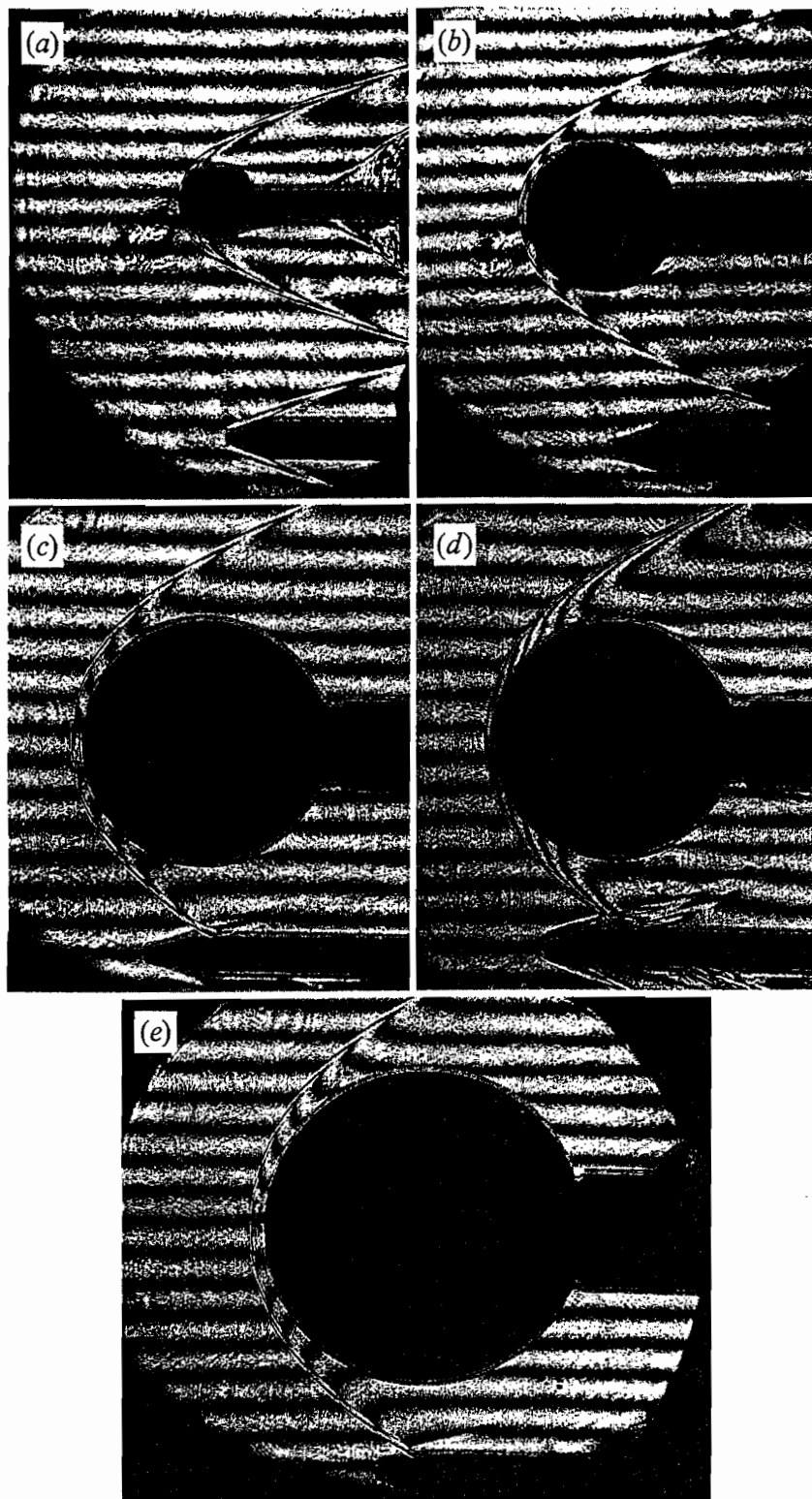


FIGURE 7. Finite fringe differential interferograms of CO_2 flow over 1, 2, 3, 3, and 4 in. diameter spheres. $\lambda = 589 \text{ nm}$. (a) $p_0 = 55 \text{ MPa}$, $h_0 = 6 \text{ MJ kg}^{-1}$. (b) $p_0 = 25 \text{ MPa}$, $h_0 = 12 \text{ MJ kg}^{-1}$. (c) $p_0 = 25 \text{ MPa}$, $h_0 = 9 \text{ MJ kg}^{-1}$. (d) $p_0 = 55 \text{ MPa}$, $h_0 = 4.6 \text{ MJ kg}^{-1}$. (e) $p_0 = 22.5 \text{ MPa}$, $h_0 = 11.4 \text{ MJ kg}^{-1}$.

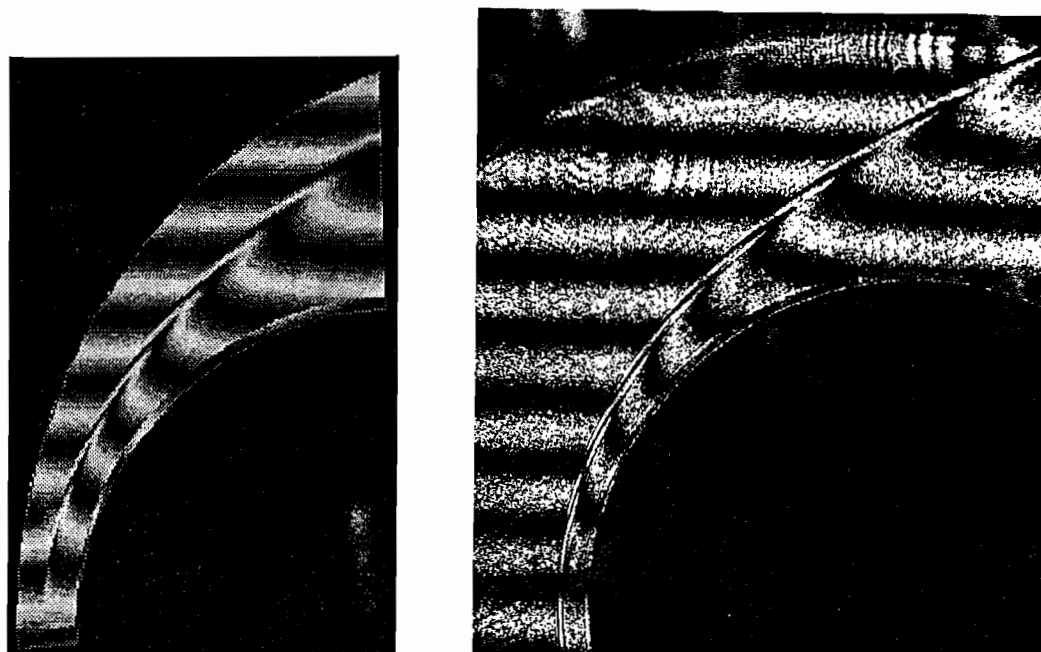


FIGURE 8. Comparison of measured (right) and computed differential interferograms in the case of air flow over a 4 in. sphere, at $p_0 = 27.5$ MPa, $h_0 = 16$ MJ kg $^{-1}$.

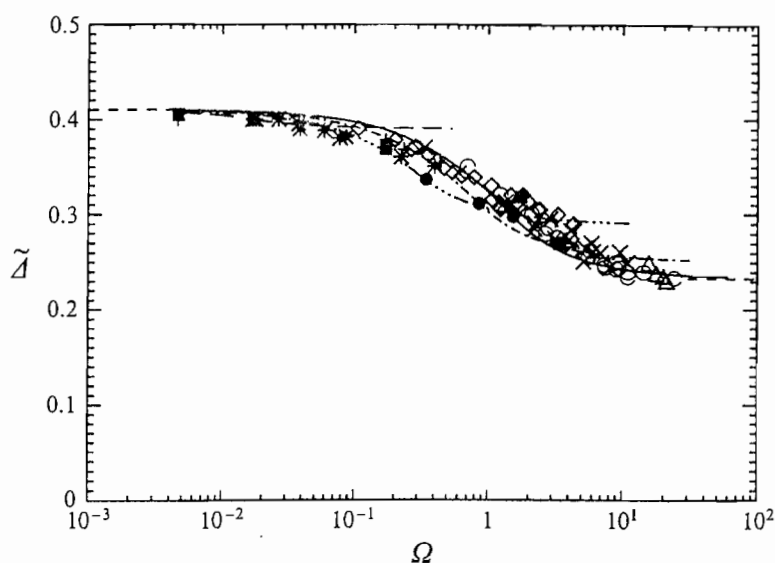


FIGURE 9. Numerical (open symbols) and experimental (full squares) results for nitrogen flow plotted in the old variables, with equations (3.1) and (3.2) superimposed. As may be seen, in these variables, the curves for different ρ_s/ρ_e are shifted relative to each other.

were taken, and compared with numerically computed interferograms. An example of such a comparison is presented in figure 8. Extensive comparisons of this kind have been made. More detail about the results of such comparisons are reported elsewhere, see e.g. Wen (1994) and Hornung, Wen & Candler (1994), Hornung (1994).

6.2. Stand-off distance

If equations (3.1) and (3.2) are plotted in the form \tilde{z} vs. the old reaction rate parameter Ω , in the only case where Ω can meaningfully be defined, i.e. for nitrogen,

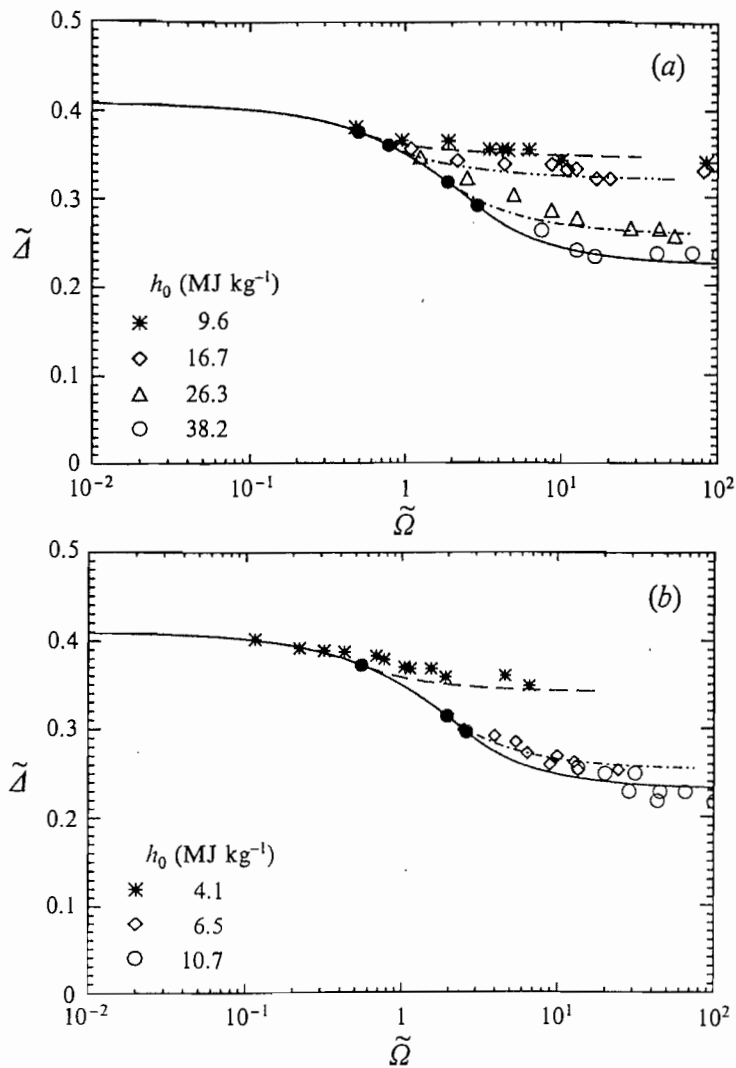


FIGURE 10. Plot of equations (3.1) and (3.2) for selected values of h_0 , resulting in different values of ρ_s/ρ_e . The symbols represent computational results for (a) air (b) carbon dioxide. The full circles are the junction points of equation (3.1) and equation (3.2). Note that the theory underestimates the stand-off distance slightly, consistently with the overestimate of the average density.

the situation presented in figure 9 results. The manner in which this causes the curves for different values of ρ_s/ρ_e to be shifted relative to each other is the reason why the mistake of thinking that only one correlating parameter, $\tilde{\Omega}$, is required, is easily made. The difference becomes clear when the results are plotted against $\tilde{\Omega}$, as in figure 10(a) which presents computational results for the case of air. Note that the value of ρ_s/ρ_e depends on h_0 . Similar results are presented in figure 10(b) for carbon dioxide flows.

In these two plots the slight underestimate of the stand-off distance by the theory that results from the overestimate of the average density is evident in the mid-range of $\tilde{\Omega}$.

Next, we compare the experimentally measured stand-off distance in both these gases with the approximate theory, see figures 11(a) and 11(b). In the case of air, the effect appears to be much smaller than is the case in figure 10(a). This is because the highest value of the enthalpy in the computed cases is 38.2 MJ kg^{-1} , whereas the experiments only range up to 20.6 MJ kg^{-1} . Clearly, the nitrogen in the air is not

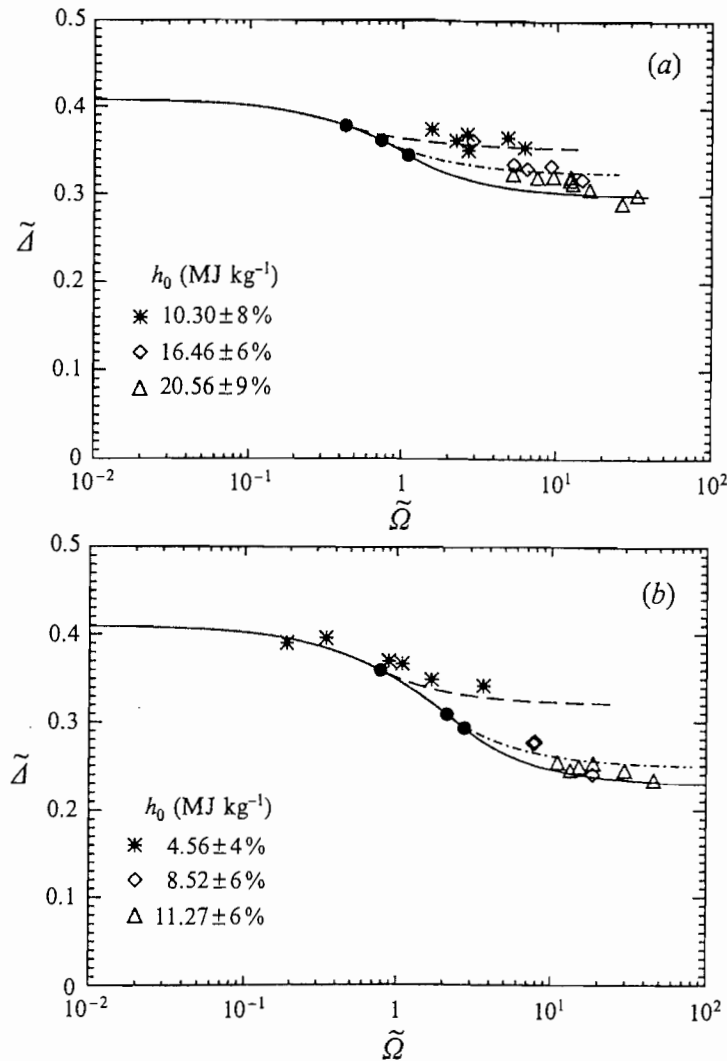


FIGURE 11. Comparison of measured dimensionless stand-off distance with the analytical theory in the case of (a) air flows (b) carbon dioxide flows.

fully dissociated at the latter value. In the case of carbon dioxide, the effect is more dramatic, because it has lower dissociation energies. In the case of air, it may also be seen that most of our experiments were conducted at conditions that are fairly close to equilibrium, since the points all lie on the large- $\tilde{\Omega}$ branch of the theory.

6.3. Stagnation-point heat flux

It remains to present an example of the measured stagnation-point heat flux. The high enthalpies of the flows studied can produce quite substantial values of this quantity. For example, on the small sphere, values up to 30 MW m^{-2} were obtained. The importance of measuring this quantity lies partly in the need to substantiate the reservoir specific enthalpy, h_0 , which is determined indirectly from the measured shock speed in the shock tube. Figure 12 shows measurements of the stagnation-point heat flux in dimensionless form (Stanton number) plotted against the free-stream Reynolds number based on the sphere diameter for three different gases. These are compared with appropriate predictions from the correlation according to Fay & Riddell (1958). The flow and surface conditions are such that full recombination of the dissociated species may be expected to occur. (Catalytic surface.) While the experiments show

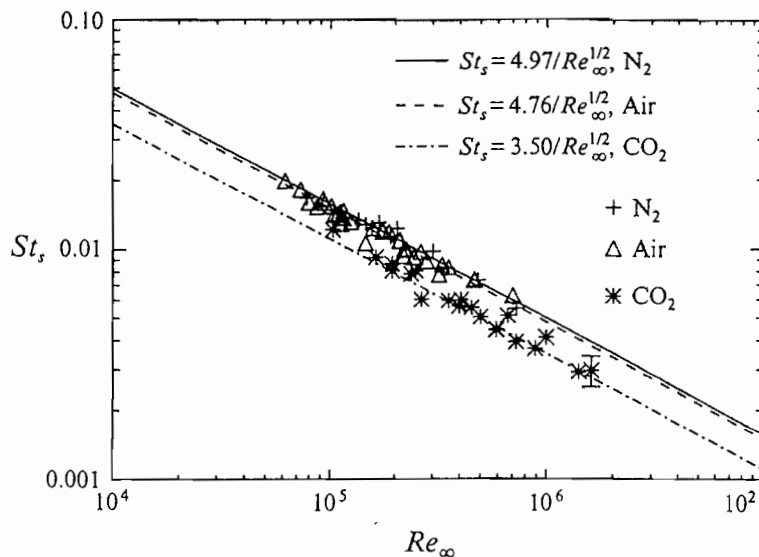


FIGURE 12. Comparison of measured dimensionless stagnation-point heat flux (symbols) with Fay & Riddell's correlation.

substantial scatter, the differences between the different gases are significant and follow the predicted differences. This provides some confirmation of the indirectly determined value of h_0 .

7. Conclusions

Theoretical, numerical and experimental results on the hypervelocity dissociating flow of nitrogen, air and carbon dioxide over spheres have been presented. An approximate theory relating the dimensionless shock stand-off distance to the dimensionless total enthalpy and a reaction rate parameter corrects and extends previous relations of this kind. A previous correlation did not take into account the effects of recombination reactions which appear through the total enthalpy parameter, nor could it deal with mixtures comprising many species with many reactions. By introducing a reaction rate parameter that is a measure of the rate of energy absorption by chemical reactions immediately behind the normal shock, scaled by the rate of input of kinetic energy, it is possible to deal with complex mixtures.

Experimental results from the hypervelocity shock tunnel T5 and numerical computations support the approximate theory and give detailed information about the flow field in the form of measured and computed differential interferograms as well as stagnation-point heat transfer data.

The work leading to the material presented in this paper was sponsored by AFOSR URI grant F49620-93-1-0338 (Dr J. Tishkoff).

REFERENCES

- CANDLER, G. V. 1988 The computation of weakly ionized hypersonic flows in thermo-chemical non-equilibrium. PhD thesis, Stanford University.
- CANDLER, G. V. & MACCORMACK, R. W. 1988 The computation of hypersonic ionized flows in chemical and thermal non-equilibrium. *AIAA Paper* 87-1546.
- FAY, J. A. & RIDDELL, F. R. 1958 Theory of stagnation point heat transfer in dissociated air. *J. Aero. Sci.* **25**, 73-85.

- HORNUNG, H. G. 1972 Non-equilibrium dissociating nitrogen flows over spheres and circular cylinders. *J. Fluid Mech.* **53**, 149–176.
- HORNUNG, H. G. 1992 Performance data of the new free-piston shock tunnel at GALCIT. *AIAA Paper* 92-3943.
- HORNUNG, H. G., CUMMINGS, E. B., GERMAIN, P., SANDERSON, S. R., STURTEVANT, B. & WEN, C.-Y. 1994 Recent results from hypervelocity research in T5. *AIAA Paper* 94-2523.
- HORNUNG, H. G., WEN, C. & CANDLER, G. V. 1994 Hypervelocity flow over spheres. *Acta Mechanica* [Suppl] **4**, 163–170.
- PARK, C. 1988 Assessment of a two-temperature kinetic model for dissociating and weakly ionizing nitrogen. *J. Thermophys. Heat Transfer* **2**, 8–16.
- PARK, C. 1989 Assessment of a two-temperature kinetic model for ionizing air. *J. Thermophys. Heat Transfer* **3**, 233–244.
- PARK, C., JAFFE, J., HOWE, J. & CANDLER, G. V. 1991 Chemical kinetic problems of future NASA missions. *AIAA Paper* 91-0464.
- REIN, M. 1989 SURF: A program for calculating inviscid supersonic reacting flows in nozzles. *GALCIT Rep.* FM 89-1 (see also *Phys. Fluids A* **4**, 873–886, 1992).
- ROCK, S. G., CANDLER, G. V. & HORNUNG, H. G. 1992 Analysis of thermo-chemical non-equilibrium models for carbon dioxide flows. *AIAA Paper* 92-2852.
- ROUSSET, B. 1995 Calibration and study of the contoured nozzle of the T5 free-piston hypervelocity shock tunnel. AeE thesis, Graduate Aeronautical Laboratories, Caltech.
- WEN C.-Y. 1994 Hypervelocity flow over spheres. PhD thesis, Graduate Aeronautical Laboratories, Caltech.
- WEN, C. & HORNUNG, H. G. 1993 Experiments on hypervelocity dissociating flow over spheres. *Proc. 19th Intl Symp. on Shock Waves, Marseille*, to appear.

15 CURVED SHOCK IN IDG

In order to introduce a specific reaction rate into the problem it is necessary to bring in the temperature. This is done via the thermal equation of state

$$T = T(p, \rho, \alpha) \quad \left[\frac{kT'}{2mV_i'^2} = T \right] \quad (15.1)$$

and the substantial derivative

$$\frac{dT}{dt} = \frac{\partial T}{\partial p} \frac{dp}{dt} + \frac{\partial T}{\partial \rho} \frac{d\rho}{dt} + \frac{\partial T}{\partial \alpha} \frac{d\alpha}{dt} \quad (15.2)$$

Using equations (11.4) to replace dp/dt and $d\rho/dt$ we obtain, along a streamline,

$$F \frac{dT}{dt} = T_p \left\{ \rho h_\alpha \frac{d\alpha}{dt} + kG \frac{\rho^2 h_p}{v} \right\} + T_p \left\{ \frac{\rho}{v} h_\alpha \frac{d\alpha}{dt} - kG \frac{\rho^2}{v} \left(h_p - \frac{1}{\rho} \right) \right\} + FT_\alpha \frac{d\alpha}{dt}$$

$$\text{or } F \frac{dT}{d\alpha} = \left(\frac{T_p}{v} + T_p \right) \rho h_\alpha + FT_\alpha + \frac{k\rho^2 G}{v} \left[T_p h_p - T_p \left(h_p - \frac{1}{\rho} \right) \right] \frac{dt}{d\alpha} \quad (15.3)$$

Into this general equation we now substitute the values given by the thermal and caloric equations of state for the ideal dissociating gas (dimensionless variables)

$$\left. \begin{aligned} T &= \frac{p}{\rho} \frac{1}{1+\alpha} \\ h &= \frac{4+\alpha}{1+\alpha} \frac{p}{\rho} + \alpha \Theta \end{aligned} \right\} \quad (15.4)$$

where we have introduced the new dimensionless variable

$$\Theta = \frac{h}{2m} \frac{\Theta_a}{V_i'^2} = \frac{1}{2K}, \text{ see eqn. (5.8).}$$

Further, we simplify the reaction rate equation by assuming

$$\varepsilon = \frac{V_i' k_0'}{C' \rho' T'^2 (1-\alpha)} \quad (15.3)$$

to be a constant for a given set of free stream conditions in order to be able to treat the problem analytically. In view of the dominance of the exponential temperature dependence this assumption is, in fact, quite good. The reaction rate is then

$$\frac{d\alpha}{dt} = \frac{1}{\varepsilon} e^{-\theta/T} \quad (15.4)$$

Note that this form completely ignores the recombination rate. For a large class of flows with convex shocks this assumption is very well justified. For example, in the case of a reentry vehicle in the regime where nonequilibrium effects are important, the characteristic length for dissociation after the bow shock is typically 1 cm, whereas the characteristic length for recombination is typically 20 m. In the case of a convex shock whose curvature radius is typically 2 m, the expansion following the shock causes the recombination length to increase further by an order of magnitude or more, so that

Recombination just does not occur (Note: straight or concave shocks different!)

For typical reentry flows, ε is approximately 10^{-5} to 10^{-6} .

Substituting from (15.2) in (15.1) we obtain

$$\frac{dT}{dx} = \frac{(1 - \rho v^2/p)\theta + T + \varepsilon k v G e^{\theta/T}}{(4+\alpha)(1 - \frac{3}{4+\alpha} \frac{\rho v^2}{p})} \quad (15.5)$$

Because of the exceptionally strong temperature dependence of the exponential term, this equation has remarkably interesting properties:

Near the shock, where the temperature is high ($T/\theta \sim 0.1$) the shock curvature is unimportant, because its coefficient ε mult. by the exponential term is approximately 10^2 . With increasing distance from the shock, both the dissociation and the expansion associated with the convex shock cause the temperature to fall. This rapidly raises $e^{\theta/T}$. E.g. when

T/θ has dropped from 0.1 to 0.067, the exponential term has grown by a factor of 150. Thus, the curvature term begins to play an important part.

The region in which the exponential term is comparable with the other terms of the numerator in (15.5) ~~is~~ ^{we} called the transition

region.

As we proceed along the streamline beyond the transition region, the exponential term rapidly acquires complete dominance because the expansion associated with the convex shock continues to reduce the temperature. The flow is then frozen, no further dissociation occurs along the streamline, and recombination is, of course, excluded a priori.

This phenomenon of the "quenching" of the dissociation reaction by the temperature drop following a convex shock is important and largely unknown. In order to understand it better, we simplify equation (15.5) further.

Assume that $M_1^2 = \infty$ and $\alpha_1 = 0$. For a straight shock G is then given by

$$(G)_{k=0} = \left[3(1-m^2) - \frac{m^2}{P} \right] \left(1 - \frac{1}{P} \right), \quad \text{--- (15.6)}$$

where $m = \sin \beta$. For $ky \ll 1$, i.e. close to the shock in terms of the curvature radius, we may approximate G after a curved shock by

$$G = 3(1-m^2) + O(\delta), \quad \text{--- (15.7)}$$

$$\text{where } \delta = \frac{1}{\ln(b\varepsilon)^{-1}} \ll 1, \quad b = \frac{3(1-m^2)}{m} k, \quad \text{--- (15.8)}$$

see Homing [9]. The same approximation leads to

$$\frac{\rho v^2}{p} = \frac{T(1+\alpha)}{m^2} \left(1 - \frac{1}{\rho}\right)^2. \quad (15.9)$$

Substituting into (15.5) gives

$$\frac{dT}{dx} = - \frac{\theta - T \left\{ (1+\alpha) \theta / m^2 - 1 \right\} + b \varepsilon (1+\alpha) T e^{\theta/T}}{(4+\alpha) \left\{ 1 - \frac{3(1+\alpha)}{4+\alpha} \frac{T}{m^2} \right\}}. \quad (15.10)$$

Far from the shock the ε term dominates and only

$$\frac{dT}{dx} = - \frac{b \varepsilon (1+\alpha) T e^{\theta/T}}{4+\alpha} \quad (15.11)$$

remains. Together with equation (15.6) this gives

$$\frac{dT}{dt} = - \frac{1+\alpha}{4+\alpha} b T, \quad (15.12)$$

$$\text{or } T = T_0 \exp \left(- \frac{1+\alpha_0}{4+\alpha_0} b t \right), \quad (15.13)$$

where α has been replaced by α_0 , the frozen value after quenching, since this corresponds to the frozen solution appropriate to a convex shock:

$$\left. \begin{aligned} p &= p_0 e^{-bt} \\ \rho &= \rho_0 \exp \left(- \frac{3bt}{4+\alpha_0} \right) \end{aligned} \right\} \quad (15.14)$$

the curvature being proportional to b , see (15.8).

Note that in this frozen solution $p \sim \rho^\gamma$ where γ is $(4+\alpha_0)/3$ as expected for IDG ^{frozen} isentropic flow.

The model equation (15.10) has been solved by matched asymptotic expansions (as well as numerically), see [2]. The asymptotic solution gives the values that are obtained by extrapolating the frozen far-field solution back to the shock explicitly:

$$\begin{aligned} \alpha_0 &= 4A_1 \left\{ 1 - \frac{1}{A_1} - \delta - \delta^2 \ln \delta - \delta^2 \left[\frac{1}{6} \lambda - 1 + \ln \left[\frac{1}{\delta(4A_1 - 3)} \right] \right] \right\} + \dots \\ T_0 &= \theta \delta \left\{ 1 + \delta \ln \delta + \delta \ln [4A_1 - 3] \right\} + \dots \\ \rho_0 &= \frac{p_2 + (4A_1 - 3)\theta B_1}{\theta \delta [4A_1 - 3]} \left\{ 1 - \delta \left[\frac{1}{p_2 + (4A_1 - 3)\theta B_1} + \ln [\delta(4A_1 - 3)] - \frac{4A_1}{4A_1 - 3} \right] \right\} + \dots \end{aligned} \quad (15.15)$$

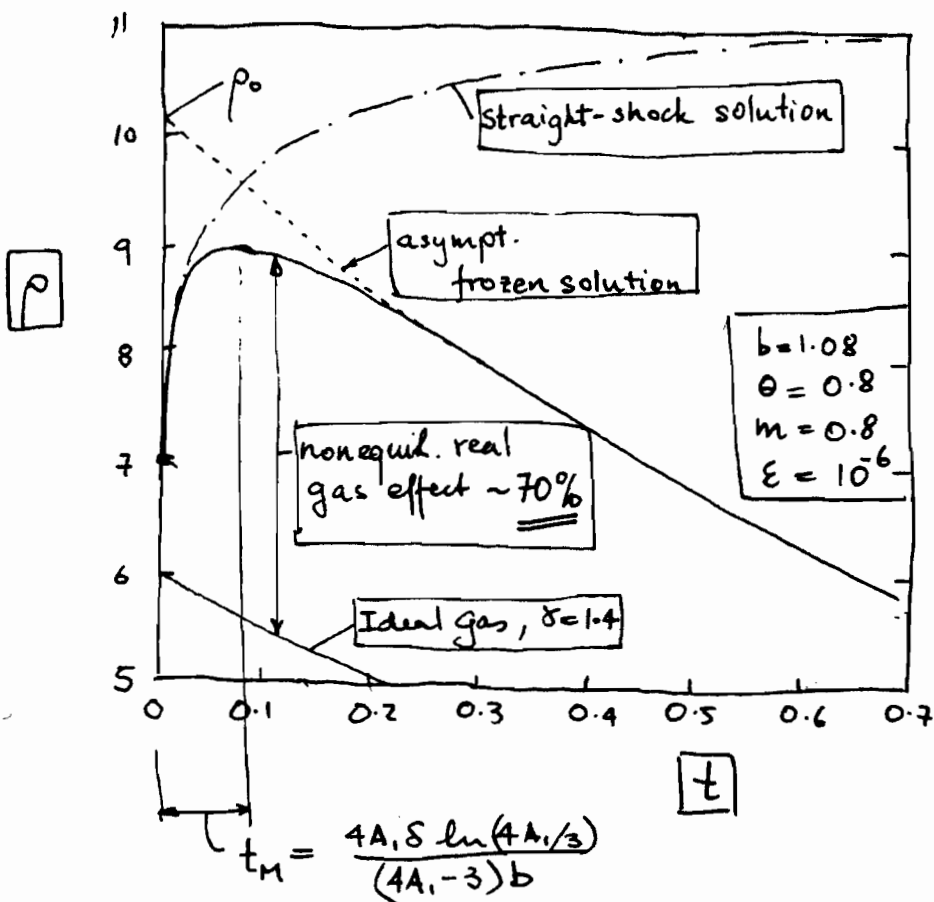
where $\lambda = \frac{3}{4} \theta / m^2$, $A_1 \doteq 1 + 0.124 m^2 / \theta$

$p_2 = 6m^2 / 7\theta$, $\delta = 1 / [\ln \{ (b\epsilon)^{-1/2} \}]$

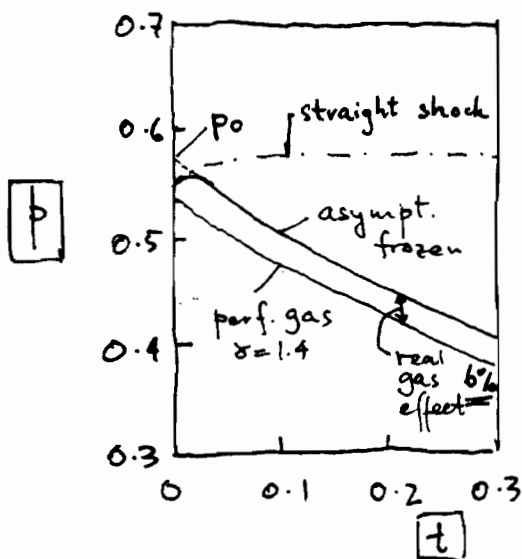
$B_1 \doteq \frac{6m^2}{49\theta} + \frac{1}{2} \left\{ 1 + \frac{3}{1 + \frac{m^2}{2\theta}} - \frac{\theta}{m^2} \right\} \left(\frac{6m^2}{49\theta} \right)^2$

$m = \sin \beta$.

The solution gives, as an example, the density distribution along a streamline. This is shown on the next page. Note how the density first follows the straight-shock solution, then departs from this in the transition solution and then follows the frozen solution which appears to have come from the value ρ_0 if extrapolated back to the shock.



Note that the time to the middle of the transition region t_M is also explicitly obtained. It is inversely proportional to the shock curvature and inversely proportional to the log of the reaction rate.



The lower diagram shows that the real gas effect is much more important in the density than in the pressure.

If the reaction is restricted to a thin layer near the shock this solution enables us to

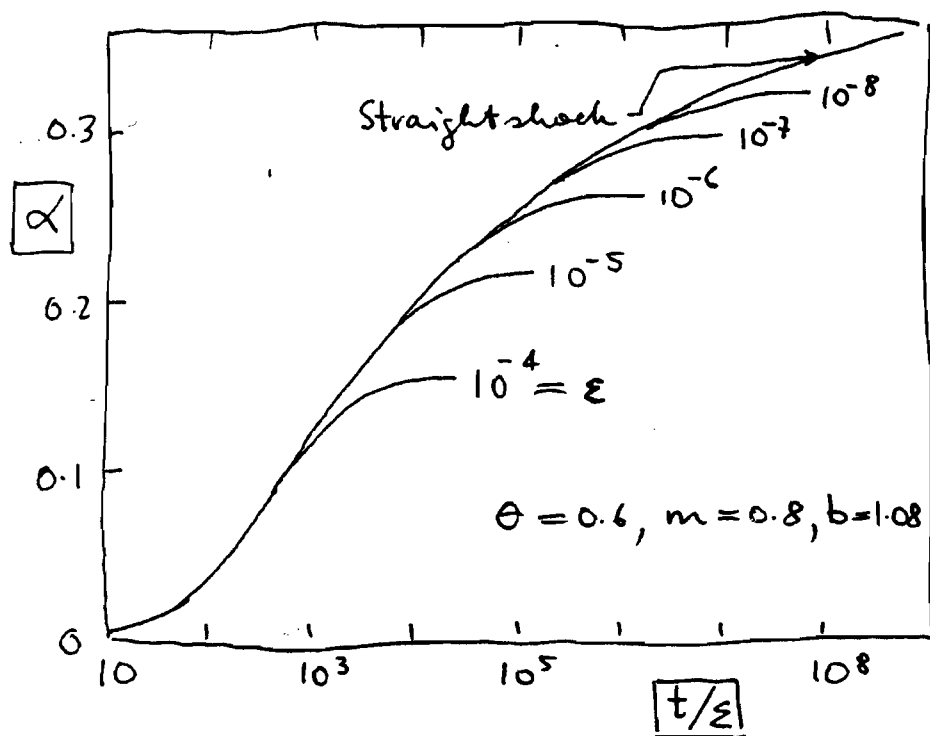
incorporate the reacting layer in the shock and to give the effective values for the downstream frozen flow explicitly. This is tantamount to having

a new set of shock-jump conditions which involve not only the freestream conditions and shock angle, but in addition the shock curvature and reaction rate. Note that this leads to a different value of α_0 for each streamline, so that the composition and entropy (while remaining constant along the streamlines after quenching) certainly vary across the streamlines.

Finally, for this chapter, we show the solution ^{for α} for

a given free stream (θ) and a given shock shape (m, b) with ε as a parameter.

As the reaction rate is increased the straight shock solution is approached more and more closely and the value of α_0 increases.

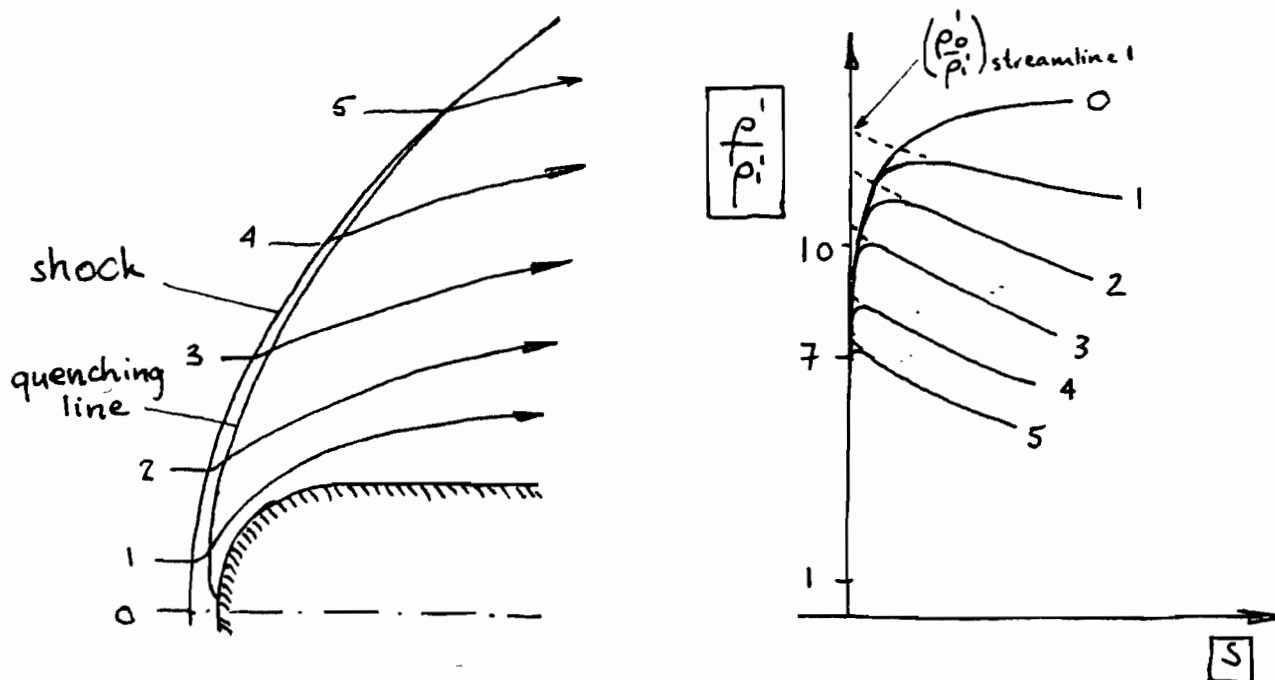


References

- [9] Hammy J. Fluid Mech. (1976) 74 pp. 143-159
 [10] Stalker R.J. AGARD FDP Conference Bristol April 1987.

16 BLUNT BODY FLOWS

The results of the theory of dissociation quenching can now be used directly to show its consequences for blunt body flows.



The sketch shows 5 streamlines in such a flow field and the corresponding density distribution along them. We have chosen the case of nitrogen flow at the free-stream conditions

$$V_i' = 6 \text{ km/s}, \quad \rho_i' = 5 \times 10^{-6} \text{ g/cm}^3, \quad \alpha_i = 0$$

and with shock curvature at the stagnation pt. of

$$k'_0 = 1/(20 \text{ cm}).$$

This gives us the dimensionless parameters

$$\Theta = \frac{k' \theta_d'}{2m' V_1'^2} = \frac{R'_{N_2} \theta_d'}{V_1'^2} = 0.93$$

$$\varepsilon = \frac{V_1' k_0'}{C'(\rho_1'.7)\left(\frac{6}{49} \theta_d'\right)^2} = 8 \times 10^{-6}$$

Further, we assume that the shock shape is a catenary, for which the curvature is related to the slope by

$$k = m^2.$$

Hence, from (15.8)

$$b = 3(1-m^2)m,$$

and we can assign a value for each of ρ_0 , α_0 , T_0 to every value of the shock slope ($m = \sin \beta$) at which the streamline of interest has pierced the shock, by using equations (15.15)

With this technique it is therefore possible to compute the downstream flow-field of a blunt body by perfect-gas computations, but with the difference that the composition of the gas, and therefore its γ varies with the streamfunction in a manner known from the application of the theory of chapter 15 and from the shock shape.

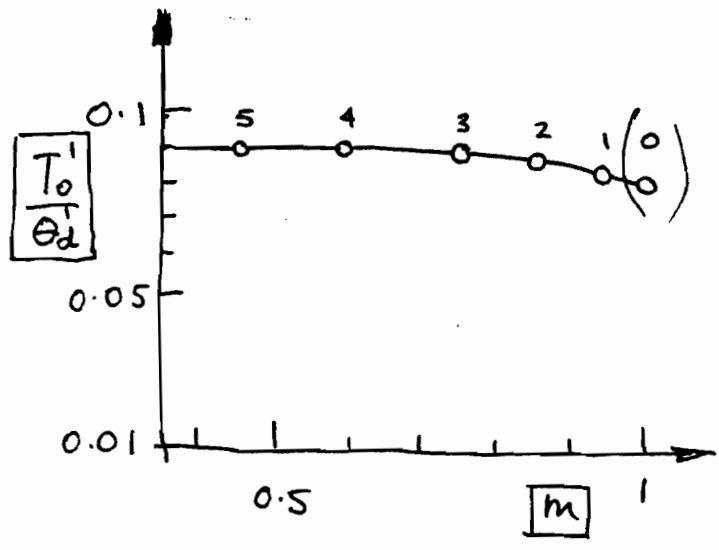
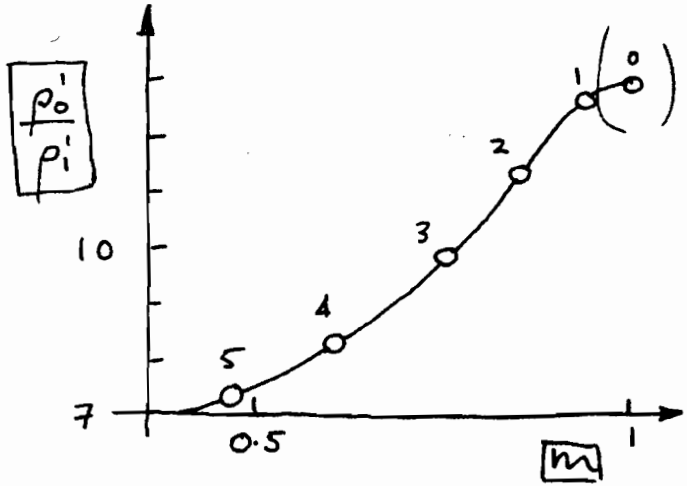
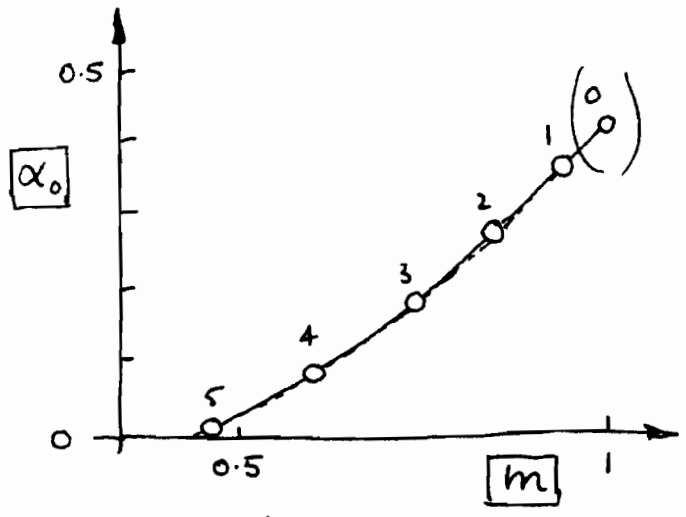
Equation 15.15 shows, incidentally, that

$$\left. \begin{array}{l} \rho_0 \sim m^2 \\ \text{and } T_0 \sim \text{indepdt of } m. \end{array} \right\} \text{————— (16.1)}$$

This contrasts with the situation at the frozen shock

$$\left. \begin{aligned} \rho_2 &\sim \text{indepdt of } m \\ T_2 &\sim m^2. \end{aligned} \right\} \text{ ————— (16.2)}$$

The manner in which the effective shock conditions



vary with $\sin \beta = m$ for the example considered here is shown in the accompanying sketches.

On each streamline the gas behaves like a perfect gas, however with a different composition on each streamline. Also, the entropy is constant along each streamline, but has a different value on each streamline. The latter is true also for a perfect gas with spatially uniform composition, but the entropy, which is

$$s(m, M_1) = \ln \left(\frac{P_2}{\rho_2^{(\gamma/\delta)}} \right) \text{ — (16.3)}$$

for a perfect gas, diatomic

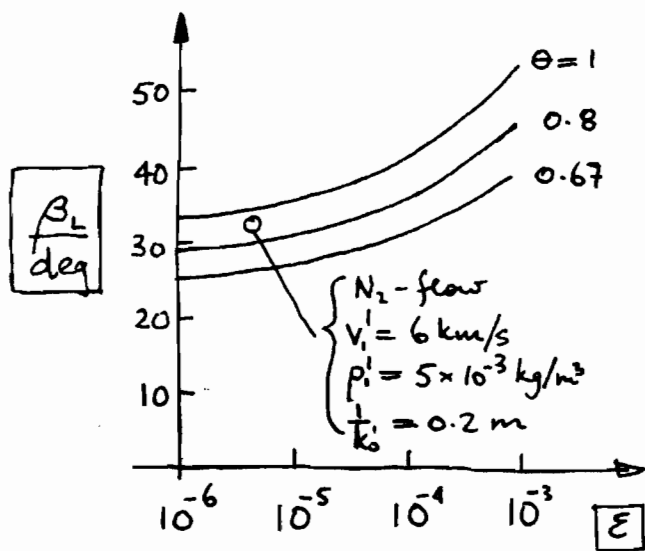
will be

$$s(m, k, \epsilon, \theta) = \ln \left\{ \left[\frac{p_0}{\rho_0} \left(\frac{4+k}{3} \right) \right]^{\frac{3}{1+\alpha_0}} \right\} \quad (16.4)$$

in the case of the ideal dissociating gas.

Outside of the streamline S , dissociation ceases to affect the flow significantly. There exists a limiting streamline in blunt body flows, outside of which no real-gas effects occur at all. The value of the shock angle β_L at which this limiting streamline crosses the shock is of interest.

It is plotted in the sketch for the case of a catenary shock ($k = m^2$) against ϵ and θ .



It should be emphasized at this point that both perfect gas flows and equilibrium flows differ significantly from non-equilibrium flows. The main difference to the equilibrium

case lies in the fact that the equilibrium flow exhibits a slightly higher α than α_0 at the shock, and recombination occurs thereafter along the streamline.

To show the transition from frozen to equilibrium blunt body flow, a set of numerical computations of nitrogen flow over a circular cylinder ~~is~~ is shown in the diagram. Lines of constant density are labelled by the value of ρ and examples of lines of constant temperature and lines of constant α are also given. In the flows with small ϵ the qualitative features of flows with dissociation quenching are clearly recognizable.

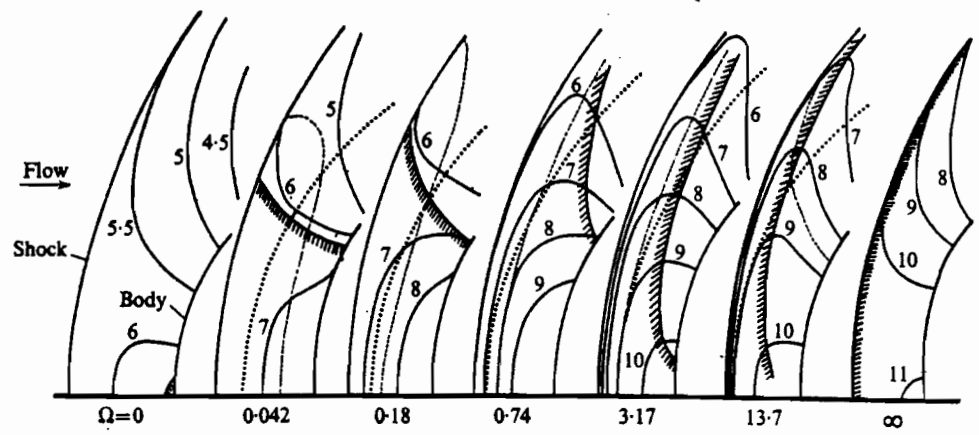
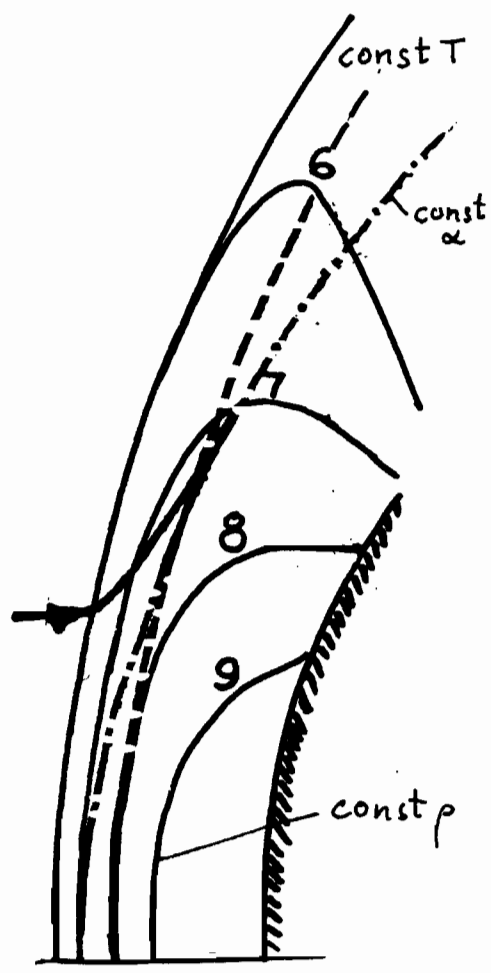


FIGURE 9. Density fields for flow over a cylinder as calculated by Garr & Marrone's method, with frozen and equilibrium flow as calculated by Lomax & Inouye's method. —, ρ/ρ_∞ ; \dots , typical α contour; ---, typical temperature contour; wavy, approximate boundary of region influenced by non-equilibrium dissociation.

In particular, choosing the case $\epsilon = 10^{-3}$, and showing it at a larger scale, together with a streamline, see next page, it can be seen that the streamline and the line of constant α merge after the density maximum, thus showing that

the composition remains constant along the streamline thereafter.



$\epsilon = 10^{-3}$

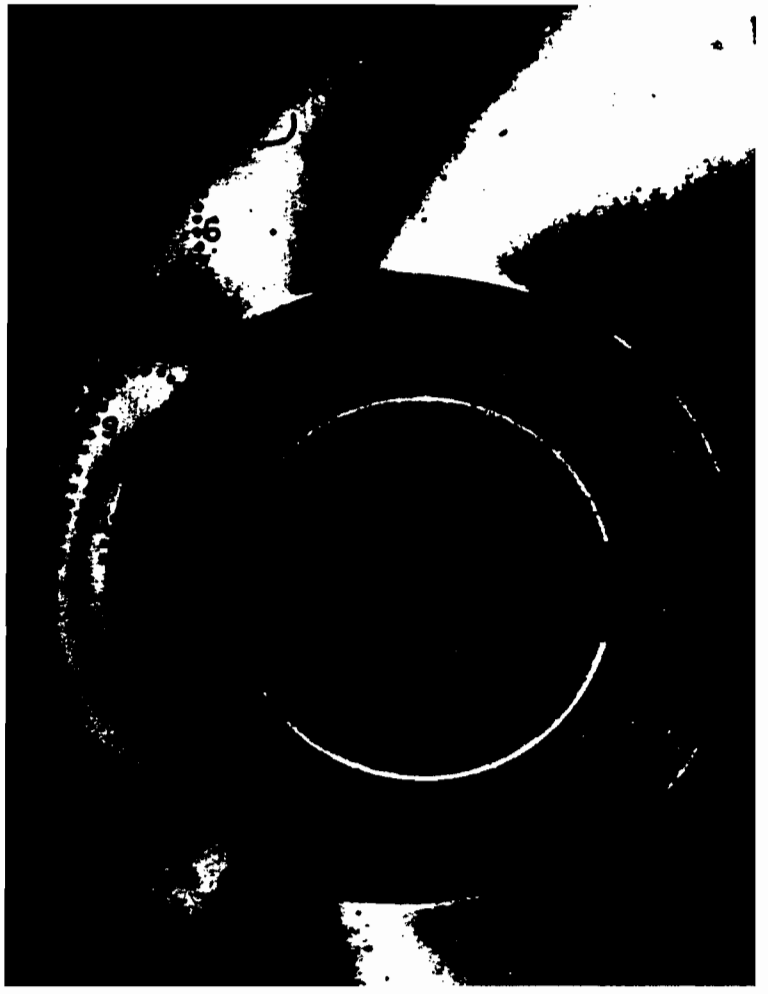
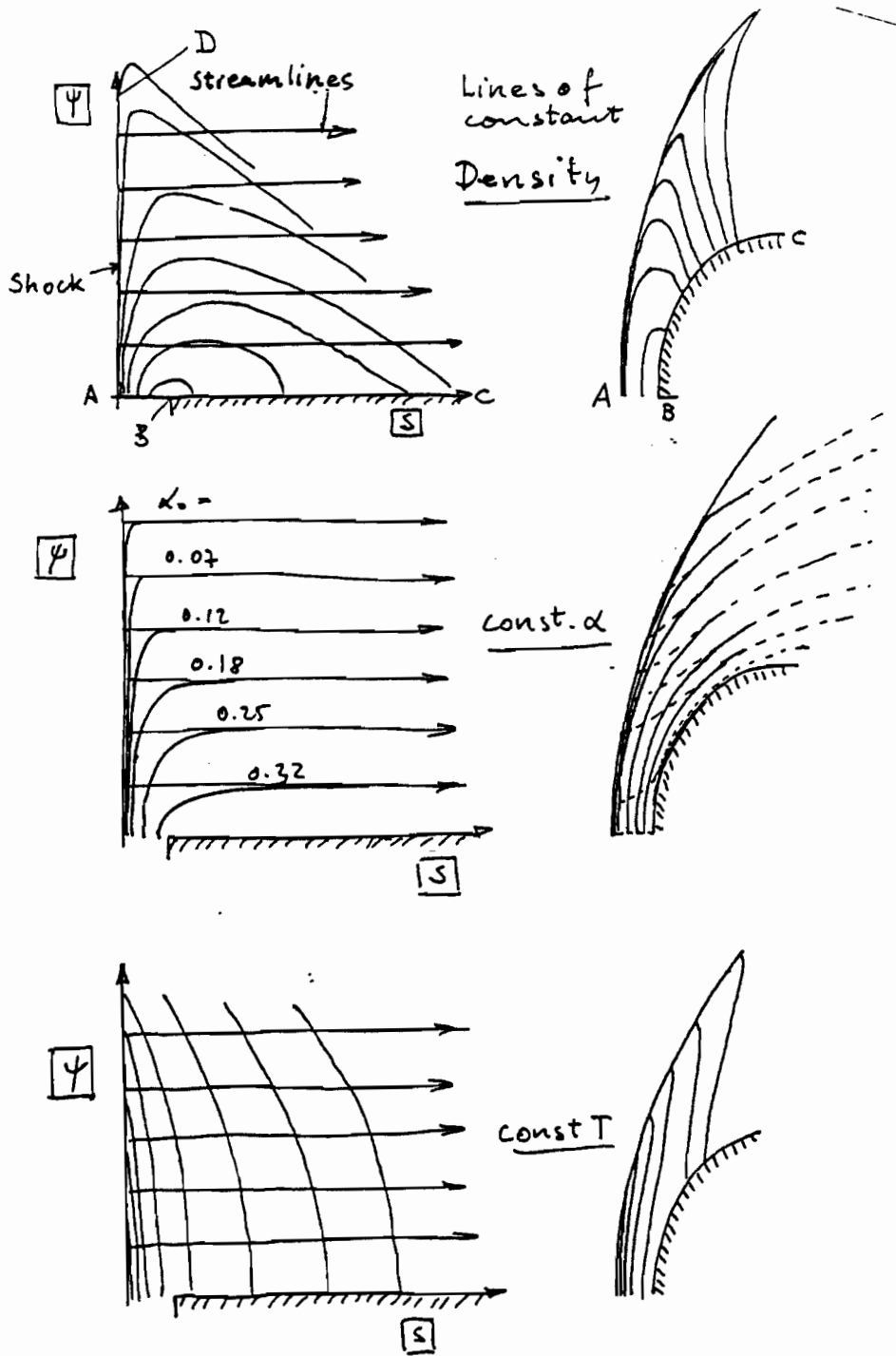


FIGURE 23. Comparison of fringe pattern at $\mu = 0.46$, $\alpha_{\infty} = 0.07$, diameter = 2 in. with density pattern calculated for $\Omega = 0.57$ by Garr & Marrone's method with the Appleton *et al.* reaction rate. Numbers on dotted lines indicate density in multiples of the free-stream density.

Next to this computed flow we show a comparison between an interferogram giving (approximately) lines of constant density in the form of interference fringes and a superimposed computed set of lines of constant density. [$\theta = 1.08$, $\alpha_{\infty} = 0.07$, $\frac{1}{k_0} = 3\text{cm}$, $\epsilon = 1.5 \times 10^{-3}$]. The fringes are only approximately lines of constant density because the refractive index depends slightly on α . The qualitative features as well as the density

levels agree. It is instructive to show the flow field in a plot of stream function Ψ vs. distance along the streamline:



Vorticity generated by a curved shock

To derive an expression for the vorticity generated by a curved shock, without making any assumptions about the properties of the gas, consider first the general momentum equation

$$\frac{\partial \underline{u}}{\partial t} + (\text{grad } \underline{u}) \underline{u} = -\frac{1}{\rho} \text{grad } p + \frac{1}{\rho} \text{div } \underline{R}$$

where the stress tensor \underline{S} has been decomposed into

$$\underline{S} = -p \underline{I} + \underline{R},$$

\underline{R} being the frictional component of the stress. Using the identity

$$(\text{grad } \underline{u}) \underline{u} = (\text{curl } \underline{u}) \times \underline{u} + \text{grad} \left(\frac{u^2}{2} \right)$$

the momentum equation may be written

$$\frac{\partial \underline{u}}{\partial t} - \underline{u} \times \underline{\omega} = -\frac{1}{\rho} \text{grad } p - \text{grad} \left(\frac{u^2}{2} \right) + \frac{1}{\rho} \text{div } \underline{R} \quad (1)$$

If local thermodynamic equilibrium applies, $\frac{1}{\rho} \text{grad } p = \text{grad } h - T \text{grad } S$. (2)
Otherwise, a term of the form $(\mu_{N_2} - 2\mu_N) d\alpha$

also has to be included, but we shall see that by using the results of chapter 15, we may use the thin-reacting-layer assumption of fast reaction quenched flows to lump this term into the shock. Thus take l.t.e. assumption outside of the thin reacting layer.:

(1) and (2) give, for steady, frictionless flow:

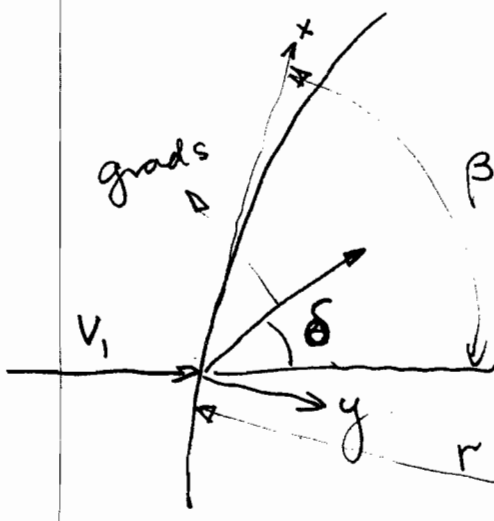
$$\boxed{-\underline{u} \times \underline{\omega} = -\text{grad } h_0 + T \text{grad } s} \quad (3)$$

If there is no heat conduction, $\text{grad } h_0 = 0$ and

$$\boxed{-\underline{u} \times \underline{\omega} = T \text{grad } s} \quad (4)$$

This is called Crocco's vortex theorem.

Now consider a curved shock:



$$dh = T ds + \frac{1}{\rho} dp$$

Across shock

$$\rho_1 v_1 = \rho_2 v_2$$

$$p_1 + \rho_1 v_1^2 = p_2 + \rho_2 v_2^2$$

$$h_1 + \frac{v_1^2}{2} = h_2 + \frac{v_2^2}{2}$$

Solve for $p_2 = p_1 + \rho_2 v_2^2 - \rho_1 v_1^2$

Replace v_2 from continuity

$$\begin{aligned} p_2 &= p_1 + \rho_1 v_1^2 \left(\frac{1}{\rho_1} - \frac{1}{\rho_2} \right) \\ &= p_1 + \rho_1 v_1^2 \sin^2 \beta \left(1 - \frac{\rho_1}{\rho_2} \right) \\ &= p_1 + \rho_1 v_1^2 \sin^2 \beta (1 - f) \end{aligned}$$

Differentiate w.r.t. β :

$$\frac{dp_2}{d\beta} = \rho_1 v_1^2 \left\{ 2 \sin \beta \cos \beta (1 - f) - \sin^2 \beta \frac{df}{d\beta} \right\}. \quad (5)$$

Solve for

$$\begin{aligned} h_2 &= h_1 + \frac{1}{2} (v_1^2 - v_2^2) \\ &= h_1 + \frac{1}{2} v_1^2 \sin^2 \beta (1 - f^2) \end{aligned}$$

Differentiate w.r.t. β :

$$\begin{aligned} \frac{dh_2}{d\beta} &= \frac{1}{2} v_1^2 \left\{ (1 - f^2) 2 \sin \beta \cos \beta \right. \\ &\quad \left. - 2 \sin^2 \beta f \frac{df}{d\beta} \right\}. \quad (6) \end{aligned}$$

Now determine

$$T \frac{ds_2}{d\beta} = \frac{dh_2}{d\beta} - \frac{1}{\rho} \frac{dp_2}{d\beta}$$

$$T_2 \frac{ds_2}{d\beta} = V_1^2 \sin \beta \left\{ (1-f^2) \cos \beta - \sin \beta \frac{df}{d\beta} \right. \\ \left. - f \left[2(1-f) \cos \beta - \sin \beta \frac{df}{d\beta} \right] \right\}$$

$$= V_1^2 \sin \beta \left\{ \cos \beta (1-f^2 - 2f + 2f^2) \right. \\ \left. + \sin \beta (f - f) \frac{df}{d\beta} \right\}$$

$$T_2 \frac{ds_2}{d\beta} = V_1^2 \sin \beta \cos \beta (1-f)^2. \quad \text{--- (7)}$$

Now the entropy is constant along the streamline (l.t.e.). Hence the vector $\text{grad } s$ is normal to the streamline. Hence write Crocco as

$$T_2 |\text{grad } s_2| = \frac{T_2 |ds_2/dx|}{\sin(\beta - \delta)} = \frac{-\omega_2 V_1 \cos \beta}{\cos(\beta - \delta)} \quad \text{--- (8)}$$

Since $T_2 \frac{ds_2}{dx} = T_2 \frac{ds_2}{d\beta} \frac{d\beta}{dx} = T_2 \frac{ds_2}{d\beta} \cdot \frac{1}{r}$

(8) gives with (7)

$$\omega_2 = -\frac{V_1}{r} \frac{(1-f)^2}{f} \cos \beta, \quad \text{--- (9)}$$

Where we have used

$$\frac{\rho_2}{\rho_1} = \frac{1}{f} = \frac{\tan \beta}{\tan(\beta - \delta)}$$

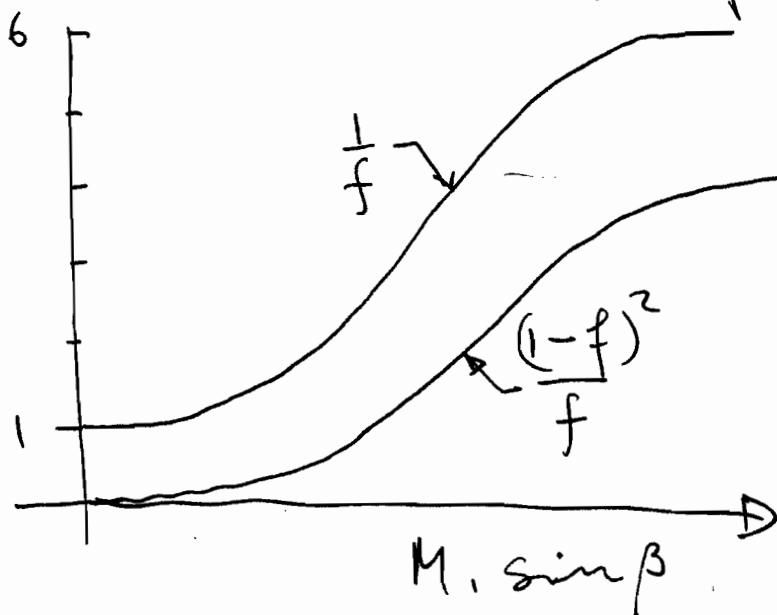
and $V_2 = V_1 \frac{\cos \beta}{\cos(\beta - \delta)}$.

(9) is a general relation for the vorticity downstream of a shock of curvature radius r , for any gas in l.t.e.

The manner in which the gas properties enter this result is through the density ratio f . For a perfect gas,

$$f = \frac{\gamma - 1 + \frac{2}{M_1^2} \sin^2 \beta}{\gamma + 1}$$

and with $\gamma = 1.4$ the function $(1-f)^2/f$



behaves as shown.

At $\beta = \frac{\pi}{2}$,

$\omega_2 = 0$ because of the $\cos \beta$ term.

At $\beta = \arcsin \frac{1}{M_1}$,

$\varepsilon = 1 \Rightarrow \omega_2 = 0$

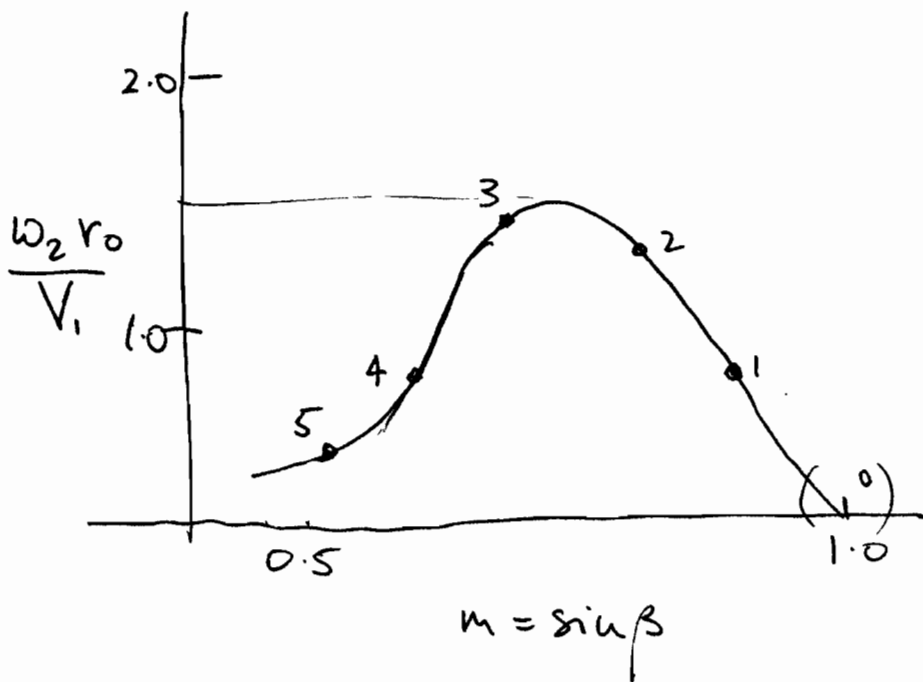
For a catenary shock,

$$\frac{r_0}{r} = \sin^2 \beta,$$

So
$$\frac{w_2 r_0}{V_1} = \sin^2 \beta \cos \beta \frac{(1-f)^2}{f}$$

With a thin reacting layer and dissociation quenching, the value of f must be replaced by ρ_1/ρ_0 where ρ_0 is the effective shock value of the density.

Hence, for the example of the 5 streamlines of chapter 16, the distribution of



velocity is such as to give a maximum at around $\beta = 60^\circ$. This maximum is larger than for

a perfect gas in the approximate ratio ^{in which} of the density ratio across the shock is larger.

Shock layer instability near the Newtonian limit of hypervelocity flows

H. G. Hornung^{a)}

Graduate Aeronautical Laboratories, California Institute of Technology, MS 105-50, Pasadena, California 91125

P. Lemieux

Exponent, Inc., 5401 McConnell Avenue, Los Angeles, California 90066

(Received 13 February 2001; accepted 15 May 2001)

The curved bow shock in hypersonic flow over a blunt body generates a shear layer with smoothly distributed vorticity. The vorticity magnitude is approximately proportional to the density ratio across the shock, which may be very large in hypervelocity flow, making the shear layer unstable. A computational study of the instability reveals that two distinct nonlinear growth mechanisms occur in such flows: First, the vortical structures formed in the layer move supersonically with respect to the flow beneath them and form shock waves that reflect from the body and reinforce the structures. Second, the structures deform the bow shock, forming triple points from which shear layers issue that feed the main shear layer. Significant differences exist between plane and axisymmetric flow. Particularly rapid growth is observed for free-stream disturbances with the wavelength approximately equal to the nose radius. The computational study indicates that the critical normal shock density ratio for which disturbances grow to large amplitudes within a few nose radii is approximately 14. This served as a guide to the design of a physical experiment in which a spherical projectile moves at high speed through propane or carbon dioxide gas. The experiment confirms the approximate value of the critical density ratio, as well as the features of the computed flows. Comparisons of calculations of perfect gas flows over a sphere with shadowgraphs of the projectile show very good agreement. The Newtonian theory of hypersonic flow, which applies at high density ratio, makes the assumption that the flow remains smooth. The results show that high density ratio also causes this assumption to fail. © 2001 American Institute of Physics. [DOI: 10.1063/1.1383591]

I. INTRODUCTION

A curved shock wave in a steady, uniform free stream generates vorticity

$$\omega = U_\infty \kappa \cos \beta (1 - \rho_\infty / \rho)^2 \rho / \rho_\infty \quad (1)$$

by the baroclinic mechanism within the shock wave (see Lighthill,¹ and Hayes and Probstein²). Here, U_∞ , ρ_∞ are free-stream speed and density, and β , κ are the shock angle and curvature at the point of interest. In hypervelocity flow of a molecular gas over a blunt body the post-shock temperature is so high that substantial dissociation occurs. One consequence is that the endothermic dissociation process absorbs a large fraction of the thermal energy of the gas, so that the temperature falls dramatically and the density rises correspondingly. Thus the density ratio, ρ / ρ_∞ , across the shock and (thin) reaction zone is very large. For example, in air flows at 7 km/s, a density ratio of 12 is typical, while in carbon dioxide flows, such as occur, e.g., in traversing the atmosphere of Mars, the density ratio may be as high as 28. This is the kind of flow of interest here. With such high density ratio, the inverse of the ratio may be neglected compared with 1 in Eq. (1).

Consider Eq. (1) in connection with flow over a blunt body. At the normal shock point, ω is zero, because the shock angle is 90° . Far downstream, where (on an asymptotically slender body) the shock approaches a straight Mach wave, the density ratio becomes one and the curvature goes to zero, so ω again vanishes. Somewhere between these limits a maximum value of ω must therefore occur. With typical shock shapes this maximum lies at approximately $\beta = 60^\circ$. Since the shock angle and curvature vary smoothly with distance along the shock, a smooth distribution of vorticity results. The shock generates a shear layer with a smooth vorticity maximum. Since the flow is compressible, the vorticity does not remain constant along streamlines even in the absence of diffusion, but is influenced by the density and pressure fields.

The stability of a shear layer with distributed vorticity has been studied extensively (see, e.g., Drazin and Reid,³ or, more relevant to the present investigation, Zhuang *et al.*⁴). A qualitative feature is that, other things being equal, layers with higher maximum vorticity and smaller thickness are more unstable (a result that follows already from scaling arguments). Not only does the high density ratio of hypervelocity flows cause proportionately higher maximum vorticity in the layer, but it also causes the shock layer, and therefore the shear layer, to be proportionately thinner. It may therefore be expected that the shear layer that results from shock

^{a)}Telephone: 626-395-4551; fax: 626-449-2677; electronic mail: hans@galcit.caltech.edu

curvature in hypervelocity flows becomes unstable at sufficiently high density ratio.

The instability of the layer has been considered by aerodynamicists for some time as a cause of boundary layer transition. This is relevant, because, far downstream the shear layer will eventually be ingested by the growing boundary layer. Since the shear layer represents the edge of a high-entropy layer close to the body, this is also known as entropy-layer swallowing (see, e.g., Stetson *et al.*⁵). There is a significant difference between inviscid flow in axial and plane symmetry in this phenomenon. The reason is that, with axial symmetry, the stretching term in the vorticity equation causes the vorticity on the body surface to be finite, while it is zero in plane symmetry; see Hayes and Probstein.² The result is that the shear layer is further from the body in plane flow so that, as regards entropy-layer swallowing, plane and axisymmetric flows behave very differently.

At a curved shock, vorticity is imparted to a material element. Even in plane flow, the vorticity of the material element is subsequently changed by the fact that the density and pressure of the material element change. In the particular case of homenthalpic, plane, steady flow of a perfect gas, the ratio of vorticity to pressure is conserved along a streamline (see, e.g., Vaszonyi⁶). Thus if the pressure is constant along a streamline, then so also is the vorticity. A relatively simple configuration for an exploratory study of the instability of a shear layer in the shock layer of a blunt body in hypersonic flow is therefore a hemicylindrically blunted wedge. This has the necessary curved bow shock followed by a constant-pressure region downstream. To illustrate the behavior of the shear layer generated in such a flow, Fig. 1 shows an example of an Euler computation of flow over a cylindrically blunted 30° wedge. Note the location of the region of maximum shear relative to the body. In plane flow, the shear layer remains at a constant distance from the wedge surface, and the growth of the shock layer outside of the shear layer leaves the shear layer virtually unchanged.

In the following, we therefore start with a computational study of the stability of the shear layer in such a flow. A disturbance is introduced to the flow by imposing an unsteady boundary condition at the inflow boundary. This study is then followed by a similar one on axisymmetric flow, to examine the difference in behavior discussed earlier. Finally, the experience gained from the computational studies is used to design a physical experiment. It turns out that in the latter it is necessary to choose a differently shaped model. Computations of this new configuration are therefore added to compare with the physical flow.

II. COMPUTATIONAL EXPERIMENT

A. The computational setup

For the computations, the software system Amrita, constructed by James Quirk (see Quirk⁷) was used. Amrita is a system that automates and packages computational tasks in such a way that the packages can be combined (dynamically linked) according to instructions written in a high-level scripting language. The present application uses features of Amrita that include the automatic construction of different

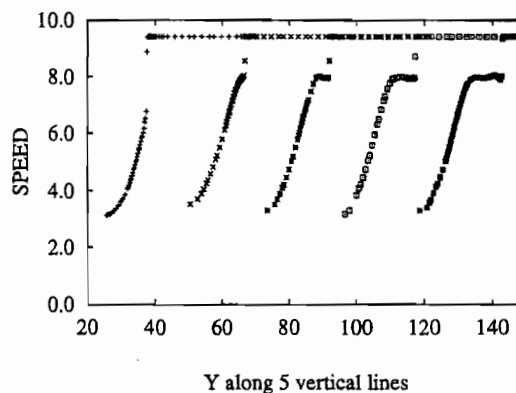
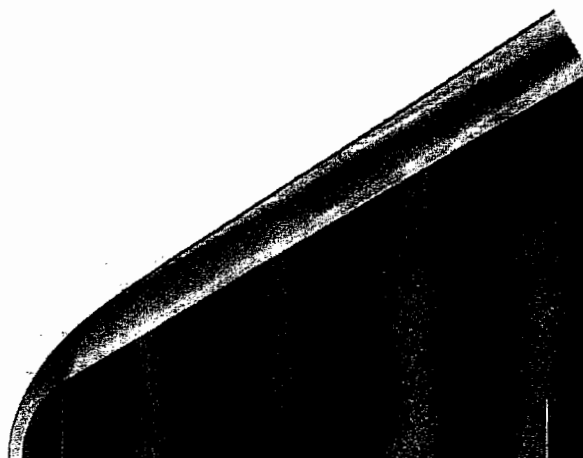


FIG. 1. Top: Pseudo-schlieren image of computed flow over cylinder-wedge, $M_\infty=9$, $\gamma=1.095$, making the normal shock density ratio 17.5. Grayshading is a monotonic function of the magnitude of the fractional density gradient. The dark region corresponds approximately to the shear layer. The white line in the flow field is the sonic line. Bottom: Five profiles of speed across the layer uniformly spaced between the two white lines show that the shear layer does not change significantly with downstream distance.

Euler solvers, automatic documentation of the codes, automatic adaptive mesh refinement according to simply chosen criteria, and scripting-language-driven computation, archiving, and post-processing of the results. The automation of the assembly and sequencing of the tasks makes for drastically reduced possibility of hidden errors. More importantly, it makes computational investigations transparent and testable by others. The ability to change one package at a time, without changing the rest of the scheme, permits easy detection of sources of error. The scope of the software system far exceeds its use here.

Adaptive mesh refinement was applied in two stages of a factor of 3 each, on a coarse grid of 40×240 cells, so that the effective grid was 360×2160 . The grid refinement criterion was a threshold value of the magnitude of the density gradient. Extensive tests were performed on different criteria and degrees of grid refinement in order to ensure that the phenomena observed were not grid-resolution related features.

In most of the following, a flux-limited, operator-split solver is used, with a body-fitted grid. With such a scheme, nonuniformity of the grid introduces numerical noise in the flow. The maximum magnitude of this noise in density is



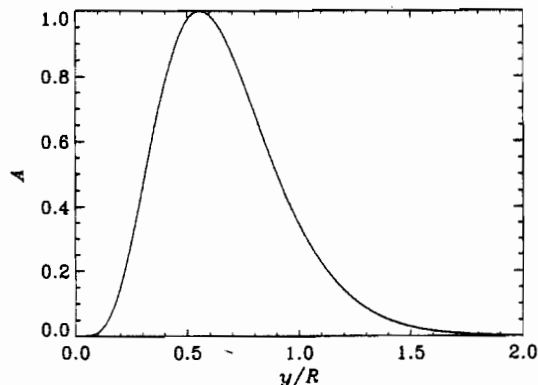


FIG. 2. Form of the amplitude function of the perturbation.

0.3% of the free-stream density in our case. Provided that the normal shock density ratio is small enough, this noise is insufficient to make the flow unstable, as in the example shown in Fig. 1. Such stable flows can then be excited with deliberately introduced disturbances, whose growth can be studied to determine the instability conditions.

B. Choice of disturbance

A suitable disturbance for excitation of instability in a shear layer is a periodic variation of the velocity component normal to the shear layer: If such a disturbance is introduced all along the inflow boundary of the computational domain, it causes trouble at the plane or axis of symmetry. We therefore choose an amplitude function, A , for the disturbance, which is of the form

$$V/U_\infty = A(y/R)\sin(2\pi U_\infty t/\lambda), \quad (2)$$

where V is the y -component of velocity, R is the nose radius, t is time, and λ is the wavelength of the disturbance. The amplitude function is

$$A(y/R) = C_1(y/R)^5 \exp(-C_2 y/R). \quad (3)$$

The numerical constants C_1 and C_2 can then be chosen to adjust the magnitude of the disturbance and the y -location of its maximum. A plot of A is presented in Fig. 2.

This is not the only type of disturbance that was applied to the problem. Others included unsteady density and pressure conditions at the inflow boundary. The behavior of each disturbance type was tested by applying it to an otherwise uniform flow. As expected, the disturbances steepen into weak shock waves on their forward side, but with the small amplitudes introduced here, visible steepening only occurred after large distances, and, for sufficiently small disturbances, effects of numerical dissipation prevent the steepening. In all the cases studied here, the disturbances decay slightly over the small distance between the inflow boundary and the bow shock.

As an example of the effect of a disturbance on the flow shown in Fig. 1, a disturbance with maximum amplitude $a = V_{\max}/U_\infty = 1.0\%$ and with maximum located at $y/R = 0.556$ was switched on at the left boundary after the flow had reached steady state. This was then repeated with differ-

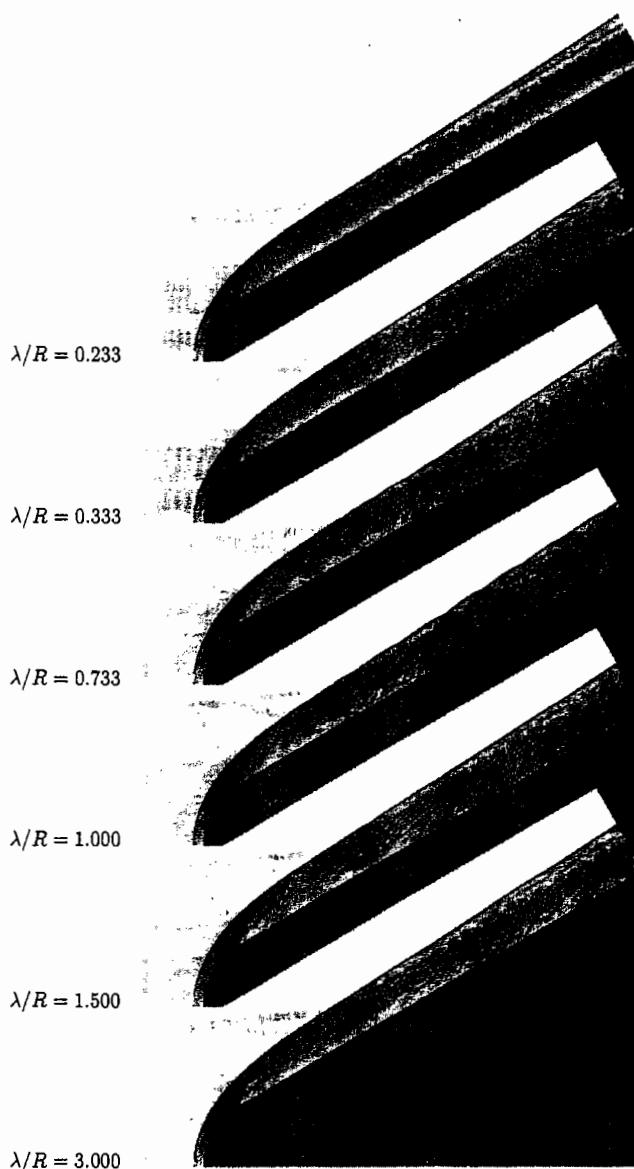


FIG. 3. Pseudo-schlieren images of the flow of Fig. 1, after a disturbance of maximum amplitude 1.0% is imposed at the left boundary. Note that the structures in the shear layer move supersonically and push shock waves that reflect from the wall. At large wavelengths the structures do not become larger, but form in packages spaced at the imposed wavelength.

ent disturbance wavelengths. A selection of the resulting pseudo-schlieren images is presented in Fig. 3.

A number of features of the growth of the disturbance emerge. At small wavelength ($\lambda/R = 0.233$) the disturbance is only slightly amplified. However, as the wavelength is increased, the growth is so strong that the structures, which move at supersonic speed relative to the flow between the shear layer and the body, push oblique shock waves into it, which are reflected from the wall and reimpinge on the shear layer.

Another feature is that the preferred wavelength that grows is quite small. In unconfined shear layers this preferred wavelength amounts to several shear-layer thicknesses, while it is of the order of the shear-layer thickness here. Also, the structures become so strong at $\lambda/R = 1.0$ that they perturb the shock wave significantly. For wavelengths



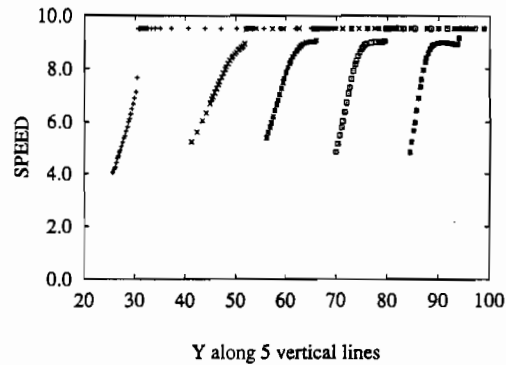
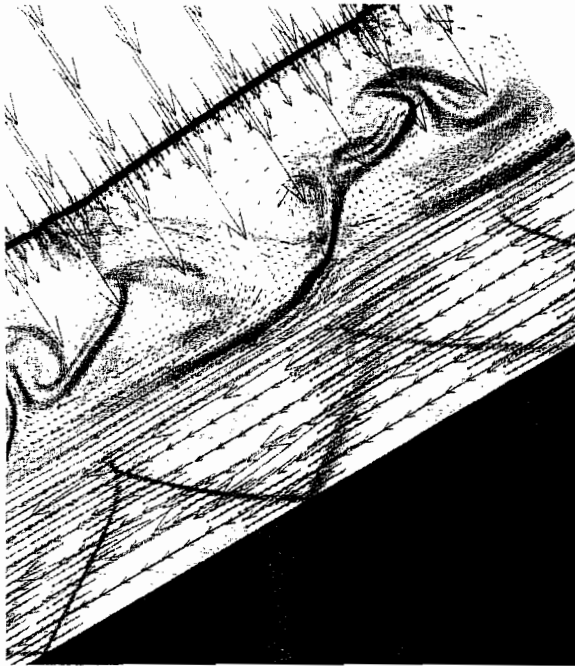


FIG. 4. Enlargement of portion of the flow in Fig. 3, case $\lambda/R=1.0$, showing vectors of velocity relative to a point approximately in one of the shear-layer structures. The length of the velocity vectors is proportional to the velocity, but the refined-grid vectors are plotted to a smaller scale. Note that the vectors show the vortical nature of the structures and identify the dark oblique lines underneath them as shock waves. Note also that the structures move approximately at the shock-parallel component of the free-stream speed.

FIG. 5. Top: Pseudo-schlieren image of computed flow over a 20° sphere-cone, $M_\infty=9$, $\gamma=1.12$, corresponding to a normal shock density ratio of 14.7. The body-fitted grid represents curved surfaces as polygons. On the spherical nose this causes waves to be emitted from the surface. These are significantly stronger in this axisymmetric case, because the polygons lie in a higher-Mach-number part of the flow. The waves are reflected from the shock and again from the body a couple of times. Although they introduce a significant disturbance they are not strong enough to cause the shear layer to become unstable at this density ratio. Bottom: Five uniformly spaced profiles of speed across the layer. Note how the vorticity of the shear layer increases with downstream distance, as a consequence of the vortex lines being stretched.

that are larger than the preferred wavelength, the imposed wavelength appears in the form of packets of the small wavelength spaced at the imposed wavelength. At larger wavelengths the growth rate is strongly reduced again. A quantitative analysis shows that, in the flows presented in Fig. 3, the density fluctuations that result in the shear layer reach values up to 20% after a distance of a few nose radii.

Figure 4 shows an enlarged view of portion of Fig. 3, case $\lambda/R=1.0$, with vectors of velocity relative to the velocity of a point moving with one of the structures. The size of the vectors is proportional to this relative velocity (but refined-grid arrows are correspondingly smaller). Three features are brought out by this. First, the shear layer structures move with a speed close to the post-shock speed and they are vortical in nature. Second, the flow below the shear layer is very fast in this reference frame, explaining the occurrence of the oblique shocks that reflect from the wall. Third, when the disturbance has grown to such a degree that the shock becomes perturbed, weak triple points form on the shock (top left of Fig. 4), from which thin shear layers emerge that feed the main shear layer with even more vorticity of the same sign. Once this mechanism sets in, as computations at higher density ratios show, the growth of the disturbance enters a catastrophic phase that eventually produces a turbulent shock layer bounded toward the free stream by an irregular unsteady shock.

C. Flow over a sphere-cone

In axisymmetric flow, the vorticity of a material element at constant pressure does not remain constant, because the

vortex lines may be stretched. Thus in the analogous model to that of the cylinder-wedge of plane flow, namely a sphere-cone, the vorticity of a material element will increase with time. This may be seen in the no-disturbance computation presented in Fig. 5. Observe the profiles of speed across the shock layer. From the second profile onward, the vorticity (the slope of the velocity profile) increases with downstream distance and the region of maximum vorticity is at or very near the body. Thus the shear layer and any structures that might develop in it will not move at a supersonic speed relative to the region between the shear layer and the body, and we may expect this region to be free of shock waves.

In this flow field a feature of blunt cone and blunt wedge flows may be observed: The shock shape near the nose is like that of a slender blunt body, i.e., like the paraboloid (in axisymmetric flow) of the blast wave analogy, which would intersect the cone far downstream. However, far downstream, where the flow becomes asymptotically like that over a sharp cone, the shock shape has to become conical, so that the shock exhibits a point of inflection.

Computations with deliberately introduced disturbances were also made in the axisymmetric case for density ratios of 14.7 and 17.5. These are presented in Figs. 6 and 7.





FIG. 6. Pseudo-schlieren images of flow over a sphere-cone at $M_\infty=9$, $\gamma=1.12$, making the normal shock density ratio 14.7, with the same free-stream disturbance as in the case of the cylinder-wedge.

D. The critical density ratio

As was pointed out earlier, the shear layer thickness decreases and its intensity increases in approximate proportion to the normal shock density ratio. Both of these increase the instability of the shear layer. In an inviscid flow the shear layer will eventually exhibit instability far downstream, of course, but a certain critical density ratio is likely to exist, below which no detectable evidence of instability exists within the computational domain, and above which it does. A large number of computations were made in both the plane and the axisymmetric flows with different disturbance amplitudes and different values of Mach number and specific heat ratio, in order to examine the influence of the normal shock density ratio on the stability.

When the normal shock density ratio was smaller than



FIG. 7. Pseudo-schlieren images of flow over a sphere-cone at $M_\infty=9$, $\gamma=1.095$, (normal shock density ratio 17.5) with the same free-stream disturbance.

11, disturbance amplitudes as large as 2% did not exhibit any growth of structures in the shear layer. On the other hand, when the normal shock density ratio was 18 or greater, it was not necessary to introduce a disturbance at all in order to cause the shear layer to become unstable within the computational domain. This indicates that the small nonuniformities in the free stream that result from the nonuniformity of the body-fitted grid (density perturbations of up to 0.3% of the free-stream density) suffice to trigger the instability of the shear layer within the computational domain. This therefore suggests that, in an experiment to test the results of the exploratory computational study, normal shock density ratios of at least 14, and preferably more should be achievable.

III. THE PHYSICAL EXPERIMENT

An example of a situation in which high normal shock density ratios occur is hypervelocity flight in a carbon-dioxide atmosphere. One might expect that such flows could be achieved in a hypervelocity test facility such as a free-piston shock tunnel, where flow speeds are achievable that produce very significant dissociation (and therefore density



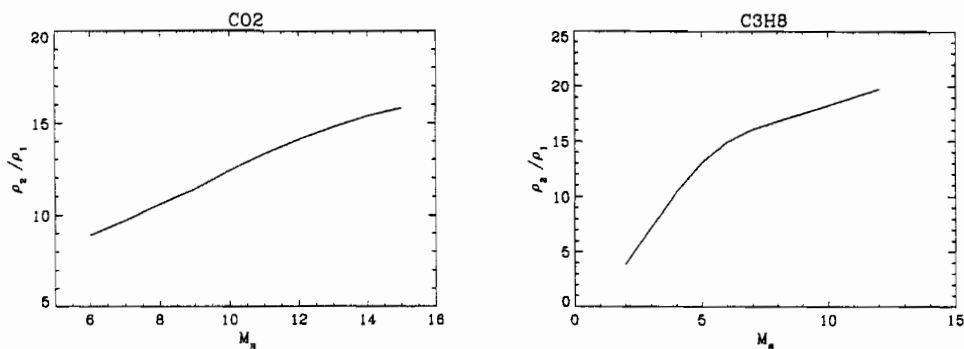


FIG. 8. Equilibrium density ratio across a normal shock in carbon dioxide (left), and in propane (right) as functions of Mach number. The upstream condition is $p_\infty = 100$ kPa, $T_\infty = 293$ K. These curves were calculated using the software package STANJAN, see Reynolds (Ref. 10).

increase) downstream of the bow shock wave of a blunt body. Unfortunately, this is not possible in a reflected shock tunnel, for the following reasons:

In a reflected shock tunnel, the high-speed flow is generated by converting the thermal energy of a stationary reservoir gas into ordered kinetic energy of flow by means of a nozzle expansion. The thermal energy of the stationary gas necessarily has to be comparable to the dissociation energy of the gas if significant dissociation is to occur after the bow shock. This means that the reservoir gas is partially dissociated. During the passage of the gas through the nozzle, some recombination does occur, but as the density decreases, there comes a point when the composition freezes. Thus the flow that arrives at the bow shock is already partially dissociated, so that the amount of dissociation that occurs after the bow shock (and therefore the amount of density increase) is smaller than would be observed in flow with an undissociated free stream. It turns out that the highest normal shock density ratio achievable in the T5 free-piston shock tunnel at Caltech is approximately 12. Experiments involving flow over a cylinder-wedge such as those studied in the exploratory computational experiment yielded only very scant evidence of instability in the shear layer; see Lemieux.⁸

An alternative to generating flow over a stationary model is to shoot a projectile into low-temperature stationary gas. A modification of T5, designed and built by Bélanger and Kaneshige,⁹ converts the facility into a light gas gun with which a 25 mm diameter projectile can be accelerated to 3 km/s and shot into a test section containing any gas between two thin mylar diaphragms. If a density ratio of 16 is to be achieved by shooting a projectile into carbon dioxide, the velocity of the projectile has to be of the order of 4 km/s. However, high density ratios can be achieved more easily by using a gas with a very small ratio of specific heats. For example, with propane (C₃H₈), a normal shock density ratio of 17 can be achieved at 2.8 km/s; see Fig. 8.¹⁰

A. Experimental setup

In the light gas gun modification of T5, a gun barrel is attached to the end of the shock tube, which reaches approximately to the middle of the dump tank. A test section attached to the far end of the dump tank contains the test gas between thin mylar diaphragms. The shock-heated and compressed helium in the shock tube serves as the driver that propels the projectile along the gun barrel, through the dump tank, and into the test section. As the projectile travels

through the test section, shadowgraph records of the flow may be taken through a window. A drawing of the test section is shown in Fig. 9.

To measure the projectile speed, three photodetectors and three pressure transducers are installed in the test section, as shown in Fig. 9. The projectile breaks a wire, providing the first timing signal for the speed determination. The photodetector signals are used together with this to calculate the projectile speed. The projectile speed can be varied from 1 to 3 km/s by changing the gas gun driver gas and conditions. At the higher speeds, it was found that nylon did not have sufficient impact strength to survive, and it was necessary to switch to the much tougher material Lexan.

B. Experimental results

At conditions where the normal shock density ratio is less than 14, the flow over the projectile is characterized by a smooth shock wave. Two examples are shown in the shadowgraphs of Figs. 10 and 11 for propane and carbon dioxide flows, respectively. In contrast, when the conditions are such that the density ratio is larger than 15 (see Figs. 12 and 13), the shock wave is significantly perturbed, so much so that the features of the flow in the central wake are completely obscured by the refraction of the light in the outer part of the axisymmetric flow in the (line-of-sight integrating) shadow-

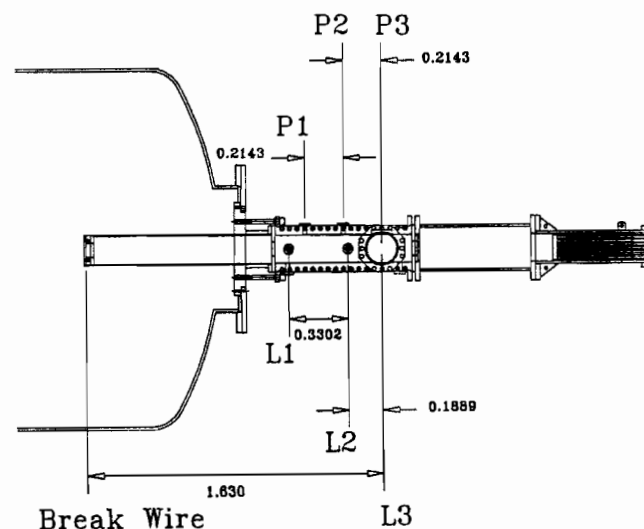


FIG. 9. Light gas gun test section. Photodetector and pressure transducer stations are labeled L and P, respectively. Dimensions shown are in meters. The stations P3 and L3 are in the middle of the window.



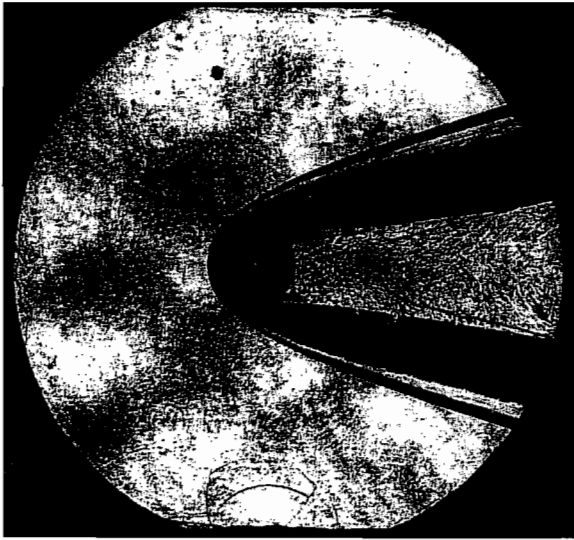


FIG. 10. Shadowgraph of projectile moving at 2.26 km/s in propane, giving a normal shock density ratio of 13. The black regions just inboard from the shock result from the very large separation of the elements of the shadowgraph system. This causes regions of large refractive index gradient to refract the beam so much that it misses one of the mirrors completely, causing that region to be black. The shock front is quite smooth, and turbulence is only evident in the central wake. The wake shocks are faintly visible.

graph. This shock wave perturbation looks similar to that of the second nonlinear amplification mechanism discussed in connection with the computations.

It is clear from these results that a dramatic change occurs in these flows in the range of normal shock density ratio around 14. In order to relate this to the phenomena that occur in the exploratory computational experiment, it is necessary to compute flows that are more nearly like the ones in the experiment.

It should be pointed out that a similar experimental observation of instability of high Mach number flow over a sphere has been made by Tumakhev,¹¹ who attributes the



FIG. 11. Shadowgraph of projectile moving at 2.7 km/s in carbon dioxide, giving a normal shock density ratio of 12. Again the shock wave is smooth, and the features are much like those of Fig. 10.

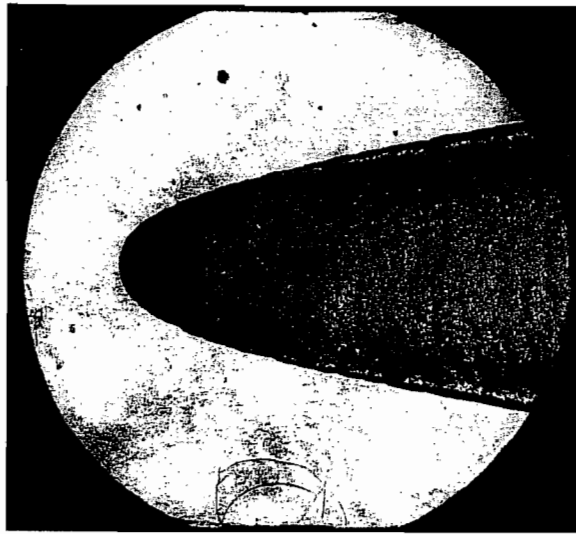


FIG. 12. Shadowgraph of projectile moving at 2.7 km/s in propane, giving a normal shock density ratio of 20. Note the dramatic perturbation of the shock wave, which manifests itself in features that stretch across the flow, obscuring the features of the central wake.

phenomenon to phase transitions. In our experiments no phase transitions occur, and we suspect that the phenomenon he observed also arises because of the shear layer instability that attends the high normal shock density ratio in his freon flows.

IV. COMPARISON WITH COMPUTATION OF FLOW OVER A SPHERE

In the experiment, the gases exhibit high-temperature real-gas effects, in particular, vibrational excitation. We simulate the flow over a sphere at conditions that are as nearly the same as those in the experiment, but with a perfect gas, by making the density ratios of the computations the same as those in the experiment. Since the density ratio de-

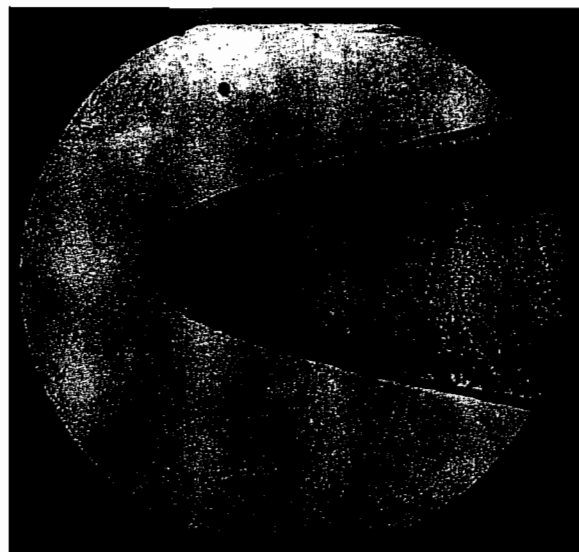


FIG. 13. Shadowgraph of projectile moving at 2.2 km/s in propane, giving a normal shock density ratio of 17. Again the features are like those in Fig. 12 and in stark contrast to the smooth shocks of Figs. 10 and 11.

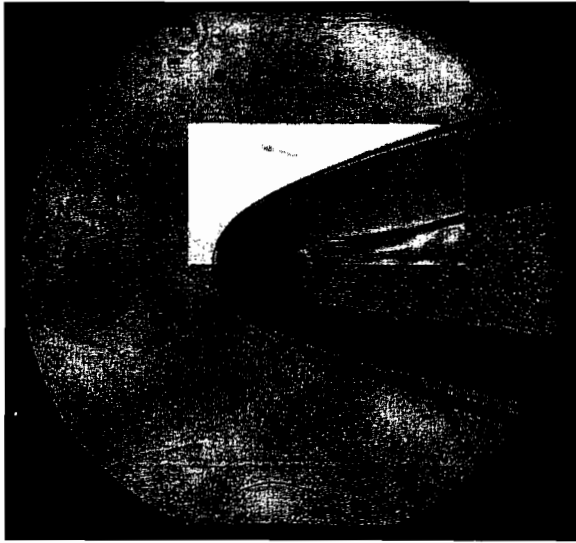


FIG. 14. Overlay of shadowgraph of Fig. 10 with pseudo-schlieren image of computation of flow over a sphere at $M_\infty = 5.5$ and $\gamma = 1.13$. The computational image, unlike the experimental one, is not line-of-sight integrating, so that it shows the details of the central wake much more pronouncedly. The disturbance at the inflow boundary is of the same form as that in the exploratory computations at an amplitude of 0.5%.

depends on both the Mach number and the specific heat ratio, a given density ratio permits the choice of the right Mach number. Using the same computational setup as for the exploratory experiment, the flow over a sphere was computed for conditions as near as possible to those in Figs. 10 and 12. The results are shown in Figs. 14 and 15 as overlays over the experimental shadowgraphs. It is important to note that, in both cases, the disturbance introduced at the inflow boundary was the same. Clearly this disturbance is damped in the low density ratio case and amplified in the high density ratio flow.

V. CONCLUSIONS

A computational study of the stability of the shear layer formed by the curved bow shock in the shock layer of a hypervelocity flow over a blunt body revealed the following results:

- (1) In plane flow over a cylinder-wedge, the shear layer is separated from the body by a roughly parallel region in which the flow is supersonic relative to the region of maximum shear.
- (2) This layer is unstable to disturbances introduced in the free stream, when the disturbance wavelength is of the order of the nose radius.
- (3) The structures formed by the instability grow by two nonlinear mechanisms. First, they push oblique shock waves into the flow beneath them that reflect from the body and reinforce them. Second, they perturb the bow shock, forming triple points from which shear layers issue that feed the shear layer.
- (4) In axisymmetric flow over a sphere-cone, the shear layer is much closer to the body, so that the structures do not move supersonically with respect to the flow between



FIG. 15. Overlay of shadowgraph of Fig. 12 with pseudo-schlieren image of computation of flow over a sphere at $M_\infty = 10$ and $\gamma = 1.07$. The disturbance amplitude is again 0.5%. Note the similarity between the experimental and computational shock perturbations.

them and the body, so that the dominant nonlinear mechanism of growth is through the perturbation of the bow shock by the structures.

- (5) A physical experiment with propane and carbon dioxide flow over a sphere confirms the computational results, giving very good agreement, and confirming the existence of a critical normal shock density ratio of around 14.

The existence of a critical density ratio, beyond which the shock layer becomes unstable, shows that the simple Newtonian theory for hypersonic flow at high density ratio may be safely applied only when the normal shock density ratio is less than about 14. This study is an example of how a relatively inexpensive exploratory computational study may be used to design an experiment, which, were it necessary to do the exploratory study experimentally, would be very expensive indeed. With this approach, the expense of the physical experiment can be kept to a minimum.

¹M. J. Lighthill, "Dynamics of a dissociating gas," *J. Fluid Mech.* **2**, 1 (1957).

²W. D. Hayes and R. F. Probstein, *Hypersonic Flow Theory* (Wiley, New York, 1959).

³P. G. Drazin and W. H. Reid, *Hydrodynamic Stability* (Cambridge University Press, Cambridge, 1981).

⁴M. Zhuang, P. E. Dimotakis, and T. Kubota, "The effect of walls on a spatially growing supersonic shear layer," *Phys. Fluids* **2**, 599 (1990).

⁵K. F. Stetson, E. R. Thompson, J. C. Donaldson, and L. G. Siler, "Laminar boundary layer stability experiments on a cone at Mach 8, Part 2: Blunt cone," AIAA Paper No. 84-0006 (1984).

⁶A. Vaszanyi, "On rotational flows," *Q. Appl. Math.* **3**, 29 (1945).

⁷J. J. Quirk, "Amrita—A computational facility (for CFD modeling)," *VKI 29th CFD Lecture Series* (von Kármán Institute for Fluid Dynamics, Brussels, 1998).

⁸P. Lemieux, "The instability of shear layers produced by curved shocks," Ph.D. thesis, Caltech (1999).

⁹J. Bélanger, M. Kaneshige, and J. E. Shepherd, "Detonation initiation by



hypervelocity projectiles," in *Shock Waves*, Proceedings of the 20th International Symposium on Shock Waves, edited by B. Sturtevant, J. E. Shepherd, and H. G. Hornung (World Scientific, Singapore, 1995).

¹⁰W. C. Reynolds, "The element potential method of chemical equilibrium analysis: Implementation in the interactive program STANJAN," Techni-

cal Report, Department of Mechanical Engineering, Stanford University (1986).

¹¹G. K. Tumakhev, "Kinetic phase transition in molecular gases and its effect on flow formation behind a detached shock wave," *J. Tech. Phys.* **52**, 690 (1982).

Experimental Hypervelocity Flow Simulation, Needs, Achievements and Limitations.

Hans Hornung

Graduate Aeronautical Laboratories
California Institute of Technology
Pasadena, California 91125, USA

Abstract

The requirements for ground simulation of hypervelocity flows are set out on the basis of the similarity parameters of the problem. This, together with the thermodynamical properties of air, the consequent heat loads on the facility and large power requirements, leads to the two most successful devices, the reflected shock tunnel and the expansion tube. After a description of the operation and the thermodynamics of these devices, their essential limitations are explained. Scale effects of these limitations are discussed. On this basis the range over which they can be applied for flow simulation is delineated.

Keywords: Hypervelocity flow, ground simulation, simulation facilities, shock tunnel, expansion tube, dissociation.

1. Introduction

The term *hypervelocity* is used to distinguish those flows in which the velocity is so large that the conditions after the bow shock on a body are such as to cause the molecular components of the gas to dissociate. The fields of human endeavor where hypervelocity flows are of importance are those in which an object traverses the atmosphere of one of the planets of the solar system. Typically this could be associated with transport to or from space in man-made vehicles, but hypervelocity flows also occur naturally, *e.g.*, when a meteorite enters a planetary atmosphere.

The term *hypersonic* flow is used to describe situations where the flow speed is large compared to the free-stream speed of sound. Such high-Mach-number flows can, of course, be generated by lowering the speed of sound far enough to keep the gas in the regime where it behaves as a perfect gas. In such *cold* hypersonic flows, the important dissociative and other real-gas effects of hypervelocity flows do not occur. In order to understand the intricacies of flows in which the chemistry of the gas is activated by the kinetic energy of the flow, it is necessary to simulate *hypervelocity* flows in the laboratory.

In the context of the earth's atmosphere the orbital velocity is 8 km/s, and the velocity at which the most severe heating problems arise is 6 km/s. In the frame of reference of the flying object, the ordered kinetic energy per unit mass of the free-stream gas is therefore 18 MJ/kg. At high enthalpy, the Mach number, which measures the square root of the ratio of the ordered kinetic energy of the flow to the thermal energy of the gas, is not so important as the ratio of the ordered kinetic energy measured in terms of the specific dissociation energy of the gas. There are usually several such characteristic chemical energies.

The characteristic specific energies relevant for air are

$$\begin{aligned} D_{N_2} &= 33.6 \text{ MJ/kg} & E_{vN_2} &= 0.992 \text{ MJ/kg} \\ D_{O_2} &= 15.5 \text{ MJ/kg} & E_{vO_2} &= 0.579 \text{ MJ/kg} \\ D_{NO} &= 20.9 \text{ MJ/kg} & E_{vNO} &= 0.751 \text{ MJ/kg}, \end{aligned}$$

where the D 's and E_v 's are specific energies of dissociation and of vibration respectively. It is not possible to simulate the numerous idiosyncrasies of a particular gas by using another gas. The specific chemical energies have definite known values, and the duplication of the ratios of the ordered kinetic energy to them in a simulation implies that the actual flow speed has to be duplicated.

It follows that the reservoir enthalpy h_0 of the flow, which is approximately equal to $V^2/2$, where V is the flow speed, has to have the same value as in flight. If the flow is accelerated from a reservoir at rest, without adding energy to it during the expansion, the reservoir enthalpy corresponding to a flow speed of 6 km/s is 18 MJ/kg, which, at a reservoir pressure of 100 MPa, implies a temperature of nearly 9000 K in air.

The high pressure is necessary to ensure that the chemical reaction rates occur at the right speed for correct simulation of nonequilibrium effects. Smaller scale requires faster reaction for correct simulation. If the temperatures are right (as is ensured by correct flow speed) the reaction rates depend mainly on the density. Rates for binary reactions, like dissociation, are linear in density, those for three-body reactions, like recombination, are quadratic in density. Thus, all reactions can never be simulated correctly except at full scale. In many cases, three-body reactions are not important and, where they are, component testing or extrapolation is necessary.

Continuous flow facilities are ruled out by the high power requirements of typically a few GW. The high speed reduces the steady flow duration requirement to a few ms, however. A convenient way to accelerate, heat and compress a gas for a short time, is to pass a shock wave over it. Many types of high-enthalpy facilities therefore embody shocks as elements.

The problem of hypervelocity simulation is not limited to speeds of the order of 6 km/s, of course. Meteorites entering planetary atmospheres typically have a speed of 20-60 km/s, and proposals for man-made vehicles have considered speeds in the vicinity of 16 km/s. Such conditions involve very strong ionization of the gas and intense radiative heat loss from it. In the following discussion, such very high speeds will not be considered, and attention will be concentrated on the range 3-7 km/s. In this range, the requirements for simulation of hypervelocity flows and some of the methods by which the simulation has been achieved to date will be presented. The paper then closes with a discussion of the limitations and achieved conditions of the different types of facilities.

This paper is a descriptive account of the reasons for the forms that hypervelocity simulation facilities have taken. It is not a detailed account of the work that has been done in the field, and only a few representative publications will be cited. A very important book on the subject is Lukasiewicz's "Experimental Methods of Hypersonics". The interested reader should consult this volume on all the questions concerning this field.

In the present paper, the two most successful facility types for hypervelocity flow simulation, the reflected shock tunnel and the expansion tube will be given prominence.

2. Requirements for Ground Simulation

2.1 Similarity in Hypervelocity Flows

To simulate a hypervelocity flow at smaller scale, all the dimensionless parameters of the problem have to be reproduced. In steady hypervelocity flows any dimensionless dependent quantity Q , say, depends on dimensionless variables as follows:

$$Q = Q(M_\infty, Re, Pr, T_w/T_0, B_n, \alpha, \beta, E_i, R_j, Le_i, c_{\infty i}).$$

Here, M_∞ is the free stream Mach number, Re and Pr are Reynolds and Prandtl numbers, which, in this context, are best defined at conditions corresponding to the gas in equilibrium after a normal shock for which the upstream conditions are those of the free stream, T_w is a representative body surface temperature, T_0 is the temperature from which a gas would have to be expanded by a steady expansion to reach the free-stream conditions, B_n is a vector of length ratios defining the body geometry, α is the angle of attack, and β is the yaw angle. E_i is a vector of dimensionless numbers relating the specific formation enthalpies of the species to the specific kinetic energy of the free-stream gas, R_j is a vector relating the characteristic lengths associated with the chemical reactions to the characteristic length of the body, Le_i are the Lewis numbers giving the dimensionless species diffusion coefficients, and $c_{\infty i}$ is a vector giving the dimensionless concentrations of the species in the free stream. Even this long list of variables is not complete, as the vibrational characteristics of the molecular species have been omitted.

Up to and including β in the above list, the variables are the same as in cold hypersonics, in which the remaining variables, which describe the thermodynamic and chemical properties of the gas, can be replaced completely by a single variable, the ratio of specific heats, which, for a perfect gas, is a constant. Clearly, the more complex thermodynamics and chemistry of the hypervelocity flow requires many more parameters to be duplicated in the scale experiments than perfect-gas cold hypersonics. For example, in air at a free-stream speed of 5 km/s, it is necessary to include at least 5 species and 8 reactions, so that, if all the geometrical parameters are exactly duplicated, there remain over 20 dimensionless variables to match. In fact, as has already been indicated in the introduction, it is not possible to simulate both binary and three-body reactions simultaneously (except at full scale) because of the difference in their dependence on the density.

In special cases, however, the problem may be considerably simplified. For example, if the gas is especially simple, such as in a single diatomic gas, there is only a single E and there are only two R 's. Only one of the R 's can be matched, and, *e.g.*, in blunt body flows, it is best to match the binary dissociation reaction. With correct E , this automatically also causes Re , Le and Pr to be matched. Thus, the problem reduces to

$$Q = Q(M, T_w/T_0, E, R, c_\infty).$$

If the Mach number is sufficiently high, and the bow shock is not of interest in regions where it becomes very weak, the Mach-number-independence principle is effective, and the number of independent parameters is down to 4. This situation can be satisfactorily simulated.

Where such simplifications are not possible, it becomes necessary to divide the flow field up into particular regions and to simulate these separately. This is sometimes referred to as component testing. An example is the testing of engine combustors by connecting the inlet of the combustor directly to the exit of the facility nozzle, thus enabling testing at almost full size. Another example is the testing of the situation on the front of a body by placing only the nose shape into the test section, so that binary scaling and Mach-number independence apply.

2.2 Power Requirement

It is really quite amazing how much power is in a hypervelocity flow. For example, a wind tunnel with a cross-sectional area of 1 m², in which the flow speed is 7 km/s, and the density is 0.01 kg/m³ requires a power of 2 GW. This is a tenth of a percent of the power consumption of the USA. It also corresponds to an energy flux of 2 GW/m², or 46 times that at the surface of the sun. It is clear, that this kind of power can not be sustained for long times.

Fortunately, it only takes a very short time to set up a steady flow over a model at such high speeds. Opinions differ about the necessary test time. A reasonably conservative value is

$$\tau = 20 \frac{L}{V_\infty},$$

where L is the model length and V_∞ is the free-stream velocity. With this value, the test time requirement for the above facility comes out to approximately 3 ms, so that the *energy* requirement is only 10 MJ. This energy can be stored over a long time and released during a short test period.

The power requirement is thus one of the reasons why short-duration facilities are necessary for hypervelocity flow simulation. Another reason arises in the case of facilities that use a steady expansion to accelerate the flow from rest. In such facilities, the thermodynamic condition in the reservoir from which the gas is expanded is such that the specific enthalpy, h_0 , has to be 20 MJ/kg or so. In air, at a pressure of 100 MPa, this corresponds to a temperature of 9500 K or so. Hence, it is necessary to limit the time for which the materials containing the flow are exposed to these conditions. With the best materials available today, 3 ms is about the limit at the conditions quoted.

2.3 Instrumentation Requirements

This topic is one that deserves at least as much space as this whole paper, and it will not be possible to deal with it here, except for the purpose of pointing to its importance. Clearly, a test in a hypervelocity simulation facility is quite expensive. It is therefore most desirable to make as extensive a set of measurements as possible, each time such a test is performed. Unfortunately, the different forms of non-intrusive testing that exist at present require different degrees of expertise, which are seldom available at the same place as the test, because of the degree of sophistication that they often require.

Among the presently used routine measurement techniques, the following are available at all high-enthalpy test facilities:

1. Surface pressure measurement

2. Surface heat flux measurement
3. Schlieren and shadow photography
4. Interferometry

Techniques that are applied relatively rarely to hypervelocity flows, but are very important for them, are

1. Mass spectrometry
2. Spectroscopy
3. Laser-induced fluorescence
4. Raman spectroscopy

These methods are able to measure species concentrations and temperature, and would therefore provide extremely important data for the analysis of results from hypervelocity facilities. In the author's opinion, it is high time that major funding be directed to the juxtaposition of modern diagnostics and hypervelocity facilities. A good example of this is the policy at the HEG laboratory in Göttingen, Germany.

3. Hypervelocity Simulation Facilities

In this section the principles of operation of the most successful types of hypervelocity facilities are presented. The thermodynamical and chemical processes which the gas undergoes in the generation of the hypervelocity flow are given prominence in this, because they define and explain the most serious disadvantages of the facility types.

3.1 Reflected-Shock Tunnel

3.1.1 Configuration and Operation

By far the most used and most productive hypervelocity simulation facility is the reflected shock tunnel. Fig. 1 shows a schematic sketch and a wave diagram of the device. Initially, the driver region is filled with high-pressure gas and a diaphragm separates it from the shock tube, which is filled with the test gas at lower pressure. The shock tube is separated from a nozzle, attached to its other end by a weak diaphragm. The nozzle and test section, as well as the dump tank, are initially evacuated. The test section and dump tank are not shown in the figure.

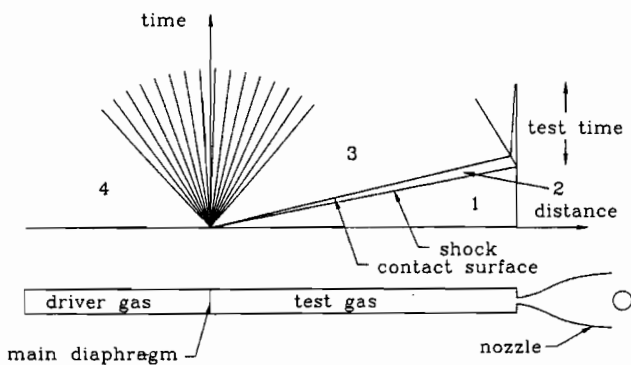


Fig. 1. Schematic sketch of reflected shock tunnel and wave diagram. The separation between the shock wave and contact surface is exaggerated to show it better

When the main diaphragm breaks, a shock wave propagates into the test gas, and an expansion wave propagates into the driver gas in such a way that the pressures and velocities in the region

between the shock wave and expansion wave are continuous across the interface between the two gases. These processes are shown in the wave diagram of Fig. 1. The initial state of the driver gas, in region 4 of the wave diagram, is processed by the expansion wave to the condition in region 3, and the initial state of the test gas, region 1, is processed by the shock wave to the condition in region 2. The states 2 and 3 are determined by the expansion wave and by the shock wave and the requirement that velocities and pressures must match across the boundary between 2 and 3. This may best be illustrated by a velocity-pressure diagram, shown in Fig. 2. The upper curve shows the locus of the states that can be reached from the initial condition of the driver gas via an expansion wave and the lower curve shows the states that can be reached from the initial state of the test gas via a shock wave. Their intersection represents the condition in regions 3 and 2, where pressures and velocities are matched. The solution thus corresponds to the intersection of the two curves in Fig. 2.

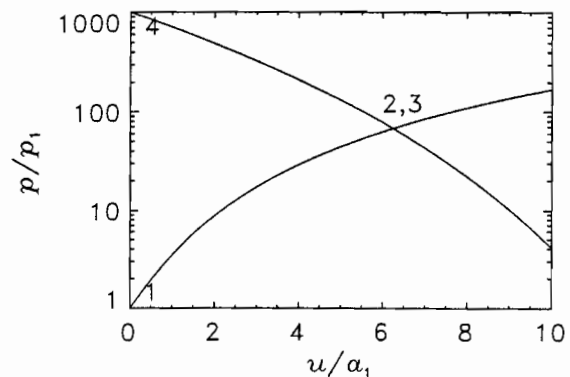


Fig. 2. Example of velocity-pressure diagram for a shock tube. The pressure p is normalized with the initial pressure of the test gas, p_1 , and the velocity u is normalized with the speed of sound in the test gas at condition 1, a_1 . In this example the gases are treated as perfect gases with specific heat ratios γ_1 and γ_4 of 7/5 and 5/3 respectively. Also, the ratio of the speeds of sound a_4/a_1 , the third parameter determining the solution, was chosen to be 5.

If a whole lot of such solutions are combined, the solutions can be shown parametrically in a diagram plotting the shock Mach number $M_s = V_s/a_1$ against the pressure ratio p_4/p_1 . This is done in Fig. 3.

In the reflected shock tunnel, the state of the test gas in region 2 is processed further by the shock wave reflected from the closed end of the shock tube. This heats and compresses the gas even more than has already been accomplished by the primary shock, but it also brings the test gas to rest again. The primary shock breaks the thin diaphragm between the shock tube and the nozzle, thus allowing the test gas to expand in a steady expansion through the nozzle.

It is important to operate the shock tunnel in such a way that the interaction between the reflected shock and the contact surface does not produce any further waves. When conditions have been chosen in such a way that this is the case, this is referred to as tailored-interface operation. The condition behind the reflected shock is then the reservoir condition of the nozzle flow, and is referred to by the subscript 0.

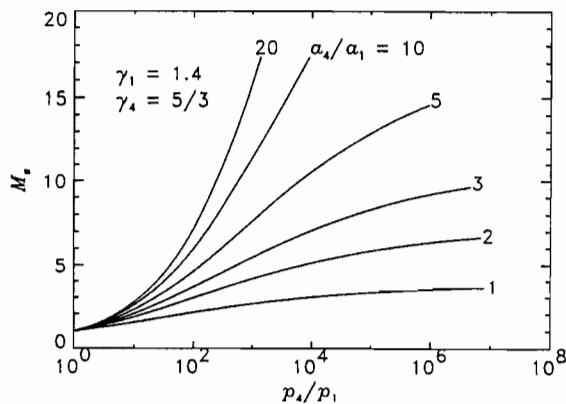


Fig. 3. The shock tube equation for monatomic driver gas and diatomic test gas, both treated as perfect gases. Note the strong dependence of the shock Mach number on the speed of sound ratio. Real-gas effects modify this diagram only slightly.

The nozzle expansion converts the thermal energy of the stationary reservoir gas into ordered kinetic energy. In doing so, the maximum flow velocity achievable is

$$V_{\infty} = \sqrt{2h_0},$$

where h_0 is the specific enthalpy of the reservoir condition. Since it is necessary to achieve speeds around 6 km/s, the reservoir specific enthalpy needs to be in the vicinity of 18 MJ/kg. In a reflected shock tunnel, a very good approximation is

$$h_0 = V_s^2.$$

It follows that the shock speed has to be about 4.3 km/s, which, in air, corresponds to $M_s = 12.5$. Referring to Fig. 3, we see that this value may not be reached with pressure ratios less than 2000 unless a_4/a_1 exceeds 8. Since the test gas speed of sound is virtually fixed by the fact that we want to use air in a laboratory at room temperature, the driver-gas sound speed has to be high.

3.1.2 Driver-Gas Conditions

Various ways have been used to increase a_4 . First, a light gas, either hydrogen or helium is used, and second, the driver gas is heated. Steady state heating is limited to about 800 K. This gives $a_4/a_1 = 4.8$ for helium driver gas and air test gas. Not only is

this too low, but it is also expensive and dangerous to contain high-pressure and high-temperature gas for an extended period. A second method is to heat the driver gas relatively quickly by combustion of a limited amount of hydrogen and oxygen mixed with the driver gas before the test. Mixtures in the proportions 14% hydrogen: 7% oxygen: 79% helium, give $a_4/a_1 \approx 7$.

While this is just about enough, another, more convenient technique is to compress the driver gas adiabatically with a heavy piston. This method has the advantage that the driver gas is hot only for a very short time, and that (as in the combustion-heated driver) the high pressure required is produced automatically. However, it also means that the driver is short, with a moving end wall, so that waves travelling between the main diaphragm station and the piston cause disturbances to the shock. With adiabatic compression, values of a_4/a_1 up to 12 are easily achievable, and the value of this parameter may be adjusted by using mixtures of helium and argon as driver gas. Monatomic gases require smaller compression ratios for the same pressure and temperature gains.

An example of a free piston driven reflected shock tunnel is shown in Fig. 4. This is the facility known as T5 at GALCIT. Similar machines exist at Canberra and Brisbane in Australia, at Göttingen in Germany, and at Tullahoma, USA.

The piston is accelerated in the compression tube by compressed air initially contained in the secondary air reservoir, thus compressing the driver gas until the diaphragm burst pressure (≈ 90 MPa) is reached. The piston speed at rupture has to be sufficiently high (≈ 170 m/s) to maintain almost constant pressure after diaphragm rupture for a short time (≈ 2 ms). Thus, the free-piston driver is a constant-pressure driver, in contrast to the constant-volume driver of the conventional shock tunnel. Fig. 5 shows a computed wave diagram for the processes in the compression and shock tubes of T5 after diaphragm rupture.

Another method of heating the driver gas is by a detonation wave travelling into a detonable mixture from the diaphragm end of the driver tube. This method has the advantage that the diaphragm may be much thinner, since it only needs to withstand the relatively low pressure before detonation. It also produces a long driver which should produce a more uniform shock propagation than the free-piston driver. A disadvantage is that, with hydrogen, the combustion produces water. The NO invariably produced in the reflected shock tunnel is likely to combine with this to form a very hostile environment for instrumentation and models.

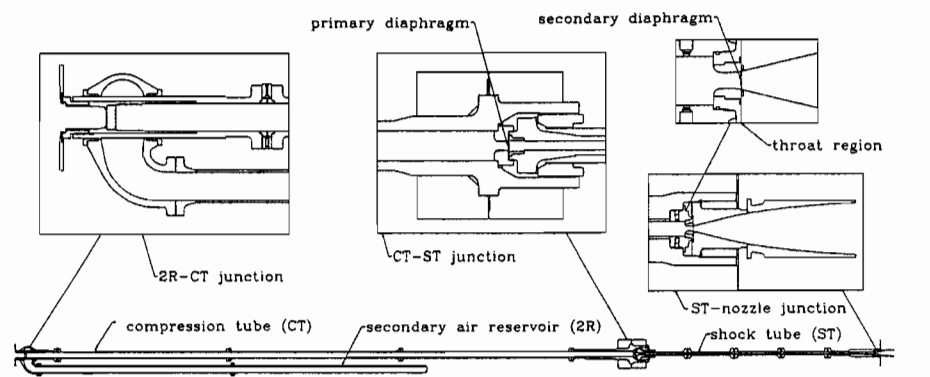


Fig. 4. Sectional view of the free-piston reflected shock tunnel T5 at GALCIT, with blow-ups of some of the parts. On the left is the 30 m long compression tube, joined to the 12 m shock tube and nozzle on the right. The test section and dump tank are not shown.

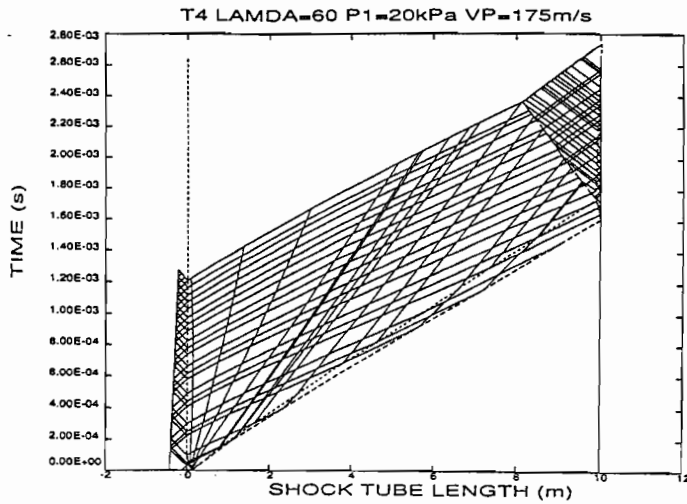


Fig. 5. Method of characteristics computation of the processes in the free-piston reflected shock tunnel. (after Hörnung and Bélanger, AIAA 90-1377).

3.1.3 Reservoir Conditions

The shock wave propagating along the shock tube generates a boundary layer on the shock tube wall, which causes the shock to decelerate. This attenuation limits the length to diameter ratio of shock tubes to approximately 100. Since the test time is proportional to the shock tube length if there are no losses, the shock tube diameter effectively is one of the limiting factors on the test time.

As the shock speed needs to be approximately 4 km/s, the specific enthalpy after the shock is 8 MJ/kg. This corresponds to $h/R = 28,000$ K, where R is the specific gas constant for air at room temperature. The process undergone by the gas may be shown in a Mollier diagram, see Fig. 6. Here the initial state of the gas in the shock tube (state 1) is shown at $s/R = 24$ on the entropy axis as a square point, and the primary shock raises the state to the coordinates $[30, 24000$ K], (state 2) see dashed line. Pressure and temperature are now 18 MPa and 4000 K. At this condition, part of the oxygen is already dissociated and some NO has been formed.

The reflected shock then increases h and s further, to the point $[33.5, 60000$ K], (state 0), where pressure and temperature are 100 MPa and 8000 K, see continuation of dashed line. The steady nozzle expansion takes the gas down in enthalpy at constant entropy to the final point on the dashed line, which then represents the free stream conditions of the tunnel.

This is not quite correct, of course, because the nozzle flow does not usually proceed in thermodynamic equilibrium all the way down to this state. At some point in the nozzle flow, the density is no longer large enough to maintain the large number of three-body collisions between particles that is required for the atomic particles to continue recombining as the gas cools in the expansion. Such non-equilibrium states can not be represented in a Mollier diagram.

3.1.4 Nozzle-Flow Freezing

The recombination reactions stop fairly suddenly in the nozzle expansion, and because the composition of the gas remains constant after this point, the phenomenon is called nozzle-flow freezing. A

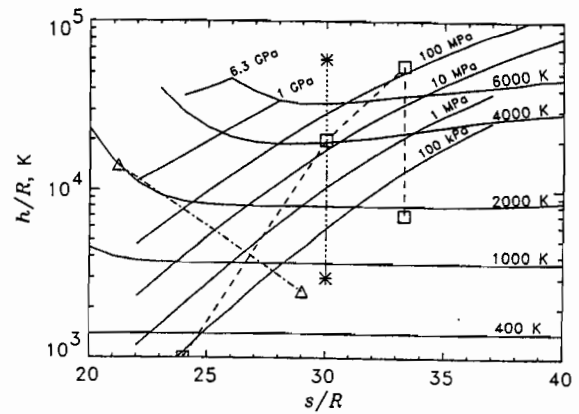


Fig. 6. Mollier diagram for equilibrium air, showing lines of constant pressure and temperature. An example of the processes in a reflected shock tunnel is shown by the dashed line. The lower asterisk represents the exit condition in an expansion tube that starts with the same shock tube conditions as in the reflected shock example. The upper asterisk represents the effective reservoir state of the expansion tube. The triangles show reservoir and exit condition of the facility proposed at Princeton.

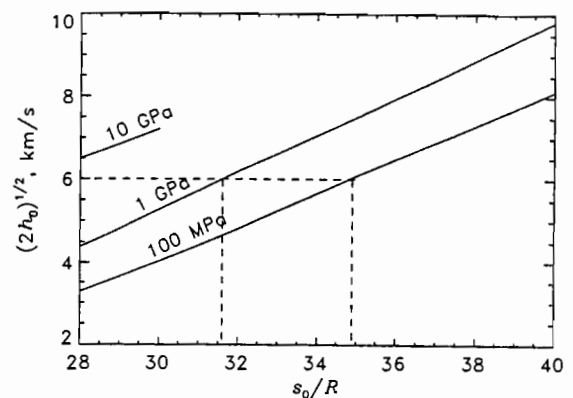
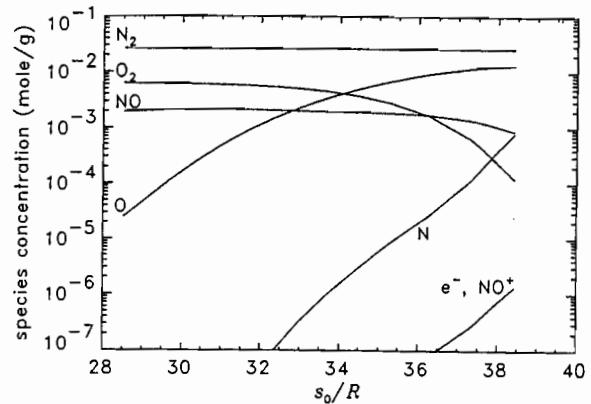


Fig. 7. TOP: For a given nozzle, the exit composition depends only on the dimensionless reservoir entropy. Example of T5 nozzle. BOTTOM: Mollier chart of the reservoir state showing lines of constant reservoir pressure. The specific reservoir enthalpy axis is plotted in the form of the maximum achievable velocity. This shows how, at a given flow speed, the specific reservoir entropy, and therefore the exit composition, depend on the reservoir pressure.

well-known feature of freezing is that, for a given nozzle, the composition of the frozen gas depends only on the reservoir specific entropy s_0 , and not on the reservoir specific enthalpy h_0 or reservoir pressure p_0 . In the example of one of the nozzles of T5, the upper part of Fig. 7 shows the frozen composition plotted against s_0/R . As may be seen, the concentration of atomic oxygen in the flow increases as s_0/R increases, until at 34 the number densities of O_2 and O are equal. Also, the fairly high concentrations of NO are unavoidable.

The lower part of Fig. 7 shows a Mollier chart of the reservoir state. Here the enthalpy coordinate has been distorted to convert it into the velocity achievable from a given reservoir state. This is because it shows the relation between the composition of the free-stream gas and the reservoir pressure. For example, to achieve 6 km/s, a reservoir pressure of 100 MPa produces the composition corresponding to $s_0/R = 34.9$, while a reservoir pressure of 1 GPa at the same enthalpy would give the lower atomic oxygen concentration corresponding to $s_0/R = 31.6$. Fig. 7 also shows that the NO concentration remains constant as s_0 is decreased. This is unavoidable with high-enthalpy reflected shock tunnels.

3.2 Expansion Tube

3.2.1 Configuration and Operation

Some of the essential limitations of the reflected shock tunnel are removed at the cost of new limitations by using an expansion tube. The expansion tube, like the reflected shock tunnel, first processes the test gas by propagating a shock wave through it, thus compressing, heating and accelerating it. The test gas is then not brought to rest as in a reflected shock tunnel, but accelerated further by an *unsteady* expansion. This is achieved by the arrangement shown in Fig. 8 also showing the wave diagram describing its operation.

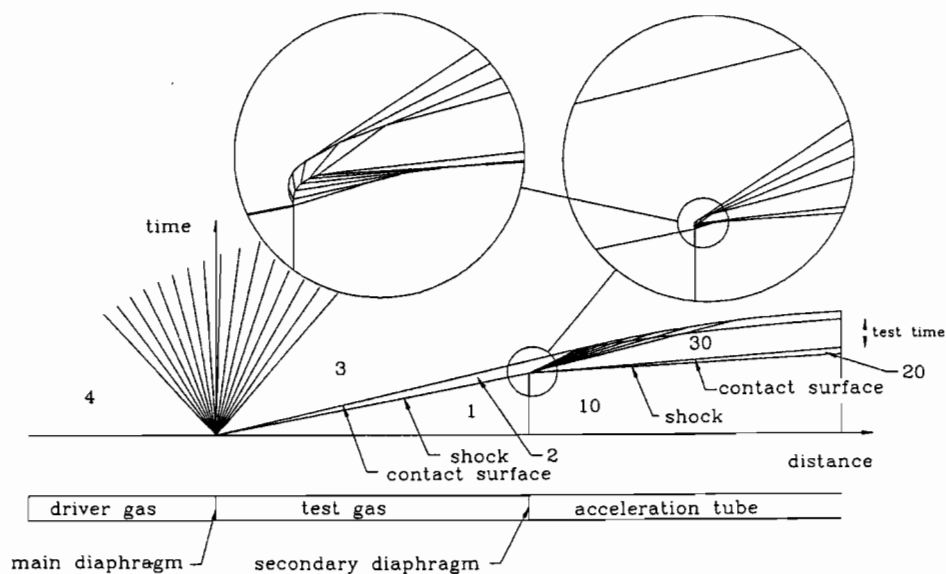


Fig. 8. Schematic sketch and wave diagram of an expansion tube. The detail in the vicinity of the rupture of the secondary diaphragm is shown in two enlarged insets. The diaphragm is accelerated to the contact surface speed over a finite opening time. This causes a reflected shock that is accelerated by the left running expansion wave transmitted from the diaphragm. Clearly, diaphragm opening time reduces the available test time.

In the expansion tube, a long acceleration tube usually of the same diameter as the shock tube is initially separated from the shock tube's downstream end by a thin secondary diaphragm. The pressures might have the initial values: 100 MPa, 100 kPa, 200 Pa in the driver, shock tube and acceleration tube respectively.

When the shock strikes the secondary diaphragm, it breaks, and the test gas acts as the driver for the shock propagating into the acceleration tube gas. The regions 10, 20 and 30 thus are analogous regions to those labelled 1, 2 and 3 in the shock tube. The processes undergone by the test gas are: 1-2 (shock), 2-3 (unsteady expansion). The conditions in the test gas after these processes may again be calculated by the shock tube equation. The result of such a calculation is shown graphically in Fig. 9. The test time is limited by the acceleration-gas test-gas contact surface, and by the leading edge of the reflection of the unsteady expansion from the driver-gas test-gas contact surface.

3.2.2 Effective Reservoir State

The expansion tube's thermodynamics may now be compared with that of the reflected shock tunnel in Fig. 6, where the lower asterisk marks the test condition of the expansion tube. The two first square symbols representing state 1 and state 2 are shared by the shock tunnel and expansion tube. The expansion tube takes the gas to a maximum temperature of 4000 K in this example, so that the atomic oxygen and NO concentrations may be kept much lower than in the shock tunnel.

At the same time, the effective specific reservoir enthalpy is more than twice the static enthalpy in region 2, since it is possible to gain total enthalpy in an unsteady expansion. This is therefore higher than after the reflected shock. To show the effective reservoir state of the expansion tube in Fig. 6 a second asterisk is plotted there, connected to state 2 with a dotted line to indicate that the gas never reaches this high enthalpy and pressure. The

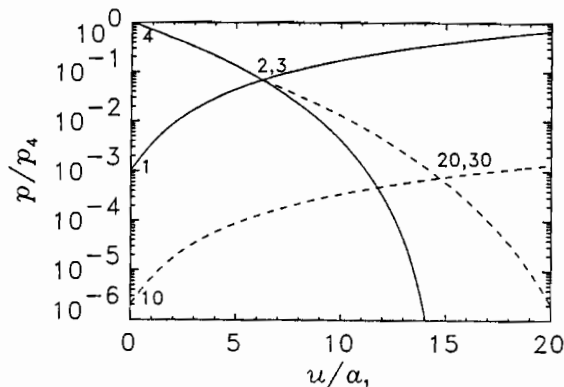


Fig. 9. Velocity-pressure plot of the processes in an expansion tube. The full lines give the solution for region 2 and the dashed lines, representing the locus of conditions achievable via a shock wave from condition 10, and the conditions achievable via an unsteady expansion from condition 2, give the solution for the test condition, 20. In this example, the driver gas is monatomic and the test and acceleration gases are diatomic. All are considered perfect gases.

lower entropy of the expansion tube causes the effective reservoir pressure to be enormous. In our example, it is around 2 GPa.

The static enthalpy h and static pressure p of the gas can remain low in the expansion tube, because the gas is not brought to rest after reaching state 2. This may be illustrated schematically in the case of h by the diagrams in Fig. 10

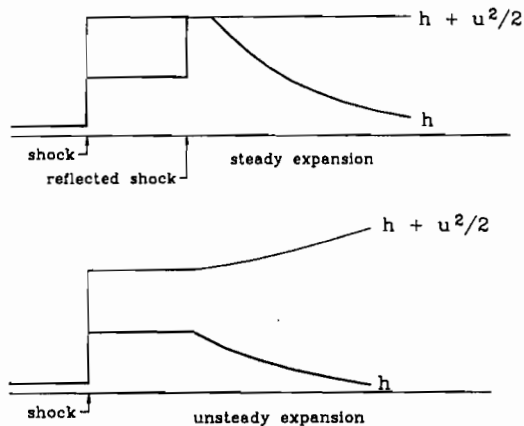


Fig. 10. Timelines of the static and effective reservoir specific enthalpy during the processes in a reflected shock tunnel (TOP), and in an expansion tube (BOTTOM). The expansion tube avoids the high value of h experienced by the test gas in the reflected shock tunnel and yet achieves even higher h_0 .

3.2.3 Free Stream Conditions

The test gas composition is practically that of state 2, because the density drops so quickly in the unsteady expansion that recombination of the atomic oxygen is not possible. Therefore it is best to operate the expansion tube with as low a value of T_2 as possible from this point of view.

If the expansion is taken to the same free stream pressure as in the reflected shock tunnel, see Fig. 6, the free stream temperature is seen to be much lower. This permits higher Mach number to be reached at the same h_0 .

3.3 Other Types of Facilities

A number of other types of facilities are in operation or are being considered. Among these the hypervelocity range is the most important. It employs a two-stage light gas gun to launch a model at the required speed into stationary gas in a long tube. This device is clearly much more expensive to operate than one in which the model is stationary. The model and instrumentation are also much more expensive, and it is difficult to test models that have high lift. However, the hypervelocity range is the only facility type in which good measurements of far wakes of bodies can be obtained.

There have been a number of other schemes, involving magneto-hydrodynamic accelerators or arc heaters. A relatively new idea being pursued at Princeton, is the optically heated continuous flow facility. This scheme aims to keep the gas below 2000 K in order to prevent the formation of NO. In Fig. 6, the process is shown by the chain-dotted line terminated by triangles. The gas is first compressed to a pressure of 1 GPa or more, and 2000 K. This makes use of the van der Waals effect that the isotherms curve up at low entropy, giving higher enthalpy. In the example shown in Fig. 6, the gas has approximately 20% of the necessary total enthalpy in this condition. The remainder of the enthalpy is added during a steady expansion by absorption of light. Success depends critically on whether the enormous power levels required (≈ 1 GW in the form of light) can be achieved and can be absorbed by the gas without causing non-equilibrium processes to produce atomic oxygen. In the author's opinion, these are very substantial questions.

4. Limitations of the Main Facility Types

All the different facility types have limitations that constrain them to be operated in regimes where conditions are acceptable and where they work. To some extent, the regimes covered by different facilities complement each other. As in the previous sections the following discussion will concentrate on the two most important types, the reflected shock tunnel and the expansion tube.

4.1 Reflected Shock Tunnel

Part of the following discussion is concerned with the effects of increasing the size of a reflected shock tunnel. In these considerations it is assumed that the ratios of lengths remain constant. In particular, the length to diameter ratio of the shock tube, which is limited by friction and heat loss at the shock tube wall, is considered to have the same value. The best value for this ratio turns out to be close to 100.

There are four main limitations to the regime that can be covered by the reflected shock tunnel:

1. The departure of the composition of the free-stream gas from that of air.
2. The fact that the test gas is brought to rest before it is accelerated again produces very high temperatures at high pressures which causes a containment problem.
3. The test time is limited by the size, by driver-gas contamination and by the containment limitation.
4. The strength of the facility limits the pressure.

4.1.1 Free-Stream Freezing

It is clear from Fig. 7 that it is not possible to produce a free-stream gas composition that is free of NO, unless the reservoir temperature is kept below 2000 K. This is therefore a hard limitation of the device if one is interested in real-gas effects in air. To set an arbitrary limit, choose the case when the molecular oxygen concentration is half of that in air. Fig. 7 may now be used to translate this limit into a line in $h_0 - p_0$ space. The top part of the figure shows that this limit is reached at $s_0/R = 35.2$. The bottom part of the figure shows how p_0 and h_0 are related along this value of s_0 . This relation is plotted in Fig. 11. As may be seen, an increase of p_0 moves the limit to significantly higher values of h_0 .

This limitation may, strictly speaking, not be represented by a single curve in $h_0 - p_0$ space, because it is dependent on the size of the facility. However, since the recombination rate in the nozzle flow is proportional to the square of the pressure (other variables being the same) quadrupling the size of the facility would only lower the line by a factor of 2 in pressure.

4.1.2 Nozzle-Throat Melting

The high temperatures and pressures seen by the containing material in a reflected shock tunnel lead to the limitation that materials can not be found that will contain the conditions for the duration of the test without melting. From experiments in T5, a copper throat is found to melt at $p_0 = 100$ MPa, $h_0 = 20$ MJ/kg, when the exposure to high heat flux lasts approximately 3 ms. From

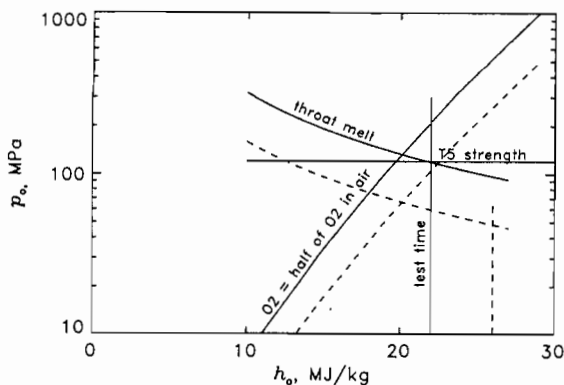


Fig. 11. Limitations on the reservoir pressure and specific enthalpy of reflected shock tunnels. The full line represents a facility of the size of T5. The dashed lines are for a facility scaled up by a factor of 4.

this result, and from the properties of copper, the heat flux to the wall may be estimated using one-dimensional unsteady heat conduction theory to be ≈ 2 GW/m². This agrees roughly with semiempirical formulas for throat heating.

Starting from this experimental point, adjusting it for the difference in the properties of copper from those of the best material found so far (tungsten-copper alloy), and extending it according to approximate formulas, the curve shown in Fig. 11 results. The basis of the approximation of this extension is that the convective heat flux is proportional to the density and the cube of the velocity, and that the exposure time is inversely proportional to the velocity.

It is important again to realize that this curve also depends on the facility size. The surface temperature reached under a given transient heat load is proportional to the square root of the exposure time (other variables being the same). The exposure time is proportional to the test time, which scales directly as the facility size (as does the *requirement* for test time). Since the heat flux is approximately proportional to pressure, quadrupling the size of the facility thus lowers the throat melt limit by a factor of 2 in p_0 , which therefore kills half of the improvement of the upscale.

4.1.3 Driver-Gas Contamination

The time interval between the arrival of the shock and the arrival of the contact surface at the right-hand end of the shock tube (see Fig. 1) is the most important factor in determining the test time. The test time can not simply be calculated from one-dimensional computations such as the one shown in Fig. 5, however, because the contact surface is in reality an extended region, and the complex interaction between the reflected shock and the boundary layer on the shock tube wall causes significantly earlier arrival of the driver gas at the nozzle throat.

At a given h_0 , the time interval between the arrival of the shock and the contact surface is directly proportional to the size of the facility (other variables being the same). As h_0 is increased, however, from the condition where the gas in region 2 is a perfect diatomic gas to where it is partially dissociated, this time interval changes down by almost a factor of 2. The speed with which the gas is drained from the reservoir through the throat into the nozzle increases as the square root of h_0 . Fortunately, the test time requirement also decreases as the square root of h_0 . However, the growth of the contact surface and the shock boundary layer interaction become more severe with increase of h_0 . As h_0 is increased, there comes a point when the test time is no longer sufficient. Though only very sparse information is available on this limit, it may be placed roughly at 22 MJ/kg for the case of T5, and this is essentially independent of p_0 .

Other things being equal, a scale increase increases the test time more than linearly, because the relative importance of the wall effects decreases. The test time *requirement* increases linearly with scale. The test time limit may therefore be expected to be moved to slightly higher h_0 in a larger facility.

4.1.4 Strength, Scale Effects

Clearly, the strength of the facility merely limits the pressure at which it can be operated, and may be represented by a line at constant p_0 .

To illustrate the effect of scaling up a facility from the size of T5 by a factor of 4, Fig. 11 also shows the displaced limits for the larger machine as dashed lines. This makes it clear that an increase of size makes strength relatively unimportant, since the throat-melt limit makes it impossible to operate at $p_0 > 70$ MPa, if $h_0 > 15$ MJ/kg in the facility scaled up by a factor of 4. As regards the throat-melt, test-time and strength limits, T5 appears to be close to the optimum scale. This was fortuitous, since the scale and strength were determined by other constraints.

4.1.5 Performance

In the region of $h_0 - p_0$ space within the above limitations, reflected shock tunnels can cover the space practically completely. In the

case of the free-piston device, this can be achieved with tailored interface operation, because of the flexibility of the speed of sound ratio a_4/a_1 of this device.

As an example, Fig. 12 shows two reservoir pressure traces obtained in T5. These are representative of the quality achievable over the range $20 \text{ MPa} < p_0 < 100 \text{ MPa}$, $5 \text{ MJ/kg} < h_0 < 22 \text{ MJ/kg}$.

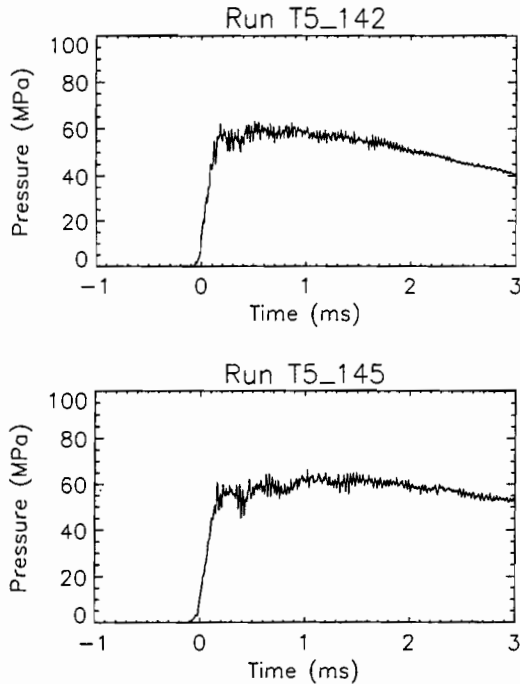


Fig. 12. Nozzle reservoir pressure traces of two runs of T5 at 22 (TOP) and 11 MJ/kg (BOTTOM).

4.2 Expansion Tube

As was pointed out in the description of the expansion tube, this facility type has the advantage that the material is exposed only to a fraction of the effective total pressure and only to a fraction of the total enthalpy. The stresses and heat loads are therefore not a serious limitation. Referring to Fig. 9 and Fig. 6 it becomes clear that for a given state 2, the effective values of p_0 and h_0 depend on the pressure p_{20} to which the flow is expanded in the unsteady expansion. It is therefore not meaningful to relate the extreme heating condition to the $h_0 - p_0$ space on this basis.

In the expansion tube a far more important concern is the short test time and the small test flow size. Consider for example a shock tube diameter of 100 mm. In the reflected shock tunnel, this provides a good flow for a nozzle exit diameter of typically 400 mm and a test duration of 1 ms at 18 MJ/kg. In the expansion tube, the same shock tube, driving an acceleration tube of the same diameter and 10 m length would produce a test flow of 100 mm exit diameter and 170 μs duration.

Fortunately, the size of the facility can be increased, since the penalty for size that plagues the reflected shock tunnel (melt limit) does not exist here. However, the test time limit remains, since the test time, which increases linearly with the size, only matches the increased test time requirement, which also increases linearly with size, unless the facility is deliberately made much larger than the models to be tested.

The friction losses in the acceleration tube set a limit on the length to diameter ratio. A reasonable maximum value is about 120. It turns out that a good shock tube length is then about 50 diameters. A rule of thumb for the optimum test time of an expansion tube is the time interval between the arrival of the primary shock and the arrival of the shock tube contact surface at the end of the shock tube. This time is given approximately by

$$\tau \approx 10 \frac{d}{\sqrt{h_0}},$$

where d is the shock tube diameter. This is smaller than the test time requirement of $20L/V_\infty$, given in section 2.2, by a factor of 1.4 if the model size L is taken to be the tube diameter d . The model therefore has to be smaller than the largest model that could be tested in the facility if size were the only constraint.

Any attempts to expand the diameter of the expansion tube at the downstream end are therefore futile, since the model size is limited by the available test time, and not by the tube diameter. (This verdict may be relaxed if the flow studied is such that less test time than $20V_\infty/L$ is required.)

The most important problem in expansion tube operation is therefore the preservation of as much as possible of the test time. An obvious factor reducing the test time is the opening time of the secondary diaphragm, which is disregarded in the ideal expansion tube calculations above. In order to show the effect of finite diaphragm opening time, Fig. 8 shows as blown up insets two successive enlargements of a portion of the wave diagram. In the largest of these, the diaphragm is shown to accelerate from rest over a finite time to become the contact surface between the acceleration and test gas. The diaphragm thus causes the incident shock to be reflected. As the diaphragm accelerates, expansion waves are transmitted to the reflected shock, weakening it and eventually causing it to become the right edge of the unsteady expansion. On the acceleration tube side of the diaphragm, compression waves are transmitted to the right, which focus to form the acceleration tube shock. The time it takes to accelerate the diaphragm clearly reduces the test time.

The reduction in test time is roughly equal to the diaphragm opening time. This is given approximately by

$$t_D \approx \sqrt{\frac{\rho \theta d}{p_2}},$$

where ρ is the density of the diaphragm material, θ is the diaphragm thickness and p_2 is the pressure in state 2. For a mylar diaphragm that is just strong enough to contain $p_1 = 100 \text{ kPa}$, and a diameter of 300 mm, this gives an opening time of approximately 70 μs . On the basis of the above rule of thumb, the test time becomes 0.7 ms at 18 MJ/kg, so that the diaphragm opening time reduces the available test time by about 10%.

All of these considerations assume the flow to be one-dimensional, and serious consequences for the test time may be expected to result also from the wall effects on the structure of the two contact surfaces, and the three-dimensionality of the diaphragm rupture.

The composition of the test gas was assumed to be that of state 2 above. This is a little pessimistic, because some recombination will occur in the unsteady expansion during the later part of the test duration, where the gas has taken a longer time to traverse the expansion wave. This will therefore cause the composition to

vary during the test time from an initial condition corresponding to that of state 2 to a final condition in which the atomic oxygen concentration, and to a lesser extent the NO concentration, are reduced slightly. The composition limit is almost independent of p_0 . The molecular oxygen will be reduced to half the value in air at $h_0 \simeq 22$ MJ/kg.

Summarizing the limitations of the expansion tube, the emphasis has to be on the test time limit. Since the diaphragm opening time is independent of h_0 , there comes a point where the enthalpy is limited by the test time. In the author's opinion, this limit is at 30 MJ/kg. The upper limit on p_0 is unimportant, since values in the GPa range are easily achievable.

4.2.1 Performance

To date, the largest expansion tube is one operated at the General Applied Sciences Laboratory in New York by a team headed by Dr. John Erdos. This has a shock tube (and acceleration tube) diameter of 150 mm. At present it has a cold helium driver, so that the enthalpy at which it can be run is limited to approximately 12 MJ/kg. A modification to equip the facility with a free-piston driver is being considered at present. This would extend the range to approximately 30 MJ/kg. The effective reservoir pressure is very high. In the GASL facility, values of up to 400 MPa have been achieved.

5. Concluding Remarks

The thermodynamics, gasdynamics and scaling laws of hypervelocity flows, the power requirements, and the properties of containing materials, were shown to lead to the two main hypervelocity flow simulation facility types: The reflected shock tunnel and the expansion tube. The simplest forms of such devices were described, giving the logic that leads to them, and a comparison of their ranges of applicability. This was done with regard only to their main features, and many subtle points of their operation had to be omitted.

The hard limitations of the reflected shock tunnel constrain this device to be restricted to specific reservoir enthalpies below 22 MJ/kg and reservoir pressures below 90-200 MPa (depending on the enthalpy in the range 25-12 MJ/kg) at the size of the presently operating facility T5. Increase of size carries severe pressure penalties. The expansion tube's most severe restriction is the short test time. This is critically constrained by the behavior of the contact surface and the opening time of the secondary diaphragm. However, there appear to be no penalties for scale increase, and the reservoir pressure obtainable is extremely high. The upper limit for the specific reservoir enthalpy is approximately 30 MJ/kg on the basis of the free stream dissociation and test time constraints.

References

Bakos R. J., J. Tamagno, O. Ryszkalla, M. V. Pulsonetti, W. Chinitz, and J. I. Erdos, 1992 "Hypersonic mixing and combustion studies in the Hypulse facility," *J. Propulsion and Power*, **8** 900-906.

Hornung, H. G. 1992 Performance data of the new free-piston shock tunnel at GALCIT, AIAA 92-3943.

Lukasiewicz, J. 1973 "Experimental Methods of Hypersonics", Marcel Dekker, Inc. New York.

Experimental Hypervelocity Flow Simulation, Needs, Achievements and Limitations.

Hans Hornung

Graduate Aeronautical Laboratories

California Institute of Technology

Pasadena, California 91125, USA

Abstract

The requirements for ground simulation of hypervelocity flows are set out on the basis of the similarity parameters of the problem. This, together with the thermodynamical properties of air, the consequent heat loads on the facility and large power requirements, leads to the two most successful devices, the reflected shock tunnel and the expansion tube. After a description of the operation and the thermodynamics of these devices, their essential limitations are explained. Scale effects of these limitations are discussed. On this basis the range over which they can be applied for flow simulation is delineated.

Keywords: Hypervelocity flow, ground simulation, simulation facilities, shock tunnel, expansion tube, dissociation.

1. Introduction

The term *hypervelocity* is used to distinguish those flows in which the velocity is so large that the conditions after the bow shock on a body are such as to cause the molecular components of the gas to dissociate. The fields of human endeavor where hypervelocity flows are of importance are those in which an object traverses the atmosphere of one of the planets of the solar system. Typically this could be associated with transport to or from space in man-made vehicles, but hypervelocity flows also occur naturally, e.g., when a meteorite enters a planetary atmosphere.

The term *hypersonic* flow is used to describe situations where the flow speed is large compared to the free-stream speed of sound. Such high-Mach-number flows can, of course, be generated by lowering the speed of sound far enough to keep the gas in the regime where it behaves as a perfect gas. In such *cold* hypersonic flows, the important dissociative and other real-gas effects of hypervelocity flows do not occur. In order to understand the intricacies of flows in which the chemistry of the gas is activated by the kinetic energy of the flow, it is necessary to simulate *hypervelocity* flows in the laboratory.

In the context of the earth's atmosphere the orbital velocity is 8 km/s, and the velocity at which the most severe heating problems arise is 6 km/s. In the frame of reference of the flying object, the ordered kinetic energy per unit mass of the free-stream gas is therefore 18 MJ/kg. At high enthalpy, the Mach number, which measures the square root of the ratio of the ordered kinetic energy of the flow to the thermal energy of the gas, is not so important as the ratio of the ordered kinetic energy measured in terms of the specific dissociation energy of the gas. There are usually several such characteristic chemical energies.

The characteristic specific energies relevant for air are

$$\begin{aligned} D_{N_2} &= 33.6 \text{ MJ/kg} & E_{vN_2} &= 0.992 \text{ MJ/kg} \\ D_{O_2} &= 15.5 \text{ MJ/kg} & E_{vO_2} &= 0.579 \text{ MJ/kg} \\ D_{NO} &= 20.9 \text{ MJ/kg} & E_{vNO} &= 0.751 \text{ MJ/kg}, \end{aligned}$$

where the D 's and E_v 's are specific energies of dissociation and of vibration respectively. It is not possible to simulate the numerous idiosyncrasies of a particular gas by using another gas. The specific chemical energies have definite known values, and the duplication of the ratios of the ordered kinetic energy to them in a simulation implies that the actual flow speed has to be duplicated.

It follows that the reservoir enthalpy h_0 of the flow, which is approximately equal to $V^2/2$, where V is the flow speed, has to have the same value as in flight. If the flow is accelerated from a reservoir at rest, without adding energy to it during the expansion, the reservoir enthalpy corresponding to a flow speed of 6 km/s is 18 MJ/kg, which, at a reservoir pressure of 100 MPa, implies a temperature of nearly 9000 K in air.

The high pressure is necessary to ensure that the chemical reaction rates occur at the right speed for correct simulation of nonequilibrium effects. Smaller scale requires faster reaction for correct simulation. If the temperatures are right (as is ensured by correct flow speed) the reaction rates depend mainly on the density. Rates for binary reactions, like dissociation, are linear in density, those for three-body reactions, like recombination, are quadratic in density. Thus, all reactions can never be simulated correctly except at full scale. In many cases, three-body reactions are not important and, where they are, component testing or extrapolation is necessary.

Continuous flow facilities are ruled out by the high power requirements of typically a few GW. The high speed reduces the steady flow duration requirement to a few ms, however. A convenient way to accelerate, heat and compress a gas for a short time, is to pass a shock wave over it. Many types of high-enthalpy facilities therefore embody shocks as elements.

The problem of hypervelocity simulation is not limited to speeds of the order of 6 km/s, of course. Meteorites entering planetary atmospheres typically have a speed of 20-60 km/s, and proposals for man-made vehicles have considered speeds in the vicinity of 16 km/s. Such conditions involve very strong ionization of the gas and intense radiative heat loss from it. In the following discussion, such very high speeds will not be considered, and attention will be concentrated on the range 3-7 km/s. In this range, the requirements for simulation of hypervelocity flows and some of the methods by which the simulation has been achieved to date will be presented. The paper then closes with a discussion of the limitations and achieved conditions of the different types of facilities.

This paper is a descriptive account of the reasons for the forms that hypervelocity simulation facilities have taken. It is not a detailed account of the work that has been done in the field, and only a few representative publications will be cited. A very important book on the subject is Lukasiewicz's "Experimental Methods of Hypersonics". The interested reader should consult this volume on all the questions concerning this field.

In the present paper, the two most successful facility types for hypervelocity flow simulation, the reflected shock tunnel and the expansion tube will be given prominence.

2. Requirements for Ground Simulation

2.1 Similarity in Hypervelocity Flows

To simulate a hypervelocity flow at smaller scale, all the dimensionless parameters of the problem have to be reproduced. In steady hypervelocity flows any dimensionless dependent quantity Q , say, depends on dimensionless variables as follows:

$$Q = Q(M_\infty, Re, Pr, T_w/T_0, B_n, \alpha, \beta, E_i, R_j, Le_i, c_{\infty i}).$$

Here, M_∞ is the free stream Mach number, Re and Pr are Reynolds and Prandtl numbers, which, in this context, are best defined at conditions corresponding to the gas in equilibrium after a normal shock for which the upstream conditions are those of the free stream, T_w is a representative body surface temperature, T_0 is the temperature from which a gas would have to be expanded by a steady expansion to reach the free-stream conditions, B_n is a vector of length ratios defining the body geometry, α is the angle of attack, and β is the yaw angle. E_i is a vector of dimensionless numbers relating the specific formation enthalpies of the species to the specific kinetic energy of the free-stream gas, R_j is a vector relating the characteristic lengths associated with the chemical reactions to the characteristic length of the body, Le_i are the Lewis numbers giving the dimensionless species diffusion coefficients, and $c_{\infty i}$ is a vector giving the dimensionless concentrations of the species in the free stream. Even this long list of variables is not complete, as the vibrational characteristics of the molecular species have been omitted.

Up to and including β in the above list, the variables are the same as in cold hypersonics, in which the remaining variables, which describe the thermodynamic and chemical properties of the gas, can be replaced completely by a single variable, the ratio of specific heats, which, for a perfect gas, is a constant. Clearly, the more complex thermodynamics and chemistry of the hypervelocity flow requires many more parameters to be duplicated in the scale experiments than perfect-gas cold hypersonics. For example, in air at a free-stream speed of 5 km/s, it is necessary to include at least 5 species and 8 reactions, so that, if all the geometrical parameters are exactly duplicated, there remain over 20 dimensionless variables to match. In fact, as has already been indicated in the introduction, it is not possible to simulate both binary and three-body reactions simultaneously (except at full scale) because of the difference in their dependence on the density.

In special cases, however, the problem may be considerably simplified. For example, if the gas is especially simple, such as in a single diatomic gas, there is only a single E and there are only two R 's. Only one of the R 's can be matched, and, *e.g.*, in blunt body flows, it is best to match the binary dissociation reaction. With correct E , this automatically also causes Re , Le and Pr to be matched. Thus, the problem reduces to

$$Q = Q(M, T_w/T_0, E, R, c_\infty).$$

If the Mach number is sufficiently high, and the bow shock is not of interest in regions where it becomes very weak, the Mach-number-independence principle is effective, and the number of independent parameters is down to 4. This situation can be satisfactorily simulated.

Where such simplifications are not possible, it becomes necessary to divide the flow field up into particular regions and to simulate these separately. This is sometimes referred to as component testing. An example is the testing of engine combustors by connecting the inlet of the combustor directly to the exit of the facility nozzle, thus enabling testing at almost full size. Another example is the testing of the situation on the front of a body by placing only the nose shape into the test section, so that binary scaling and Mach-number independence apply.

2.2 Power Requirement

It is really quite amazing how much power is in a hypervelocity flow. For example, a wind tunnel with a cross-sectional area of 1 m², in which the flow speed is 7 km/s, and the density is 0.01 kg/m³ requires a power of 2 GW. This is a tenth of a percent of the power consumption of the USA. It also corresponds to an energy flux of 2 GW/m², or 46 times that at the surface of the sun. It is clear, that this kind of power can not be sustained for long times.

Fortunately, it only takes a very short time to set up a steady flow over a model at such high speeds. Opinions differ about the necessary test time. A reasonably conservative value is

$$\tau = 20 \frac{L}{V_\infty},$$

where L is the model length and V_∞ is the free-stream velocity. With this value, the test time requirement for the above facility comes out to approximately 3 ms, so that the *energy* requirement is only 10 MJ. This energy can be stored over a long time and released during a short test period.

The power requirement is thus one of the reasons why short-duration facilities are necessary for hypervelocity flow simulation. Another reason arises in the case of facilities that use a steady expansion to accelerate the flow from rest. In such facilities, the thermodynamic condition in the reservoir from which the gas is expanded is such that the specific enthalpy, h_0 , has to be 20 MJ/kg or so. In air, at a pressure of 100 MPa, this corresponds to a temperature of 9500 K or so. Hence, it is necessary to limit the time for which the materials containing the flow are exposed to these conditions. With the best materials available today, 3 ms is about the limit at the conditions quoted.

2.3 Instrumentation Requirements

This topic is one that deserves at least as much space as this whole paper, and it will not be possible to deal with it here, except for the purpose of pointing to its importance. Clearly, a test in a hypervelocity simulation facility is quite expensive. It is therefore most desirable to make as extensive a set of measurements as possible, each time such a test is performed. Unfortunately, the different forms of non-intrusive testing that exist at present require different degrees of expertise, which are seldom available at the same place as the test, because of the degree of sophistication that they often require.

Among the presently used routine measurement techniques, the following are available at all high-enthalpy test facilities:

1. Surface pressure measurement

2. Surface heat flux measurement
3. Schlieren and shadow photography
4. Interferometry

Techniques that are applied relatively rarely to hypervelocity flows, but are very important for them, are

1. Mass spectrometry
2. Spectroscopy
3. Laser-induced fluorescence
4. Raman spectroscopy

These methods are able to measure species concentrations and temperature, and would therefore provide extremely important data for the analysis of results from hypervelocity facilities. In the author's opinion, it is high time that major funding be directed to the juxtaposition of modern diagnostics and hypervelocity facilities. A good example of this is the policy at the HEG laboratory in Göttingen, Germany.

3. Hypervelocity Simulation Facilities

In this section the principles of operation of the most successful types of hypervelocity facilities are presented. The thermodynamical and chemical processes which the gas undergoes in the generation of the hypervelocity flow are given prominence in this, because they define and explain the most serious disadvantages of the facility types.

3.1 Reflected-Shock Tunnel

3.1.1 Configuration and Operation

By far the most used and most productive hypervelocity simulation facility is the reflected shock tunnel. Fig. 1 shows a schematic sketch and a wave diagram of the device. Initially, the driver region is filled with high-pressure gas and a diaphragm separates it from the shock tube, which is filled with the test gas at lower pressure. The shock tube is separated from a nozzle, attached to its other end by a weak diaphragm. The nozzle and test section, as well as the dump tank, are initially evacuated. The test section and dump tank are not shown in the figure.

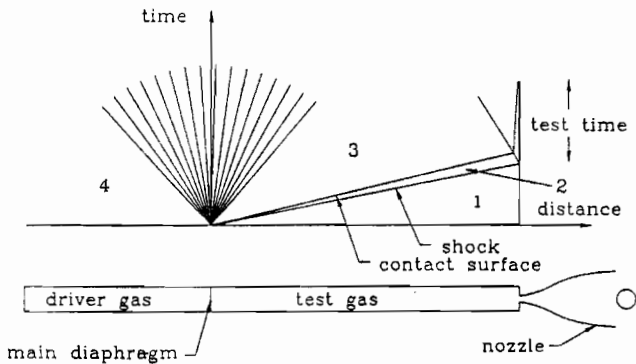


Fig. 1. Schematic sketch of reflected shock tunnel and wave diagram. The separation between the shock wave and contact surface is exaggerated to show it better

When the main diaphragm breaks, a shock wave propagates into the test gas, and an expansion wave propagates into the driver gas in such a way that the pressures and velocities in the region

between the shock wave and expansion wave are continuous across the interface between the two gases. These processes are shown in the wave diagram of Fig. 1. The initial state of the driver gas, in region 4 of the wave diagram, is processed by the expansion wave to the condition in region 3, and the initial state of the test gas, region 1, is processed by the shock wave to the condition in region 2. The states 2 and 3 are determined by the expansion wave and by the shock wave and the requirement that velocities and pressures must match across the boundary between 2 and 3. This may best be illustrated by a velocity-pressure diagram, shown in Fig. 2. The upper curve shows the locus of the states that can be reached from the initial condition of the driver gas via an expansion wave and the lower curve shows the states that can be reached from the initial state of the test gas via a shock wave. Their intersection represents the condition in regions 3 and 2, where pressures and velocities are matched. The solution thus corresponds to the intersection of the two curves in Fig. 2.

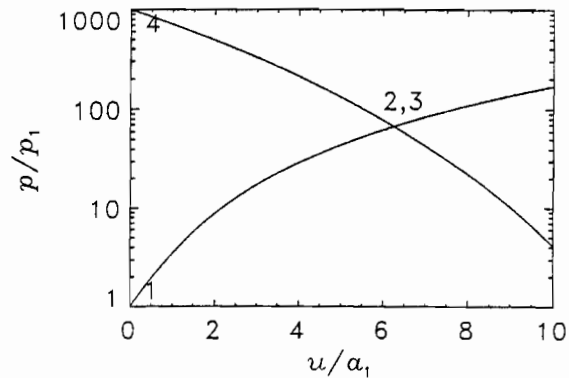


Fig. 2. Example of velocity-pressure diagram for a shock tube. The pressure p is normalized with the initial pressure of the test gas, p_1 , and the velocity u is normalized with the speed of sound in the test gas at condition 1, a_1 . In this example the gases are treated as perfect gases with specific heat ratios γ_1 and γ_4 of 7/5 and 5/3 respectively. Also, the ratio of the speeds of sound a_4/a_1 , the third parameter determining the solution, was chosen to be 5.

If a whole lot of such solutions are combined, the solutions can be shown parametrically in a diagram plotting the shock Mach number $M_s = V_s/a_1$ against the pressure ratio p_4/p_1 . This is done in Fig. 3.

In the reflected shock tunnel, the state of the test gas in region 2 is processed further by the shock wave reflected from the closed end of the shock tube. This heats and compresses the gas even more than has already been accomplished by the primary shock, but it also brings the test gas to rest again. The primary shock breaks the thin diaphragm between the shock tube and the nozzle, thus allowing the test gas to expand in a steady expansion through the nozzle.

It is important to operate the shock tunnel in such a way that the interaction between the reflected shock and the contact surface does not produce any further waves. When conditions have been chosen in such a way that this is the case, this is referred to as tailored-interface operation. The condition behind the reflected shock is then the reservoir condition of the nozzle flow, and is referred to by the subscript 0.

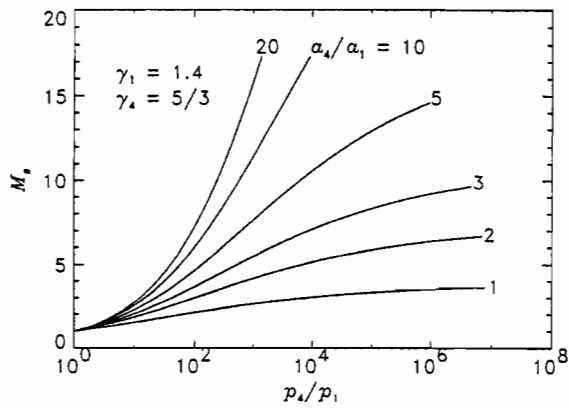


Fig. 3. The shock tube equation for monatomic driver gas and diatomic test gas, both treated as perfect gases. Note the strong dependence of the shock Mach number on the speed of sound ratio. Real-gas effects modify this diagram only slightly.

The nozzle expansion converts the thermal energy of the stationary reservoir gas into ordered kinetic energy. In doing so, the maximum flow velocity achievable is

$$V_{\infty} = \sqrt{2h_0},$$

where h_0 is the specific enthalpy of the reservoir condition. Since it is necessary to achieve speeds around 6 km/s, the reservoir specific enthalpy needs to be in the vicinity of 18 MJ/kg. In a reflected shock tunnel, a very good approximation is

$$h_0 = V_s^2.$$

It follows that the shock speed has to be about 4.3 km/s, which, in air, corresponds to $M_s = 12.5$. Referring to Fig. 3, we see that this value may not be reached with pressure ratios less than 2000 unless a_4/a_1 exceeds 8. Since the test gas speed of sound is virtually fixed by the fact that we want to use air in a laboratory at room temperature, the driver-gas sound speed has to be high.

3.1.2 Driver-Gas Conditions

Various ways have been used to increase a_4 . First, a light gas, either hydrogen or helium is used, and second, the driver gas is heated. Steady state heating is limited to about 800 K. This gives $a_4/a_1 = 4.8$ for helium driver gas and air test gas. Not only is

this too low, but it is also expensive and dangerous to contain high-pressure and high-temperature gas for an extended period. A second method is to heat the driver gas relatively quickly by combustion of a limited amount of hydrogen and oxygen mixed with the driver gas before the test. Mixtures in the proportions 14% hydrogen: 7% oxygen: 79% helium, give $a_4/a_1 \approx 7$.

While this is just about enough, another, more convenient technique is to compress the driver gas adiabatically with a heavy piston. This method has the advantage that the driver gas is hot only for a very short time, and that (as in the combustion-heated driver) the high pressure required is produced automatically. However, it also means that the driver is short, with a moving end wall, so that waves travelling between the main diaphragm station and the piston cause disturbances to the shock. With adiabatic compression, values of a_4/a_1 up to 12 are easily achievable, and the value of this parameter may be adjusted by using mixtures of helium and argon as driver gas. Monatomic gases require smaller compression ratios for the same pressure and temperature gains.

An example of a free piston driven reflected shock tunnel is shown in Fig. 4. This is the facility known as T5 at GALCIT. Similar machines exist at Canberra and Brisbane in Australia, at Göttingen in Germany, and at Tullahoma, USA.

The piston is accelerated in the compression tube by compressed air initially contained in the secondary air reservoir, thus compressing the driver gas until the diaphragm burst pressure (≈ 90 MPa) is reached. The piston speed at rupture has to be sufficiently high (≈ 170 m/s) to maintain almost constant pressure after diaphragm rupture for a short time (≈ 2 ms). Thus, the free-piston driver is a constant-pressure driver, in contrast to the constant-volume driver of the conventional shock tunnel. Fig. 5 shows a computed wave diagram for the processes in the compression and shock tubes of T5 after diaphragm rupture.

Another method of heating the driver gas is by a detonation wave travelling into a detonable mixture from the diaphragm end of the driver tube. This method has the advantage that the diaphragm may be much thinner, since it only needs to withstand the relatively low pressure before detonation. It also produces a long driver which should produce a more uniform shock propagation than the free-piston driver. A disadvantage is that, with hydrogen, the combustion produces water. The NO invariably produced in the reflected shock tunnel is likely to combine with this to form a very hostile environment for instrumentation and models.

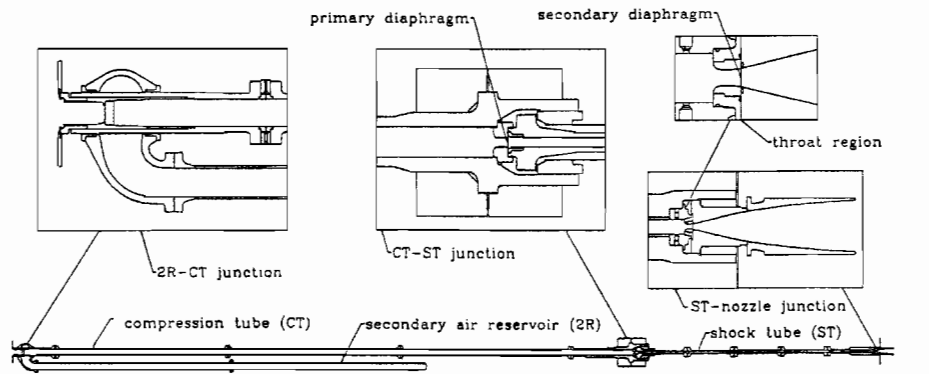


Fig. 4. Sectional view of the free-piston reflected shock tunnel T5 at GALCIT, with blow-ups of some of the parts. On the left is the 30 m long compression tube, joined to the 12 m shock tube and nozzle on the right. The test section and dump tank are not shown.

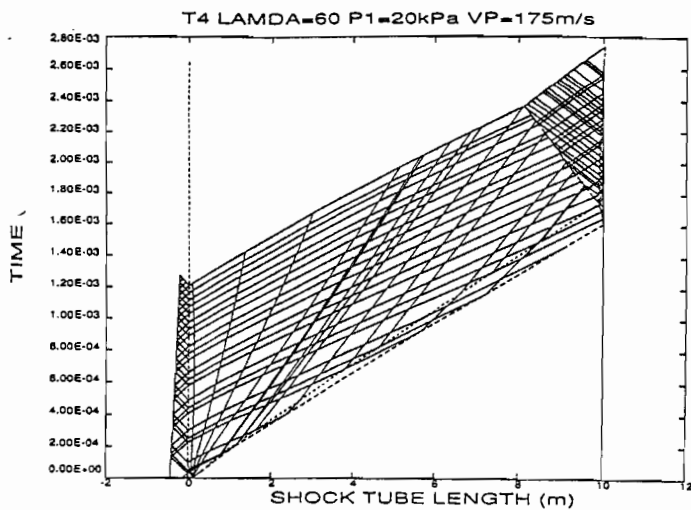


Fig. 5. Method of characteristics computation of the processes in the free-piston reflected shock tunnel. (after Hornung and Bélanger, AIAA 90-1377).

3.1.3 Reservoir Conditions

The shock wave propagating along the shock tube generates a boundary layer on the shock tube wall, which causes the shock to decelerate. This attenuation limits the length to diameter ratio of shock tubes to approximately 100. Since the test time is proportional to the shock tube length if there are no losses, the shock tube diameter effectively is one of the limiting factors on the test time.

As the shock speed needs to be approximately 4 km/s, the specific enthalpy after the shock is 8 MJ/kg. This corresponds to $h/R = 9000$ K, where R is the specific gas constant for air at room temperature. The process undergone by the gas may be shown in a Mollier diagram, see Fig. 6. Here the initial state of the gas in the shock tube (state 1) is shown at $s/R = 24$ on the entropy axis as a square point, and the primary shock raises the state to the coordinates $[30, 24000$ K], (state 2) see dashed line. Pressure and temperature are now 18 MPa and 4000 K. At this condition, part of the oxygen is already dissociated and some NO has been formed.

The reflected shock then increases h and s further, to the point $[33.5, 60000$ K], (state 0), where pressure and temperature are 100 MPa and 8000 K, see continuation of dashed line. The steady nozzle expansion takes the gas down in enthalpy at constant entropy to the final point on the dashed line, which then represents the free stream conditions of the tunnel.

This is not quite correct, of course, because the nozzle flow does not usually proceed in thermodynamic equilibrium all the way down to this state. At some point in the nozzle flow, the density is no longer large enough to maintain the large number of three-body collisions between particles that is required for the atomic particles to continue recombining as the gas cools in the expansion. Such non-equilibrium states can not be represented in a Mollier diagram.

3.1.4 Nozzle-Flow Freezing

The recombination reactions stop fairly suddenly in the nozzle expansion, and because the composition of the gas remains constant after this point, the phenomenon is called nozzle-flow freezing. A

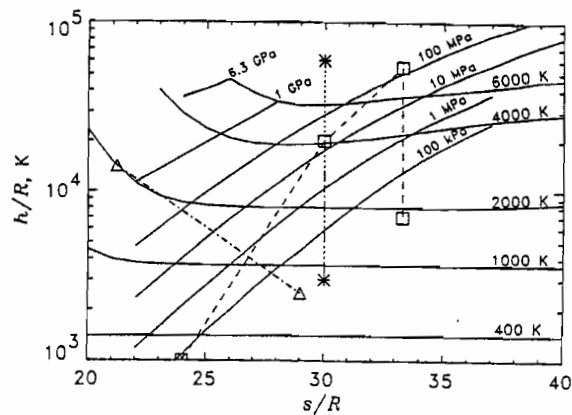


Fig. 6. Mollier diagram for equilibrium air, showing lines of constant pressure and temperature. An example of the processes in a reflected shock tunnel is shown by the dashed line. The lower asterisk represents the exit condition in an expansion tube that starts with the same shock tube conditions as in the reflected shock example. The upper asterisk represents the effective reservoir state of the expansion tube. The triangles show reservoir and exit condition of the facility proposed at Princeton.

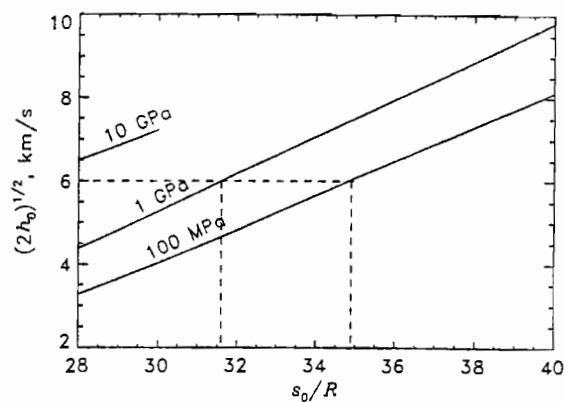
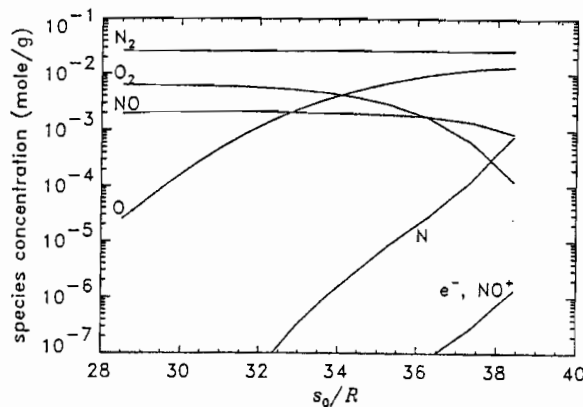


Fig. 7. TOP: For a given nozzle, the exit composition depends only on the dimensionless reservoir entropy. Example of T5 nozzle. BOTTOM: Mollier chart of the reservoir state showing lines of constant reservoir pressure. The specific reservoir enthalpy axis is plotted in the form of the maximum achievable velocity. This shows how, at a given flow speed, the specific reservoir entropy, and therefore the exit composition, depend on the reservoir pressure.

well-known feature of freezing is that, for a given nozzle, the composition of the frozen gas depends only on the reservoir specific entropy s_0 , and not on the reservoir specific enthalpy h_0 or reservoir pressure p_0 . In the example of one of the nozzles of T5, the upper part of Fig. 7 shows the frozen composition plotted against s_0/R . As may be seen, the concentration of atomic oxygen in the flow increases as s_0/R increases, until at 34 the number densities of O_2 and O are equal. Also, the fairly high concentrations of NO are unavoidable.

The lower part of Fig. 7 shows a Mollier chart of the reservoir state. Here the enthalpy coordinate has been distorted to convert it into the velocity achievable from a given reservoir state. This is because it shows the relation between the composition of the free-stream gas and the reservoir pressure. For example, to achieve 6 km/s, a reservoir pressure of 100 MPa produces the composition corresponding to $s_0/R = 34.9$, while a reservoir pressure of 1 GPa at the same enthalpy would give the lower atomic oxygen concentration corresponding to $s_0/R = 31.6$. Fig. 7 also shows that the NO concentration remains constant as s_0 is decreased. This is unavoidable with high-enthalpy reflected shock tunnels.

3.2 Expansion Tube

3.2.1 Configuration and Operation

Some of the essential limitations of the reflected shock tunnel are removed at the cost of new limitations by using an expansion tube. The expansion tube, like the reflected shock tunnel, first processes the test gas by propagating a shock wave through it, thus compressing, heating and accelerating it. The test gas is then not brought to rest as in a reflected shock tunnel, but accelerated further by an *unsteady* expansion. This is achieved by the arrangement shown in Fig. 8 also showing the wave diagram describing its operation.

In the expansion tube, a long acceleration tube usually of the same diameter as the shock tube is initially separated from the shock tube's downstream end by a thin secondary diaphragm. The pressures might have the initial values: 100 MPa, 100 kPa, 200 Pa in the driver, shock tube and acceleration tube respectively.

When the shock strikes the secondary diaphragm, it breaks, and the test gas acts as the driver for the shock propagating into the acceleration tube gas. The regions 10, 20 and 30 thus are analogous regions to those labelled 1, 2 and 3 in the shock tube. The processes undergone by the test gas are: 1-2 (shock), 2-3 (unsteady expansion). The conditions in the test gas after these processes may again be calculated by the shock tube equation. The result of such a calculation is shown graphically in Fig. 9. The test time is limited by the acceleration-gas test-gas contact surface, and by the leading edge of the reflection of the unsteady expansion from the driver-gas test-gas contact surface.

3.2.2 Effective Reservoir State

The expansion tube's thermodynamics may now be compared with that of the reflected shock tunnel in Fig. 6, where the lower asterisk marks the test condition of the expansion tube. The two first square symbols representing state 1 and state 2 are shared by the shock tunnel and expansion tube. The expansion tube takes the gas to a maximum temperature of 4000 K in this example, so that the atomic oxygen and NO concentrations may be kept much lower than in the shock tunnel.

At the same time, the effective specific reservoir enthalpy is more than twice the static enthalpy in region 2, since it is possible to gain total enthalpy in an unsteady expansion. This is therefore higher than after the reflected shock. To show the effective reservoir state of the expansion tube in Fig. 6 a second asterisk is plotted there, connected to state 2 with a dotted line to indicate that the gas never reaches this high enthalpy and pressure. The

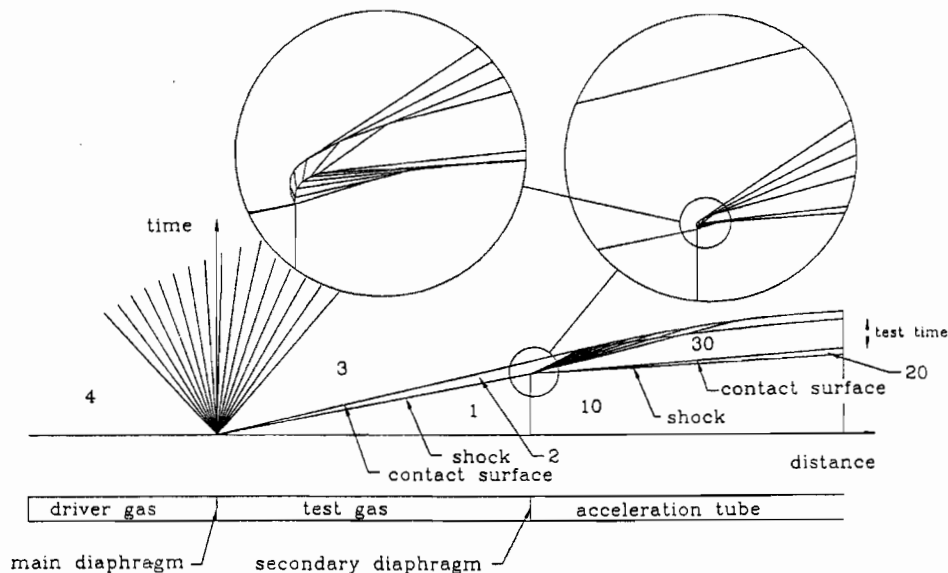


Fig. 8. Schematic sketch and wave diagram of an expansion tube. The detail in the vicinity of the rupture of the secondary diaphragm is shown in two enlarged insets. The diaphragm is accelerated to the contact surface speed over a finite opening time. This causes a reflected shock that is accelerated by the left running expansion wave transmitted from the diaphragm. Clearly, diaphragm opening time reduces the available test time.

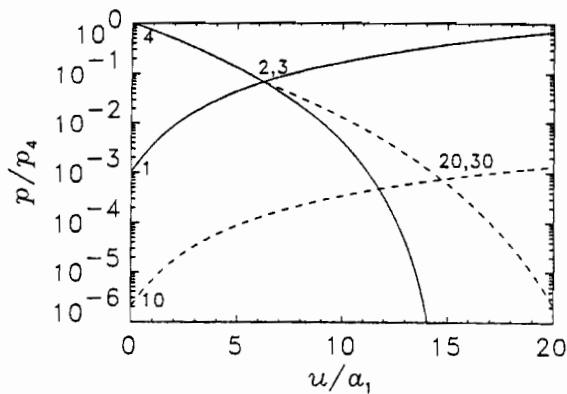


Fig. 9. Velocity-pressure plot of the processes in an expansion tube. The full lines give the solution for region 2 and the dashed lines, representing the locus of conditions achievable via a shock wave from condition 10, and the conditions achievable via an unsteady expansion from condition 2, give the solution for the test condition, 20. In this example, the driver gas is monatomic and the test and acceleration gases are diatomic. All are considered perfect gases.

lower entropy of the expansion tube causes the effective reservoir pressure to be enormous. In our example, it is around 2 GPa.

The static enthalpy h and static pressure p of the gas can remain low in the expansion tube, because the gas is not brought to rest after reaching state 2. This may be illustrated schematically in the case of h by the diagrams in Fig. 10

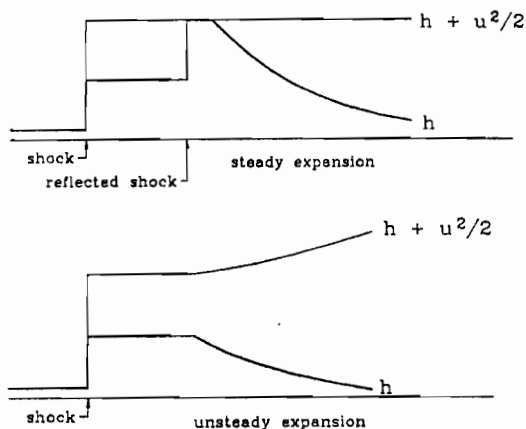


Fig. 10. Timelines of the static and effective reservoir specific enthalpy during the processes in a reflected shock tunnel (TOP), and in an expansion tube (BOTTOM). The expansion tube avoids the high value of h experienced by the test gas in the reflected shock tunnel and yet achieves even higher h_0 .

3.2.3 Free Stream Conditions

The test gas composition is practically that of state 2, because the density drops so quickly in the unsteady expansion that recombination of the atomic oxygen is not possible. Therefore it is best to operate the expansion tube with as low a value of T_2 as possible from this point of view.

If the expansion is taken to the same free stream pressure as in the reflected shock tunnel, see Fig. 6, the free stream temperature is seen to be much lower. This permits higher Mach number to be reached at the same h_0 .

3.3 Other Types of Facilities

A number of other types of facilities are in operation or are being considered. Among these the hypervelocity range is the most important. It employs a two-stage light gas gun to launch a model at the required speed into stationary gas in a long tube. This device is clearly much more expensive to operate than one in which the model is stationary. The model and instrumentation are also much more expensive, and it is difficult to test models that have high lift. However, the hypervelocity range is the only facility type in which good measurements of far wakes of bodies can be obtained.

There have been a number of other schemes, involving magneto-hydrodynamic accelerators or arc heaters. A relatively new idea being pursued at Princeton, is the optically heated continuous flow facility. This scheme aims to keep the gas below 2000 K in order to prevent the formation of NO. In Fig. 6, the process is shown by the chain-dotted line terminated by triangles. The gas is first compressed to a pressure of 1 GPa or more, and 2000 K. This makes use of the van der Waals effect that the isotherms curve up at low entropy, giving higher enthalpy. In the example shown in Fig. 6, the gas has approximately 20% of the necessary total enthalpy in this condition. The remainder of the enthalpy is added during a steady expansion by absorption of light. Success depends critically on whether the enormous power levels required (≈ 1 GW in the form of light) can be achieved and can be absorbed by the gas without causing non-equilibrium processes to produce atomic oxygen. In the author's opinion, these are very substantial questions.

4. Limitations of the Main Facility Types

All the different facility types have limitations that constrain them to be operated in regimes where conditions are acceptable and where they work. To some extent, the regimes covered by different facilities complement each other. As in the previous sections the following discussion will concentrate on the two most important types, the reflected shock tunnel and the expansion tube.

4.1 Reflected Shock Tunnel

Part of the following discussion is concerned with the effects of increasing the size of a reflected shock tunnel. In these considerations it is assumed that the ratios of lengths remain constant. In particular, the length to diameter ratio of the shock tube, which is limited by friction and heat loss at the shock tube wall, is considered to have the same value. The best value for this ratio turns out to be close to 100.

There are four main limitations to the regime that can be covered by the reflected shock tunnel:

1. The departure of the composition of the free-stream gas from that of air.
2. The fact that the test gas is brought to rest before it is accelerated again produces very high temperatures at high pressures which causes a containment problem.
3. The test time is limited by the size, by driver-gas contamination and by the containment limitation.
4. The strength of the facility limits the pressure.

4.1.1 Free-Stream Freezing

It is clear from Fig. 7 that it is not possible to produce a free-stream gas composition that is free of NO, unless the reservoir temperature is kept below 2000 K. This is therefore a hard limitation of the device if one is interested in real-gas effects in air. To set an arbitrary limit, choose the case when the molecular oxygen concentration is half of that in air. Fig. 7 may now be used to translate this limit into a line in $h_0 - p_0$ space. The top part of the figure shows that this limit is reached at $s_0/R = 35.2$. The bottom part of the figure shows how p_0 and h_0 are related along this value of s_0 . This relation is plotted in Fig. 11. As may be seen, an increase of p_0 moves the limit to significantly higher values of h_0 .

This limitation may, strictly speaking, not be represented by a single curve in $h_0 - p_0$ space, because it is dependent on the size of the facility. However, since the recombination rate in the nozzle flow is proportional to the square of the pressure (other variables being the same) quadrupling the size of the facility would only lower the line by a factor of 2 in pressure.

4.1.2 Nozzle-Throat Melting

The high temperatures and pressures seen by the containing material in a reflected shock tunnel lead to the limitation that materials can not be found that will contain the conditions for the duration of the test without melting. From experiments in T5, a copper throat is found to melt at $p_0 = 100$ MPa, $h_0 = 20$ MJ/kg, when the exposure to high heat flux lasts approximately 3 ms. From

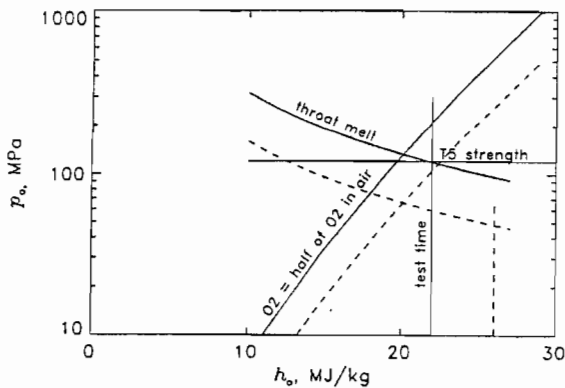


Fig. 11. Limitations on the reservoir pressure and specific enthalpy of reflected shock tunnels. The full line represents a facility of the size of T5. The dashed lines are for a facility scaled up by a factor of 4.

this result, and from the properties of copper, the heat flux to the wall may be estimated using one-dimensional unsteady heat conduction theory to be ≈ 2 GW/m². This agrees roughly with semiempirical formulas for throat heating.

Starting from this experimental point, adjusting it for the difference in the properties of copper from those of the best material found so far (tungsten-copper alloy), and extending it according to approximate formulas, the curve shown in Fig. 11 results. The basis of the approximation of this extension is that the convective heat flux is proportional to the density and the cube of the velocity, and that the exposure time is inversely proportional to the velocity.

It is important again to realize that this curve also depends on the facility size. The surface temperature reached under a given transient heat load is proportional to the square root of the exposure time (other variables being the same). The exposure time is proportional to the test time, which scales directly as the facility size (as does the *requirement* for test time). Since the heat flux is approximately proportional to pressure, quadrupling the size of the facility thus lowers the throat melt limit by a factor of 2 in p_0 , which therefore kills half of the improvement of the upscale.

4.1.3 Driver-Gas Contamination

The time interval between the arrival of the shock and the arrival of the contact surface at the right-hand end of the shock tube (see Fig. 1) is the most important factor in determining the test time. The test time can not simply be calculated from one-dimensional computations such as the one shown in Fig. 5, however, because the contact surface is in reality an extended region, and the complex interaction between the reflected shock and the boundary layer on the shock tube wall causes significantly earlier arrival of the driver gas at the nozzle throat.

At a given h_0 , the time interval between the arrival of the shock and the contact surface is directly proportional to the size of the facility (other variables being the same). As h_0 is increased, however, from the condition where the gas in region 2 is a perfect diatomic gas to where it is partially dissociated, this time interval changes down by almost a factor of 2. The speed with which the gas is drained from the reservoir through the throat into the nozzle increases as the square root of h_0 . Fortunately, the test time requirement also decreases as the square root of h_0 . However, the growth of the contact surface and the shock boundary layer interaction become more severe with increase of h_0 . As h_0 is increased, there comes a point when the test time is no longer sufficient. Though only very sparse information is available on this limit, it may be placed roughly at 22 MJ/kg for the case of T5, and this is essentially independent of p_0 .

Other things being equal, a scale increase increases the test time more than linearly, because the relative importance of the wall effects decreases. The test time *requirement* increases linearly with scale. The test time limit may therefore be expected to be moved to slightly higher h_0 in a larger facility.

4.1.4 Strength, Scale Effects

Clearly, the strength of the facility merely limits the pressure at which it can be operated, and may be represented by a line at constant p_0 .

To illustrate the effect of scaling up a facility from the size of T5 by a factor of 4, Fig. 11 also shows the displaced limits for the larger machine as dashed lines. This makes it clear that an increase of size makes strength relatively unimportant, since the throat-melt limit makes it impossible to operate at $p_0 > 70$ MPa, if $h_0 > 15$ MJ/kg in the facility scaled up by a factor of 4. As regards the throat-melt, test-time and strength limits, T5 appears to be close to the optimum scale. This was fortuitous, since the scale and strength were determined by other constraints.

4.1.5 Performance

In the region of $h_0 - p_0$ space within the above limitations, reflected shock tunnels can cover the space practically completely. In the

case of the free-piston device, this can be achieved with tailored interface operation, because of the flexibility of the speed of sound ratio a_4/a_1 of this device.

As an example, Fig. 12 shows two reservoir pressure traces obtained in T5. These are representative of the quality achievable over the range $20 \text{ MPa} < p_0 < 100 \text{ MPa}$, $5 \text{ MJ/kg} < h_0 < 22 \text{ MJ/kg}$.

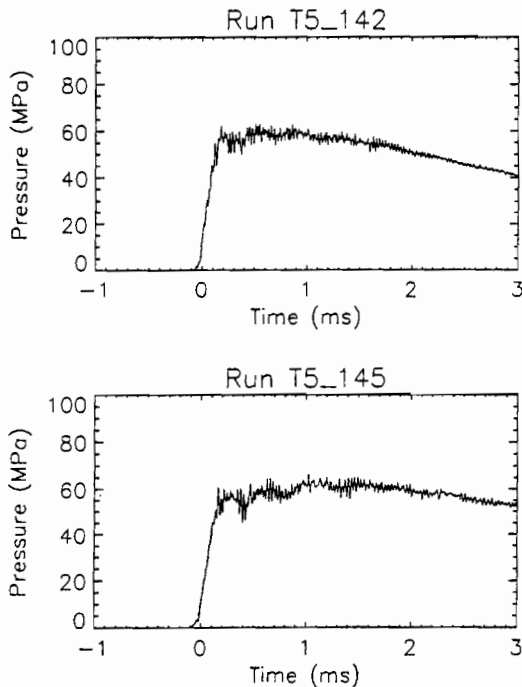


Fig. 12. Nozzle reservoir pressure traces of two runs of T5 at 22 (TOP) and 11 MJ/kg (BOTTOM).

4.2 Expansion Tube

As was pointed out in the description of the expansion tube, this facility type has the advantage that the material is exposed only to a fraction of the effective total pressure and only to a fraction of the total enthalpy. The stresses and heat loads are therefore not a serious limitation. Referring to Fig. 9 and Fig. 6 it becomes clear that for a given state 2, the effective values of p_0 and h_0 depend on the pressure p_{20} to which the flow is expanded in the unsteady expansion. It is therefore not meaningful to relate the extreme heating condition to the $h_0 - p_0$ space on this basis.

In the expansion tube a far more important concern is the short test time and the small test flow size. Consider for example a shock tube diameter of 100 mm. In the reflected shock tunnel, this provides a good flow for a nozzle exit diameter of typically 400 mm and a test duration of 1 ms at 18 MJ/kg. In the expansion tube, the same shock tube, driving an acceleration tube of the same diameter and 10 m length would produce a test flow of 100 mm exit diameter and 170 μs duration.

Fortunately, the size of the facility can be increased, since the penalty for size that plagues the reflected shock tunnel (melt limit) does not exist here. However, the test time limit remains, since the test time, which increases linearly with the size, only matches the increased test time requirement, which also increases linearly with size, unless the facility is deliberately made much larger than the models to be tested.

The friction losses in the acceleration tube set a limit on the length to diameter ratio. A reasonable maximum value is about 120. It turns out that a good shock tube length is then about 50 diameters. A rule of thumb for the optimum test time of an expansion tube is the time interval between the arrival of the primary shock and the arrival of the shock tube contact surface at the end of the shock tube. This time is given approximately by

$$\tau \approx 10 \frac{d}{\sqrt{h_0}}$$

where d is the shock tube diameter. This is smaller than the test time requirement of $20L/V_\infty$, given in section 2.2, by a factor of 1.4 if the model size L is taken to be the tube diameter d . The model therefore has to be smaller than the largest model that could be tested in the facility if size were the only constraint.

Any attempts to expand the diameter of the expansion tube at the downstream end are therefore futile, since the model size is limited by the available test time, and not by the tube diameter. (This verdict may be relaxed if the flow studied is such that less test time than $20V_\infty/L$ is required.)

The most important problem in expansion tube operation is therefore the preservation of as much as possible of the test time. An obvious factor reducing the test time is the opening time of the secondary diaphragm, which is disregarded in the ideal expansion tube calculations above. In order to show the effect of finite diaphragm opening time, Fig. 8 shows as blown up insets two successive enlargements of a portion of the wave diagram. In the largest of these, the diaphragm is shown to accelerate from rest over a finite time to become the contact surface between the acceleration and test gas. The diaphragm thus causes the incident shock to be reflected. As the diaphragm accelerates, expansion waves are transmitted to the reflected shock, weakening it and eventually causing it to become the right edge of the unsteady expansion. On the acceleration tube side of the diaphragm, compression waves are transmitted to the right, which focus to form the acceleration tube shock. The time it takes to accelerate the diaphragm clearly reduces the test time.

The reduction in test time is roughly equal to the diaphragm opening time. This is given approximately by

$$t_D \approx \sqrt{\frac{\rho \theta d}{p_2}}$$

where ρ is the density of the diaphragm material, θ is the diaphragm thickness and p_2 is the pressure in state 2. For a mylar diaphragm that is just strong enough to contain $p_1 = 100 \text{ kPa}$, and a diameter of 300 mm, this gives an opening time of approximately 70 μs . On the basis of the above rule of thumb, the test time becomes 0.7 ms at 18 MJ/kg, so that the diaphragm opening time reduces the available test time by about 10%.

All of these considerations assume the flow to be one-dimensional, and serious consequences for the test time may be expected to result also from the wall effects on the structure of the two contact surfaces, and the three-dimensionality of the diaphragm rupture.

The composition of the test gas was assumed to be that of state 2 above. This is a little pessimistic, because some recombination will occur in the unsteady expansion during the later part of the test duration, where the gas has taken a longer time to traverse the expansion wave. This will therefore cause the composition to

vary during the test time from an initial condition corresponding to that of state 2 to a final condition in which the atomic oxygen concentration, and to a lesser extent the NO concentration, are reduced slightly. The composition limit is almost independent of p_0 . The molecular oxygen will be reduced to half the value in air at $h_0 \simeq 22$ MJ/kg.

Summarizing the limitations of the expansion tube, the emphasis has to be on the test time limit. Since the diaphragm opening time is independent of h_0 , there comes a point where the enthalpy is limited by the test time. In the author's opinion, this limit is at 30 MJ/kg. The upper limit on p_0 is unimportant, since values in the GPa range are easily achievable.

4.2.1 Performance

To date, the largest expansion tube is one operated at the General Applied Sciences Laboratory in New York by a team headed by Dr. John Erdos. This has a shock tube (and acceleration tube) diameter of 150 mm. At present it has a cold helium driver, so that the enthalpy at which it can be run is limited to approximately 12 MJ/kg. A modification to equip the facility with a free-piston driver is being considered at present. This would extend the range to approximately 30 MJ/kg. The effective reservoir pressure is very high. In the GASL facility, values of up to 400 MPa have been achieved.

5. Concluding Remarks

The thermodynamics, gasdynamics and scaling laws of hypervelocity flows, the power requirements, and the properties of containing materials, were shown to lead to the two main hypervelocity flow simulation facility types: The reflected shock tunnel and the expansion tube. The simplest forms of such devices were described, giving the logic that leads to them, and a comparison of their ranges of applicability. This was done with regard only to their main features, and many subtle points of their operation had to be omitted.

The hard limitations of the reflected shock tunnel constrain this device to be restricted to specific reservoir enthalpies below 22 MJ/kg and reservoir pressures below 90-200 MPa (depending on the enthalpy in the range 25-12 MJ/kg) at the size of the presently operating facility T5. Increase of size carries severe pressure penalties. The expansion tube's most severe restriction is the short test time. This is critically constrained by the behavior of the contact surface and the opening time of the secondary diaphragm. However, there appear to be no penalties for scale increase, and the reservoir pressure obtainable is extremely high. The upper limit for the specific reservoir enthalpy is approximately 30 MJ/kg on the basis of the free stream dissociation and test time constraints.

References

- Bakos R. J., J. Tamagno, O. Ryszkalla, M. V. Pulsonetti, W. Chinitz, and J. I. Erdos, 1992 "Hypersonic mixing and combustion studies in the Hypulse facility," *J. Propulsion and Power*, **8** 900-906.
- Hornung, H. G. 1992 Performance data of the new free-piston shock tunnel at GALCIT, AIAA 92-3943.
- Lukasiewicz, J. 1973 "Experimental Methods of Hypersonics", Marcel Dekker, Inc. New York.

19 ABSORPTION OF SOUND BY RELAXATION

19.1 Linear Wave Equation

Take a gas at rest and in chemical equilibrium at conditions p_0, ρ_0, α_0 . Now perturb this state with a time and space dependent perturbation so that the new condition is in a state

$$p = p_0 + p', \quad \rho = \rho_0 + \rho', \quad \alpha = \alpha_0 + \alpha', \quad u = u', \quad (19.1)$$

where the primed variables are time and space dependent. Assume that the space-dependence is restricted to one dimension, namely x , so that the other components of the perturbation velocity are zero. Also assume that the perturbations are small, so that only linear terms in the perturbation quantities need to be retained. This means that the reaction rate equation in the general form

$$\frac{D\alpha}{Dt} = W(p, \rho, \alpha)$$

also needs to be linearized:

$$W(p_0 + p', \rho_0 + \rho', \alpha_0 + \alpha') = W(p_0, \rho_0, \alpha_0) + (W_p)_0 p' + (W_\rho)_0 \rho' + (W_\alpha)_0 \alpha', \quad (19.2)$$

where the subscript variables denote partial differentiation. The subscript 0 indicates that the partial derivatives are taken at the rest condition. Note that the first term on the right hand side of this equation has to be zero, since we assumed the rest state to be an equilibrium state at which W vanishes, and $\alpha_0 = \alpha^*(p_0, \rho_0)$. Though this already gives us the linearized form of W , it is useful to relate W to the deviations from equilibrium. For that purpose rewrite the equilibrium form of W ,

$$W(p, \rho, \alpha^*(p, \rho)) = 0$$

for the perturbed state:

$$W(p + p', \rho + \rho', \alpha^*(p + p', \rho + \rho')) = 0. \quad (19.3)$$

Again retaining only linear terms, and noting that $W(p_0, \rho_0, \alpha_0) = 0$, we obtain

$$(W_p)_0 p' + (W_\rho)_0 \rho' = -(W_\alpha)_0 [(\alpha_p^*)_0 p' + (\alpha_\rho^*)_0 \rho']. \quad (19.4)$$

Combining this with equation (19.2), we obtain

$$W = (W_\alpha)_0 [\alpha' - (\alpha_p^*)_0 p' - (\alpha_\rho^*)_0 \rho']. \quad (19.5)$$

This result is easier to understand when $\alpha_0 - \alpha_0$ is added inside the square brackets:

$$W = (W_\alpha)_0 \left[\alpha_0 + \alpha' - \{ \alpha_0 + (\alpha_p^*)_0 p' + (\alpha_\rho^*)_0 \rho' \} \right]. \quad (19.6)$$

The expression in curly brackets is recognized as the equilibrium value of α pertaining to the perturbed state, so that the linearized reaction rate equation becomes

$$\frac{D\alpha}{Dt} = W = -\frac{\alpha - \alpha^*}{t_r}, \quad (19.7)$$

where we have used the abbreviation $(W_\alpha)_0 = -1/t_r$.

If we neglect friction and heat conduction, the energy equation applies in the form

$$\frac{Dh}{Dt} - \frac{1}{\rho} \frac{Dp}{Dt} = 0.$$

Writing the caloric equation of state as

$$h = h(p, \rho, \alpha),$$

and substituting in the energy equation, the result is

$$\left(h_p - \frac{1}{\rho} \right) \left(\frac{Dp}{Dt} - a_f^2 \frac{D\rho}{Dt} + B \frac{D\alpha}{Dt} \right) = 0, \quad (19.8)$$

where

$$B(p, \rho, \alpha) = -a_f^2 \frac{h_\alpha}{h_\rho}, \quad (19.9)$$

and

$$a_f^2 = -\frac{h_\rho}{h_p - 1/\rho}$$

is the frozen speed of sound squared. Since the first bracket of equation (19.8) is not identically zero, the equation may be written as

$$p_t + up_x - a_f^2(\rho_t + u\rho_x) = -B(\alpha_t + u\alpha_x) = -BW. \quad (19.10)$$

Using the continuity equation in this,

$$p_t + up_x + \rho a_f^2 u_x = -BW. \quad (19.11)$$

We can now proceed to linearize the momentum equation, 19.10, the rate equation, and (19.11), we obtain

$$\begin{aligned} \rho_0 u_t + p'_x &= 0, \\ p'_t - a_f^2 \rho'_t &= -B_0 W, \\ \alpha'_t &= W, \\ p'_t + \rho_0 a_f^2 u_x &= -B_0 W, \end{aligned}$$

where the linearized form (19.7) is to be used for W , and $B_0 = B(p_0, \rho_0, \alpha_0)$. By eliminating p' , ρ' and α' from these equations, a single third order partial differential equation is obtained, which may be written after tedious algebra as

$$\tau \frac{\partial}{\partial t} (u_{tt} - a_{f0}^2 u_{xx}) + (u_{tt} - a_{e0}^2 u_{xx}) = 0, \quad (19.13)$$

where

$$\tau = \frac{t_r}{1 + B_0(\alpha_p^*)_0}, \quad (19.14)$$

and

$$a_e^2 = -\frac{h_\rho + h_\alpha \alpha_p^*}{h_p + h_\alpha \alpha_p^* - 1/\rho}$$

is the square of the equilibrium speed of sound as before.

19.2 Dispersion and Absorption of Harmonic Waves

Equation 19.13 gives some interesting information. If $\tau = 0$, the gas is in equilibrium, and 19.13 correctly degenerates to the wave equation with the equilibrium speed of sound. In the other limit when $\tau = \infty$,

$$\frac{\partial}{\partial t} (u_{tt} - a_{f0}^2 u_{xx}) = 0$$

results. If we take the gas to be initially at rest, so that for times before it was perturbed, $u = 0$, it follows that

$$u_{tt} - a_{f0}^2 u_{xx} = 0$$

in that limit. Thus, we obtain the wave operator with the frozen speed of sound, as expected.

The behavior of the complete equation may be studied further by assuming the perturbation to take the form of harmonic sound waves

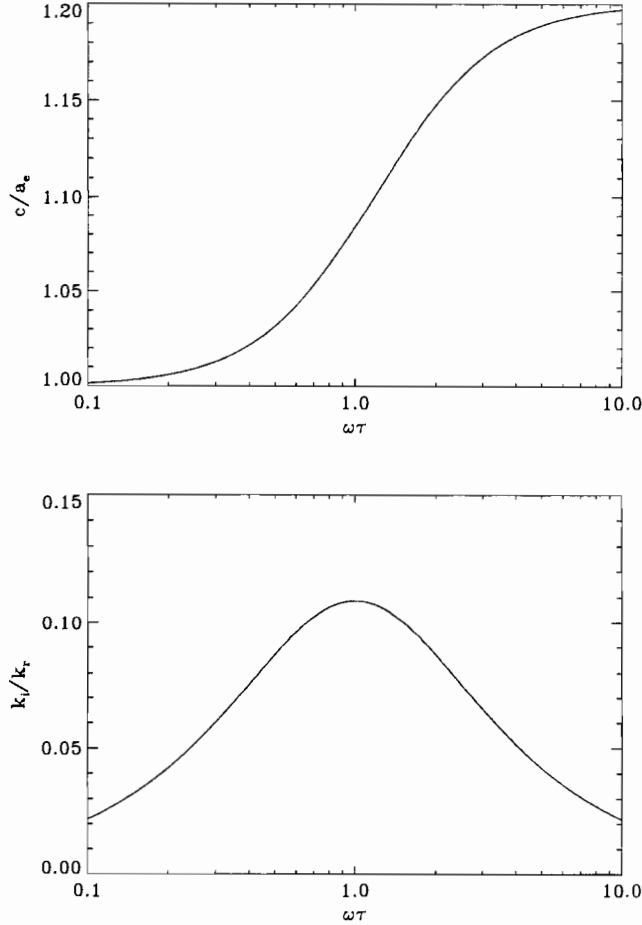
$$u = Ae^{i(\omega t - kx)}, \quad (19.15)$$

where A is the amplitude, ω the frequency, and $k = k_r + ik_i$ is the complex wave number of the wave. Substituting 19.15 in 19.13, and cancelling the common factor u , a relation between ω and k results:

$$k^2 = \frac{\omega^2}{a_{e0}^2} \frac{1 + i\omega\tau}{1 + i\omega\tau a_{f0}^2/a_{e0}^2}. \quad (19.16)$$

As $\omega\tau \rightarrow 0$, $k_r \rightarrow \pm\omega/a_{e0}$, $k_i \rightarrow 0$; this corresponds to undamped sound waves propagating at the equilibrium sound speed. The plus and minus signs indicate the directions of propagation. For $\omega\tau \rightarrow \infty$, on the other hand, $k_r \rightarrow \pm\omega/a_{f0}$, $k_i = 0$, i. e., undamped waves propagating at the frozen sound speed, as expected. The imaginary part of the wave number does not vanish for intermediate values of $\omega\tau$, however, so that under such circumstances

the wave is damped or amplified, depending on the relative magnitude of a_e and a_f . If the frozen sound speed is smaller than the equilibrium sound speed, the wave is amplified. This contradicts experience and corresponds to an unstable gas. In reality, $a_f > a_e$, so that damping is physically observed.



Dispersion curve for phase velocity of sound wave in a relaxing gas with $a_f/a_e = 1.2$ and corresponding absorption.

The relevant quantities c/a_e , where c is the phase velocity ω/k_r of the wave, and k_i/k_r as a measure of the damping rate, are obtained as functions of $x = \omega\tau$ and the ratio $a = a_f/a_e$ as follows:

$$m = \left(\frac{a^4 + x^2}{1 + x^2} \right)^{1/4},$$

$$\theta = \frac{1}{2} \arctan \left(\frac{(a^2 - 1)x}{a^2 + x^2} \right),$$

$$\frac{c}{a_e} = \frac{a}{m \cos \theta},$$

$$\frac{k_i}{k_r} = \tan \theta.$$

Graphs of these curves are shown in Fig. 1.

19.3 Relation to Bulk Viscosity

Sound waves are, of course, also absorbed by other dissipative effects such as viscosity, heat conduction and diffusion. These phenomena do not, however, provide sufficient damping to explain the physically observed damping rate, especially at high frequency, where the relaxation effect contributes significantly to the damping rate. Rotational and vibrational relaxation, which can be treated with the above analysis, contribute to the damping, albeit at different frequencies. The damping of ultrasound waves can also be used to measure the characteristic relaxation times of different processes.

When the period of oscillation of a sound wave $2\pi/\omega$ is large compared with τ , i. e., for $\omega\tau \ll 1$, the state of the gas deviates only very slightly from equilibrium. In this limit, equation (19.16) may be approximated by

$$k^2 = \frac{\omega^2}{a_{e0}^2} \left[1 - i\omega\tau \frac{a_{f0}^2 - a_{e0}^2}{a_{e0}^2} \right]. \quad (19.17)$$

An analogous formula is obtained for the absorption of sound in a non-relaxing gas with bulk viscosity, μ_b , but with negligible shear viscosity and thermal conductivity:

$$k^2 = \frac{\omega^2}{a_{e0}^2} \left[1 - \frac{i\omega\mu_b}{\rho_0 a_{e0}^2} \right]. \quad (19.18)$$

Thus, relaxation may be regarded as giving a contribution to the bulk viscosity

$$\mu_b = \rho_0\tau(a_{f0}^2 - a_{e0}^2) \quad (19.19)$$

for low frequencies. This result, that relaxation processes may be described by processes analogous to the action of bulk viscosity, is general for the behavior of all relaxation processes at frequencies that are small compared to $1/\tau$.

References:

E. Becker: Gasdynamik, Teubner, Stuttgart, 1965.

J. F. Clarke and M. McChesney: Dynamics of Relaxing Gases, Butterworths, 1976.



Non-equilibrium

The exchanges between the energy levels occur through collisions. If a collision is sufficiently energetic to bump one of the collision partners into a higher vibrational state, this will happen.

Since low energy collisions are much more frequent than high energy ones, the most probable step is from i to $i+1$. In equilibrium, the energy is E^* given by formula on previous page. Actual vib. energy might be different if flow through a shock wave or non-equil expansion.

The vibrational rate equation is written as

$$\frac{dE_v}{dt} = \frac{E_v^* - E_v}{\tau}$$

$$\text{and } \tau = \frac{C}{p} e^{\left(\frac{k_2}{T}\right)^{\frac{1}{3}}}$$

is a model that fits experimental data reasonably well.

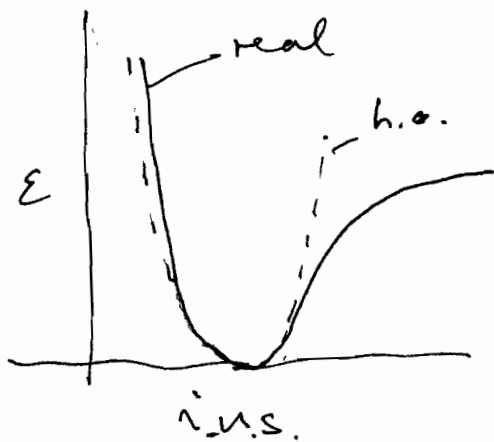
	C (atm μs)	k_2 (k)
O_2	5.4×10^{-5}	3×10^6
N_2	7.1×10^{-4}	1.9×10^6
NO	4.8×10^{-3}	1.4×10^5

Vibrational Relaxation

So far we have assumed that the vibrational energy is small cf. dissociation. This is ok if we deal with a diatomic gas at high speed. But, for example at lower speeds where $T \approx 3000\text{K}$: N_2 or in CO_2 with 4 vibrational degrees of freedom, more energy goes into vib.

Equilibrium

Model the energy states as if the molecule were a harmonic oscillator



Permissible energy states are (quantum mechanics):

$$E_i = \left(i + \frac{1}{2}\right) h \nu$$

(equally spaced)

$$\nu = \text{frequency} = \sim 10^{13} \text{ Hz}$$

Ground-state vib energy not = 0.

Vibrational partition function

$$Q_v = \sum_{i=0}^{\infty} e^{-ih\nu/kT}$$

Sum of ~~harmonic~~ geometrical progression

$$1 + x + x^2 + \dots = \frac{1}{1-x}$$

Where $x = e^{-h\nu/kT}$

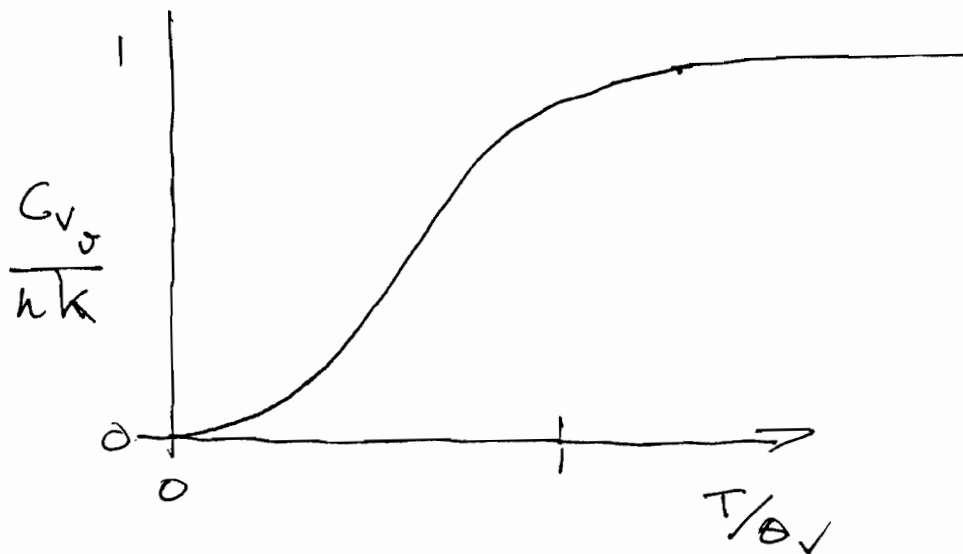
$$Q_v = \frac{1}{1 - e^{-h\nu/kT}} = \frac{1}{1 - e^{-\theta_v/T}}$$

Now $E_v = nkT^2 \frac{\partial}{\partial T} (\ln Q_v)$ (Statistical Mechanics)

$$E_v = \frac{nk\theta_v}{e^{\theta_v/T} - 1}$$

$$C_{v,v} = nk \left(\frac{\theta_v}{T} \right)^2 \frac{e^{\theta_v/T}}{(e^{\theta_v/T} - 1)^2}$$

$$C_{v,v} = nk \left[\frac{\theta_v/2T}{\sinh(\theta_v/2T)} \right]^2$$



Ae234 Final Assignment, due June 3, 2002

In a free-piston shock tunnel experiment, the driver conditions are generated by an adiabatic compression of helium from an initial condition at 90 kPa and 300 K by a volumetric compression ratio of 56, at which point the diaphragm bursts. Determine the conditions in the helium driver gas at diaphragm burst.

The initial conditions in the shock tube are: Test gas: nitrogen, pressure: 80 kPa, temperature: 300 K. Determine the primary shock speed by assuming perfect gas behavior of the nitrogen and the helium driver gas.

Using the IDG model, calculate the equilibrium conditions after the primary shock. Calculate the relaxation distance after the primary shock to check that it is small compared with the shock tube diameter (90 mm). Use the result to check the validity of the assumption made in the shock speed determination.

Calculate the equilibrium conditions and the relaxation distance after the reflected shock. Check that the assumption of equilibrium is justified by comparing the relaxation distance with the shock tube diameter (90 mm).

Assume that these conditions correspond to tailored interface operation, *i. e.*, that the reflected shock passes through the interface between driver gas and test gas without reflections. Hence take the conditions after the reflected shock to be the reservoir conditions for a nozzle flow. Determine the specific enthalpy of the reservoir. Compare this with the square of the primary shock speed.

Calculate the flow through a conical nozzle of half-angle 7 deg. and throat diameter 15 mm, from this reservoir, assuming the flow to be in equilibrium from the reservoir through the throat and to an area ratio of at least 3. Check this assumption by estimating the relaxation distance at that point in the nozzle.

Calculate the nozzle flow up to an area ratio of 400 by making a nonequilibrium computation. Give the conditions at the nozzle exit.

Calculate the flow after an oblique shock at shock angle 67 deg. in the flow at the nozzle exit (assume uniform free stream there) by making an appropriate nonequilibrium shock computation. Make a plot of the flow variables vs. distance from the shock.

ON TRANSITION AND TRANSITION CONTROL IN HYPERVELOCITY FLOW

H. G. Hornung, P. H. Adam, P. Germain, K. Fujii and A. Rasheed
(Graduate Aeronautical Laboratories, California Institute of Technology)

ABSTRACT: The results of a major program of research into the effects on transition of the vibrational and dissociational relaxation processes that occur in high-enthalpy flows are presented. Relaxation effects are found to influence transition significantly, causing the transition Reynolds number of flows over slender cones to be increased by almost an order of magnitude. Transition is also shown to be further delayed by as much as a factor of two through suitable wall porosity. The relationship between absorption of acoustic waves by relaxation, and their amplification in the flow over a swept cylinder shows that very significant transition delay may occur through relaxation effects. These new effects need to become part of the equipment of designers of hypervelocity vehicles.

I INTRODUCTION

Heat loads and forces on hypervelocity vehicles depend critically on the location of transition from laminar to turbulent flow. Though significant progress has been made toward the understanding of transition, it is still the most severe uncertainty in the aerodynamic design of such vehicles.

Two important features of hypervelocity flow set it apart from other flow regimes with respect to the transition problem. First, the dominant instability mode at sufficiently high Mach number is the second or Mack[1] mode, in which acoustic perturbations become trapped in the boundary layer, grow in amplitude and eventually cause the boundary layer to become turbulent. This is in contrast to the situation in low speed flows, where the viscous instability is usually responsible for the path to transition. Second, the relaxation processes associated with vibrational excitation and dissociation (which occur in hypervelocity flows because of aerodynamic heating) provide mechanisms for damping acoustic waves, and may therefore be expected to affect the second mode. The effects of vibrational excitation and dissociation are quite subtle however, since they also affect the mean structure and therefore the stability properties of the boundary layer.

A large part of the experimental work on the problem of stability and transition at high Mach number has been done in cold hypersonic facilities. In such facilities, the test gas is expanded from a reservoir at relatively low temperature (of order 1000 K), so that the high Mach number is produced, not so much by raising the speed, but mainly by lowering the speed of sound. Important examples of the work in this regime are the experiments of Demetriades[2], Stetson *et al.* [3] and Kendall[4]. (Reshotko[5] presented a very good review). Together with the linear stability analysis by Mack[1], experiments of this kind provide a substantial basis for understanding the path to transition in cold hypersonic flow. They are, however, not able to capture the phenomena that occur in hypervelocity flows because of the vibrational excitation and dissociation that characterize them.

Some of the specific problems of hypervelocity boundary layer stability have been addressed computationally by a number of authors. They include the work of Malik and Anderson[6], who considered equilibrium vibration and dissociation, and Stuckert and Reed[7] who assumed vibrational equilibrium but finite-rate chemistry. Both found that the new effects caused the boundary layer to be destabilized. However, more recent work by Johnson *et al.*[8] found that non-equilibrium chemistry had a strong damping effect, in agreement with recent experimental evidence. The apparent contradiction between the results of these investigations is not too surprising, in view of the complicated manner in which the rate processes can influence the stability problem, and the many parameters involved in it.

In this paper we present the results of an extensive experimental program of research

conducted over the last decade, in which the focus is specifically on the regime where relaxation processes associated with vibrational excitation and dissociation are important. In the laboratory, such flows can only be maintained for very short times, since they require the gas to be expanded from a reservoir at very high temperature and very high pressure, conditions at which it can be contained only for a period of typically 2 ms. This, and the aggressive environment of the high temperatures and pressures make it impossible to use many techniques that are available to experiments in longer-duration, cold facilities. It is therefore necessary to approach the problem with more indirect methods that use such simple evidence as the location of transition in a careful exploration of the parameter space. Fortunately, the frequencies of the most strongly amplified modes are typically 1-3 MHz, so that the short test time is not a serious limitation.

II SLENDER CONE EXPERIMENTS

Much of the work on transition in hypersonic flow has been performed on the simplest possible shape, namely the slender cone. The flow over a slender cone has the advantages that the streamwise pressure gradient is zero, and that it is free of side effects. The first experiments to be performed in the newly completed T5 hypervelocity free-piston shock tunnel in 1991-1993 were designed for a 5 deg half-angle cone also, in order to be able to compare the new high enthalpy results with those from the cold hypersonic wind tunnels. A diagram of the model built for these experiments is shown in Figure 1.

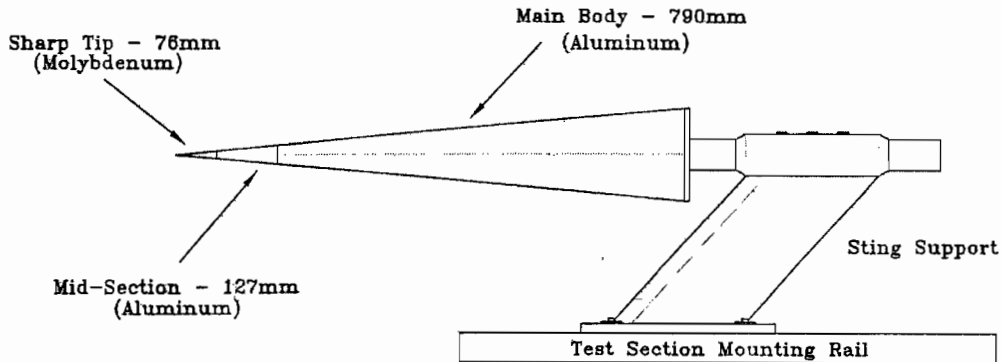


Figure 1. Slender cone model built for T5 experiments. The main body is hollow and instrumented with thermocouple surface heat flux gauges.

The first series of experiments (for details see Germain and Hornung[9]) explored the behavior of the transition location on the cone as a function of the total enthalpy of the flow in air and nitrogen. The transition location was determined from the distinct rise in heat flux. An example of how this is done is shown in Fig. 2.

In hypervelocity flow simulation it is important to reproduce the actual speed of the flow, so that the vibrational excitation and dissociation are reproduced correctly. This is often done at the expense of reproducing the Mach number. This is the case in the T5 experiments also, where the free-stream Mach number is typically 5.5, but the speed ranges up to 6 km/s. Thus, the boundary layer edge temperature in a free-flight situation is very different than in the T5 experiments, but the temperature profile in the *inner part* of the boundary layer is almost the same in both cases. This is illustrated in the calculated temperature profiles for the two cases, see Figure 3. This comparison of the temperature profiles suggests that the T5 tests may well be suitable for comparing the high temperature real-gas effects that occur in free flight with those that occur in the T5 experiments, but it is more meaningful to compare the two in terms of the Reynolds number evaluated at the reference condition. The reference temperature is where the wall and boundary layer edge conditions are identified by the subscripts w and e

$$\frac{T^*}{T_e} = 0.5 + \frac{\gamma - 1}{2} \frac{\sqrt{P_r}}{6} M_e^2 + 0.5 \frac{T_w}{T_e},$$

respectively. Clearly, the reference temperatures in the two cases are nearly the same, while the edge temperatures are very different.

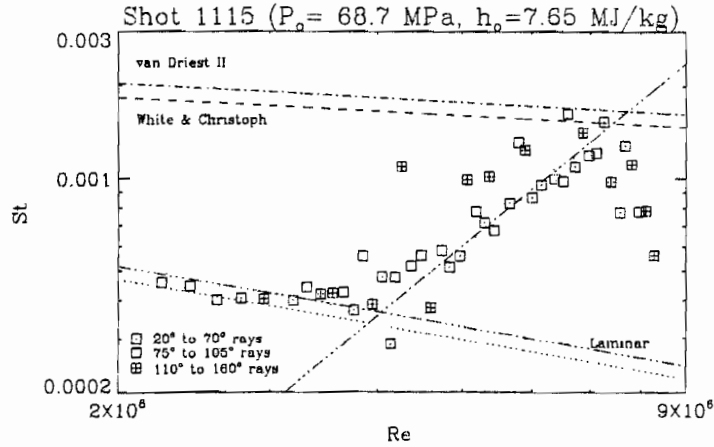


Figure 2. Plot of Stanton number against boundary-layer edge Reynolds number for one experiment on the cone. As may be seen, the Stanton number follows the theoretical laminar flow line (dotted line) at low Reynolds numbers, and rises up toward the turbulent level (as given by two turbulence models) at high Reynolds number. The transition Reynolds number is determined by a straight line fit of the transitional data.

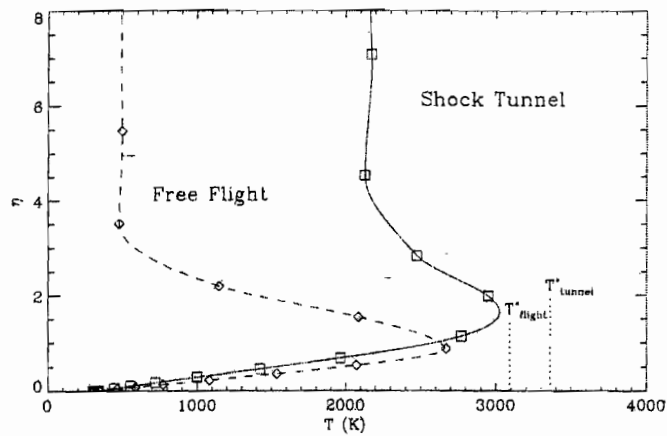


Figure 3 Typical T5 and free-flight boundary layer temperature profiles in laminar boundary layer coordinates for a total enthalpy of 14 MJ/kg.

The results of experiments in nitrogen and air flows are plotted in Figure 4 in the form of the Reynolds number at transition, evaluated at the reference temperature and based on the distance from the cone tip to the transition location, versus the total enthalpy of the flow. Two new features are brought out by this plot. First, a significant increase in transition Reynolds number (evaluated at reference conditions) with total enthalpy increase is observed, and second, this increase is slightly larger in air than in nitrogen. This led us to suspect that transition is significantly influenced by high-enthalpy real-gas effects, and that it might be interesting to explore what happens in other gases, such as helium, which behaves like a perfect gas in our total enthalpy range, and carbon dioxide, which exhibits strong vibrational and dissociational effects in this range. The first experiment, with helium showed that, even at 15 MJ/kg, the transition Reynolds number was the same as the low enthalpy value. A dramatically larger transition Reynolds number was observed in carbon dioxide flows, also shown in Figure 4, (for

details see Adam and Hornung [12]).

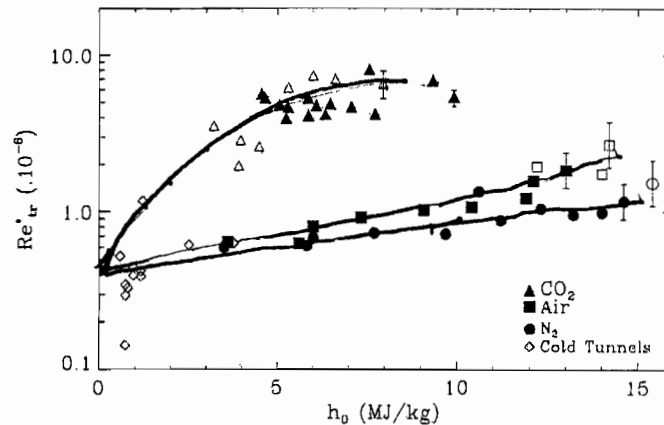


Figure 4 Transition Reynolds number evaluated at reference conditions as function of total enthalpy. Open symbols correspond to cases where the flow was laminar to the end of the cone. The lines are least-square fits to the points. The cold tunnel data are from papers by and Demetriades [10] and DiCristina [11]. The carbon dioxide results are superimposed on this plot as triangular symbols. Note the large transition delay relative to the nitrogen results.

In later experiments on transition control the low-Reynolds-number gap in the carbon dioxide data was filled in, see Figure 10. It is clear from these results that a dramatic transition delay which is completely absent at low speeds is evident at high enthalpy, and that the magnitude of the phenomenon and the enthalpy at which it sets in are different for different gases.

It was at this point that Graham Candler and his group became interested in testing our results by making linear stability computations at the conditions of our experiments. Their results agreed with the trends observed in the nitrogen and air flows, and illustrated dramatically how strongly thermochemical non-equilibrium effects can influence the growth rate of disturbances. Examples of their results are shown in Figure 5. These results also establish the acoustic Mack mode as being responsible for the path to transition in the T5 experiments.

Just as these experiments had been completed, Norman Malmuth of Rockwell Science Center and Sasha Fedorov of Moscow Institute of Physics and Technology started to discuss with us the possibility of controlling transition in hypersonic flow. They had shown theoretically that the acoustic mode could also be damped by wall porosity, see Fedorov and Malmuth[13]. This led to the research project described in the next section.

III PASSIVE CONTROL OF TRANSITION

Simply stated, the acoustic disturbances are trapped and amplified in the boundary layer, which acts like a wave guide for them. It has been known (early work on the subject included that of Kirchhoff and Rayleigh) that acoustic disturbances are absorbed in wall porosity by viscous action and heat conduction. Fedorov and Malmuth quantified the damping rate in a hypersonic boundary layer and suggested types of porosity for optimum results. At the conditions of the cone experiments in T5, small-diameter, deep, blind holes that are closely spaced were predicted to produce suitable damping. The proportions of the configurations chosen are related to the boundary layer thickness in the schematic sketch of Figure 6.

With such a fine distribution of blind holes, the sheer number of holes required (some 15 million) appears to be prohibitive. After finding a company (Actionlaser, in Sydney, Australia) that was able to make holes at the required spacing and diameter in a stainless steel sheet of 0.5 mm thickness, we decided to wrap such a sheet around the aluminum cone and remake the intermediate part of the tip to provide a flush transition from the (non-porous) tip

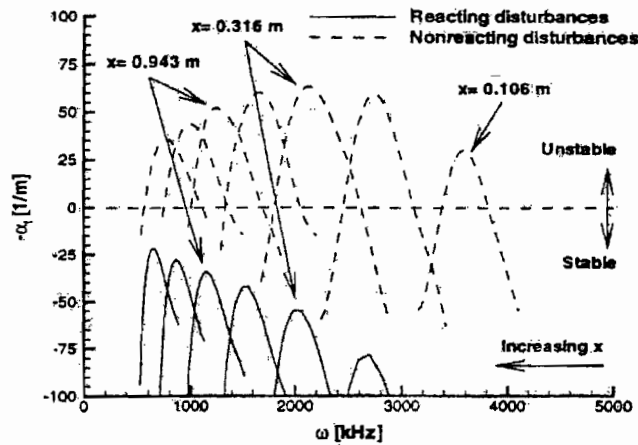
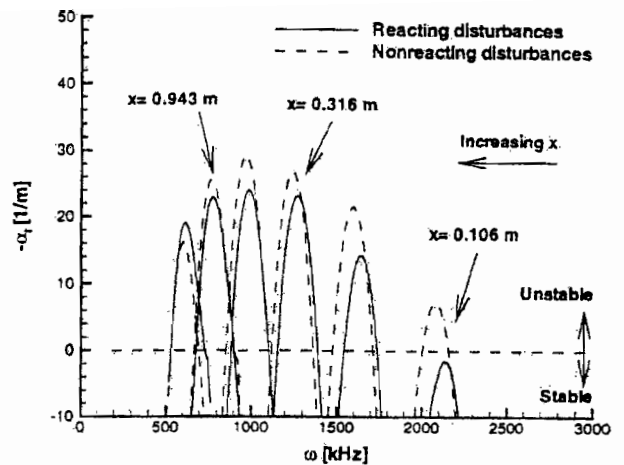


Figure 5. Results of linear stability calculations with thermochemical non-equilibrium at the conditions of T5 shot 1162 in air at 9.3 MJ/kg (left) and shot 1150 at 4.0 MJ/kg in carbon dioxide (right). The graphs show growth rate of disturbances as functions of disturbance frequency at several distances along the cone. To examine the damping effect of finite rate processes, the dotted curves show the same results but with the rate processes turned off. Note how the rate processes completely stabilize the disturbances in the case of carbon dioxide. (reproduced from Johnson et al. [8]).

to the porous surface. In order to provide a control experiment in every shot by making half of the cone surface porous and half non-porous, the porous sheet was formed into a half cone and welded to a similar half cone sheet without holes. The resulting hollow cone was then slipped over the aluminum cone at a low temperature (190 K) to take advantage of the difference in the thermal expansion coefficients of stainless steel and aluminum, which thus provides an interference fit of approximately 0.1 mm. At the same time, disassembly is still possible by cooling to liquid nitrogen temperature.

As may be imagined, the process of getting this model manufactured and assembled

required a considerable effort in development work. To do this, several attempts had to be

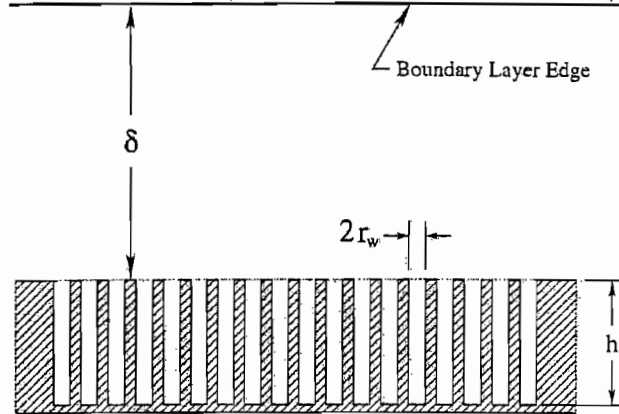


Figure 6. Showing the approximate proportions of the hole diameter, spacing and depth in relation to the laminar boundary layer thickness. With a typical boundary layer thickness of one mm, This makes the desirable hole depth 0.5 mm and the hole diameter and spacing 0.06 mm.

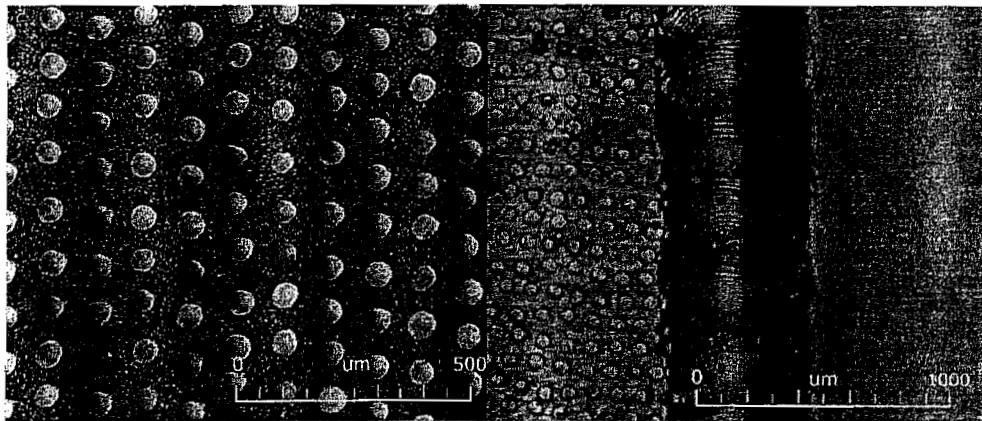


Figure 7. Left: Magnified image of the stainless steel Actionlaser perforated sheet. At this scale the grain boundaries of the metal can be resolved. Note that the length of the half-millimeter scale bar is equal to the depth of the holes. Right: Micrograph of the weld joining the porous and solid sides along a generator of the cone. The weld is 0.5 mm wide.

made in the rolling of the sheet into an accurate conical shape, and in the extremely fine and accurate welding of the sheets. An impression of part of this task is given by the micrographs of Figure 7. The cone was then instrumented with thermocouple heat flux gauges as in the previous experiments. The same procedure for determining the transition location was applied, this time separately on the smooth and on the porous side.

The results obtained in nitrogen flow are shown in Figure 8. They confirm approximately the results of the previous experiments and exhibit a dramatic transition delay on the porous side of the cone. The increase of the transition Reynolds number is typically 400,000 which is as much as 80% at the low-enthalpy end of the range. Both at the low and at the high end of the range, transition could not even be achieved on the porous side, the boundary layer remaining laminar all the way to the end of the cone. The effect is shown dramatically in Figure 9, which shows a shadowgraph that includes the boundary layers on both sides of the cone.

The results for carbon dioxide flows are shown in Figure 10. Again, the data from the solid side of the cone agree with the previous data of Figure 4, and extend these to lower enthalpy, where the transition Reynolds number decreases sharply, confirming the damping effect of the rate processes. However, now we see a very different effect of the porosity. At low enthalpy, transition is delayed by the porosity, but at approximately 3 MJ/kg, a crossover

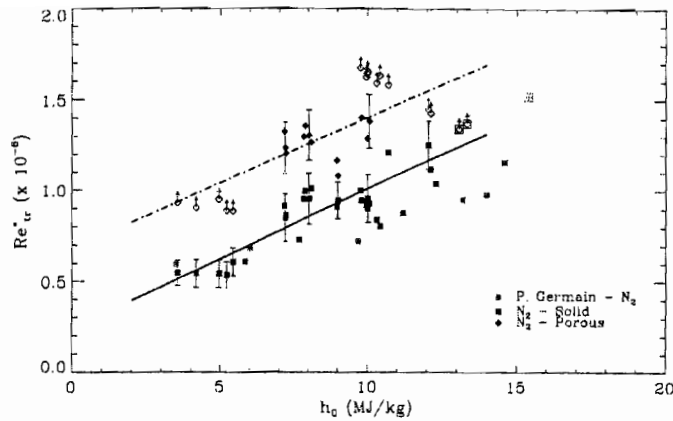


Figure 8. Plot of transition Reynolds number vs total enthalpy for the N₂ data. Dark squares show the results from the non-porous side of the cone. Gray squares show the nitrogen data from Figure 4 for comparison. The filled diamonds show the values from the porous side of the cone. As may be seen, transition is very significantly delayed on the porous side. The open diamonds symbolize situations in which the boundary layer was laminar on the porous side all the way to the end of the cone. In these cases, the Reynolds number plotted is that based on the length of the cone. The lines are linear fits to the points to guide the eye. (For more detail, see Rasheed *et al.* [14])

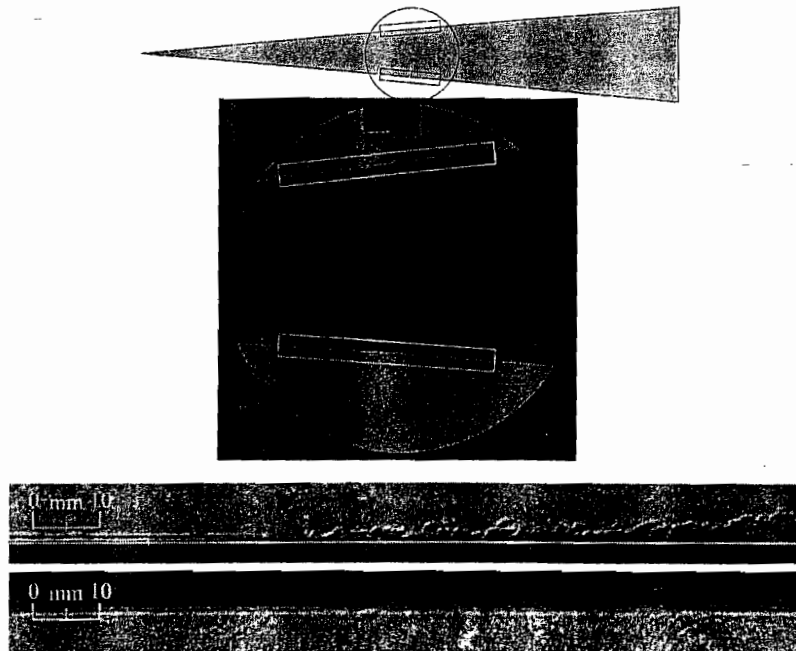


Figure 9. The schematic at the top shows the location of the viewing window relative to the cone. The next frame down shows a shadowgraph taken through this window of nitrogen flow at 9.8 MJ/kg and reservoir pressure of 48.2 MPa. At the top surface, which is the smooth side of the cone, the boundary layer changes from laminar at the left to turbulent at the right, while, at the bottom, it is laminar all the way to the end of the picture. The white rectangular boxes in the main image are shown enlarged at the bottom for a more detailed view.

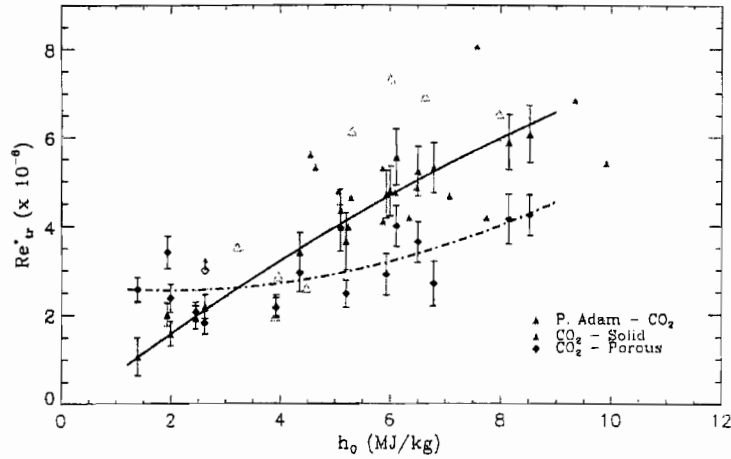


Figure 10. Transition Reynolds number versus total enthalpy in carbon dioxide. Previous data from Figure 5 are shown gray. The triangles and diamonds represent values on the non-porous and porous side respectively. The lines are second order fits to the respective points to guide the eye. Clearly, the porous wall ceases to be active as a means of transition delay at total enthalpy of approximately 3 MJ/kg, and advances transition above this value.

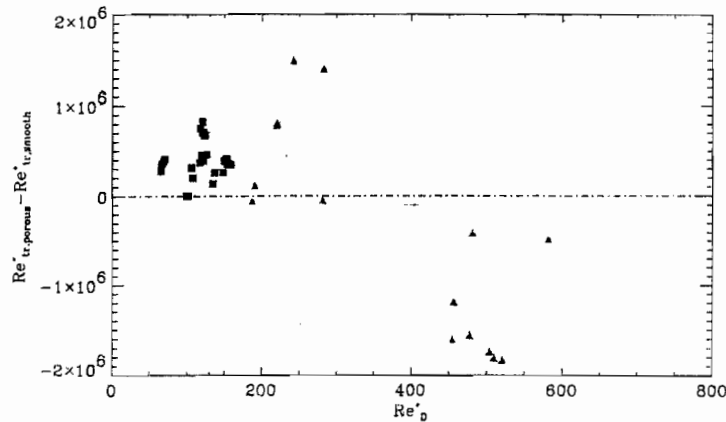


Figure 11. Difference between reference transition Reynolds numbers on the porous side and non-porous side plotted against Reynolds number based on hole diameter. The dark points are cases in which transition was not observed, so they are plotted too low. Note that a cross-over occurs at a Reynolds number of about 300.

occurs, and the porosity causes transition to be advanced at higher enthalpy by as much as 50%. Speculating on what might be the cause of this crossover, one might argue that the rate processes are so active in carbon dioxide that there is not much of the acoustic mode left to damp, or that, perhaps, the high Reynolds number that is reached with the flow still laminar, might make the holes act like roughness elements and cause the boundary layer to be tripped. To examine this question Figure 11 shows a plot of the transition Reynolds number difference (porous minus non-porous) against Reynolds number based on the hole diameter.

In Figure 11, the squares and triangles represent nitrogen and carbon dioxide flows respectively. The dark squares are cases in which the boundary layer remained laminar all the way to the end of the cone, so that they should be plotted at some unknown higher value of the ordinate. The dark gray points are cases where transition was delayed to a known position, and the light gray points are cases where transition was advanced. As may be seen, the crossover occurs at a Reynolds number based on the hole diameter between 200 and 300. Reda's[15]

experiments in a ballistic range indicate that roughness elements cause transition to turbulence if the Reynolds number based on the roughness height is 192 or greater. We conclude that the transition Reynolds number on a smooth cone in carbon dioxide at high enthalpy is so high (as much as 5 times as high as in nitrogen) that the Reynolds number based on the hole diameter is so large as to make the holes act as roughness elements that trip the boundary layer.

IV ATTACHMENT LINE TRANSITION

The dramatic influence of relaxation effects on transition in the case of a slender cone caused us to ask whether it would be possible to change the relation between the most unstable frequency in the boundary layer and the frequency of the strongest relaxation damping effect. Since the most unstable frequency of the second mode is inversely proportional to the

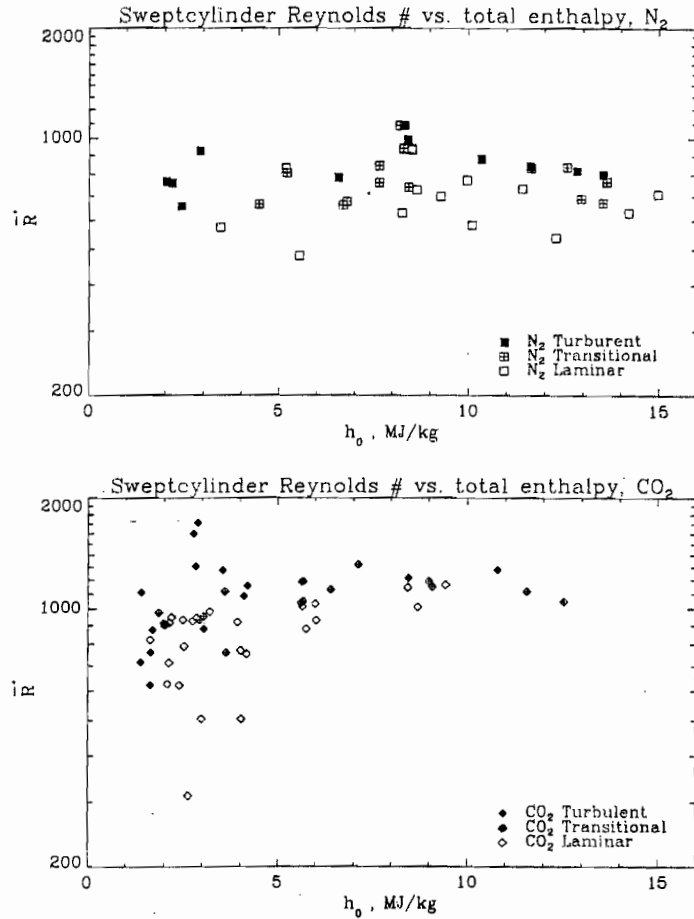


Figure 12 Swept-cylinder Reynolds number plotted against total enthalpy for nitrogen (top) and carbon dioxide (bottom). The full and open symbols represent cases in which the boundary layer is turbulent and laminar respectively, and the symbols with the plus sign show intermittent turbulent and laminar values of the heat flux, *i. e.*, are transitional. Clearly, the swept-cylinder Reynolds number at transition in nitrogen is virtually independent of total enthalpy, while its value in carbon dioxide is not only substantially higher, but exhibits a distinct total enthalpy dependence. (see Fujii and Hornung [17]).

boundary layer thickness, the flow that suggests itself is the boundary layer on a swept cylinder, which has a very small thickness. In addition, for highly cooled wall boundary layers, such as in the T5 flows, the first mode is not active, since the generalized inflection point disappears in

such flows. Thus, we again expect the acoustic mode to be dominant.

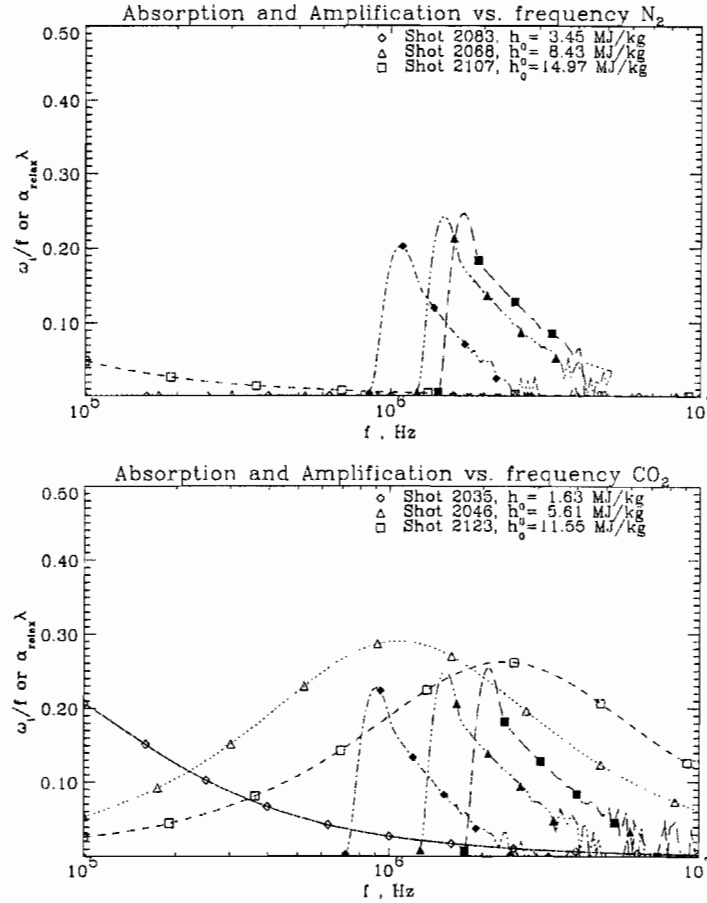


Figure 13. Comparison of the absorption rate per wavelength due to relaxation (open symbol) with the amplification rate per cycle from linear stability calculations for several particular T5 shots. Top: nitrogen, bottom: carbon dioxide. Note how the frequencies of maximum absorption and amplification coincide at high enthalpy in CO₂, while they are widely disparate in N₂.

The appropriate Reynolds number for flow over a swept cylinder is that based on a characteristic length defined as the square root of the kinematic viscosity divided by the stretching rate along the surface in a plane perpendicular to the cylinder axis

$$\eta = \sqrt{\frac{\nu_e}{dw_e/dz}}$$

The Reynolds number defined with this length and evaluated at the reference condition is referred to as the swept-cylinder Reynolds number.

Experiments performed by Creel *et al.* [16] in the quiet tunnel at NASA Langley observed transition when the swept-cylinder Reynolds number was between 650 and 700. The experiments performed in T5 were with a 50 mm diameter cylinder swept at 60deg, and equipped with surface thermocouple heat flux gauges. The results are shown in Figure 12 for both nitrogen and carbon dioxide. Note that, again, the transition Reynolds number is significantly higher in carbon dioxide than in nitrogen. Also, CO₂ shows a dependence on total enthalpy whereas this is absent in nitrogen. An important feature of these results is that the transition Reynolds number is as high or higher than the value from the quiet tunnel, ranging up

to 1100 in CO₂.

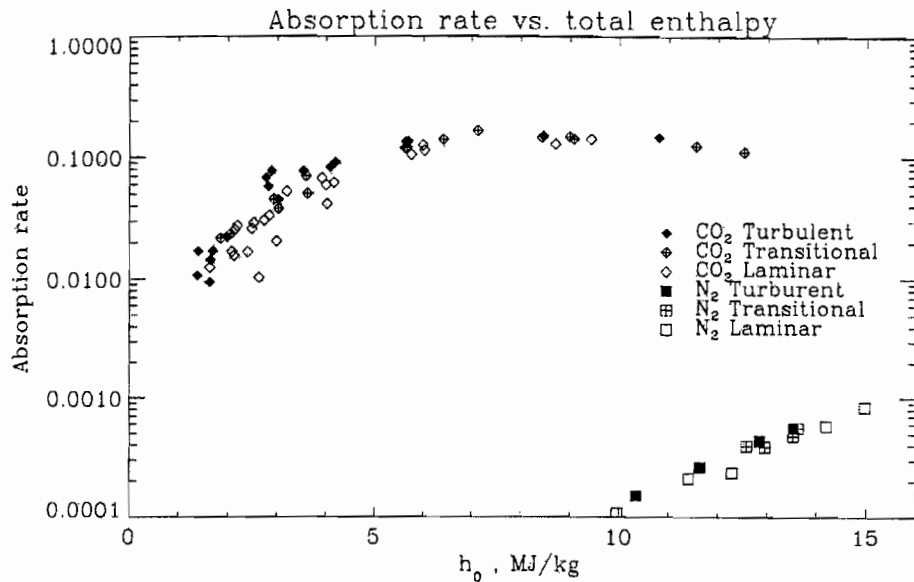


Figure 14. Absorption rate per wavelength for all the experiments performed on the swept cylinder as a function of total enthalpy.

In order to examine the reasons for this behavior, the theory of sound absorption by relaxation phenomena presented by Clarke and McChesney[18] was extended to cases where multiple modes of relaxation are active. Furthermore, the amplification rate per cycle of the acoustic mode was calculated using non-relaxing laminar boundary layer calculations with the axisymmetric analogy proposed by Cooke[19]. Details of these calculations can be found in Fujii and Hornung[17]. For this presentation we only show the results, see Figure 13. From these two diagrams, it is clear that the frequency at which maximum growth would be observed is right in the region where the strongest damping occurs in the case of CO₂, while virtually no damping may be expected in the case of N₂.

Plotting the absorption rates versus total enthalpy in Figure 14 for all the experiments, the difference between the two gases is brought out dramatically. The curve for CO₂ follows the behavior of the swept-cylinder transition Reynolds number of Figure 12 qualitatively.

V. CONCLUSIONS

An extensive series of experiments performed in the high-enthalpy shock tunnel T5 demonstrate conclusively that the relaxation processes of vibrational excitation and dissociation can have very dramatic stabilizing effects on transition in flows over slender cones and over swept cylinders. The mechanism by which this damping occurs is through the influence of relaxation on acoustic waves. In addition it was demonstrated that transition could be delayed very significantly by suitable blind porosity of the surface in the case of the slender cone. In both cases the effects are large, so that they must become part of the equipment of design teams.

ACKNOWLEDGEMENTS

The work described in this paper was supported by AFOSR Grants F49610-92-J-0110, (Dr. L. Sakell), F49620-93-1-0338, (Dr. J. Tishkoff), and F49620-98-1-0353, (Dr. S. Walker).

REFERENCES

1. Mack, L.M. Boundary-Layer Stability Theory, Special Course on Stability and Transition of

- Laminar Flow, AGARD Report Number 709, 1984.
2. Demetriades, A., An Experiment on the Stability of Hypersonic Laminar Boundary Layers, *Journal of Fluid Mechanics*, 7(3):385-396, 1960.
 3. Stetson, K.F., Thompson, E.R., Donaldson, J.C., and Siler, L.G. Laminar Boundary Layer Stability Experiments on a Cone at Mach 8. Part I: Sharp Cone, AIAA Paper 83-1761, 1983 (16th Fluid and Plasma Dynamics Conference, July 12-14, Danvers, MA, USA).
 4. Kendall, J.M., Wind Tunnel Experiments Relating to Supersonic and Hypersonic Boundary-Layer Transition, *AIAA Journal*, 13(3):290-299, 1975.
 5. Reshotko, E., Boundary-Layer Stability and Transition, *Annual Review of Fluid Mechanics*, 8:311-349, 1976.
 6. Malik, M.R. and Anderson, E.C., Real Gas Effects on Hypersonic Boundary-Layer Stability, *Physics of Fluids A*, 3(5):803-821, 1991.
 7. Stuckert, G. and Reed, H., Linear Disturbances in Hypersonic, Chemically Reacting Shock Layers, *AIAA Journal*, 32(7):1384-1393, 1994.
 8. Johnson, H.B., Seipp, T., and Candler, G.V., Numerical Study of Hypersonic Reacting Boundary Layer Transition on Cones, *Physics of Fluids*, 10(10):2676-2685, October 1998.
 9. Germain, P. and Hornung, H.G., Transition on a Slender Cone in Hypervelocity Flow, *Experiments in Fluids*, 22:183-190, 1997.
 10. Demetriades, A. Hypersonic Viscous Flow over a Slender Cone. Part III: Laminar Instability and Transition, AIAA Paper 74-535, 1974 (7th Fluid and Plasma Dynamics Conference, June 17-19, Palo Alto, CA, USA).
 11. DiCristina, V., Three Dimensional Laminar Boundary Transition on a Sharp 8 deg Cone at Mach 10, *AIAA Journal*, 8(5):852-856, 1970.
 12. Adam, P. and Hornung, H.G., Enthalpy Effects on Hypervelocity Boundary Layer Transition: Ground Test and Flight Data, *Journal of Spacecraft and Rockets*, 34(5):614-619, 1997
 13. Fedorov, A.V. and Malmuth, N.D., Hypersonic Flow Stabilization by Ultrasonically Transparent Wall, Technical Report SCNM96-1, Rockwell Science Center, 1996. see also Fedorov, A.V., Malmuth, N.D., Rasheed, A. and Hornung, H.G., Stabilization of hypersonic boundary layers by porous coatings, *AIAA Journal* 39: 605-610, 2001.
 14. Rasheed, A., Hornung, H.G., Fedorov, A.V., and Malmuth, N.D. *AIAA Journal* (accepted for publication)
 15. Reda, D.C. Roughness-Dominated Transition on Nosetips, Attachment Lines and Lifting-Entry Vehicles, AIAA Paper 2001-0205, 2001 (39th AIAA Aerospace Sciences Meeting and Exhibit, January 8-11, Reno, NV, USA).
 16. Creel, T.R., Beckwith, I.E. and Chen, F.J., Transition on swept leading edges at Mach 3.5 *Journal of Aircraft*, 24(10):710-717, October 1987.
 17. Fujii, K. and Hornung, H.G., An experiment of high-enthalpy effect on attachment line transition AIAA Paper 2001-2779, 2001.
 18. Clarke, J.F., and McChesney, M. *The Dynamics of Real Gases*. Butterworths, 1964.
 19. Cooke, J.C. An axially symmetric analogue for general three-dimensional boundary layers, Technical Report R&M 3200, British Aeronautical Research Council, 1961.

CLASS NOTES: Ae 234

17. Flow Over A Convex Corner

The maximum speed that a flow can reach by adiabatic expansion from a given state is determined by the energy equation

$$h' + \frac{V'^2}{2} = h'_0 \quad (17.1)$$

as

$$V'_{\max} = \sqrt{2h'_0}, \quad (17.2)$$

provided that all of the enthalpy can be converted into kinetic energy in the expansion. In the case of the IDG, (17.1) reads

$$R' \{(4 + \alpha)T' + \alpha\theta'_d\} + \frac{V'^2}{2} = h'_0, \quad (17.3)$$

where $R' = \frac{k'}{2m'}$ is the specific gas constant for the molecular gas. Hence

$$V' = \sqrt{2h'_0 - 2R' \{(4 + \alpha)T' + \alpha\theta'_d\}}. \quad (17.4)$$

If the gas is in equilibrium throughout the expansion, it will be completely recombined as the temperature drops, and all the energy contained in the dissociation will be recovered. Hence, for equilibrium flow, equation (17.2) applies. On the other hand, if the flow freezes during the expansion at some value of α , say α_0 , then an amount

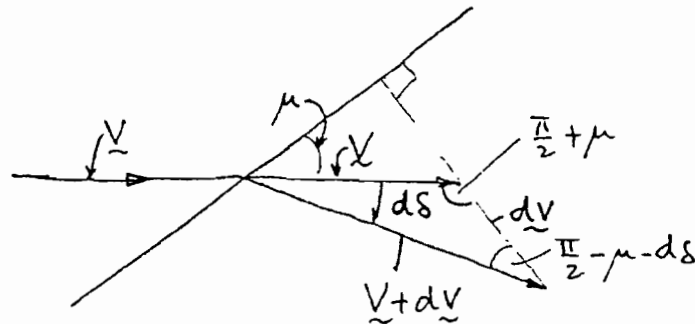
$$\alpha_0 R' \theta'_d$$

of energy remains locked in the dissociation and does not become available to the kinetic energy of the flow. Consequently, the maximum speed in the case of frozen flow is reduced to

$$V'_{\max} = \sqrt{2(h'_0 - R' \alpha_0 \theta'_d)}. \quad (17.5)$$

We want to map expansion flows in the $V\delta$ -plane. Consider a weak expansion wave or a Mach line that deflects a flow through a small angle $d\delta$ and increases the velocity vector

\underline{V} by a small amount $d\underline{V}$. The wave is able to impart momentum to the fluid only in a direction normal to itself. Hence $d\underline{V}$ must be at right angles to the wave.



It follows that

$$\begin{aligned} \frac{|\underline{V} + d\underline{V}|}{\underline{V}} &= \frac{\sin\left(\frac{\pi}{2} + \mu\right)}{\sin\left[\frac{\pi}{2} - (\mu + d\delta)\right]} = \frac{\cos \mu}{\cos(\mu + d\delta)} = \frac{\cos \mu}{\cos \mu \cos d\delta - \sin \mu \sin d\delta} \\ &= \frac{1}{1 - \tan \mu \cdot d\delta} = 1 + \tan \mu \cdot d\delta \text{ for } d\delta \rightarrow 0. \end{aligned}$$

If

$$d\delta \rightarrow 0 \left. \vphantom{\frac{|\underline{V} + d\underline{V}|}{\underline{V}}} \right\} \frac{|\underline{V} + d\underline{V}|}{\underline{V}} = 1 + \frac{|d\underline{V}|}{|\underline{V}|} + 0(\delta^2) = 1 + \frac{dV}{V}.$$

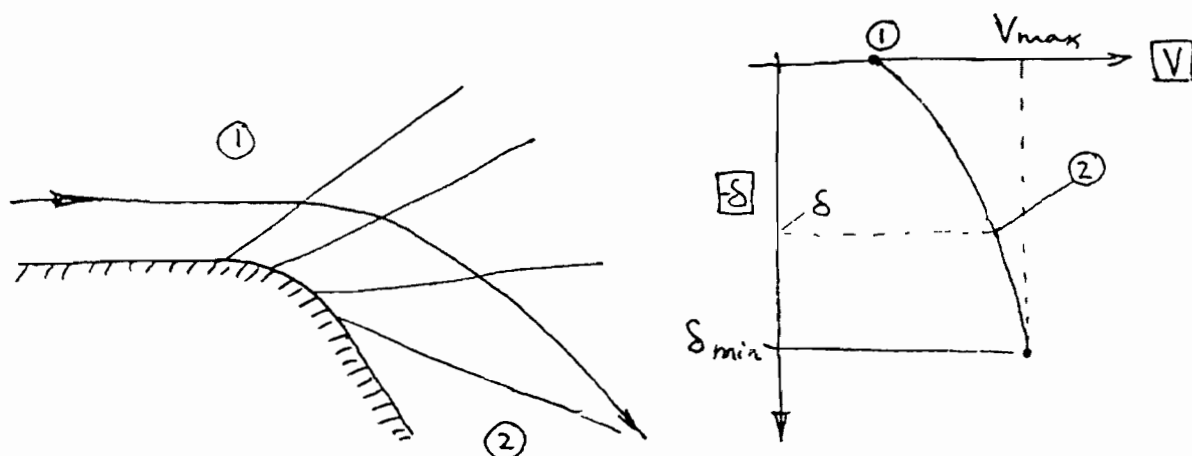
Hence

$$\frac{d\delta}{dV} = \frac{\cot \mu}{V},$$

or

$$\boxed{\frac{d\delta}{dV} = -\frac{\sqrt{V^2/a^2 - 1}}{V}}, \quad (17.6)$$

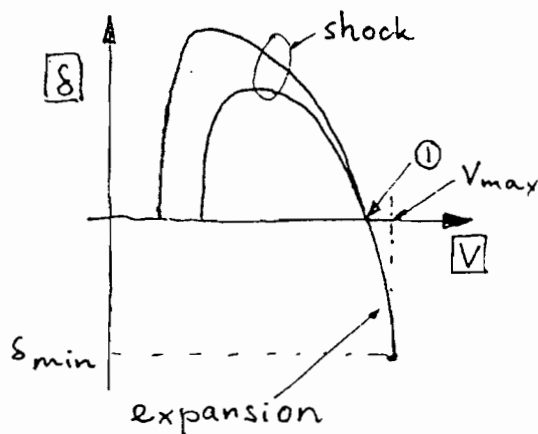
since $\sin \mu = \frac{a}{V}$, being the speed of sound. (17.6) is the differential equation of Prandtl-Meyer flow, see Liepmann & Roshko, Vincenti & Kruger etc.. In order to make further use of (17.6) it is necessary to relate the speed of sound to V via the energy equation and the caloric equation of state. In the case of a perfect gas, the equation may be integrated



formally and a final state (2) may be related to an initial state (1) and a total turning angle.

It turns out that to each initial state there corresponds a maximum value of $|\delta| = |\delta_{\min}|$ which is reached when the flow is fully expanded to the maximum velocity corresponding to that initial state.

If the initial state is undissociated ($\alpha_1 = 0$), no further recombination can occur and there is no difference between frozen and equilibrium flow. This is in contrast to the case of deflection by a shock.

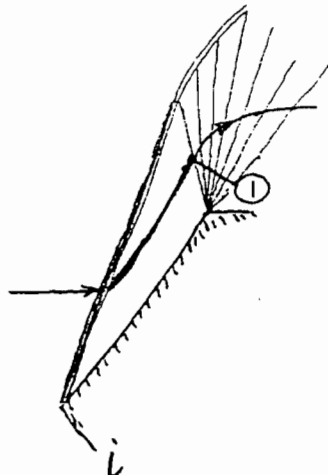


The difference between the maximum speed and V_1 depends on the Mach number. For example, in frozen flow,

$$\frac{V_{\max} - V_1}{a_1} = \sqrt{\frac{2}{\gamma - 1}} \sqrt{1 + \frac{\gamma - 1}{2} M_1^2} - M_1. \quad (17.7)$$

As may be seen, this goes to zero as $M_1 \rightarrow \infty$.

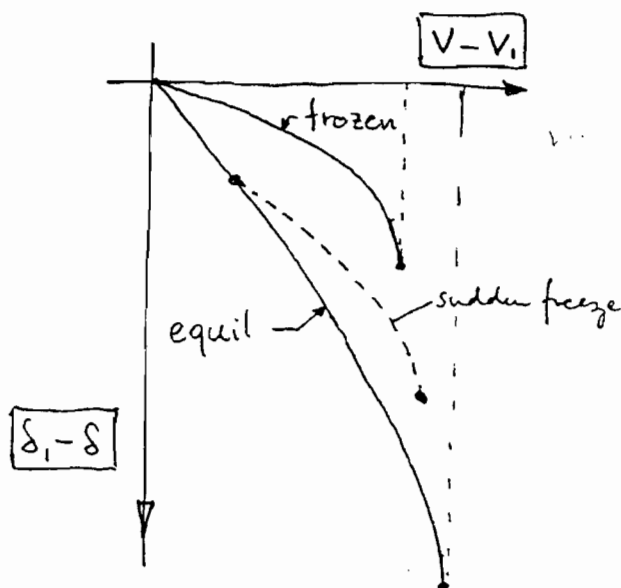
A more interesting case to consider is that where the *initial state is dissociated*, such as occurs, for example at the trailing edge of a wedge, where a shock causes the initial dissociation and an expansion occurs from the dissociated state.



This flow exhibits two important differences between equilibrium and frozen flow:

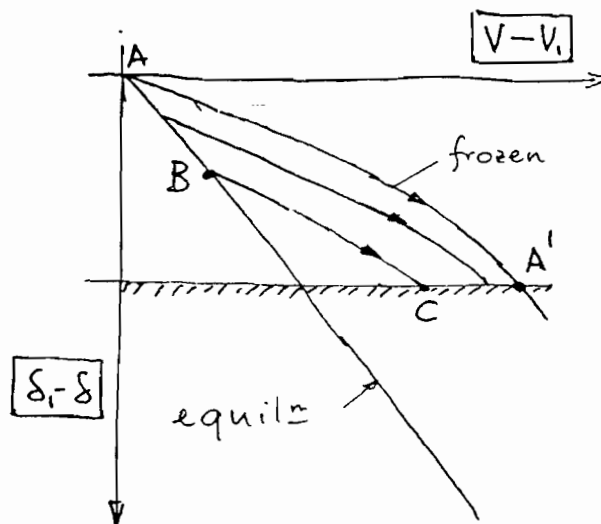
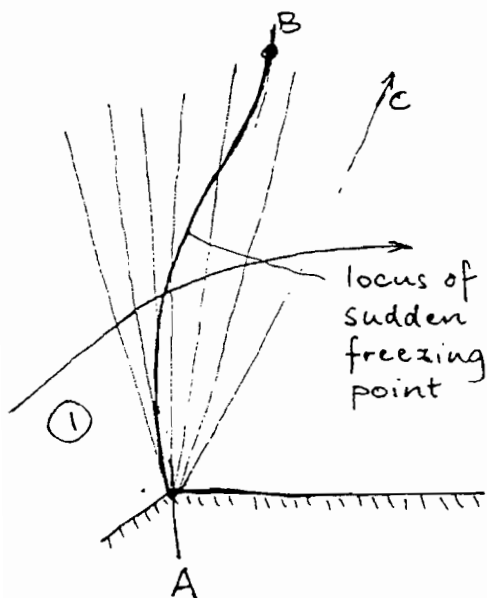
First, the maximum speed that is reached from the dissociated initial state is different (see eqn. (17.5)).

Second, the path along which the streamline map proceeds in the $V\delta$ -plane is different in the two cases. In order to illustrate this, the δV -map is drawn here with an exaggerated V -scale and relative to the state (1). In this diagram we also show as a dashed line the streamline map that would be observed if the flow were to proceed in equilibrium first and sudden freezing were occurring within the expansion.

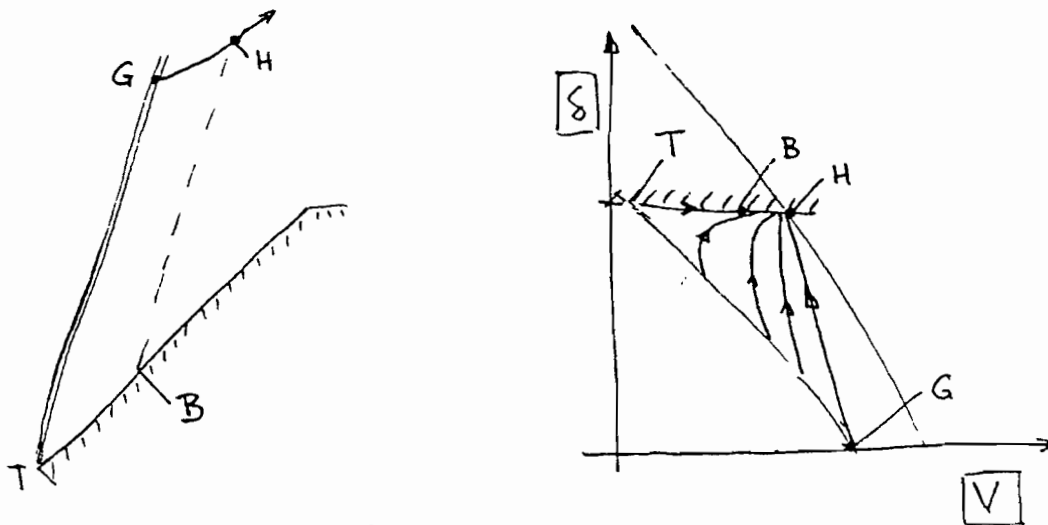


This flow would exhibit an intermediate V_{\max} and an intermediate δ_{\min} . Sudden freezing is actually a good model for this flow. Clearly, however, the freezing will occur further downstream from the first Mach wave for streamlines further from the corner, because the recombination rate demanded by the flow is smaller there (passage time through expansion longer). Hence, even for an assumed uniform state along the first Mach wave, the state at the last Mach wave will not be uniform. The next diagram illustrates the features of the flow in the physical and the $V\delta$ -plane, for the case $|\delta| < |\delta_{\min \text{ frozen}}|$.

The point A in the physical plane maps into the line AA^1 in the $V\delta$ -plane. The point B indicates the angle downstream of which no recombination occurs, no matter how far the streamline is away from the surface.



Clearly, there exists a velocity gradient across the flow after the expansion: $C - A^1$, the higher speed occurring near the wall. This is in contrast to the case of flow over a wedge where vorticity of the opposite sign is generated by the nonequilibrium, see sketch.



The expansion flows considered in this section assume that some recombination does occur in the expansion. For this to be the case it is necessary for the product of density and size of the flow (ρL) to be much larger than in the flows that exhibit dissociation quenching. In the large class of particularly important flows where the latter is true, it is therefore not necessary to consider nonequilibrium effects in expansion around a convex corner. In these flows the frozen expansion curve in the $V\delta$ -plane is appropriate.

Ae234 Summary

1 Introduction

In an introductory part, background information on chemical thermodynamics was presented, including:

Chemical equilibrium corresponds to minimization of the Gibbs Function, This leads to the Law of Mass Action.

A review of Statistical Mechanics showed how the Law of Mass Action can be formulated in terms of the partition functions of the chemical species.

It was shown how, in the case of a symmetrical diatomic gas, the Law of Mass Action and the caloric properties of the gas may be approximated by a particularly simple equation, Lighthill's ideal dissociating gas (IDG).

The non-equilibrium behavior of the IDG was shown to be well approximated by the Freeman model.

2 Normal shock

The features of the flow after an equilibrium and a non-equilibrium normal shock were derived. In the relaxation zone the density, temperature and velocity are most strongly affected, while the pressure and enthalpy are practically constant after the shock.

3 Speed of sound, nozzle flows

It was shown that the speed of sound is smaller in equilibrium flow than in frozen flow.

The singularity at the throat in steady expansion equilibrium nozzle flows is displaced downstream of the geometrical throat when the recombination reaction proceeds at a finite rate.

Because the recombination rate is proportional to the square of the density, the rapid drop in density in a nozzle expansion causes the recombination to stop fairly suddenly at some point, a phenomenon called sudden freezing. The composition of the flow is constant thereafter. In contrast to flow downstream of a shock, non-equilibrium in nozzle flows most strongly affects the pressure and temperature, and has practically no influence on the density and velocity.

4 Oblique and curved shock

The flow after an oblique shock follows directly from the normal shock results. It is convenient to map the flow into the $V\delta$ -plane, in which the frozen and equilibrium shock locuses are different, and the streamline can be mapped.

In a small range of shock angles, the flow immediately downstream of the frozen shock is subsonic and accelerates to supersonic flow again. This behavior of the sonic line has implications for shock detachment (see wedge flow later).

The equations for the flow immediately downstream of a curved shock were solved to write down expressions for the gradients at the shock. This led to a number of results, including the streamline curvature and behavior of the streamline in the $V\delta$ -plane. The gradient of any quantity has two contributions. One from the shock curvature and one from the chemical reaction.

It was shown how a simple argument using the $V\delta$ - map can be used to predict that the process of shock detachment from a wedge is much more gradual in relaxing flow than in frozen or equilibrium flow. This was shown to be substantiated dramatically by experiments and computation. Similar behavior is exhibited by shock detachment from a cone.

5 Blunt-body flows

An analysis was presented that led to an analytical result about the shock stand-off distance on a sphere showing its dependence on a reaction rate parameter and on a parameter measuring the flow kinetic energy in terms of the dissociation energy. The reaction rate parameter was formulated for a complex gas (rather than IDG), and illustrates the way in which the reaction rate enters the flow problem.

The phenomenon of reaction quenching was presented, in which the cooling caused by the shock curvature causes the dissociation reaction to be terminated. In the case when the quenching occurs close to the shock, a boundary layer type of analysis was presented that is able to formulate effective shock jump conditions for the flow downstream of the quenching line. These shock jump conditions incorporate shock curvature, reaction rate parameter and kinetic energy parameter in addition to the usual oblique shock parameters.

The curved shock on a blunt body generates vorticity that is concentrated around the streamline that crosses the shock at a shock angle of about 60° . It was shown by computations that the shear layer thus generated becomes unstable within a few nose radii of the nose if the density ratio across a normal shock is 14 or higher, as is the case in strongly dissociating blunt body flows. Experimental results were presented that dramatically confirm this instability.

6 Transition

It was shown that chemical or vibrational relaxation absorbs sound if the frequency is near the inverse relaxation time. In high Mach number flows, the instability that leads to transition of a laminar boundary layer to turbulence is acoustic in nature. Relaxation processes could therefore delay transition.

Experimental results were presented that show dramatically that transition delays of up to a factor of 5 can be achieved through this phenomenon. Results from linear stability computations were presented that support the idea that the observed transition delay was caused by the damping of acoustic noise through relaxation.

Results were also presented that showed that transition could be delayed by suitable wall porosity, thus further substantiating the acoustic instability.

7 Experimental flow simulation

Arguments were presented (power, material) that led to the need to operate hypervelocity flow simulation facilities for short test times. Quick heating need suggests shock waves. The most successful arrangements are the reflected shock tunnel and the expansion tube. The need to heat the driver follows from the requirement to achieve flow speeds of 6 km/s. Performance and limitations of the facility types were discussed.

8 Conclusion

This course aimed to characterize the influence of relaxation on the elements of gasdynamics. Many of the discoveries in this field are not yet documented in textbooks, and some of them have very important implications for design of entry vehicles and heat shields. They may even become useful to you some day.

